UNIVERSITY OF AMSTERDAM

UvA-DARE (Digital Academic Repository)

Mechanistic investigations of metal-catalyzed (poly)esterification reactions

Wolzak, L.A.

Publication date
2022
Document Version
Final published version

Link to publication

Citation for published version (APA):
Wolzak, L. A. (2022). *Mechanistic investigations of metal-catalyzed (poly)esterification reactions*.

General rights
It is not permitted to download or to forward/distribute the text or part of it without the consent of the author(s) and/or copyright holder(s), other than for strictly personal, individual use, unless the work is under an open content license (like Creative Commons).

Disclaimer/Complaints regulations
If you believe that digital publication of certain material infringes any of your rights or (privacy) interests, please let the Library know, stating your reasons. In case of a legitimate complaint, the Library will make the material inaccessible and/or remove it from the website. Please Ask the Library: https://uba.uva.nl/en/contact, or a letter to: Library of the University of Amsterdam, Secretariat, Singel 425, 1012 WP Amsterdam, The Netherlands. You will be contacted as soon as possible.

UvA-DARE is a service provided by the library of the University of Amsterdam (https://dare.uva.nl)

Download date:11 Nov 2022

Mechanistic investigations of metal-catalyzed (poly)esterification reactions

Lukas Wolzak

Mechanistic investigations of metal-catalyzed (poly)esterification reactions

ACADEMISCH PROEFSCHRIFT

ter verkrijging van de graad van doctor
aan de Universiteit van Amsterdam
op gezag van de Rector Magnificus
prof. dr. ir. K.I.J. Maex
ten overstaan van een door het College voor Promoties ingestelde commissie,
in het openbaar te verdedigen in de Agnietenkapel
op dinsdag 5 juli 2022, te 15.00 uur

door
Lukas Adriaan Wolzak
geboren te Hoorn

Promotiecommissie

Promotoren	prof. dr. M. Tromp	Rijksuniversiteit Groningen
		Universiteit van Amsterdam
	prof. dr. J.N.H. Reek	Universiteit van Amsterdam
Copromotor	dr. T.J. Korstanje	
Overige leden	prof. dr. R.W. Fischer	Technische Universität München
	prof. dr. Ir. A.J. Minnaard	Rijksuniversiteit Groningen
	prof. dr. G.J.M. Gruter	Universiteit van Amsterdam
	prof. dr. J.H. van Maarseveen	Universiteit van Amsterdam
	dr. J.C. Slootweg	Universiteit van Amsterdam
	prof. dr. B. de bruin	Universiteit van Amsterdam

Faculteit der Natuurwetenschappen, Wiskunde en Informatica

ISBN: 978-94-6421-775-9

MIX
Paper from responsible sources
FSC® C128610
FSC www.fsc.org

The research described in this thesis was carried out at the Van 't Hoff Institute for Molecular Sciences, University of Amsterdam, the Netherlands, and is financially supported by the Advanced Research Center for Chemical Building Blocks (ARC CBBC) which is co-founded and co-financed by the Netherlands Organization for Scientific Research (NWO, contract 736.000.000) and the Netherlands Ministry of Economic Affairs and Climate.

“It’s as close as chemists can ever come to magic”

Benjamin List on the science of catalysis

Table of Contents

Chapter 1

Metal-catalyzed (poly)esterification reactions

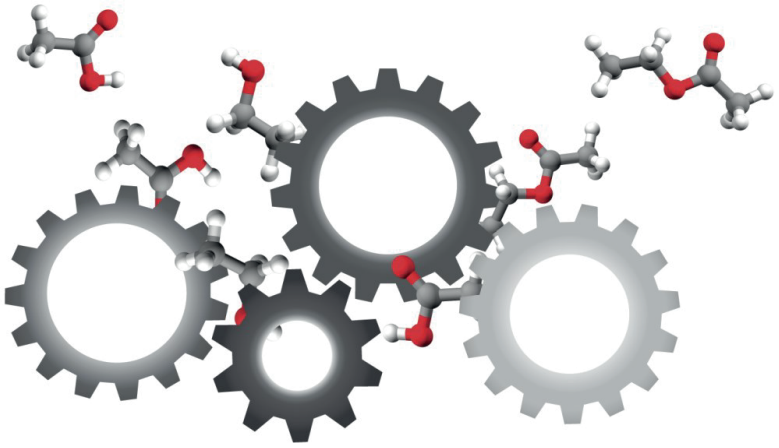

Introduction

The ester functionality is a prominent structural motif in nature. It gives many plants and fruits their pleasant aroma, and it is present in our bodies a.o. in the form of fatty acids esters such as glycerides. Moreover, these lipids are a crucial source of animal fats and vegetable oils.[1,2] Besides esters of natural origin, also man-made organic molecules containing the ester linkage find widespread use in our society (Figure 1.1).[3,4] The ester bond can be found in pesticides, herbicides and pharmaceuticals such as aspirin, fenofibrate and tamiflu.[5–7] In addition, the ester moiety is essential in the food and cosmetic industry as it is a structural element in preservatives, flavoring agents and fragrances.[8–12] Apart from fine chemicals, esters are ubiquitous structural motifs in lubricants, surfactants, biofuels and solvents.[13–16] Furthermore, polymers based on the ester moiety form another important class of ester-containing products. Polyesters for instance, are versatile polymers that are indispensable for the production of plastics, fibers, packaging, elastomers, coatings and paints.[17–20]

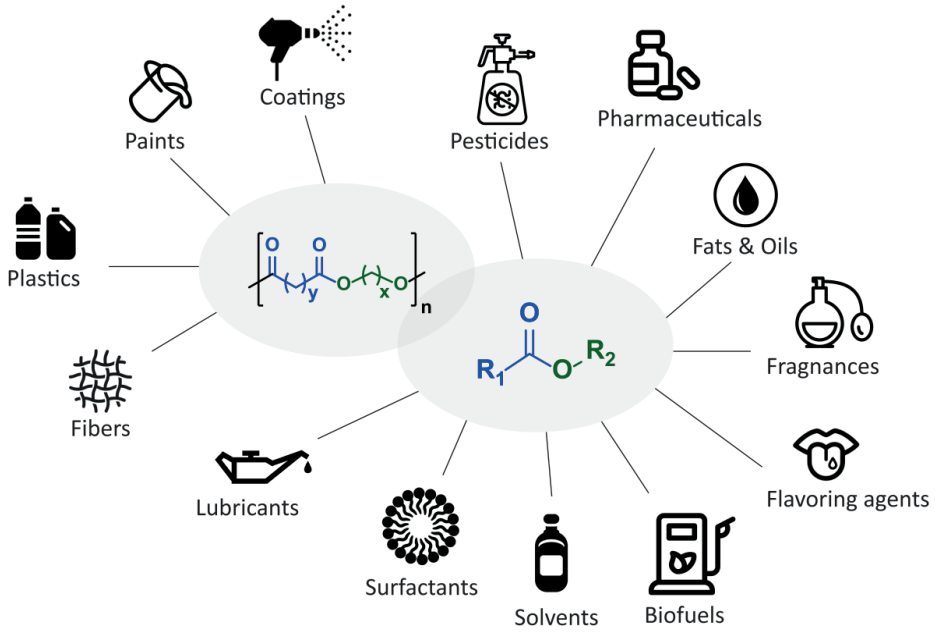

Figure 1.1. Ester- and polyester-containing products.

1.1 Ester synthesis

Given the omnipresence of ester-containing molecules in our society, the development of sustainable industrial routes to manufacture them is important. This requires an efficient utilization of materials, as well as the elimination of waste products and hazardous substances.[21–25] To meet this demand, the following aspects during ester synthesis need to be avoided: 1) the generation of side products that are considered waste, 2) the need for stoichiometric amounts of coupling reagents, 3) a non-equimolar stoichiometry of the substrates. Other factors that need consideration are: 4) the type of solvent used or solvent-free conditions, 5) the amount of energy required for the reaction and 6) the use of a catalyst, which can reduce the reaction time, the reaction temperature and direct selectivity when required.

In general, esters are synthesized via the coupling of two functional groups, which results in the ester product and a side product. The nature of this side product determines to a large extent how sustainable the reaction is. For example, the use of activated substrates, such acyl chlorides and acid anhydrides, results in the formation of side products that are considered waste. To separate these from the desired ester product requires undesirable additional purification steps (Figure 1.2A).[3]

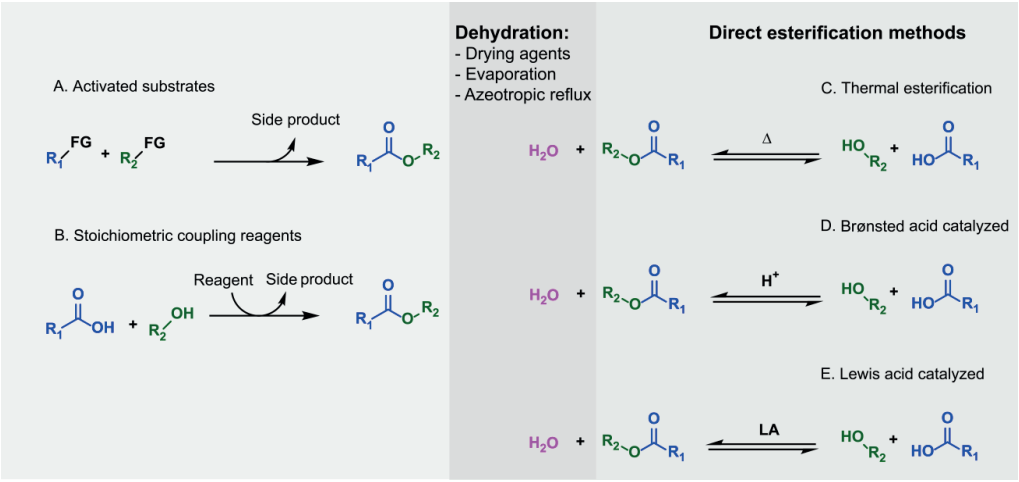

Figure 1.2. Methods for ester synthesis.

The formation of ester bonds with the help of stoichiometric coupling reagents, to *in situ* form activated substrates, is another important synthetic organic methodology. A wide

variety of different stoichiometric coupling reagents such as dicyclohexylcarbodiimide (Steglich esterification)[26], triphenylphosphine in combination with an azodicarboxylate (Mitsunobu reaction)[27], benzoic anhydrides (Shiina esterification)[28] or 2,4,6-trichlorobenzoylchloride (Yamaguchi esterification)[29] are commonly applied for small-scale ester synthesis. However, the application of stoichiometric coupling reagents also leads to the formation of unwanted waste products (Figure 1.2B).[30,31] The poor atom economy of these reactions makes them unviable as routes for the production of bulk chemical on an industrial scale. In contrast, the direct coupling of carboxylic acids and alcohols has the advantage that only water is formed as a side product (Figure 1.2C, D and E), resulting in a significantly lower environmental impact. The unfavorable thermodynamics of these reactions, however, lead to a reaction equilibrium. In order to drive the equilibrium towards ester formation, several strategies can be employed: 1) usage of an excess of carboxylic acid or alcohol, 2) the application of dehydrating agents such as NaH, $MgSO_4$, SiO_2, $(Me_2SiO)_4$ or molecular sieves to sequester the stoichiometrically formed reaction water, or (3) evaporation or azeotropic distillation to drive the formed reaction water out of the reaction mixture.

The utilization of an excess of substrate or dehydrating agent is often undesirable as it results in additional waste products and/or contamination of the ester product. Evaporation or azeotropic distillation is therefore the preferred route to remove water from the reaction mixture at an industrial scale. Hereby, the equilibrium is shifted towards the reaction products and complete conversion of the carboxylic acid and alcohol substrate can be achieved. Elevated temperatures are however required to enable evaporation or distillation conditions. To sustain high reaction temperatures a considerable amount of energy is required. In addition, the harsh reaction conditions required for removal of water are not compatible with sensitive substrates and esters products. Overall, direct esterification provides a sustainable route towards the ester functionality. The applicability of this reaction is however impeded due to the requirement for harsh reaction conditions to ensure dehydration via evaporation or azeotropic distillation.

1.2 Polyester synthesis

For the synthesis of polyesters, the step-growth polymerization of diols with diacids or the self-condensation of hydroxyl acids is a frequently used method (Figure 1.3).[32] These

monomers can also be readily obtained from biomass, providing a route towards renewable polyesters.[18,33–35] Similar to ester synthesis, the unfavorable equilibrium conditions require a strategy to enable the complete transformation of substrates into the desired polyester. For the synthesis the use of a large excess of one of the substrates or a dehydrating agent is not viable. Therefore, high temperatures and additionally reduced pressure are often required to remove the formed water from the reaction mixture. Due to these harsh conditions, certain problems commonly appear. More specifically, the volatility of monomers, the thermal instability of monomers and polyesters and the formation of side products can cause a disbalance in the stoichiometry.[18] To circumvent these difficulties, a two-step procedure is often followed. In the initial step, esterification is performed to obtain oligomers and the water side product is distilled off. In the subsequent polycondensation step, the oligomers form the desired polyester by increasing the temperature and reducing the pressure (Scheme 1.3A and B). Alternatively, polyesters can be obtained via a transesterification reaction starting from the dimethyl ester and an excess of diol to obtain oligomers with an alcohol end group. In the subsequent polycondensation step the polyester is then formed via transesterification reactions. Thereby any esterification steps and the formation of water are avoided (Scheme 1.3C). High temperatures are required for all these step-growth polyester synthesis routes which hampers the development of complex architectures and highly functionalized polymers with controllable properties.

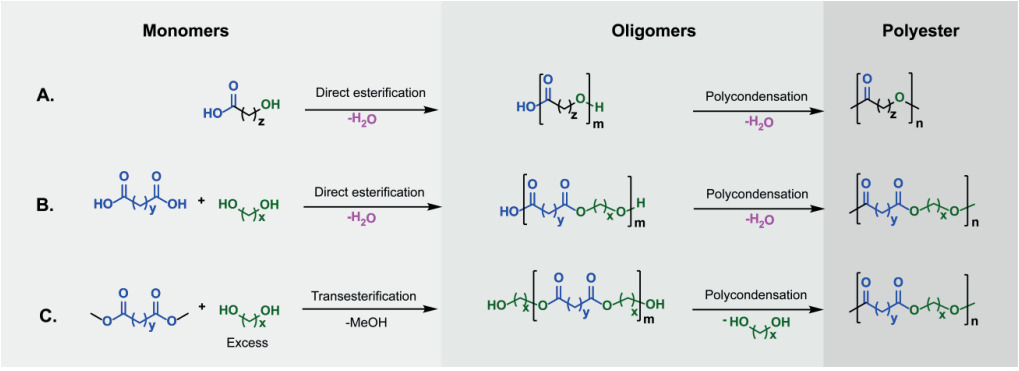

Figure 1.3. Step-growth polyester synthesis.

2. Catalysis

Given the demanding conditions required for the direct esterification of carboxylic acids and alcohols, catalysts that can enable mild reaction conditions are highly desirable (Figure 1.2D and E). The literature offers numerous examples of different direct (poly)esterification catalyst, which can be categorized as: 1) Brønsted acids, 2) Lewis acids, 3) Enzymatic catalysts.[36–40] Although a wide variety of different direct (poly)esterification catalysts is reported, there is still a need for novel catalysts. Since they can enable mild reaction conditions, shorten reaction times and steer selectivity. Ideally, these catalyst need to be based on abundant and non-toxic materials. Besides the search for novel catalysts there is also a need for strategies to overcome the unfavorable equilibrium conditions without the need for dehydration methods, as such ensuring a complete conversion of equimolar amounts of reactants into products under mild reaction conditions.[41] Therefore significant efforts have been directed towards the development of such direct (poly)esterification protocols. This has resulted in various catalytic methods where the catalytic center is protected from the formed reaction water, for example via the application of hydrophobic pockets, micelles or biphasic systems.[42–49] Importantly, in these systems the catalyst is designed as such that it is involved in creating the desired reaction environment. Lewis or Brønsted acidic catalysts decorated with long alkyl or even fluoroalkyl tails are prime examples, as these additional groups can provide a hydrophobic environment around the catalytic center or make the catalyst reside in the apolar solvent in biphasic systems.[50]

2.1 Brønsted Acids

In the initial phase of the reaction the direct esterification reaction is catalyzed by the carboxylic acid itself. However, this effect rapidly decreases when the reaction progresses and the concentration of carboxylic acid reduces. Consequently, long reaction times are required to reach equilibrium. As early as 1895, Fischer and Speier reported on direct esterification catalyzed by strong Brønsted acids.[51] Nevertheless, Brønsted acid such as H_2SO_4, HCl, triflic acid, *p*-toluenesulfonic acid (PTSA), H_3PO_4 and polyphosphoric acid are still relevant catalysts in industry.[3,18] Operational concerns however arise due to the corrosive nature of the strong Brønsted acids. Therefore the *in situ* generation of strong Brønsted acids via more benign precursors such as tert-butyl-nitrite[52] or CBr_4 (via the photoirradiation)[53] is more desirable.

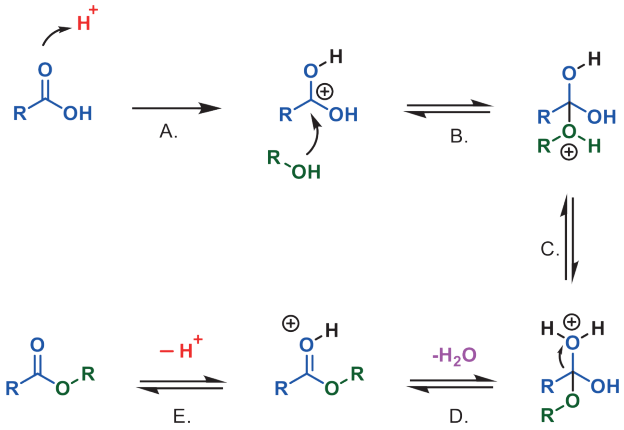

Figure 1.4. Brønsted acid-catalyzed esterification of carboxylic acid and alcohol.

The catalytic role of the strong Brønsted acid starts by activation of the carbonyl moiety of the carboxylic acid, to make it more susceptible to the nucleophilic attack of the alcohol (Figure 1.4A). After this nucleophilic attack (Figure 1.4B), proton transfer to one of the hydroxy groups provides a new oxonium ion (Figure 1.4C). Subsequent loss of water (Figure 1.4D) and deprotonation affords the ester product (Figure 1.4E). Although strong Brønsted acids are very effective (poly)esterification catalysts, they also catalyze side reactions. This could result in the unwanted dehydration of alcohols, self-condensation of alcohols and ester decomposition.[54]

In the quest of catalytic methodologies that can operate without dehydration, Tanabe and co-workers reported in 2000 on an ammonium triflate ($[Ph_2NH_2]^+[OTf]^-$) catalyst. Besides functioning as a Brønsted acidic direct esterification catalyst, the ammonium triflate is also able to form a hydrophobic pocket around the catalytic center (Figure 1.5A).[42] This strategy enabled esterification at a reaction temperature of 80 °C without removal of water from the reaction mixture. In 2005, Ishihara and co-workers further extended Tanabe's concept with a series of bulky *N*,*N*-di-arylammonium pentafluorobenzenesulfonates. Interestingly, while these type of catalysts were milder, less Brønsted acidic, they displayed a higher activity. Yet, for effective catalysis a non-polar solvent, such as heptane was required.[55–57] Another method to overcome the unfavorable equilibrium conditions was developed by Kobayashi and co-workers. They explored the use of dodecylbenzenesulfonic acid (DBSA) as a surfactant-type Brønsted acid catalyst (Figure 1.5B).[43,44] Here, the alkyl tail of the catalyst assembles with the substrates to a micelle, affording a hydrophobic interior. Consequently, water formed during the reaction

is readily expelled. This strategy proved to be very effective even permitting direct esterification in water.

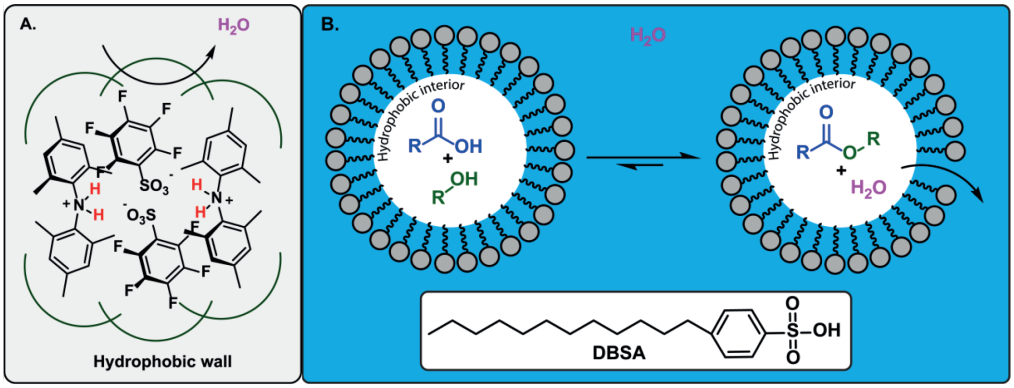

Figure 1.5. Approaches for Brønsted acid catalyzed esterification without dehydration.

2.2 Lewis acidic metals

To overcome the disadvantages related to the use of strong Brønsted acids, the search for more benign catalysts primarily focused on Lewis acidic metals. The number of different metals that have been applied as (poly)esterification catalyst is overwhelming and covers a significant part of the periodic table.[3,58–60] Similar to Brønsted acids, Lewis acidic metals activate the carbonyl function of the carboxylic acid to enable the nucleophilic attack of the alcohol. This step is followed by proton transfer and carbon-oxygen bond breaking to furnish the ester product together with water (Figure 1.6).

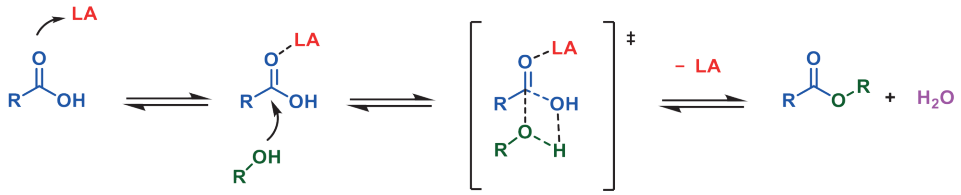

Figure 1.6. Simplified mode of carbonyl activation by a Lewis acidic metal.

However, Lewis acidic metals are more sterically congested than simple Brønsted acids. As a consequence, the exact mode of activation of the carboxylic acid, and the subsequent bond-making and -breaking steps are expected to be more complex. In this overview,

Lewis acidic catalysts based on tin, titanium, zirconium, hafnium, zinc and antimony will be reviewed, since these form the majority of catalysts that are reported and are of industrial relevance. In addition, the metal triflates will be discussed because of the profound activity of these type of Lewis acids. In general, there will be a focus on studies that have attempted to provide structural elucidation of the catalyst and mechanistic insight in Lewis acidic metal-based direct (poly)esterification catalysts.

2.2.1 Tin

Lewis acidic Sn^{IV} compounds are widely used in industry as (trans)esterification catalysts.[61,62] Despite their Lewis acidic character simple Sn^{IV} halides tend to be ineffective as catalyst. Interestingly, the milder $SnCl_2$ is known to be an effective catalyst.[63–65] For Sn^{IV} complexes, the presence of one or two electron-donating alkyl groups (typically *n*-butyl) is required to afford an active catalyst.[66] Examples of this type of Sn^{IV} catalysts are: *n*-BuSnOOH[67], *n*-$BuSnCl_2OH$[68], *n*-Bu_2SnO[67], dibutyltindilaurate[62] and distannoxanes.[69] The addition of these alkyl groups is proposed to moderate the Lewis acidity of the Sn^{IV} center. Moreover, for distannoxanes, which have a ladder like structure with Sn^{IV}–O–Sn^{IV} connectivity, the alkyl groups also create a hydrophobic shield around the active site.[70] Extensive work on these distannoxanes in relation to (trans)esterification reactions has been performed by Otera and co-workers. Although they are primarily known as transesterification catalysts,[71] (poly)esterification reactions are also reported.[72,73] The unique structure of the 1,3-disubstituted tetraalkyldistannoxanes enables direct esterification without the need for water removal at mild temperatures. Nonetheless, these reactions were performed with a large excess of the alcohol substrate since it also functioned as the solvent. To achieve equimolar esterification, Otera and co-workers decorated a distannoxane with fluoroalkyl tails and performed (trans)esterification reactions in a biphasic systems.[45–49] In such a system the catalyst resides in a fluorocarbon solvent, where also the ester and water are formed and subsequently expelled to the organic layer. This fluorous biphasic technique enabled full conversion of equimolar amounts of carboxylic acid and alcohol without dehydration. In addition, the catalyst could be quantitively recovered from the fluorocarbon solvent or directly used in the next reaction without diminished catalytic activity.[46] The profound catalytic activity of the distannoxanes has been attributed to two Sn^{IV} atoms being in close proximity. This enables an interaction between the bound alkoxy groups and the activated carbonyl group of the carboxylic acid (Figure 1.7).[74] However, this so-called template effect was questioned after

particular distannoxanes proved to be unstable in the presence of carboxylic acid. Alternatively, it was proposed that monotin-carboxylate compounds of the formula $R_2Sn(OAc)X$ (X = Br, Cl, OAc) are the actual catalysts. Moreover, for distannoxanes possessing tin-bromide or -chloride bonds the *in situ* formation of HBr and HCl has also been considered.[75] In summary, the mode of operation of dialkyltin compounds as (trans)esterification catalysts has been the topic of multiple studies over the past decades. Yet, the origin of their activity is still under debate. For both mono- and dialkyltin compounds the stoichiometric chemistry, with carboxylic acids and alcohols, is dominated by the formation of multinuclear assemblies.[76] The existence of these multinuclear tin complexes under catalytically relevant conditions remains to be investigated.

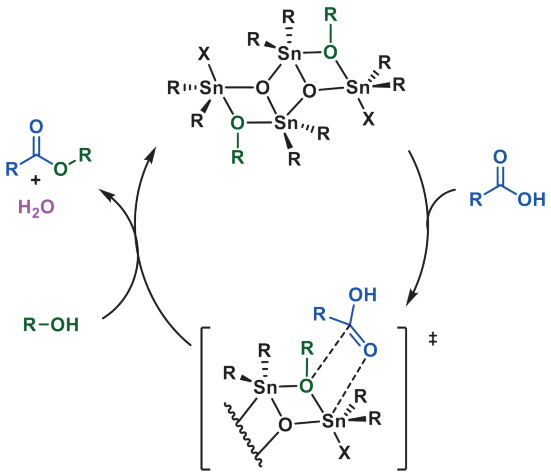

Figure 1.7. Proposed reaction mechanism for 1,3-disubstituted tetraalkyldistannoxane-catalyzed esterification. Adapted from reference 74.

2.2.2 Group(IV) metals

The high valent nature of the group(IV) metals provides a Lewis acidic metal center that can enable the direct (poly)esterification of carboxylic acids and alcohols. This beneficial characteristic, in combination with their abundancy, has resulted in Ti^{IV} compounds, such as titanium alkoxides[69,77–79], $TiCl_4$[80] and $TiCl(OTf)_3$,[81] being commonly reported catalysts. However, titanium compounds generally suffer from a poor selectivity due to pronounced transesterification activity.[80] Another disadvantage of Ti^{IV} compounds is their low ability to withstand water. Consequently, the protection by chelating agents has become a

widely patented method. The merger of a Ti^{IV} alkoxide with an additional ligand such as acetylacetonate,[82,83] lactic acid,[84] diethanolamine,[85] triethanolamine,[86–88] α-hydroxycarboxylic acid,[89] tetrakis(2-hydroxyethyl)ethylenediamine[90] or phosphoric acid[59,91] has resulted in a broad selection of Ti^{IV} catalysts with improved water stability. They mainly find their application in polyester synthesis. Although the application of a ligand provides a more robust titanium catalyst, hydrolysis and thermal degradation remain of concern, since these processes result in retarded activity and unwanted discoloration of the polyester.[58,59] Extensive work on hafnium- and zirconium-catalyzed direct (poly)esterification has been performed by the group of Yamamoto. Starting from the year 2000, they reported on Hf^{IV}- and Zr^{IV}-catalyzed direct esterification of equimolar amounts of carboxylic acids and alcohols.[54,80,92,93] From the group(IV) metal salts evaluated, $HfCl_4{\cdot}2THF$ proved to be a very effective catalyst. The effectiveness of $HfCl_4{\cdot}2THF$ was partially attributed to the improved moisture stability of $HfCl_4{\cdot}2THF$ over $HfCl_4$ and $Hf(O^tBu)_4$, which generally perform less well. In addition, Hf^{IV} salts are also more hydrolytically stable than Zr^{IV} salts. Nevertheless, these reactions were almost exclusively performed in a hydrocarbon solvent with azeotropic dehydration of the reaction mixture over NaH or molecular sieves. Importantly, Hf^{IV} and Zr^{IV} salts were found not to be active in transesterification reactions which is in contrast to common Ti^{IV} catalysts. Due to this profound selectivity for esterification, it was proposed that the active catalyst is a metal carboxylate. These metal carboxylates would form *in situ* via exchange reactions with the carboxylic acid substrate.

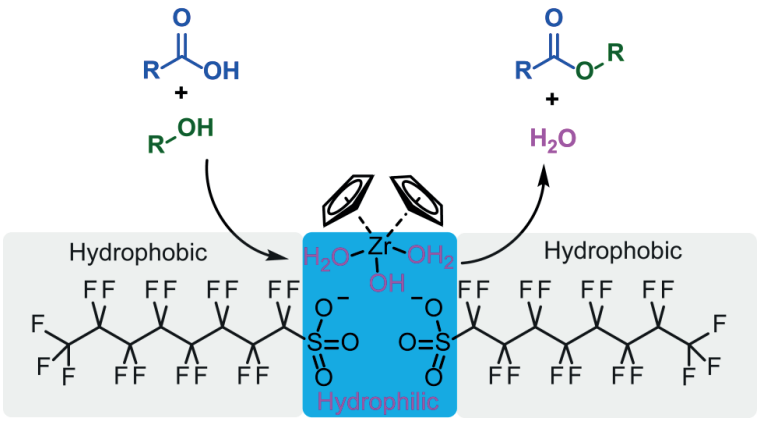

Figure 1.8. Zirconocene complex with perfluorooctanesulfonate tails for Lewis acid catalyzed esterification without dehydration. Adapted from reference 50.

In 2004, the same group also demonstrated that $HfOCl_2 \cdot 8H_2O$, $ZrOCl_2 \cdot 8H_2O$ and $Zr(OAc)_x(OH)_y$ are useful direct esterification catalysts.[94] The authors mentioned that $ZrOCl_2 \cdot 8H_2O$ can form the ionic cluster $[Zr_4(OH)_8(H_2O)_{16}]Cl_8 \cdot 12H_2O]$, from which ligand exchange reactions with alcohols and carboxylic acids can occur. Nevertheless, the exact mechanism for direct esterification still remains unclear. In 2017, the group of Au designed a zirconocene complex decorated with perfluorooctanesulfonate groups (Figure 1.8) to enable equimolar direct esterification without the need for dehydration under solvent-free conditions.[50] The authors claim to have a micro-catalytic system that combines the advantages of the Kobayashi and Otera systems, where the water side product readily leaves the catalyst due to the hydrophobic exterior of the complex. Consequently, the equilibrium conditions are obscured. However, in 2020 Lundberg and co-workers demonstrated that $Zr(Cp)_2(OTf)_2 \cdot THF$ is also an effective direct esterification catalyst in the absence of any water scavengers, although this catalyst was not active under solvent-free conditions but required benzotrifluoride as a solvent.[95] To investigate whether the reaction is truly catalyzed by Lewis acidic Zr^{IV}, the possibility of hydrolytic decomposition of $Zr(Cp)_2(OTf)_2 \cdot THF$ with the release of triflic acid was investigated. But a different response from triflic acid and the zirconocene complex made the authors conclude that the reaction was zirconium-catalyzed.

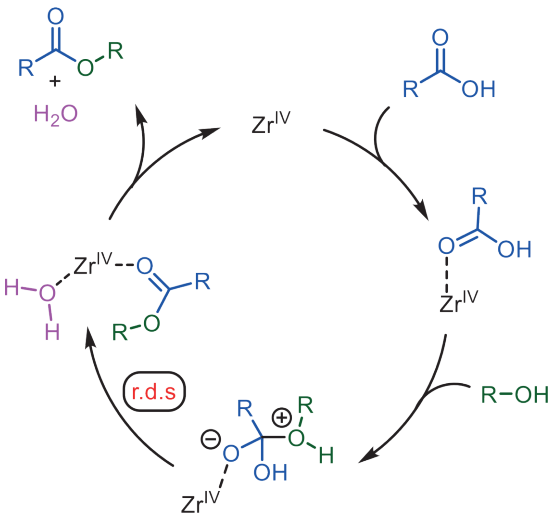

Figure 1.9. Proposed reaction mechanism for $Zr(Cp)_2(OTf)_2 \cdot THF$ catalyzed esterification. Adapted from reference 95.

To further elucidate the catalytic mechanism, various spectroscopic and kinetic experiments were performed. Coordination of the carboxylic acid via the carbonyl function to the Lewis acidic zirconium was demonstrated by ^{13}C NMR spectroscopy with BzOH-α-^{13}C as substrate. In addition, kinetic experiments revealed a positive rate dependence on zirconium and a close to zero order in both alcohol and carboxylic substrate. Furthermore, the absence of any product inhibition indicated that the collapse of the tetrahedral intermediate, formed after nucleophilic attack of the alcohol, is the rate determining step (Figure 1.9).

Taken together, the group(IV) metals remain a prominent class of direct (poly)esterification catalysts. Titanium-based catalysts are widely patented but their application has several disadvantages: 1) poor selectivity due to activity in transesterification reaction, 2) hydrolytic degradation of the catalyst, and 3) discoloration of the reaction product.[96] In the past two decades Hf^{IV} and Zr^{IV} compounds have emerged as effective catalysts with a remarkable selectivity for direct esterification over transesterification. Although the potential of these catalysts is evident, the price of zirconium and hafnium compounds hampers their industrial application.

2.2.3 Zinc

Due to their availability and non-toxic nature, many Zn^{II} catalyst such as ZnO,[97,98] $ZnCO_3$,[97] $Zn(BF_4)$,[97] $Zn(OTf)_2$,[97,99,100] $Zn(ClO_4)_2$,[97,101] $ZnCl_2$,[97,102] $Zn(oleate)_2$,[103] $Zn(laurate)_2$,[103,104] $Zn(NO_3)_2$,[97,102] $ZnSO_4$,[102,105] and $Zn(OAc)_2$[97,102,106] have been applied in the direct esterification reaction. For these catalysts, methods based on azeotropic distillation, as well as solvent-free protocols with a dehydrating agent have been explored.[107] Lewis acidic $Zn(OTf)_2$ proved to be a very effective direct esterification catalyst, especially in combination with microwave radiation. Although the decomposition of $Zn(OTf)_2$ into triflic acid could be the origin of the catalytic activity, this transformation was not observed during IR spectroscopy studies.[100] In order to improve the activity and recyclability, Zn^{II} salts also have been heterogenized on different supports.[108–113] The differences in activity for Zn^{II} salts have been ascribed to the nature of the counterion: poorly coordinating anions such as perchlorate or triflate leave a more accessible Zn center for catalysis, while anions such as nitrate result in a more coordinatively saturated complex.[97,107]

2.2.4 Antimony

Despite concerns about the scarcity and toxicity for humans, antimony-based compounds are still prominent polycondensation catalysts, in particular for the synthesis of polyethylene terephthalate (PET).[96,114–118] For PET synthesis, common antimony catalysts are Sb_2O_3 and $Sb(OAc)_3$, with distinct activity in the polycondensation of bis(hydroxyethyl)terephthalate (BHET).

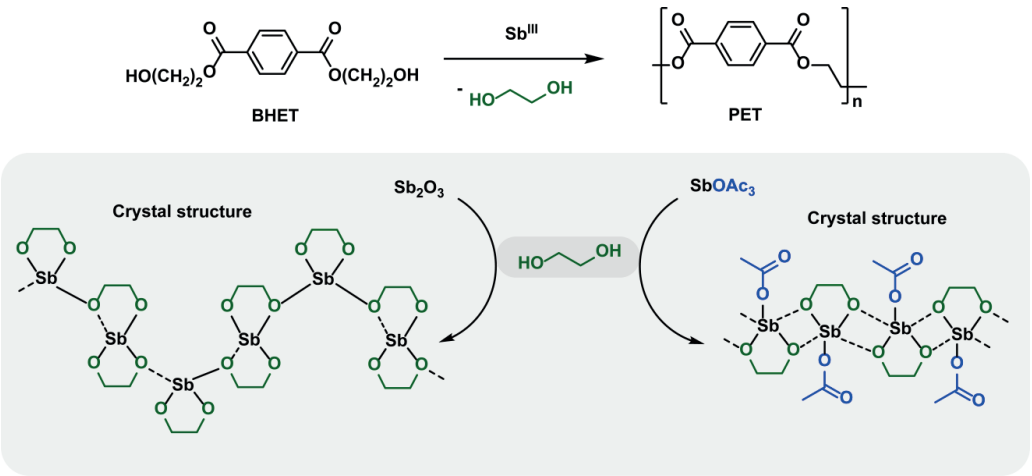

Figure 1.10. Antimony-catalyzed polyethylene terephthalate synthesis. Adapted from reference 120.

Regarding the mode of activation, the antimony catalysts is proposed to coordinate the ester carbonyl group of BHET and promote nucleophilic attack of the alcohol group of another molecule.[119] Parkin and co-workers structurally characterized a series of antimony ethylene glycolate compounds.[120] They found that Sb_2O_3 and $Sb(OAc)_3$ catalysts are transformed *in situ* via a reaction with ethylene glycol to form antimony glycolates with the formula $[Sb_2(OCH_2CH_2O)_3]_n$ or $[Sb(OCH_2CH_2O)(OAc)]_n$ (Figure 1.10). The molecular structure of both $[Sb_2(OCH_2CH_2O)_3]_n$ and $[Sb(OCH_2CH_2O)(OAc)]_n$ were determined to be polymeric with either a one-dimensional chain or a two-dimensional sheet. Yet, the presence of these polymeric catalysts in solution at the required elevated temperatures for polycondensation remains unelucidated. Additionally, BHET can also be obtained via the antimony-catalyzed esterification reaction of terephthalic acid with an excess of ethylene glycol.[118] While it can be expected that the presence of carboxylic acid will

structurally alter the catalyst, the exact structure of antimony-based catalysts during a direct esterification reaction is still unknown.

2.2.5 Metal triflates

Metal triflates, being strong Lewis acids, have become a popular class of catalysts since they can enable (poly)esterification reactions at very mild temperatures (< 100 °C).[18,121] Takasu and co-workers reported on the use of rare earth metal triflates and $Sc(OTf)_3$ in the synthesis of aliphatic polyesters based on succinic acid and a variety of diols, under reduced pressure at temperatures as low as 35 °C.[122] These mild reaction conditions allowed the use of thermally unstable monomers containing carbon-carbon double bonds and bromo functionalities.[123] In addition, polyesters containing hydroxyl groups could be obtained via a single step polycondensation of dicarboxylic acids and diols having secondary hydroxyl groups under kinetic control (Figure 1.11).[124]

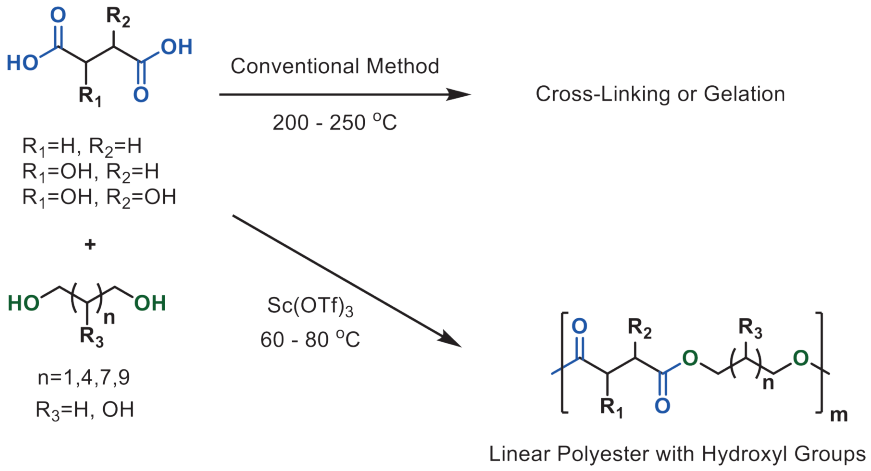

Figure 1.11. Chemoselective dehydrative polycondensation of dicarboxylic acids and diols having pendant hydroxyl groups. Adapted from reference 124.

This direct route towards functionalized polyesters enables the construction of new advanced materials as well as the application of monomers derived from biomass. More recently, Kricheldorf and co-workers reported on the synthesis of poly(butylenesuccinate) from sebacic acid and various diols at 80 °C under reduced pressure catalyzed by $Bi(OTf)_3$.[125] Although metal triflates were found to be very efficient (poly)esterification

catalysts, the exact role of the triflate anion in catalysis is often not well-studied and the activity is fully ascribed to the metal cation. For $Bi(OTf)_3$ it was found that the catalytic activity, in the esterification of various carboxylic acids with methanol, was completely suppressed in the presence of molecular sieves or a base. Therefore the authors concluded that the reaction was actually catalyzed by triflic acid which is formed *in situ* from $Bi(OTf)_3$.[126]

2.2.6 Effect of reaction conditions on Lewis acidic metals

Many different Lewis acidic metals display activity in direct (poly)esterification reactions. Drawing parallels between protocols is however challenging because of the variety in applied reaction conditions. This diversity is mainly caused by the need for dehydration which can be achieved via either dehydrating agents, azeotropic reflux or evaporation. Moreover, differences in polarity of the reaction mixture, reaction temperature, type of solvent or application of reduced pressure are observed. All these reaction parameters are expected to have a distinct effect on the catalytic performance of Lewis acidic metals. For example, for group(IV)-based direct (poly)esterification catalysts it is known that effective dehydration is necessary to prevent hydrolytic degradation of the catalyst. Therefore reaction conditions that have an influence on the water concentration in the reaction mixture are expected to affect the catalytic performance of these group(IV)-based direct (poly)esterification catalysts

3. Mechanistic insight

Although the Lewis acidic metals are the most prominent class of (poly)esterification catalysts, the origin of their catalytic activity remains elusive. Often, this is simply ascribed to the Lewis acidic nature of the metal center. However, not all Lewis acidic metals are active (poly)esterification catalysts. In general, the structure of the active species that is formed *in situ* remains unclear. Lewis acidic metal salts are transformed in the reaction mixture via ligand coordination and ligand exchange reactions. The alcohol, carboxylic acid, and ester can all coordinate neutrally to the metal center (Figure 1.12A, B and C). Moreover, ligand exchange reactions with the carboxylic acid and alcohol can be expected for metals with monodentate ligands. For carboxylic acids, this provides a metal carboxylate with either a monodentate (η^1), chelating (η^2) or bridging (μ) mode (Figure

1.12D). while for the alcohol substrate such a reaction results in a metal alkoxide with either a monodentate (η^1) or bridging (μ) mode (Figure 1.12E). These multiple coordination possibilities permit a wide variety in possible geometries and severely complicates the structural prediction of the active catalyst.

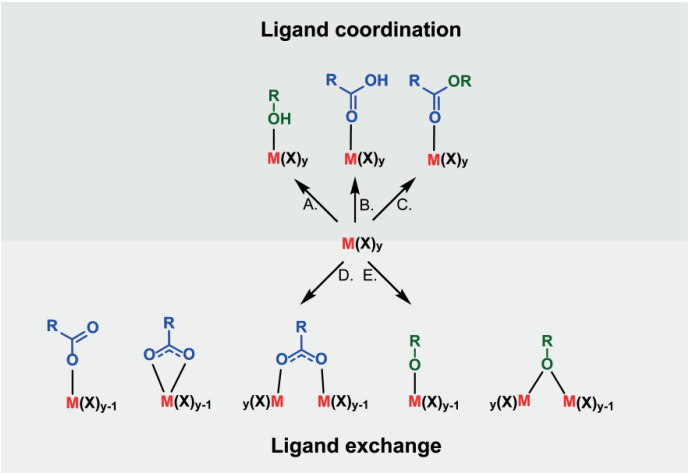

Figure 1.12. Ligand coordination and exchange reactions at Lewis acidic metals.

To illustrate what type of elaborate structures can form *in situ* in a protic environment, we refer to the work of Lundberg and co-workers.[127] They concluded, based on extensive spectroscopic and computational studies, that $ZrCl_4$ is altered to a dinuclear zirconium complex in a direct amidation reaction (Figure 1.13). In summary, the variety of possible transformations of Lewis acidic metal salts in the reaction medium makes mechanistic studies into poly(esterification) catalysts a challenging endeavor.

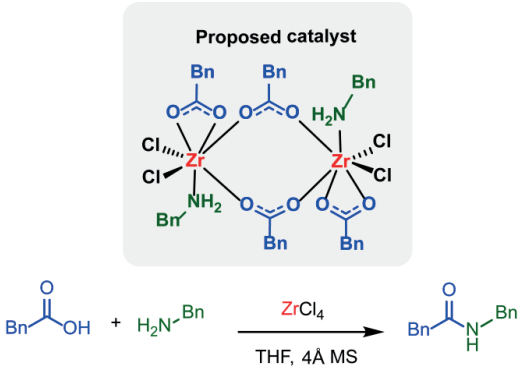

Figure 1.13. $ZrCl_4$-catalyzed amidation reaction. Adapted from reference 127.

4. New routes for ester synthesis

While the direct condensation of carboxylic acids and alcohols remains a very important route towards ester formation, significant advances in the synthesis of esters from other functional groups have been made. Transition metal catalysis has enabled the direct oxidative esterification of alcohols to esters[128], the alkoxycarbonylation of C-H bonds to esters[129], dehydrogenation of alcohols to esters[130] and the addition of carboxylic acids into alkynes and alkenes to form esters bonds.[131] Thus far, the cross-coupling reaction of aryl halides and carboxylic acids to form *O*-aryl esters has remained a challenging transformation. Although the palladium-catalyzed C_{aryl}–O_{acyl} bond formation is reported, these protocols require an excess of silver salt at elevated temperatures.[132,133] In general, palladium-catalyzed C_{aryl}-hetero bond formations are hampered by a high barrier for reductive elimination from Pd^{II} intermediates. Therefore catalytic protocols, for example Buchwald-Hartwig amination, require specialized ligands or high reaction temperatures.[134,135] Compared to palladium, nickel has a lower electronegativity making it more nucleophilic. As a result, reductive elimination from Ni^{II} intermediates is energetically even more unfavorable compared to their palladium counter parts.[136,137] Furthermore palladium catalysis are dominated by two oxidation states (Pd^0 and Pd^{II}), while for nickel there are four different oxidation states accessible (Ni^0, Ni^I, Ni^{II}, Ni^{III}). This makes nickel a very versatile metal with remarkable possibilities in terms of catalytic mechanisms. In 2016 MacMillan, Buchwald and co-workers made use of this characteristic of nickel by combining a Ni^{II} precatalyst with an iridium photocatalyst ($Ir[dF(CF)_3ppy]_2(dtbbpy)PF_6$) to enable the amination of aryl halides under very mild reaction conditions.[138] In their approach the photocatalyst was proposed to play a dual role: 1) it reduces the Ni^I intermediate, via single electron transfer (SET), to a Ni^0 state. Subsequently the Ni^0 intermediate can undergo oxidative addition to form a Ni^{II} state and 2) it facilitates the generation of a Ni^{III} intermediate, again via SET (Figure 1.14, mechanism A). This Ni^{III} complex, which is more electrophilic than Ni^{II}, can undergo facile reductive elimination. In 2017 MacMillan and co-workers further extended their concept and demonstrated that the merger of nickel with photoredox-catalysis also enabled the synthesis of *O*-aryl esters.[139] Here the photocatalyst ($Ir(ppy)_3$) was proposed to have a different role since it facilitates the generation of an excited Ni^{II} intermediate via energy transfer (EnT) (Figure 1.14, Mechanism B). Also this excited Ni^{II} intermediate can undergo facile reductive elimination. The combination of photoredox and nickel catalysis proved to be a key discovery that enabled the synthesis of C_{aryl}-hetero bond formations under mild conditions. Therefore the seminal work by MacMillan attracted considerable

attention and the field of nickel-catalyzed cross coupling reactions has grown enormously in recent years. Besides methodologies that make use of photocatalysts, also protocols that combine nickel catalysis with electrocatalysis have been developed to construct C_{aryl}-hetero bonds.[140–144] In addition, significant advances in the understanding of the mechanisms by which nickel-catalyzed cross coupling reactions occur have been made.[145,146]

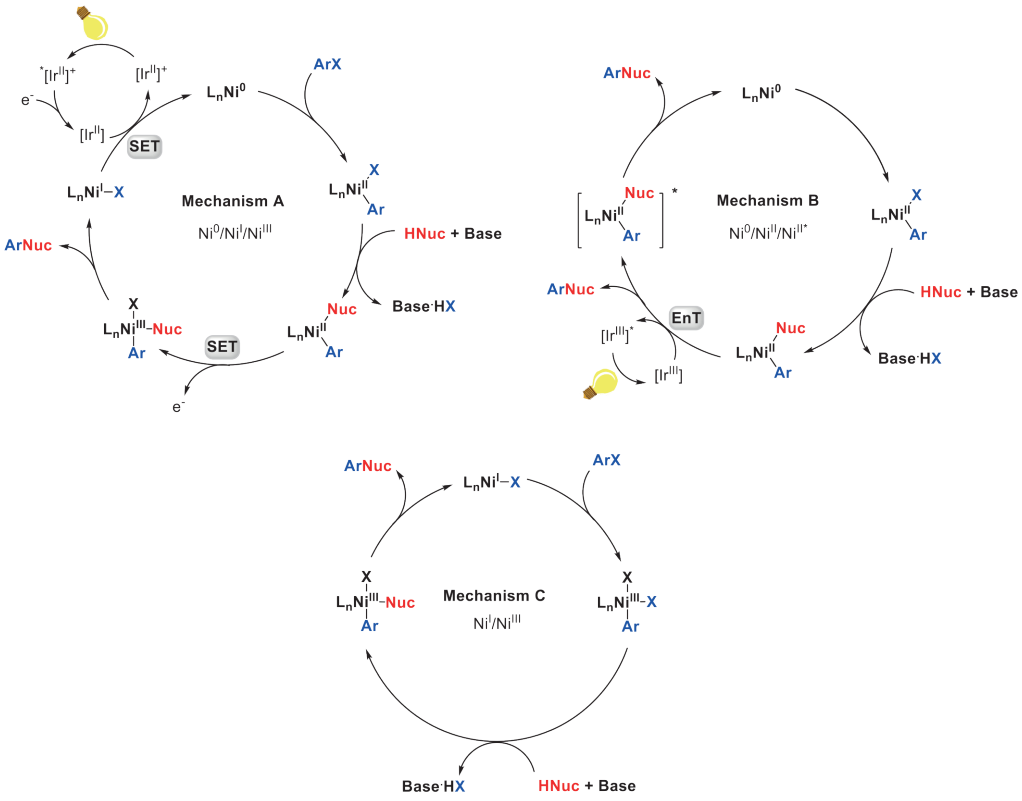

Figure 1.14. Overview of mechanisms to enable nickel catalyzed C_{aryl}-heteroatom bond formations. Adapted from references 136 and 150.

Next to the proposed $Ni^0/Ni^{II}/Ni^{III}$ and $Ni^0/Ni^{II}/Ni^{II*}$ catalytic cycles another mechanistic possibility was considered by Nocera and co-workers after photodriven nickel-catalyzed cross-coupling reactions revealed quantum yields of $\Phi_{Ni} > 1$.[147–149] These findings ruled out the requirement for an excited Ni^{II} intermediate and are indicative for a self-sustained mechanism. For that reason a Ni^I/Ni^{III} catalytic cycle was proposed (Figure 1.14, mechanism C). In this mechanism the photocatalyst only serves to continuously reactivate

formed Ni^{II} species. The formation of these inactive Ni^{II} states is facile via exergonic comproportionation pathways of Ni^{III} with Ni^{I}. The proposed self-sustained Ni^{I}/Ni^{III} catalytic cycle only requires a suitable reducing agent and has no need for photons. The group of Nocera showed that a self-sustained Ni^{I}/Ni^{III} catalytic cycle is indeed a relevant mechanism by performing nickel-catalyzed C_{aryl}-hetero bond formations, including carboxylate *O*-arylation, in the dark with zinc as heterogeneous reducing agent.[148] In summary, nickel catalysis in combination with photoredox catalysis, electrocatalysis or heterogeneous reducing agents have emerged as an efficient route to construct *O*-aryl esters. Various approaches have been developed to facilitate the demanding reductive elimination step via the generation of either excited Ni^{II} or Ni^{III} intermediates (Figure 1.14, Mechanism A, B and C).[136,150] For the nickel-catalyzed synthesis of *O*-aryl esters, recent developments primarily focused on replacing iridium- and ruthenium-based photocatalysts for organic photocatalysts.[151–155]

Outline of this thesis

In the past decades, significant progress has been made towards the direct (poly)esterification of carboxylic acids and alcohols catalyzed by Lewis acidic metals. Furthermore, various elegant strategies to overcome the unfavorable equilibrium conditions and to enable ester formation with equimolar amounts of reactants, without the need for dehydration, have been reported. Nevertheless, insights in the origin of the catalytic activity of Lewis acidic metal remains limited. In this dissertation we present studies on commonly used Ti^{IV}- and Sn^{IV}-based Lewis acidic catalysts, to elucidate the structure of the *in situ* formed catalyst, potential intermediates and provide mechanistic understanding. Moreover, to expand the number of catalytic strategies that can manufacture ester bonds at mild conditions, we investigated the cross-coupling reaction of aryl halides with carboxylic acids to form *O*-aryl esters.

In ***Chapter 2*** a mechanistic study of titanium aminotriphenolate esterification catalyst is described. We found that the application of the tetradendate aminotriphenolate ligand prevents the uncontrolled exchange reactions with carboxylic acids, alcohols and esters commonly associated with titanium alkoxide catalysts. This strategy affords a well-defined monomeric catalyst. Moreover, mechanistic understanding is obtained via stoichiometric reactions combined with kinetic experiments and density functional theory (DFT) calculations. We show that Lewis acidity is not the sole factor determining catalytic activity.

In ***Chapter 3*** the well-known monoalkyltin(IV) catalysts for (poly)esterification are discussed. With the help of various spectroscopic techniques as well as stoichiometric and catalytic reactions, the transformation of these complexes at relevant reaction temperatures was studied. We demonstrate that only monomeric and dimeric tin complexes are present during catalysis, whereas the stoichiometric chemistry of *n*-butyltin(IV) carboxylates is dominated by the formation of multinuclear tin assemblies. In addition, a reaction mechanism is proposed based on kinetic experiments and DFT calculations.

The mechanistic studies, described in Chapters 2 and 3, provide new insights in the type of titanium and tin complexes that are formed *in situ* under direct esterification conditions and into their mode of operation. To gain a better understanding of the observed catalytic activity, the deactivation of the catalyst under catalytic conditions is studied in ***Chapter 4***. Via kinetic analysis of polyesterification reactions, we show that catalytic performance for

Lewis acidic catalysts is crucially determined by the robustness against hydrolytic degradation.

In the search of more efficient routes to obtain *O*-aryl esters, the nickel-catalyzed cross-coupling of aryl halides with carboxylic acids is explored in ***Chapter 5***. We perform a mechanistic examination of carboxylate *O*-arylation under thermal conditions, in the presence and absence of an exogeneous 2,2'-bipyridine-ligand. The obtained results provide insights into the competition between productive catalysis and deleterious pathways (comproportionation and protodehalogenation) that exist for all fundamental elementary steps. Moreover, via spectroscopic and catalytic studies we unveil the resting state of the nickel catalyst, the crucial role of the alkylamine base, and the formation of a Ni^{I}-Ni^{III} dimer upon reduction.

Overall, the findings acquired in the research presented in this thesis, provide valuable insights in the structure of *in situ* formed catalysts, reaction intermediates and reaction mechanisms. Thereby, the obtained knowledge will be of use for the development of novel (poly)esterification catalyst, based on abundant and non-toxic materials.

References

1 M. Kirubakaran and V. Arul Mozhi Selvan, *Renew. Sustain. Energy Rev.*, 2018, **82**, 390–401.
2 A. S. Belousov, A. L. Esipovich, E. A. Kanakov and K. V. Otopkova, *Sustain. Energy Fuels*, 2021, **5**, 4512–4545.
3 J. Otera, J. Nishikido, *Esterification. Methods, Reactions, and Applications*, Wiley-VCH Verlag GmbH & Co., Weinheim, 2nd edn., 2010.
4 W. Riemenschneider and H. Bolt, *Esters, Organic. In Ullmann's Encyclopedia of Industrial Chemistry, (Ed.).*, 2005.
5 M. Tsakos, E. S. Schaffert, L. L. Clement, N. L. Villadsen and T. B. Poulsen, *Nat. Prod. Rep.*, 2015, **32**, 605–632.
6 Y. Deng, T. Yang, H. Wang, C. Yang, L. Cheng, S. F. Yin, N. Kambe and R. Qiu, *Recent Progress on Photocatalytic Synthesis of Ester Derivatives and Reaction Mechanisms*, Springer International Publishing, 2021, vol. 379.
7 G. A. Kraus and T. Goronga, *Synthesis (Stuttg).*, 2007, **2**, 1765–1767.
8 S. Q. Liu, R. Holland and V. L. Crow, *Int. Dairy J.*, 2004, **14**, 923–945.
9 B. N. Paulino, A. Sales, L. Felipe, G. M. Pastore, G. Molina and J. L. Bicas, *Curr. Opin. Food Sci.*, 2021, **37**, 98–106.
10 K. M. Sumby, P. R. Grbin and V. Jiranek, *Food Chem.*, 2010, **121**, 1–16.
11 J. W. Lee and C. T. Trinh, *Curr. Opin. Biotechnol.*, 2020, **61**, 168–180.
12 N. R. Khan and V. K. Rathod, *Process Biochem.*, 2015, **50**, 1793–1806.
13 P. Nagendramma and S. Kaul, *Renew. Sustain. Energy Rev.*, 2012, **16**, 764–774.
14 M. A. Hossain, M. A. Mohamed Iqbal, N. M. Julkapli, P. San Kong, J. J. Ching and H. V. Lee, *RSC Adv.*, 2018, **8**, 5559–5577.
15 I. Ambat, V. Srivastava and M. Sillanpää, *Renew. Sustain. Energy Rev.*, 2018, **90**, 356–369.
16 T. Issariyakul and A. K. Dalai, *Renew. Sustain. Energy Rev.*, 2014, **31**, 446–471.
17 K. Pang, R. Ã. Kotek and A. Tonelli, *Prog. Polym. Sci.*, 2006, **31**, 1009–1037.
18 X. Zhang, M. Fevre, G. O. Jones and R. M. Waymouth, *Chem. Rev.*, 2018, **118**, 839–885.
19 C. Vilela, A. F. Sousa, A. C. Fonseca, A. C. Serra, J. F. J. Coelho, C. S. R. Freire and A. J. D. Silvestre, *Polym. Chem.*, 2014, **5**, 3119–3141.
20 M. Rabnawaz, I. Wyman, R. Auras and S. Cheng, *Green Chem.*, 2017, **19**, 4737–4753.
21 R. A. Sheldon, *ACS Sustain. Chem. Eng.*, 2018, **6**, 32–48.
22 B. M. Trost, *Angew. Chemie Int. Ed. English*, 1995, **34**, 259–281.
23 R. A. Sheldon, *Green Chem.*, 2007, **9**, 1273–1283.
24 R. A. Sheldon, *Green Chem.*, 2017, **19**, 18–43.
25 P. Anastas and N. Eghbali, *Chem. Soc. Rev.*, 2010, **39**, 301–312.
26 B. Neises and W. Steglich, *Org. Synth.*, 1985, **63**, 183–192.
27 O. Mitsunobu, T. Obata and T. Mukaiyama, *Bull. Chem. Soc. Jpn.*, 1967, **40**, 2380–2382.
28 I. Shiina, S. Miyoshi, M. Miyashita and T. Mukaiyama, *Chem. Lett.*, 1994, 23, 515–518.
29 J. Inanaga, K. Hirata, H. Saeki, T. Katsuki and M. Yamaguchi, *Bull. Chem. Soc. Jpn.*, 1979, 52, 1989–1993.
30 N. F. Nikitas, M. K. Apostolopoulou, E. Skolia, A. Tsoukaki and C. G. Kokotos, *Chem. - A Eur. J.*, 2021, **27**, 7915–7922.
31 S. Gaspa, I. Raposo, L. Pereira, G. Mulas, P. C. Ricci, A. Porcheddu and L. De Luca, *New J. Chem.*, 2019, **43**, 10711–10715.
32 E. Gabirondo, A. Sangroniz, A. Etxeberria, S. Torres-Giner and H. Sardon, *Polym. Chem.*, 2020, **11**, 4861–4874.
33 H. Sardon, D. Mecerreyes, A. Basterretxea, L. Avérous and C. Jehanno, *ACS Sustain. Chem. Eng.*, 2021, **9**, 10664–10677.
34 Q. Zhang, M. Song, Y. Xu, W. Wang, Z. Wang and L. Zhang, *Prog. Polym. Sci.*, 2021, **120**, 101430.
35 J. Iglesias, I. Martínez-Salazar, P. Maireles-Torres, D. Martin Alonso, R. Mariscal and M. López Granados, *Chem. Soc. Rev.*, 2020, **49**, 5704–5771.
36 R. Sirsam, D. Hansora and G. A. Usmani, *J. Inst. Eng. Ser. E*, 2016, **97**, 167–181.
37 A. F. Lee, J. A. Bennett, J. C. Manayil, K. Wilson and A. F. Lee, *Chem Soc Rev*, 2014, **43**, 7887–7916.
38 M. E. Borges and L. Díaz, *Renew. Sustain. Energy Rev.*, 2012, **16**, 2839–2849.

39 Y. Román-Leshkov and M. E. Davis, *ACS Catal.*, 2011, **1**, 1566–1580.
40 V. S. Gamayurova, M. E. Zinov, K. L. Shnaider and G. A. Davletshina, *Biocatalysis*, 2021, **13**, 58–72.
41 J. Otera, *Angew. Chem. Int. Ed.*, 2001, **40**, 2044–2045.
42 K. Wakasugi, T. Misaki, K. Yamada and Y. Tanabe, *Tetrahedron Lett.*, 2000, **41**, 5249–5252.
43 K. Manabe, X. M. Sun and S. Kobayashi, *J. Am. Chem. Soc.*, 2001, **123**, 10101–10102.
44 K. Manabe, S. Iimura, X. M. Sun and S. Kobayashi, *J. Am. Chem. Soc.*, 2002, **124**, 11971–11978.
45 J. Otera, *Acc. Chem. Res.*, 2004, **37**, 288–296.
46 J. Xiang, S. Toyoshima, A. Orita and J. Otera, *Angew. Chemie - Int. Ed.*, 2001, **40**, 3670–3672.
47 J. Xiang, A. Orita and J. Otera, *ChemInform*, 2003, **34**, 4117–4119.
48 J. Xiang, A. Orita and J. Otera, *J. Organometalic Chem.*, 2002, **648**, 246–250.
49 A. Orita, S. Man-E and J. Otera, *J. Am. Chem. Soc.*, 2006, **128**, 4182–4183.
50 Z. Tang, Q. Jiang, L. Peng, X. Xu, J. Li, R. Qiu and C. T. Au, *Green Chem.*, 2017, **19**, 5396–5402.
51 A. Fischer, E. Speier, *Chem. Ber.*, 1895, **28**, 3252–3258.
52 Y. Zheng, Y. Zhao, S. Tao, X. Li, X. Cheng, G. Jiang and X. Wan, *European J. Org. Chem.*, 2021, **2021**, 2713–2718.
53 S. Y. A. Lee, H. C. Yang and F. Y. Su, *Tetrahedron Lett.*, 2001, **42**, 301–303.
54 K. Ishihara, *Tetrahedron*, 2009, **65**, 1085–1109.
55 A. Sakakura, S. Nakagawa and K. Ishihara, *Tetrahedron*, 2006, **62**, 422–433.
56 K. Ishihara, S. Nakagawa and A. Sakakura, *J. Am. Chem. Soc.*, 2005, **127**, 4168–4169.
57 K. . Wakasugi, T. Misaki, K. Yamada and Y. Tanabe, *Tetrahedron Lett.*, 2000, **41**, 5249–5252.
58 U. K. Thiele, *Int. J. Polym. Mater.*, 2001, **50**, 387–394.
59 K. Pang, R. Kotek and A. Tonelli, *Prog. Polym. Sci.*, 2006, **31**, 1009–1037.
60 E. Fradet, A. Maréchal, in *Advances in Polymer Sciences*, Springer Berlin Heidelberg, 1982.
61 A. G. Davies, *J. Chem. Res.*, 2010, **34**, 181–190.
62 A. B. Ferreira, A. Lemos Cardoso and M. J. da Silva, *ISRN Renew. Energy*, 2012, **2012**, 1–13.
63 M. da Silva, A. Julio and K. dos Santos, *Catal. Sci. Technol.*, 2015, **5**, 1261.
64 A. L. Cardoso, S. C. G. Neves and M. J. da Silva, *Energies*, 2008, **1**, 79–92.
65 C. S. Cho, D. T. Kim, H. J. Choi, T. J. Kim and S. C. Shim, *Bull. Korean Chem. Soc.*, 2002, **23**, 539–540.
66 M. R. Meneghetti and S. M. P. Meneghetti, *Catal. Sci. Technol.*, 2015, **5**, 765–771.
67 Y. C. Brito, D. A. C. Ferreira, D. M. D. A. Fragoso, P. R. Mendes, C. M. J. D. Oliveira, M. R. Meneghetti and S. M. P. Meneghetti, *Appl. Catal. A Gen.*, 2012, **443**–**444**, 202–206.
68 R. X. E. Willemse, W. Ming and A. M. Van Herk, *Macromolecules*, 2005, **38**, 6876–6881.
69 J. Nowicki, D. Stańczyk, J. Drabik, J. Mosio-Mosiewski, P. Woszczyński and M. Warzała, *JAOCS, J. Am. Oil Chem. Soc.*, 2016, **93**, 973–981.
70 J. Otera, N. Dan-oh and H. Nozaki, *J. Org. Chem.*, 1991, **56**, 5307–5311.
71 B. Jousseaume, C. Laporte, M. C. Rascle and T. Toupance, *Chem. Commun.*, 2003, **3**, 1428–1429.
72 J. Otera, *Chem. Rev.*, 1993, **93**, 1449–1470.
73 M. Ishii, M. Okazaki, Y. Shibasaki, M. Ueda and T. Teranishi, *Biomacromolecules*, 2001, **2**, 1267–1270.
74 J. Otera, N. Dan-oh and H. Nozaki, *J. Org. Chem.*, 1991, **56**, 5307–5311.
75 E. Crawford, T. Lohr, E. M. Leitao, S. Kwok and J. S. McIndoe, *Dalt. Trans.*, 2009, 9110–9112.
76 V. Chandrasekhar, S. Nagendran and V. Baskar, *Coord. Chem. Rev.*, 2002, **235**, 1–52.
77 M. I. Siling and T. N. Laricheva, *Russ. Chem. Rev.*, 1996, **279**, 279–286.
78 L. Chen, J. Xu, W. Xue and Z. Zeng, *Korean J. Chem. Eng.*, 2018, **35**, 82–88.
79 Du Pont Tyzor. Organic Titanates, Product information, https://studyres.com/doc/8911192/dupont-tyzor--product-information---tyzor, (accessed 4 January 2019).
80 K. Ishihara, S. Ohara and H. Yamamoto, *Science*, 2000, **290**, 1140–1142.
81 J. Izumi, I. Shiina and T. Mukaiyama, *Chem. Lett.*, 1995, **24**, 141–142.
82 C. Chen and Y. S. Munot, *J. Org. Chem*, 2005, **70**, 8625–8627.
83 H. Nestler, D. Barfurth, *US pat.*, US1986/4617408, 1986.
84 D. E. Putzig, *US Pat.*, US2000/6166170, 2000.
85 D. L. Deardorff, *US Pat.*, US1988/4788172, 1988.
86 D. Barfurth, H. Nestler, *US Pat.*, US1986/4621148, 1986.
87 D. W. Brook, P. D. Kay, *US Pat.*, US1975/3892791, 1975.

88 J. Wiegner, V. Voerckel, D. Runkel, R. Eckert, *US Pat.*, US2012/0316316A1, 2012.
89 M. Schönnagel, A. T. W. Cooper, *EP Pat.*, EP2765149A1, 2013.
90 A. A. D. Tulloch, A. Cooper, R. H. Duncon, *US Pat*., US2010/0292449A1, 2010.
91 H. A. Alidedeoglu, T. Ding, G. Kannan, *US Pat.*, US2017/9670313B2, 2017.
92 K. Ishihara, M. Nakayama, S. Ohara and H. Yamamoto, *Synlett*, 2001, 1117–1120.
93 K. Ishihara, M. Nakayama, S. Ohara and H. Yamamoto, *Tetrahedron*, 2002, **58**, 8179–8188.
94 M. Nakayama, A. Sato, K. Ishihara and H. Yamamoto, *Adv. Synth. Catal.*, 2004, **346**, 1275–1279.
95 P. Villo, O. Dalla-Santa, Z. Szabó and H. Lundberg, *J. Org. Chem.*, 2020, **85**, 6959–6969.
96 L. Papadopoulos, A. Zamboulis, N. Kasmi, M. Wahbi, C. Nannou, D. A. Lambropoulou, M. Kostoglou, G. Z. Papageorgiou and D. N. Bikiaris, *Green Chem.*, 2021, **23**, 2507–2524.
97 M. Melchiorre, M. E. Cucciolito, M. Di Serio, F. Ruffo, O. Tarallo, M. Trifuoggi and R. Esposito, *ACS Sustain. Chem. Eng.*, 2021, **9**, 6001–6011.
98 A. Nagvenkar, S. Naik and J. Fernandes, *Catal. Commun.*, 2015, **65**, 20–23.
99 M. Shekarriz, S. Taghipoor, A. A. Khalili and M. S. Jamarani, *J. Chem. Res.*, 2003, 172–173.
100 E. Altman, G. D. Stefanidis, T. Van Gerven and A. Stankiewicz, *Ind. Eng. Chem. Res.*, 2012, **51**, 1612–1619.
101 G. Bartoli, J. Boeglin, M. Bosco, M. Locatelli, M. Massaccesi, P. Melchiorre and L. Sambri, *Adv. Synth. Catal.*, 2005, **347**, 33–38.
102 K. Mantri, R. Nakamura, K. Komura and Y. Sugi, *Chem. Lett.*, 2005, **34**, 1502–1503.
103 M. S. A. Serafini and G. M. Tonetto, *Catalysts*, 2019, **9**, 1–15.
104 E. J. M. De Paiva, S. Sterchele, M. L. Corazza, D. Y. Murzin, F. Wypych and T. Salmi, *Fuel*, 2015, **153**, 445–454.
105 L. Gang and P. Wenhui, *Kinet. Catal.*, 2010, **51**, 559–565.
106 C. Song, Y. Qi, T. Deng, X. Hou and Z. Qin, *Renew. Energy*, 2010, **35**, 625–628.
107 R. Esposito, M. Melchiorre, A. Annunziata, M. E. Cucciolito and F. Ruffo, *ChemCatChem*, 2020, **12**, 5858–5879.
108 S. L. Barbosa, M. J. Dabdoub, G. R. Hurtado, S. I. Klein, A. C. M. Baroni and C. Cunha, *Appl. Catal. A Gen.*, 2006, **313**, 146–150.
109 L. Dai, Q. Zhao, M. Fang, R. Liu, M. Dong and T. Jiang, *RSC Adv.*, 2017, **7**, 32427–32435.
110 R. Aafaqi, A. R. Mohamed and S. Bhatia, *J. Chem. Technol. Biotechnol.*, 2004, **79**, 1127–1134.
111 M. Pramanik, M. Nandi, H. Uyama and A. Bhaumik, *Green Chem.*, 2012, **14**, 2273–2281.
112 G. Corro, F. Bañuelos, E. Vidal and S. Cebada, *Fuel*, 2014, **115**, 625–628.
113 D. Singh, P. Patidar, A. Ganesh and S. Mahajani, *Ind. Eng. Chem. Res.*, 2013, **52**, 14776–14786.
114 P. Westerhoff, P. Prapaipong, E. Shock and A. Hillaireau, *Water Res.*, 2008, **42**, 551–556.
115 D. Dupont, S. Arnout, P. T. Jones and K. Binnemans, *J. Sustain. Metall.*, 2016, **2**, 79–103.
116 M. L. C. M. Henckens, P. P. J. Driessen and E. Worrell, *Resour. Conserv. Recycl.*, 2016, **108**, 54–62.
117 L. Papadopoulos, A. Zamboulis, N. Kasmi, M. Wahbi, C. Nannou, D. A. Lambropoulou, M. Kostoglou, G. Z. Papageorgiou and D. N. Bikiaris, *Green Chem.*, 2021, **23**, 2507–2524.
118 U. K. Thiele, *Int. J. Polym. Mater.*, 2001, **50**, 387–394.
119 J. S. Chung, *J. Macromol. Sci. Part A - Chem.*, 1990, **27**, 479–490.
120 S. M. Biros, B. M. Bridgewater, A. Villeges-estrada, J. M. Tanski and G. Parkin, *Inorg. Chem.*, 2002, **41**, 4051–4057.
121 S. Kobayashi, M. Sugiura, H. Kitagawa and W. W. L. Lam, *Chem. Rev.*, 2002, **102**, 2227–2302.
122 A. Takasu, Y. Oishi, Y. Iio, Y. Inai and T. Hirabayashi, *Macromolecules*, 2003, **36**, 1772–1774.
123 A. Takasu, Y. Iio, T. Mimura and T. Hirabayashi, *Polym. J.*, 2005, **37**, 946–953.
124 A. Takasu, Y. Shibata, Y. Narukawa and T. Hirabayashi, *Macromolecules*, 2007, **40**, 151–153.
125 P. Buzin, M. Lahcini, J. Schellenberg, G. Schwarz and H. R. Kricheldorf, *Macromolecules*, 2010, **43**, 6511.
126 F. H. A. Kwie, C. Baudoin-Dehoux, C. Blonski and C. Lherbet, *Synth. Commun.*, 2010, **40**, 1082–1087.
127 H. Lundberg, F. Tinnis, J. Zhang, A. G. Algarra, F. Himo and H. Adolfsson, *J. Am. Chem. Soc.*, 2017, **139**, 2286–2295.
128 S. Tang, J. Yuan, C. Liu and A. Lei, *Dalt. Trans.*, 2014, **43**, 13460–13470.
129 B. Liu, F. Hu and B. F. Shi, *ACS Catal.*, 2015, **5**, 1863–1881.
130 M. Trincado, J. Bösken and H. Grützmacher, *Coord. Chem. Rev.*, 2021, **443**, 213967.
131 F. Luo, C. Pan and J. Cheng, *Synlett*, 2012, 357–366.

132 L. Li, F. Song, X. Zhong, Y. D. Wu, X. Zhang, J. Chen and Y. Huang, *Adv. Synth. Catal.*, 2020, **362**, 126–132.
133 H. Kitano, H. Ito and K. Itami, *Org. Lett.*, 2018, **20**, 2428–2432.
134 R. Dorel, C. P. Grugel and A. M. Haydl, *Angew. Chemie - Int. Ed.*, 2019, **58**, 17118–17129.
135 P. Ruiz-Castillo and S. L. Buchwald, *Chem. Rev.*, 2016, **116**, 12564–12649.
136 C. Zhu, H. Yue, J. Jia and M. Rueping, *Angew. Chemie - Int. Ed.*, 2021, **60**, 17810–17831.
137 J. B. Diccianni and T. Diao, *Trend Chem.*, 2019, 1–15.
138 E. B. Corcoran, M. T. Pirnot, S. Lin, S. D. Dreher, D. A. Dirocco, I. W. Davies, S. L. Buchwald and D. W. C. Macmillan, *Science*, 2016, **353**, 279–283.
139 E. R. Welin, C. Le, D. M. Arias-Rotondo, J. K. McCusker and D. W. C. MacMillan, *Science*, 2017, **355**, 380–385.
140 Y. Kawamata, J. C. Vantourout, D. P. Hickey, P. Bai, L. Chen, Q. Hou, W. Qiao, K. Barman, M. A. Edwards, A. F. Garrido-Castro, J. N. Degruyter, H. Nakamura, K. Knouse, C. Qin, K. J. Clay, D. Bao, C. Li, J. T. Starr, C. Garcia-Irizarry, N. Sach, H. S. White, M. Neurock, S. D. Minteer and P. S. Baran, *J. Am. Chem. Soc.*, 2019, **141**, 6392–6402.
141 E. O. Bortnikov and S. N. Semenov, *J. Org. Chem.*, 2021, **86**, 782–793.
142 H. J. Zhang, L. Chen, M. S. Oderinde, J. T. Edwards, Y. Kawamata and P. S. Baran, *Angew. Chemie - Int. Ed.*, 2021, **60**, 20700–20705.
143 E. Richmond and J. Moran, *Synth.*, 2018, **50**, 499–513.
144 Y. Mo, Z. Lu, G. Rughoobur, P. Patil, N. Gershenfeld, A. I. Akinwande, S. L. Buchwald and K. F. Jensen, *Science*, 2020, **368**, 1352–1357.
145 N. A. Till, S. Oh, D. W. C. MacMillan and M. J. Bird, *J. Am. Chem. Soc.*, 2021, **143**, 9332–9337.
146 N. A. Till, L. Tian, Z. Dong, G. D. Scholes and D. W. C. MacMillan, *J. Am. Chem. Soc.*, 2020, **142**, 15830–15841.
147 R. Sun, Y. Qin, S. Ruccolo, C. Schnedermann, C. Costentin and D. G. Nocera, *J. Am. Chem. Soc.*, 2019, **141**, 89–93.
148 R. Sun, Y. Qin and D. G. Nocera, *Angew. Chemie - Int. Ed.*, 2020, **59**, 9527–9533.
149 Y. Qin, R. Sun, N. P. Gianoulis and D. G. Nocera, *J. Am. Chem. Soc.*, 2021, **143**, 2005–2015.
150 O. S. Wenger, *Chem. - A Eur. J.*, 2021, **27**, 2270–2278.
151 D. L. Zhu, H. X. Li, Z. M. Xu, H. Y. Li, D. J. Young and J. P. Lang, *Org. Chem. Front.*, 2019, **6**, 2353–2359.
152 B. Pieber, J. A. Malik, C. Cavedon, S. Gisbertz, A. Savateev, D. Cruz, T. Heil, G. Zhang and P. H. Seeberger, *Angew. Chemie - Int. Ed.*, 2019, **58**, 9575–9580.
153 M. He, S. Yang, X. Yu and M. Bao, *Synlett*, 2021, **32**, A-E.
154 J. Lu, B. Pattengale, Q. Liu, S. Yang, S. Li, J. Huang and J. Zhang, *J. Am. Chem. Soc.*, 2018, **140**, 13719–13725.
155 W. Zu, C. Day, L. Wei, X. Jia and L. Xu, *Chem. Commun.*, 2020, **56**, 8273–8276.

Chapter 2

Titanium-catalyzed esterification reactions: beyond Lewis acidity

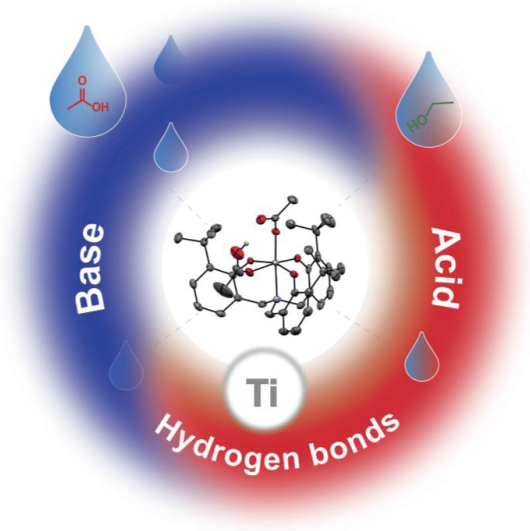

Abstract: Esterification is a key reaction and used in many synthetic and industrial processes, yet the detailed mechanism of operation of often-used (Lewis acid) catalysts is unknown and subject of little research. Here, we report on mechanistic studies of a titanium aminotriphenolate catalyst, using stoichiometric and catalytic reactions combined with kinetic data and density functional theory (DFT) calculations. While often only the Lewis acidity of the Ti-center is taken into account, we found that the amphoteric nature of this catalyst, combining this Lewis acidity with Brønsted basicity of a Ti-bound and *in situ* formed carboxylate group, is crucial for catalytic activity. Furthermore, hydrogen bonding interactions are essential to pre-organize substrates and to stabilize various intermediates and transition states and thus enhancing the overall catalytic reaction. These findings are not only applicable to this class of catalysts, but could be important for many other esterification catalysts.

This work is based on: L.A. Wolzak, J.I. van der Vlugt, K.J. van den Berg, J.N.H. Reek, M. Tromp, T.J. Korstanje, *ChemCatChem*, **2020**, 12, 5229-5235.

Introduction

Esterification is one of the most important reactions in organic synthesis and widely applied in industry, ranging from the production of aspirin to polyesters.[1] Although the direct, uncatalyzed transformation of a carboxylic acid and an alcohol to an ester is possible, it requires temperatures up to 250 °C to achieve full conversion under equilibrium conditions.[1] As early as 1895, Fischer and Speier described the first catalytic esterification reaction using sulfuric acid as a strong Brønsted acid.[2] In general, for Brønsted acid catalyzed esterification the active species is the protonated carboxylic acid and nucleophilic attack by the alcohol and water formation are the rate limiting steps.[3] Despite being very effective esterification catalysts, strong Brønsted acids also give rise to unwanted side reactions such as the dehydrative etherification of alcohols. The activation of the carbonyl function of the carboxylic acid substrate and subsequent nucleophilic attack by the alcohol onto the electron-deficient carbonyl carbon can also be promoted by Lewis acidic metal ions (Figure 1), which typically allow for milder reaction conditions and a wider substrate scope.[4–9] As such, recent developments in esterification catalysis have relied heavily on optimizing the Lewis acidity of the metal center.[10–14]

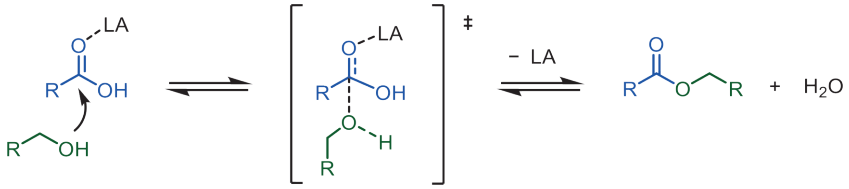

Figure 2.1. Schematic representation for Lewis acid (LA) catalyzed esterification.

This does, however, not need to be the sole factor that controls activity, as mildly Lewis acid metal alkoxides, carboxylates, and oxides are also active esterification catalysts.[15,16] Mechanistic proposals that take other factors besides Lewis acidity into account are scarce. Hydrogen bonding interactions between the hydroxyl group of the carboxylic acid and a Lewis basic oxygen bound to the metal center have been proposed, but only in a qualitative description of the reaction mechanism.[17–19] Titanium(IV) compounds, especially titanium alkoxides, are often employed as esterification catalyst due to their inherent Lewis acidity and non-toxic nature.[20–23] Mechanistic insight into the role of these titanium derivatives is, however, hampered by the rapid uncontrolled exchange reactions with carboxylic acids, alcohols and esters (Figure 2).[24,25] In addition, facile hydrolysis leads to very complex reaction mixtures consisting of titaniumdioxide, oxo-alkoxides and oligomeric structures.[26–28] Here, we report a mechanistic investigation on the use of

titanium aminotriphenolate complexes showing the amphoteric nature of the catalyst. Both the Lewis acidity and Brønsted basicity are important for the overall performance in esterification reactions. The catalysts based on the tetradentate aminotriphenolate ligands are robust, display remarkable stability to hydrolysis and are stable under acidic conditions.[29–32] This can be of importance for the application of these complexes, and the stability also allows the isolation of relevant reaction intermediates. The steric and electronic properties of the tetradentate aminotriphenolate ligand can be modified, making it a perfect platform for optimization of catalyst properties and a detailed mechanistic study (Figure 2).[33]

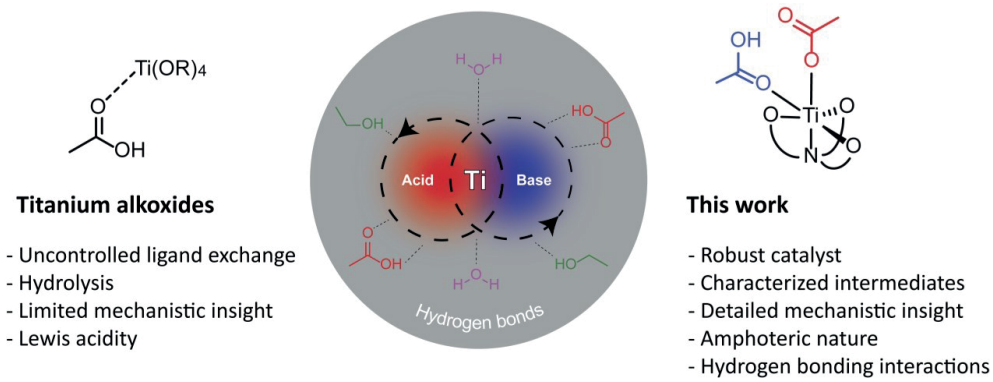

Figure 2.2. Comparison between titanium(IV) alkoxides and the titanium aminotriphenolate catalyst studied here.

Results and Discussion

Aminotriphenols **1**–**5** (Figure 2.3) are readily available via electrophilic aromatic substitution of the corresponding phenol with hexamethylenetetramine or reductive amination of the appropriate salicylic aldehydes.[34–36] The reaction of Ti(^{i}OPr)$_4$ with one equiv. of **1**–**5** yielded the mononuclear, C_3-symmetric complexes **6**–**10**.[37] Ligand exchange of the apical isopropoxide group is facile under acidic conditions.[32] Reaction of complex **6** with 20 equivalents of acetic acid resulted in complex **11**, which was isolated as an orange powder. ^{1}H NMR analysis revealed a sharp singlet corresponding to the six methylene hydrogens in the ligand framework, a broad singlet corresponding to six hydrogens of two acetate fragments and also a strongly deshielded signal at 14.5 ppm, integrating for one

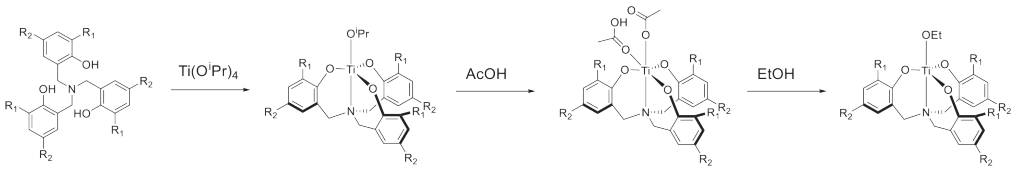

1. R_1 = tBu, R_2 = H
2. R_1 = tBu, R_2 = NO_2
3. R_1 = tBu, R_2 = OMe
4. R_1 = Me, R_2 = Me
5. R_1 = H, R_2 = H

6. R_1 = tBu, R_2 = H
7. R_1 = tBu, R_2 = NO_2
8. R_1 = tBu, R_2 = OMe
9. R_1 = Me, R_2 = Me
10.R_1 = H, R_2 = H

11. R_1 = tBu, R_2 = H
12. R_1 = H, R_2 = H

13. R_1 = tBu, R_2 = H

Figure 2.3. Aminotriphenol ligands **1** – **5** and corresponding titanium complexes **6** – **13**.

hydrogen (Figure 2.14). This indicates that besides apical exchange of the isopropoxide for an acetate ligand, an intact acetic acid molecule has also entered the coordination sphere of Ti^{IV}, resulting in an overall octahedral coordination. Upon addition of D_2O to species **11**, the strongly downfield signal disappeared, demonstrating facile exchange of the acidic hydrogen of acetic acid (Figure 2.15). The singlet for the methylene hydrogens is remarkable, as it reveals that the barrier for inversion of the rotor-shaped ligand is significantly lower than in complex **6**.[37]

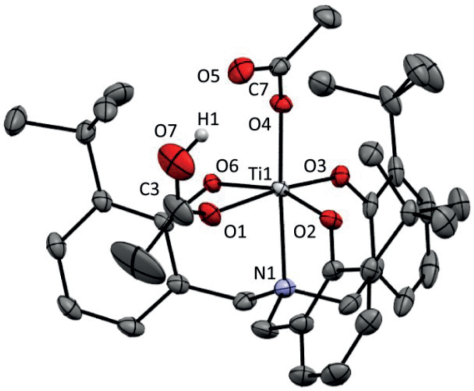

Figure 2.4. ORTEP view of solid state structure of complex **11**. Ellipsoids are given at 50% probability level. H atoms, except for H_1 in between O_7 and O_5, and disorder in C_3 and O_7 are omitted for clarity. Selected bond distances (Å): Ti_1-O_1 = 1.864(1), Ti_1-O_2 = 1.823(1), Ti_1-O_3 = 1.878(1), Ti_1-O_4 = 1.947(1), Ti_1-O_6 = 2.120(1), Ti_1-N_1 = 2.239(1), C_3-O_6 = 1.24(1), C_3-O_7 = 1.29(2), C_1-O_4 = 1.287(2), C_1-O_5 = 1.237(2). Selected angles (°): N_1-Ti_1-O_4 = 176.07(5), O_4-Ti_1-O_6 = 92.33(5), O_1-Ti_1-O_2 = 98.13(5). Colors correspond to titanium (light gray), oxygen (red), nitrogen (purple), and carbon (gray).

In addition, a variable temperature ^{1}H NMR experiment further supported that both an acetate and an acetic acid group are coordinated to the titanium center: six doublets corresponding to three different methylene groups are observed at -65 °C, indicating loss of C_3 symmetry of this complex (Figure 2.19). Suitable crystals for single crystal X-ray diffraction were obtained via slow evaporation of a benzene solution of complex **11**. The molecular structure (Figure 2.4) displays a slightly distorted octahedral complex with an $O_1 - Ti - O_2$ angle of 98.13(5)°. The difference in C – O bond lengths of the two carboxylate moieties indicates coordination of both an acetate and an acetic acid group to titanium, with the proton (H_1) sandwiched between both groups.

To demonstrate that the apical exchange of the isopropyl group is also possible for sterically less encumbered ligands, the unsubstituted complex **10** was treated with an excess of acetic acid. Attempts to isolate the newly formed complex proved to be cumbersome, but *in situ* formation of the acetic acid/acetate complex **12** was demonstrated by ^{1}H NMR spectroscopy (Figure 2.20). We studied the catalytic activity of complexes **6** – **10** (1 mol%) in a model esterification reaction between benzoic acid and heptanol in a 1:10 ratio (Table 2.1).

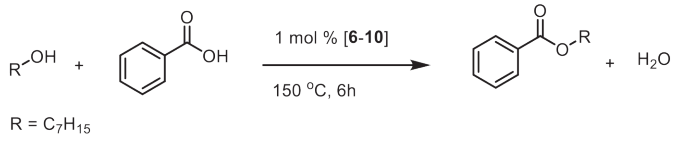

Table 2.1. Catalyst screening in model esterification reaction.

Entry[a]	Complex	Conv. [%] Benzoic acid	Yield [%] Heptylbenzoate
1	no cat.	10	6
2	**6**	31	26
3	**7**	40	36
4	**8**	19	19
5	**9**	48	48
6	**10**	62	62
7	Ti(^{i}OPr)$_4$	79	79

[a] All reactions were performed with benzoic acid (5 mmol), heptanol (50 mmol), and Ti-catalyst (1 mol%, 0.05 mmol), at 150 °C for 6 h. Yield and conversion were determined by GC analysis with pentadecane as internal standard.

An excess of the alcohol was used in order to drive the reaction to completion without the need for dehydrating agents or azeotropic distillation. The uncatalyzed reaction hardly provided any heptylbenzoate (entry 1), while the presence of catalytic amounts of complexes **6** – **8** gave a moderate increase in the efficiency of the reaction (entries 2 – 4). The reaction with the sterically less hindered complexes **9** – **10** resulted in a further increase in yield (48% and 62%, entries 5 and 6), although they could not match the activity of $Ti(^{i}OPr)_4$ (79% yield, entry 7). The trend in activity for catalysts **6** – **8** (**8** > **6** > **7**), related to the electronic properties of the phenoxy ligands (OMe > H > NO_2), suggesting that a more Lewis acidic titanium center leads to higher activity. In addition, the steric bulk in the *ortho*-position of the phenol motif of complexes **6** and **9** clearly impedes activity in catalysis (entries 2 and 5). Full conversion of benzoic acid was achieved with complex **10** after 24 h (>99% yield heptylbenzoate) demonstrating the non-equilibrium conditions of the model reaction (Figure 2.8). Furthermore, the addition of molecular sieves as dehydrating agent only gave a slight increase in the formation of heptylbenzoate at reaction times > 6 h (Figure 2.8). To investigate the reaction mechanism underlying the titanium aminotriphenolate-catalyzed esterification, initial kinetic and stoichiometric experiments were performed.

For complex **10** an order in catalyst of 0.80 was found in the concentration range 1.56 to 9.33 mM (0.25 to 1.5 mol%) (Figure 2.9, Table 2.3), which lends support to a mononuclear mechanism.[38] The activation energy was experimentally determined via an Arrhenius plot of the different rates of the reaction between 150 – 180 °C (Figure 2.10, Table 2.4). We found an energy of 20.1 kcal mol^{-1}, which is in good agreement with other titanium based esterification catalysts.[25] In order to establish the resting state during catalysis, an aliquot was taken from the model esterification reaction catalyzed by complex **6** after 30 minutes reaction time, and studied with mass spectrometry. The two observed species have an experimental mass of 669.3291 m/z and 663.4111 m/z which correlates to complexes where the apical isopropoxide group is exchanged for a heptoxy or a benzoate group (Figure 2.26). To further deduce the exact structure of the resting state, complex **6** was treated with 10 equiv. of acetic acid and 100 equiv. of ethanol in toluene at 110 °C. After 24 h, at which point the reaction had not yet reached completion, the mixture was evaporated and complex **11** was isolated with only minor impurities, suggesting that in the resting state both a carboxylate and a carboxylic acid are coordinated to titanium.[39] To demonstrate the facile formation of the alkoxy-substituted complex, complex **11** was dissolved in an excess of dry ethanol and stirred for 15 min. at RT. After evaporation of the solvent the new complex **13** was isolated (Figure 2.3), bearing an ethoxy group in the

apical position, as determined by NMR spectroscopy and mass spectrometry. Given these results, we conclude that complex **11** is the resting state during catalysis, while complex **13** is the end-of-catalysis state when an excess of alcohol is used, and possibly also an off-cycle complex.

The reaction mechanism for the most active titanium aminotriphenolate complex **10** was further examined with DFT-D3 calculations at the BP86/TZ2P level of theory (Figure 2.5, see experimental section for other, energetically less favorable calculated reaction pathways (Figure 2.7)).[40,41] The reaction starts with the acetic acid/acetate complex **A**, which is an analogue of the well characterized complex **11**, followed by transition state $\mathbf{TS_{AB}}$, involving a rotation of the apical acetic acid. Intermediate **B** is significantly higher in energy than complex **A** (ΔG = 7.6 kcal mol^{-1}), due to the loss of the favorable hydrogen bonding interaction between the acetic acid and the acetate group.

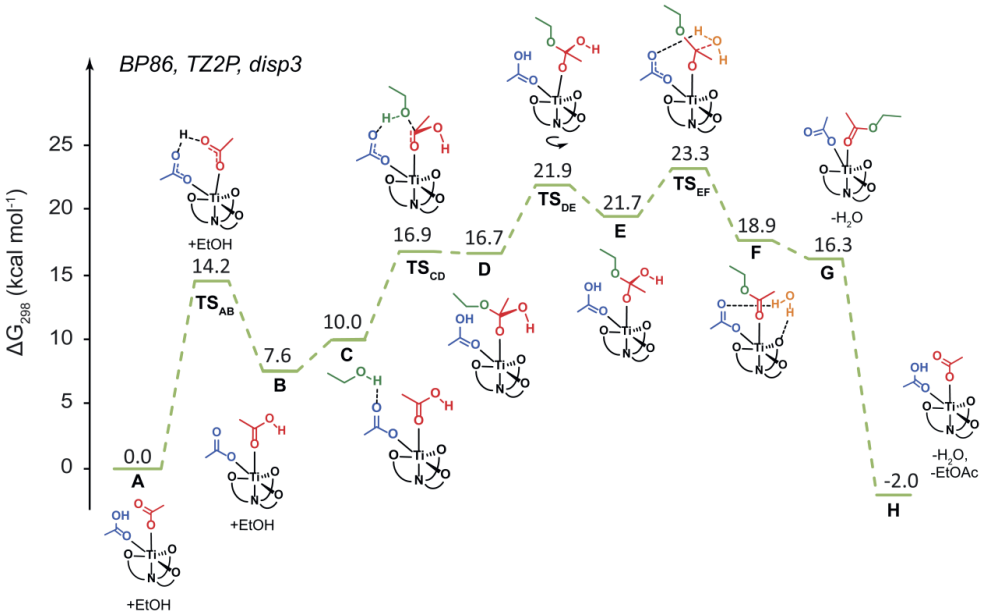

Figure 2.5. Proposed reaction pathway for the esterification reaction catalyzed by complex **10** (in the catalytic cycle hydrogen bonds are indicated with black dashed lines).

Nucleophilic attack of the alcohol is facile with a $\Delta\Delta G^{\ddagger}$ of 6.9 kcal/mol for $\mathbf{TS_{CD}}$. This step is favorable because the alcoholic hydrogen is hydrogen bonded to the acetate group that can also accept the proton and thus acts as an internal base. The combined action of a Brønsted basic acetate group and a Lewis acidic titanium center, results in overall

amphoteric character for this catalyst. The beneficial effect of using an amphoteric catalyst for esterification reactions has already been observed for metal hydroxides and alkoxides in the 1960s,[42] but is rarely mentioned in more recent studies. A counterclockwise rotation of intermediate **D**, **TS_{DE}**, involves a rotation and requires the cleavage of two hydrogen bonds, in order to pre-organize intermediate **E** for water formation. The third transition state, **TS_{EF}**, concerns the actual cleavage of the carbon-hydroxyl oxygen bond in structure **E** in order to form the ester. Consecutive loss of water and the ester product results in an overall slightly exergonic process (ΔG = -2.0 kcal mol^{-1}). The total energy profile shows that two transitions states (**TS_{DE}** and **TS_{EF}**) are close in free energy (1.3 kcal mol^{-1}), showing that both these transitions state can be the rate determining transitions state.

The optimized structures for the transition states **TS_{DE}** and **TS_{EF}** reveal the presence of hydrogen bonding interactions (Figure 2.6). During **TS_{DE}**, hydrogen bonds are formed between H_A and O_B of the ligand framework as well as between the acetic acid hydrogen (H_B) and O_A. These interactions pre-organize the complex for water formation (intermediate **E**) and are thus necessary to enhance the next step in the reaction, where water is expelled.

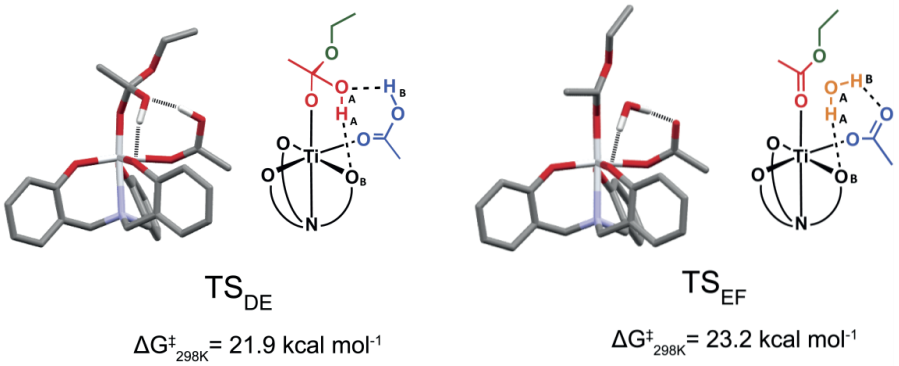

Figure 2.6. Calculated transition states **TS_{DE}** and **TS_{EF}** (optimized with DFT-D3 at the BP86/def-TZ2P level of theory) and ChemDraw representations thereof. All hydrogen atoms have been omitted for clarity (except hydrogens **A** and **B** involved in hydrogen bonds, indicated with black dashed lines).

Hydrogen bonding interactions between both water hydrogens (H_A and H_B) and the ligand oxygen (O_B) and the substrate oxygen (O_A) respectively, remain in **TS_{EF}**, showing that these

contribute to a lower energy of this rate determining transition state, thus enhancing the overall reaction rate.

Additional DFT calculations were performed to evaluate the catalytic activity of Ti-complexes based on C_3-symmetric tetradentate ligand with different *para*-substituents on the aromatic rings within (Table 2.2). These calculations show that for the transition states **TS_{CD}**, **TS_{DE}** and **TS_{EF}** the relative barrier, $\Delta\Delta G^{\ddagger}$ (the free energy difference between the transition state and its preceding intermediate), is indeed lowered by an electron-withdrawing nitro-substituent (entry 1), which leads to a more Lewis acid metal center. However, the effect of a *para*-substituent on the overall activation energy of the reaction is small, with only 0.6 kcal mol^{-1} difference between the methoxy- or nitro-substituted versions and the unsubstituted ligand, thus showing that here the Lewis acidity of the metal center is only a minor factor to modulate the overall activation energy and reaction rate.

Table 2.2. Influence of the *para*-substituent of the ligand on the relative barrier and the overall barrier of transition states **TS_{CD}, TS_{DE}** and **TS_{EF}**.

		TS_{CD}		**TS_{DE}**		**TS_{EF}**	
Entry[a]	**Para-substituent**	$\Delta\Delta G^{\ddagger}$	$\Delta G^{\ddagger}$	$\Delta\Delta G^{\ddagger}$	$\Delta G^{\ddagger}$	$\Delta\Delta G^{\ddagger}$	$\Delta G^{\ddagger}$
1	$-NO_2$	6.1	16.4	5.1	21.2	3.5	22.6
2	-H	6.8	16.8	5.3	21.9	3.7	23.2
3	-OMe	7.5	16.1	6.1	22.6	4.0	22.6

[a] Values are given in kcal mol^{-1}.

Based on these kinetic experiments and DFT calculations, we propose a catalytic pathway as depicted in Figure 2.5. In all geometries, including transition states, hydrogen bonding interactions are present between the ligand, the acetate/acetic acid group and the alcohol. Nucleophilic attack by the alcohol has a moderate energy barrier due to favorable preorganization of both the alcohol and the titanium-bound acetic acid via hydrogen bonding interactions with the acetate group and an oxygen of the ligand framework. As a result, proton transfer from the alcohol to the acetate group, which acts as a proton reservoir for water formation, is facile. **TS_{DE}** is a rotation, which requires the breakage of a hydrogen bond, in order to have the adequate geometry for water formation. The subsequent carbon-oxygen bond breaking, **TS_{EF}**, therefore has a notably low barrier for a bond-breaking step. Overall, this mechanism shows that there are three essential

prerequisites for an active catalyst: Lewis acidity of the Ti metal, favorable hydrogen bonding interactions between both reactants and the ligand, and a Brønsted basic group to facilitate proton transfer. This is in strong contrast with the common assumption that the Lewis acidity of the metal is the sole crucial (rate determining) factor for catalytic activity. The generality of our findings is demonstrated by the fate of many esterification catalysts under reaction conditions. The acidic reaction medium results in ligand exchange reactions, leading to the *in situ* formation of amphoteric metal carboxylates,[24] which could well have a similar mode of operation as the titanium aminotriphenolates presented in this study.

Conclusions

In summary, we have shown that the amphoteric nature of Ti-aminotriphenolate complexes, combining a Lewis acidic metal center with a Brønsted basic ligand site, in combination with preorganization via hydrogen bonding interactions, is essential for the catalytic activity of titanium aminotriphenolate complexes in the esterification reaction. Experimental and computational findings demonstrate that Lewis acidity is not the only key factor for catalytic activity, contrary to what often is assumed in literature. DFT calculations support favorable pre-organization via hydrogen bonding interactions with the ligand and elucidate the role of the additional acetate group as internal base. This acetate group enhances the nucleophilicity of the alcohol and subsequently stores the proton of the alcohol, which later on in the reaction is expelled in the form of water. We believe that these insights do not only apply to this particular class of titanium complexes, but are also important for other esterification catalysts, including often-used titanium alkoxides, and as such can help the rational design of new catalysts for esterification reactions.

Experimental Section

General Experimental Details

Dichloromethane and acetonitrile were distilled from CaH_2, *n*-pentane and Et_2O from sodium/benzophenone and toluene from sodium under argon atmosphere. Ethanol was degassed and dried over 3Å molecular sieves. All other chemicals were obtained from Merck or Fluorochem and were used without further purification. All air-sensitive materials were manipulated using standard Schlenk techniques or by the use of an argon-filled glovebox (MBraun Unilab). The NMR solvents CD_2Cl_2, toluene-d_8 and C_6D_6 were dried over molecular sieves and degassed via three cycles of freeze-pump-thaw. ^1H and ^{13}C NMR spectra were recorded on a 300 or 400 MHz Bruker AVANCE spectrometer . Spectra were referenced against residual solvent signal. FD-HRMS spectra were collected on an AccuTOF GC v 4g, JMS-T100GCV Mass spectrometer (JEOL, Japan) equipped with a Carbotec emitter. A typical current rate of 51.2 mA/min over 1.2 min and a flashing current 40 mA on every spectra of 30 ms was used. High resolution ESI-HRMS spectra were recorded on a JEOL AccuTOF LC-Plus JMS-T100LP spectrometer in CH_3CN. IR spectra were recorded on a Bruker Alpha FTIR machine. GC analysis for heptylbenzoate and benzoic acid was performed on a Thermo Scientific Trace GC Ultra equipped with a Restek stabilwax-DA column (30 m x 0.25 mm x 0.25 µm). Temperature program: initial temperature 50 °C, heat to 200 °C with 20 °C min^{-1}, hold for 10 min, heat to 250°C with 50 °C min^{-1}, hold for 3 minutes. Inlet temperature 250 °C, split ratio of 30, 1.0 mL min^{-1} helium flow, FID temperature 250 °C. Esterification reactions were performed in a Radley

Single crystal x-ray diffraction

X-ray Crystal Structure Determination of complex **11**: X-ray intensities were measured on a Bruker D8 Quest Eco diffractometer equipped with a Triumph monochromator (l = 0.71073 Å) and a CMOS Photon 100 detector at a temperature of 150(2) K. Intensity data were integrated with the Bruker APEX3 software.[43] Absorption correction and scaling was performed with SADABS.[44] The structures were solved using intrinsic phasing with the program SHELXT.[45] Least-squares refinement was performed with SHELXL-2014[46] against F2 of all reflections. Non-hydrogen atoms were refined with anisotropic displacement parameters. The H atoms were placed at calculated positions using the instructions AFIX 13, AFIX 43 or AFIX 137 with isotropic displacement parameters having values 1.2 or 1.5 times Ueq of the attached C atoms. CCDC 1941519 contain the supplementary crystallographic data for this paper. These data can be obtained free of charge from The Cambridge Crystallographic Data Centre via www.ccdc.cam.ac.uk/data_request/cif.

Computational details

Geometry optimizations were carried out with the Amsterdam Density Functional (ADF) program package using version 2017.201.[40,41] We used the BP86 functional in combination with the TZ2P basis set and a large frozen core.[47–49] Grimme's dispersion corrections (version 3, disp3) were used to include Van der

Waals interactions.[50] All minima (no imaginary frequencies) and transition states (one imaginary frequency) were characterized by calculating the Hessian matrix. ZPE and gas-phase thermal corrections (enthalpy, 298 K) from these analyses were calculated.

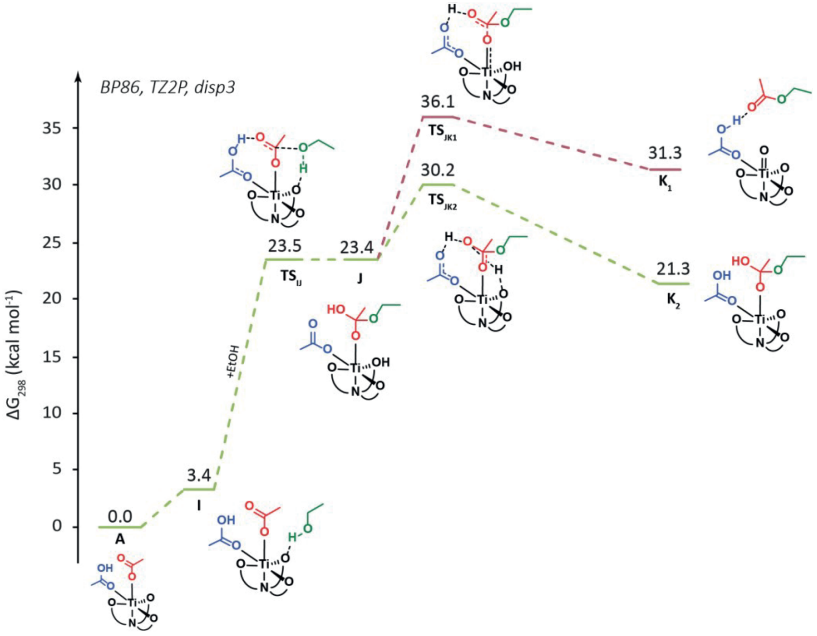

Figure 2.7: Alternative, higher lying, reaction pathways for the esterification of acetic acid and ethanol catalyzed by complex **10**.

Synthesis and catalysis

The triphenolamines **1**-**5** and titanium complexes **6**-**10** were synthesized via literature procedures.[34–37]

Complex **7**

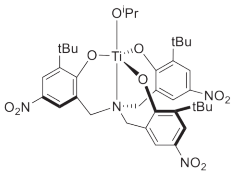

Under nitrogen atmosphere ligand **2** (100 mg, 0.16 mmol) was dissolved in 10 mL dry Et_2O. This solution was slowly added to $Ti(^iOPr)_4$ (46 µL, 0.16 mmol) in 5 mL dry Et_2O. The reaction mixture immediately changed to orange and over a period of 12 h a pale yellow precipitate formed. After filtration the solid material was dissolved in a minimum amount of DCM and precipitated with Et_2O (15 mL). Subsequent filtration afforded complex 7 (76 mg, 64%). ^{1}H NMR (300 MHz, CD_2Cl_2): δ 8.19 (d, *J* = 2.8 Hz, 3H, H_{Ar}), 8.01 (d, *J* = 2.8 Hz, 3H, H_{Ar}), 3.58 (br s, 6H, NCH_2), 1.58 (d, *J* = 6.2 Hz, 6H, $OCHCH_3$), 1.51 (s, 27H, tBu), the $OCH(CH_3)_2$ proton overlaps with the solvent peak (δ 5.32). ^{1}H NMR (300 MHz, C_6D_6): δ 8.32 (d, *J* = 2.8 Hz, 3H, H_{Ar}), 7.77 (d, *J* = 2.7 Hz, 3H, H_{Ar}), 5.18 (h, *J* = 6.0 Hz, 1H, $OCH(CH_3)_2$), 2.88 (br s, 3H, NCH_2), 2.19 (br s, 3H, NCH_2), 1.47 (d, *J* = 6.1 Hz, 6H, $OCHCH_3$), 1.35 (s, 27H, tBu). ^{13}C NMR (100 MHz, CD_2Cl_2): δ 167.20 (C_{Ar}), 141.22 (C_{Ar}), 138.32 (C_{Ar}), 125.33 (C_{Ar}), 124.05 (CH_{Ar}), 123.62 (CH_{Ar}), 84.03

(C<u>H</u>(CH$_3$)$_2$), 58.13 (N<u>C</u>H$_2$), 35.61 (<u>C</u>(CH$_3$)$_3$), 29.34 (C(<u>C</u>H$_3$)$_3$), 26.40 (OCH(<u>C</u>H$_3$)$_2$). FD-HRMS (*m/z, pos*): Calculated for [$C_{36}H_{46}N_4O_{10}Ti$] 742.2697; found 742.2679 [M]$^+$.

Complex **11**

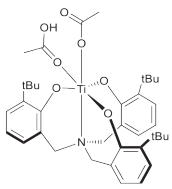

Under nitrogen atmosphere complex **6** (100 mg, 0.165 mmol) was dissolved in 5 mL dry toluene and 20 equivalents of acetic acid (188 µL, 3.29 mmol) were added dropwise to give an orange reaction mixture. After stirring at room temperature for 10 min the solvent was removed in vacuo. The remaining orange powder was triturated three times with 10 mL dry acetonitrile and dried under vacuum. Yield 102 mg (93 %). ^{1}H NMR (400 MHz, CD_2Cl_2): δ 14.51 (s, 1H, O-<u>H</u>-O), 7.21 (d, *J* = 6.2 Hz, 3H, <u>H</u$_{Ar}$), 7.02 (d, *J* = 7.4 Hz, 3H, <u>H</u$_{Ar}$), 6.77 (t, *J* = 7.6 Hz, 3H, <u>H</u$_{Ar}$), 3.74 (s, 3H, NC<u>H</u$_2$), 1.85 (br s, 6H, C<u>H</u$_3$), 1.39 (s, 27H, C(C<u>H</u$_3$)$_3$). Addition of D_2O resulted in the disappearance of the singlet at δ 14.51 and a new singlet at δ 4.76 (HDO). ^{13}C NMR (125 MHz, CD_2Cl_2): δ 178.28 (br s, OO<u>C</u>CH$_3$), 161.66 (<u>C</u$_{Ar}$), 136.69 (<u>C</u$_{Ar}$), 127.83 (<u>C</u>H$_{Ar}$), 126.88 (<u>C</u>H$_{Ar}$), 125.55 (<u>C</u$_{Ar}$), 120.33 (<u>C</u>H$_{Ar}$), 60.89 (N<u>C</u>H$_2$), 35.01 (<u>C</u>(CH$_3$)$_3$), 29.87 (C(<u>C</u>H$_3$)$_3$). The methyl carbons of the acetate and acetic acid group were not observed due to their fluxional behavior. FD-HRMS (*m/z, pos*): Calculated for [$C_{36}H_{48}NO_4Ti$] 607.2777; found 607.2948 [M-CH$_3$COOH]$^+$. ESI-HRMS (*m/z, pos*): Calculated for [$C_{33}H_{42}NO_3Ti$] 548.26475; found 548.26665 [M-CH$_3$COO-CH$_3$COOH]$^+$. IR-ATR (cm^{-1}): 1658 (s, $\nu_{as\ COO}$). Crystals suitable for X-ray analysis were grown via slow evaporation of a concentrated benzene solution.

$C_{37}H_{49}NO_7Ti$, Fw = 667.67, plate, 0.560×0.537×0.267 mm, monoclinic, P21/c (No: 14)), a = 17.7368(10), b = 11.9329(6), c = 18.0144(10) Å, β = 110.227(2)°, V = 3577.6(3) Å3, Z = 4, Dx = 1.240 g/cm3, m = 0.287 mm-1. 132094 Reflections were measured up to a resolution of (sin q/l)max = 0.77 Å-1. 8199 Reflections were unique (Rint = 0.0399), of which 7049 were observed [I>2s(I)]. 452 Parameters were refined with 105 restraints. R1/wR2 [I > 2s(I)]: 0.0382/0.0922. R1/wR2 [all refl.]: 0.0482/ 0.0989. S = 1.076. Residual electron density between -0.402 and 0.318 e/Å3. CCDC 1941519.

Complex **12**

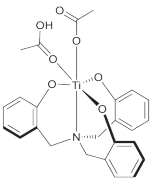

Complex **10** (5 mg, 0.01 mmol) was reacted with acetic acid (10 µL, 0.18 mmol) in dry C_6D_6 in an NMR tube under nitrogen atmosphere. ^{1}H NMR (400 MHz, C_6D_6): δ 7.12 – 6.55 (m, 12H, <u>H</u$_{Ar}$), 3.74 (br s, 1H, free C<u>H</u>OH(CH$_3$)$_2$), 3.38 (s, 6H, NC<u>H</u$_2$), 0.99 (d, *J* = 5.8, 6H, free (CHOH(C<u>H</u$_3$)$_2$). The methyl groups of the coordinated acetic acid and acetate group are not observed due to exchange with free acetic acid.

Complex **13**

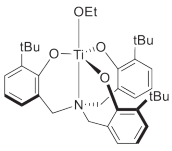

Complex **11** (34 mg, 0.05 mmol) was dissolved in 2 mL dry EtOH under nitrogen atmosphere to give a yellow suspension after 30 minutes of stirring at room temperature. Removal of ethanol and residual acetic acid in vacuo resulted in the isolation of complex 13 as a pale yellow powder (28 mg, 92%). ^{1}H NMR (400 MHz, C_6D_6): δ 7.38 (d, *J* = 7.7 Hz, 3H, <u>H</u$_{Ar}$), 6.92 (d, *J* = 7.5 Hz, 3H, <u>H</u$_{Ar}$), 6.85 (d, *J* = 7.3 Hz, 3H, <u>H</u$_{Ar}$), 5.20 (q, *J* = 7.0 Hz, 2H, OC<u>H</u$_2$CH$_3$), 3.98 (br s, 3H, NC<u>H</u$_2$), 2.57 (br s, 3H, NC<u>H</u$_2$), 1.74 (t, *J* = 6.9 Hz, 3H,

$OCH_2\underline{C}H_3$), 1.72 (s, 27H, $C(\underline{C}H_3)_3$). ^{13}C NMR (100 MHz, C_6D_6): δ 167.76 ($\underline{C}_{Ar}$), 136.16 ($\underline{C}_{Ar}$), 126.26 ($\underline{C}H_{Ar}$), 125.06 ($\underline{C}_{Ar}$), 120.24 ($\underline{C}H_{Ar}$), 73.14 ($O\underline{C}H_2CH_3$), 58.23 ($\underline{C}$), 34.71 ($\underline{C}$), 29.44 ($C(\underline{C}H_3)_3$), 19.46 ($OCH_2\underline{C}H_3$). One of the aromatic carbons, $\underline{C}H_{Ar}$, overlaps with the C_6D_6 signal at δ 128.06, see cross peak in HSQC (6.85; 128.06). FD-HRMS (*m/z, pos*): Calculated for $[C_{35}H_{47}NO_4Ti]$ 593.2988; found 593.2982.

Reaction of complex **6** with acetic acid and ethanol

To examine the formation of complex **15** during catalysis, a solution of complex **6** (30 mg, 0.05 mmol) in 5 mL dry toluene was reacted with 20 equivalents acetic acid (57 µL, 0.97 mmol) and ~200 equivalents of ethanol (575 µL, 9.86 mmol). The reaction mixture was brought to reflux and stirred for 24 h. An aliquot was taken and ethyl acetate was detected by GC analysis. About 2.5 mL of the reaction mixture was evaporated to dryness which resulted in the isolation of complex 11 with minor impurities (~10 mg, 61%). ^1H NMR (300 MHz, CD_2Cl_2): δ 7.21 (d, *J* = 6.2 Hz, 3H, $\underline{H}_{Ar}$), 7.02 (d, *J* = 7.4 Hz, 3H, $\underline{H}_{Ar}$), 6.77 (t, *J* = 7.6 Hz, 3H, $\underline{H}_{Ar}$), 3.74 (s, 6H, $NC\underline{H}_2$), 1.83 (br s, 6H, $C\underline{H}_3$), 1.39 (s, 27H, $C(C\underline{H}_3)_3$). The $COO\underline{H}$ proton at δ 14.51 was not observed.

Catalytic esterification of benzoic acid with heptanol

In a carousel reaction station under a nitrogen atmosphere benzoic acid (610.6 mg, 5 mmol) was dissolved in heptanol (7.14 mL, 50 mmol). Two different runs were performed, for the catalyzed reactions 1 mol% catalyst was used. To half of the reaction mixtures 1 g of activated powdered 4 Å molecular sieves were added and for all samples pentadecane (0.41 mL, 1.5 mmol) was used as internal standard. Samples for GC analysis were taken after 3 h, 6 h, 10 h and 24 h (averaged over 2 runs).

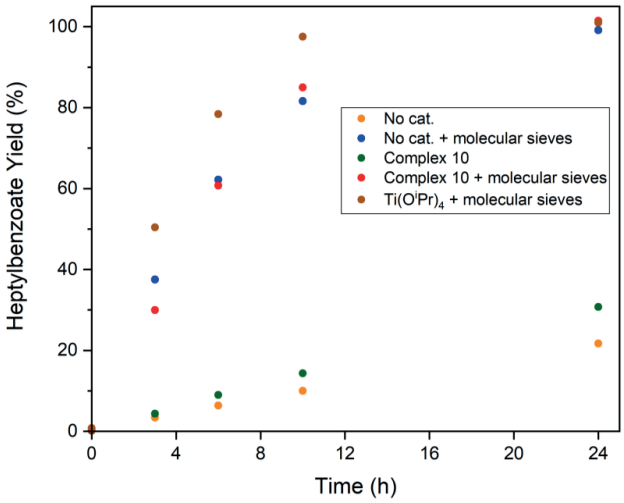

Figure 2.8. Heptylbenzoate formation.

Determination of order of reaction

In a carousel reaction station under a nitrogen atmosphere benzoic acid (610.6 mg, 5 mmol) was dissolved in heptanol (7.14 mL, 50 mmol). Two different runs were performed with complex **10** added as a powder (0.25, 0.5, 1 and 1.5 mol%) and pentadecane (0.41 mL, 1.5 mmol) as internal standard. Samples for GC analysis were taken after 1 h and 2 h. The rate (K) was determined via a tangent line of the heptyl benzoate concentration between 1 h and 2 h.

Table 2.3. Reaction rate between 1 h and 2 h at various catalyst loadings.

Catalyst (mol%)	K (mol/L*s)
0.25	$0.426\ 10^{-2}$
0.25	$0.484\ 10^{-2}$
0.50	$0.680\ 10^{-2}$
0.50	$0.670\ 10^{-2}$
1.00	$1.478\ 10^{-2}$
1.00	$1.549\ 10^{-2}$
1.50	$1.743\ 10^{-2}$
1.50	$1.708\ 10^{-2}$

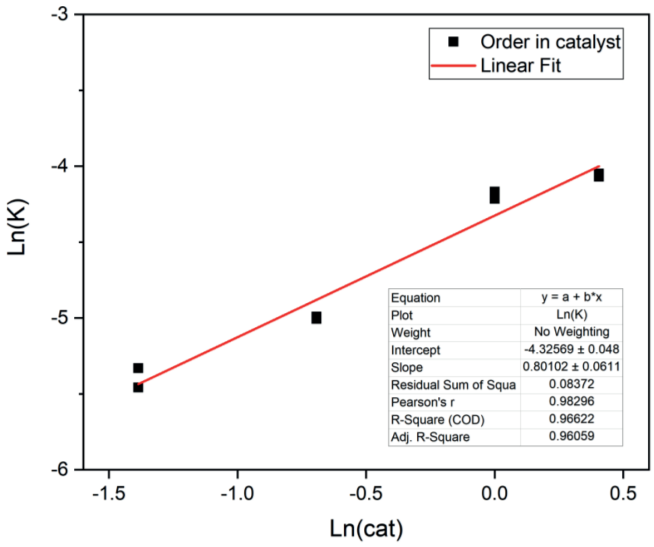

Figure 2.9. Order in catalyst.

Determination of activation energy

In a carousel reaction station under a nitrogen atmosphere benzoic acid (610.6 mg, 5 mmol) was dissolved in heptanol (7.14 mL, 50 mmol). Complex **10** was added as a powder (21,97 mg, 1 mol%) and pentadecane (0.41 mL, 1.5 mmol) as internal standard. Four different runs were performed in duplo at 150 °C, 160 °C, 170 °C and 180 °C and samples for GC analysis were taken after 1 h and 2 h. The rate (K) was determined via a tangent line of the heptyl benzoate concentration between 1 h and 2 h. The activation energy is given by 10108 * 8.3145 = 84.04 KJ*mol^{-1} or 20.09 Kcal*mol^{-1}.

Table 2.4. Reaction rate between 1h and 2h at various temperatures.

T (K)	K (mol/L*s)
423	1.478 10^{-5}
423	1.674 10^{-5}
433	3.263 10^{-5}
433	2.094 10^{-5}
443	5.865 10^{-5}
443	5.217 10^{-5}
453	6.811 10^{-5}
453	7.439 10^{-5}

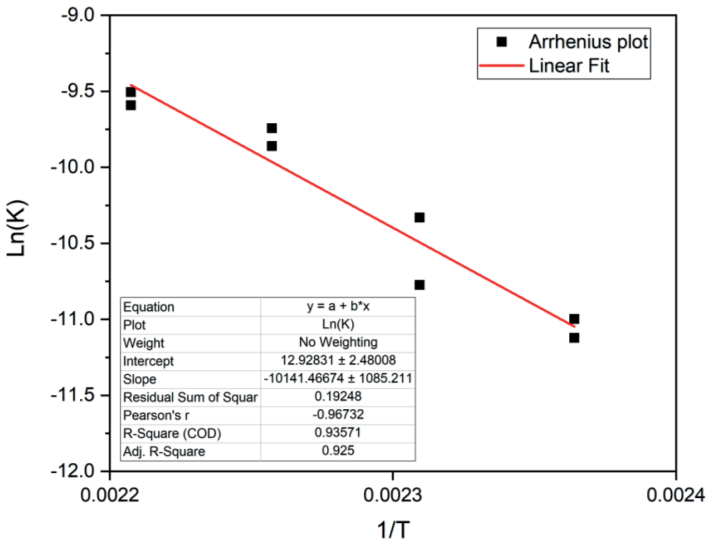

Figure 2.10. Arrhenius plot.

Spectra

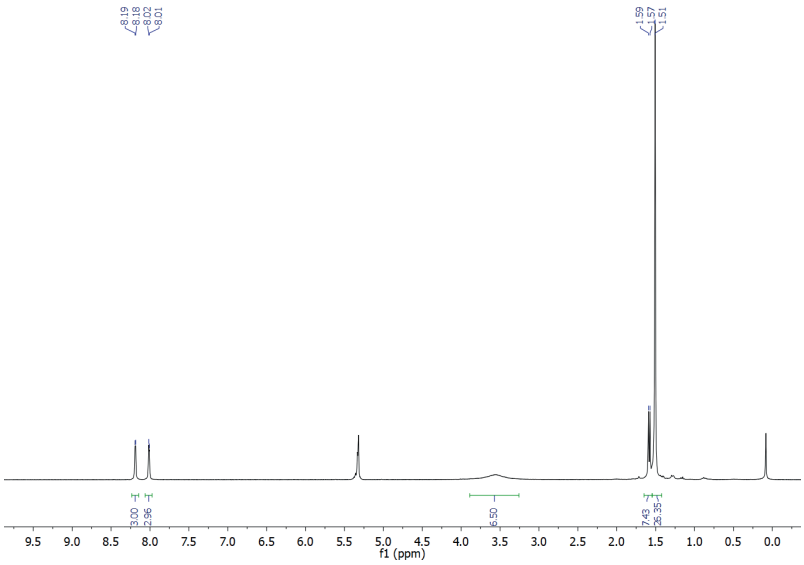

Figure 2.11. ^{1}H NMR of **7,** CD_2Cl_2.

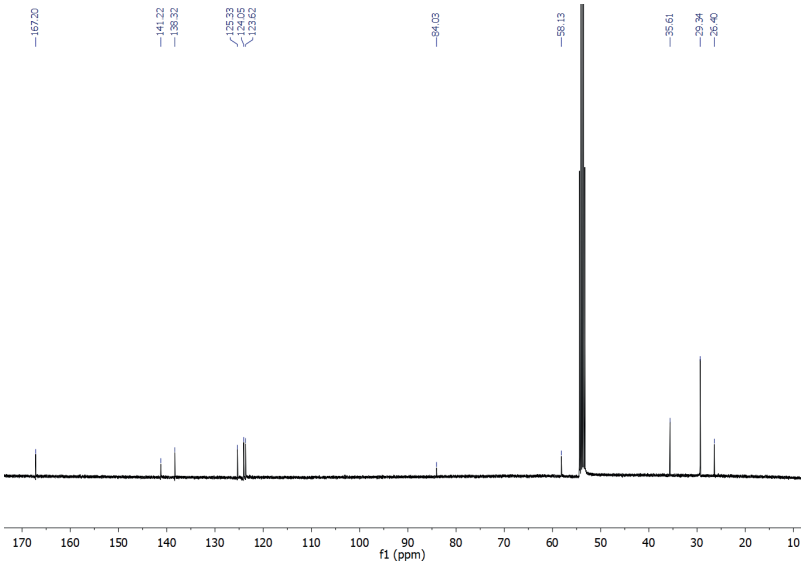

Figure 2.12. ^{13}C NMR of **7,** CD_2Cl_2.

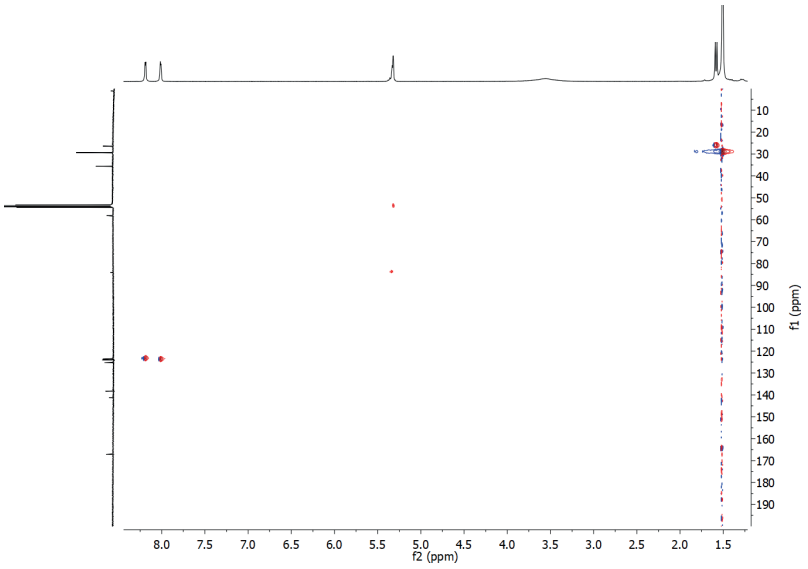

Figure 2.13. ^{1}H ^{13}C HSQC NMR of **7,** CD_2Cl_2.

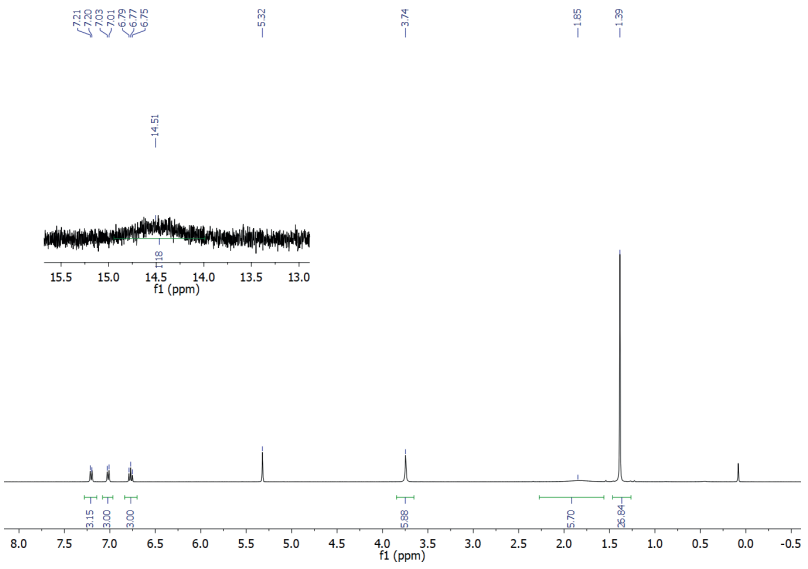

Figure 2.14. ^{1}H NMR of **11,** CD_2Cl_2.

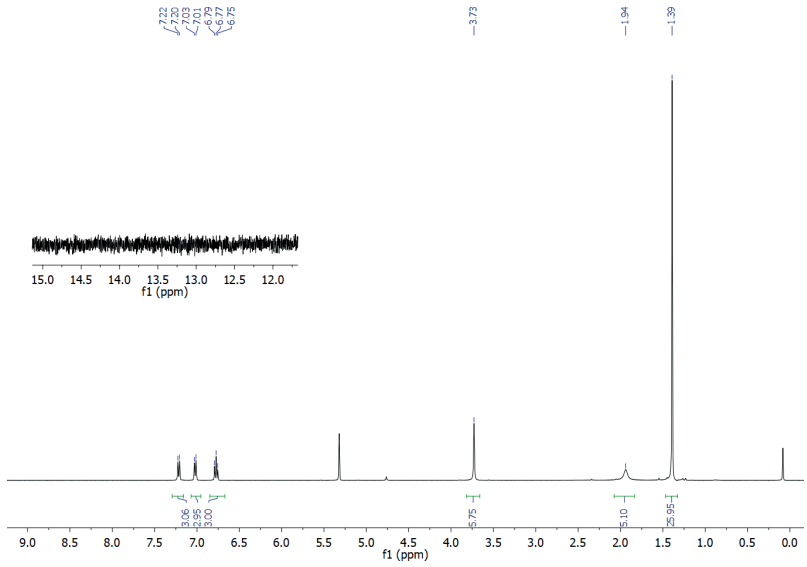

Figure 2.15. ^{1}H NMR of **11** upon addition of D_2O, CD_2Cl_2.

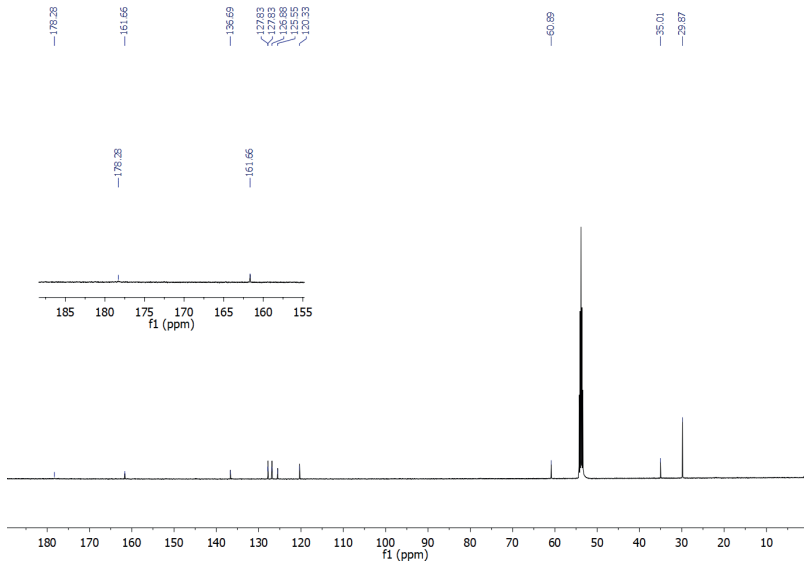

Figure 2.16. ^{13}C NMR of **11**, CD_2Cl_2.

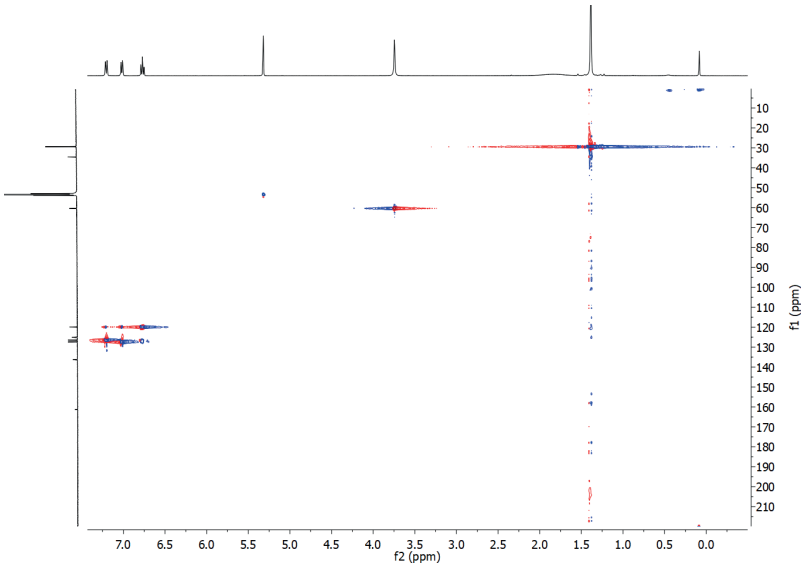

Figure 2.17. ^{1}H ^{13}C HSQC NMR of **11**, CD_2Cl_2.

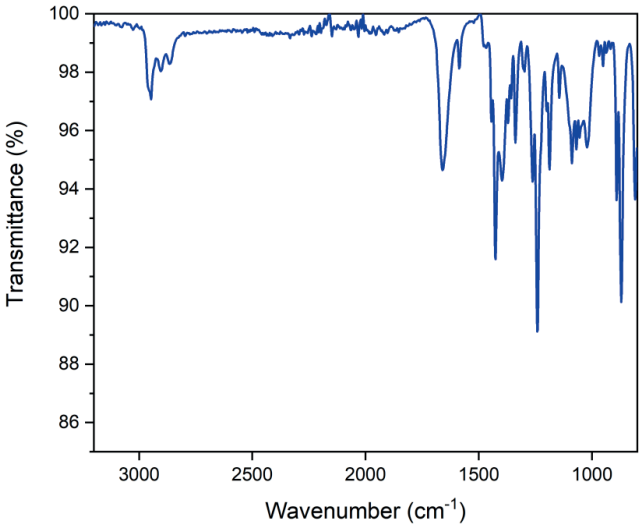

Figure 2.18. ATR IR spectrum of **11**.

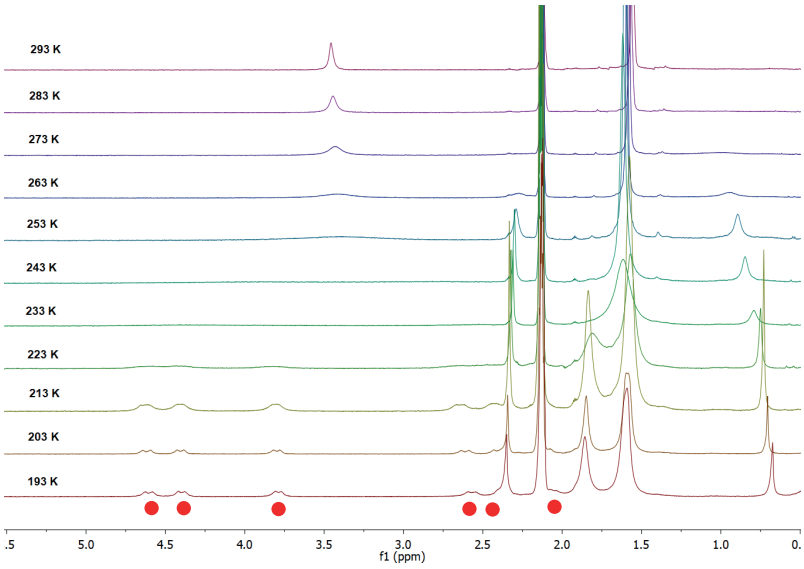

Figure 2.19. VT ^{1}H NMR (193 to 293 K) of **11**, tol-d_8. Methylene protons indicated with a red dot.

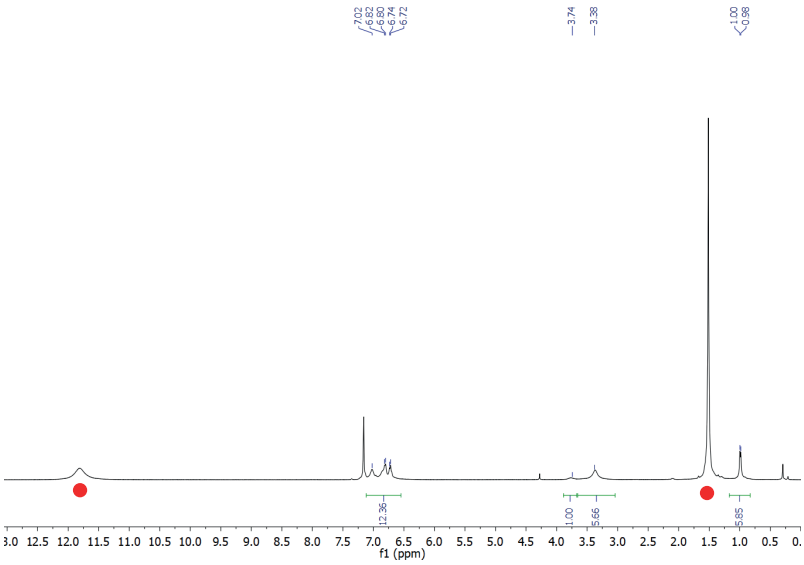

Figure 2.20. ^{1}H NMR of **12**, C_6D_6. Acetic acid signals indicated with a red dot.

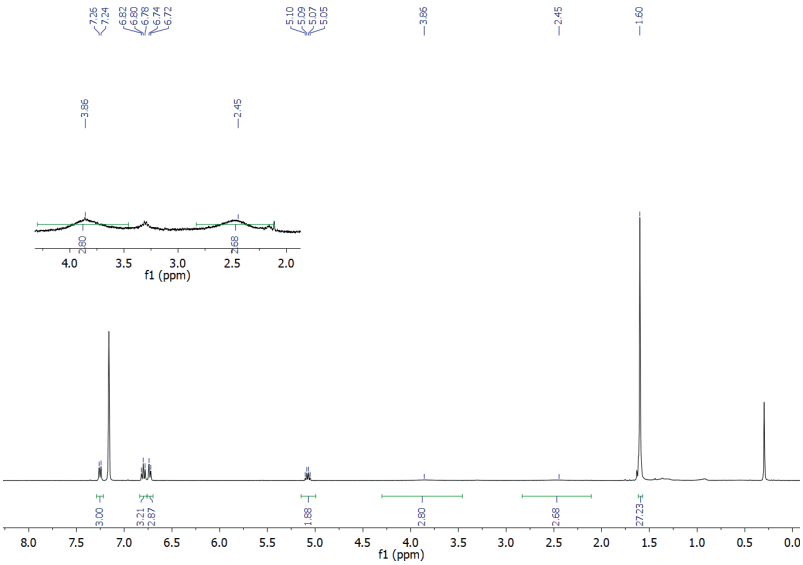

Figure 2.21. ^{1}H NMR of **13**, C_6D_6.

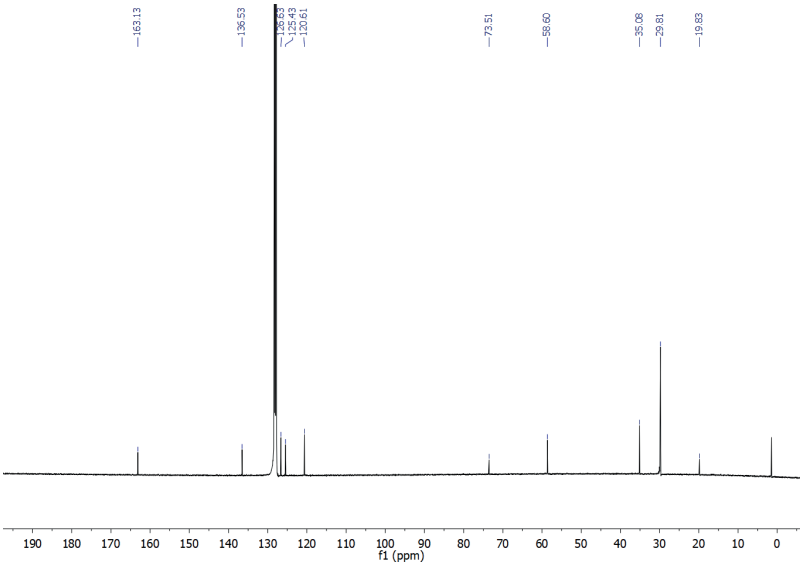

Figure 2.22. ^{13}C NMR of **13**, C_6D_6.

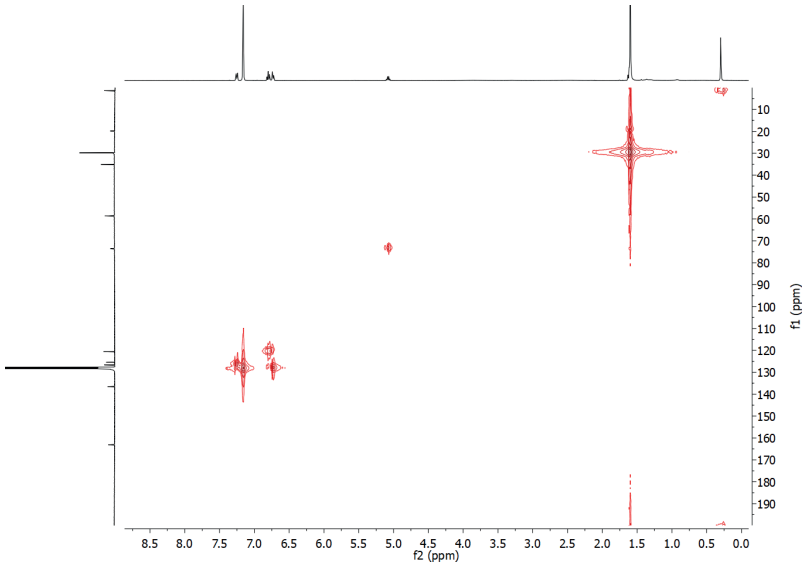

Figure 2.23. ^{1}H ^{13}C HSQC NMR of **13**, C_6D_6.

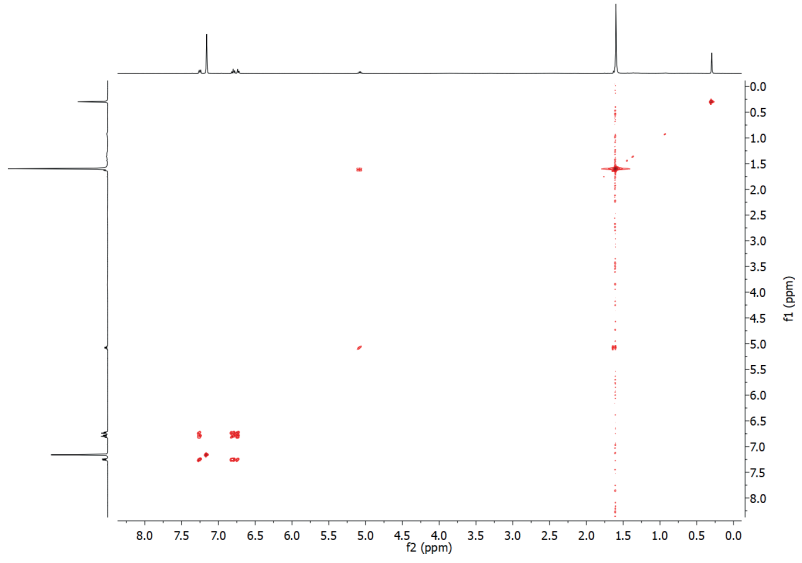

Figure 2.24. ^{1}H COSY NMR of **13**, C_6D_6.

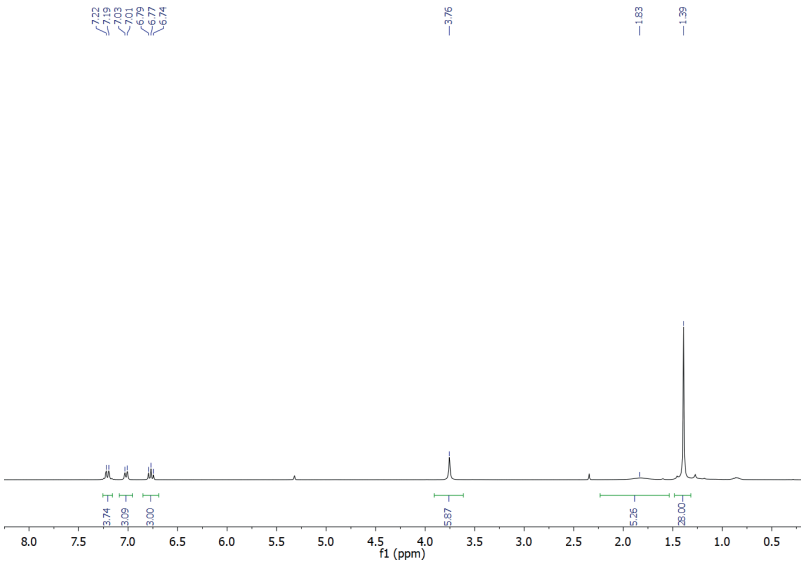

Figure 2.25. ^{1}H NMR of **6** after reaction with acetic acid and ethanol, CD_2Cl_2.

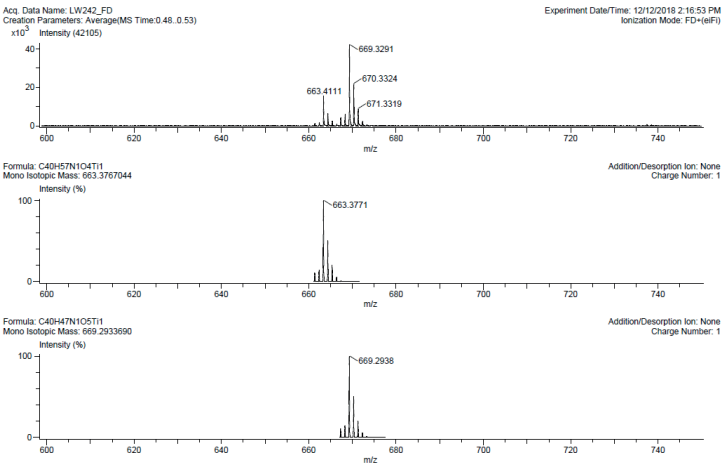

Figure 2.26. FD-HRMS of esterification reaction catalyzed by complex **6** (after 30 min reaction time).

References

1 J. Otera, J. Nishikido, *Esterification. Methods, Reactions, and Applications*, Wiley-VCH Verlag GmbH & Co., Weinheim, 2nd edn., 2010.
2 A. Fischer, E. Speier, *Chem. Ber.*, 1895, **28**, 3252–3258.
3 J. Clayden, N. Greeves and S. Warren, *Organic Chemistry*, Oxford University press, Oxford, 2nd edn., 2012.
4 Y. Román-Leshkov and M. E. Davis, *ACS Catal.*, 2011, **1**, 1566–1580.
5 J. J. Li, *Fischer-Speier esterification. In: Name Reactions*, Springer, Berlin, Heidelberg, 2002.
6 G. Bartoli, J. Boeglin, M. Bosco, M. Locatelli, M. Massaccesi, P. Melchiorre and L. Sambri, *Adv. Synth. Catal.*, 2005, **347**, 33–38.
7 T. Kawabata, T. Mizugaki, K. Ebitani and K. Kaneda, *Tetrahedron Lett.*, 2003, **44**, 137–140.
8 H. E. Hoydonckx, D. E. De Vos, S. a. Chavan and P. a. Jacobs, *Top. Catal.*, 2004, **27**, 83–96.
9 A. B. Ferreira, A. Lemos Cardoso and M. J. da Silva, *ISRN Renew. Energy*, 2012, **2012**, 1–13.
10 J. Bahamonde Santos, A.; Martinez, M.; Mira, *Chem. Eng. Technol.*, 1996, **19**, 538–542.
11 K. Ishihara, M. Nakayama, S. Ohara and H. Yamamoto, *Tetrahedron*, 2002, **58**, 8179–8188.
12 M. Nakayama, A. Sato, K. Ishihara and H. Yamamoto, *Adv. Synth. Catal.*, 2004, **346**, 1275–1279.
13 D. Dupont, S. Arnout, P. T. Jones and K. Binnemans, *J. Sustain. Metall.*, 2016, **2**, 79–103.
14 K. Ishihara, S. Ohara and H. Yamamoto, *Science*, 2000, **290**, 1140–1142.
15 M. R. Meneghetti and S. M. P. Meneghetti, *Catal. Sci. Technol.*, 2015, **5**, 765–771.
16 K. Manabe and S. Kobayashi, *Adv. Synth. Catal.*, 2002, **344**, 270–273.
17 F. Pilati, P. Manaresi, B. Fortunato, A. Munari and V. Passalacqua, *Polymer (Guildf).*, 1981, **22**, 1566–1570.
18 F. Pilati, P. Manaresi, B. Fortunato, A. Munari and P. Monari, *Polymer (Guildf).*, 1983, **24**, 1479–1483.
19 W. Tian, Z. Zeng, W. Xue, Y. Li and T. Zhang, *Chinese J. Chem. Eng.*, 2010, **18**, 391–396.
20 L. Chen, J. Xu, W. Xue and Z. Zeng, *Korean J. Chem. Eng.*, 2018, **35**, 82–88.
21 US Patent US 2012/0316316 A1, 2012.
22 F. Ahmadnian, F. Velasquez and K. H. Reichert, *Macromol. React. Eng.*, 2008, **2**, 513–521.
23 Y. Yang, S. Yoon, Y. Hwang and B. Song, *Bull. Korean Chem. Soc.*, 2012, **33**, 3445–3447.
24 E. Leverd, F. Fradet, A. Maréchal, *Eur. Polym. J.*, 1987, **23**, 695–698.
25 E. Fradet, A. Maréchal, in *Advances in Polymer Sciences*, Springer Berlin Heidelberg, 1982.
26 K. Pang, R. Kotek and A. Tonelli, *Prog. Polym. Sci.*, 2006, **31**, 1009–1037.
27 M. Bonchio, G. Licini, G. Modena, O. Bortolini, S. Moro and W. A. Nugent, *J. Am. Chem. Soc.*, 1999, **121**, 6258–6268.
28 S. Doeuff, M. Henry, C. Sanchez and J. Livage, *J. Non. Cryst. Solids*, 1987, **89**, 206–216.
29 S. Gendler, S. Segal, I. Goldberg, Z. Goldschmidt and M. Kol, *Inorg. Chem.*, 2006, **45**, 4783–4790.
30 C. Zonta, E. Cazzola, M. Mba and G. Licini, *Adv. Synth. Catal.*, 2008, **350**, 2503–2506.
31 S. D. Bull, M. G. Davidson, C. L. Doherty, A. L. Johnson and M. F. Mahon, *Chem. Commun.*, 2003, 1750–1751.
32 V. Ugrinova, G. a Ellis and S. N. Brown, *Chem. Commun.*, 2004, 468–469.
33 G. Licini, M. Mba and C. Zonta, *J. Chem. Soc. Dalt. Trans.*, 2009, 5265–5277.
34 L. J. Prins, M. M. Blázquez, A. Kolarović and G. Licini, *Tetrahedron Lett.*, 2006, **47**, 2735–2738.
35 D. Lionetti, A. J. Medvecz, V. Ugrinova, M. Quiroz-Guzman, B. C. Noll and S. N. Brown, *Inorg. Chem.*, 2010, **49**, 4687–4697.
36 P. Zardi, K. Wurst, G. Licini and C. Zonta, *J. Am. Chem. Soc.*, 2017, **139**, 15616–15619.
37 M. Kol, M. Shamis, I. Goldberg, Z. Goldschmidt, S. Alfi and E. Hayut-Salant, *Inorg. Chem. Commun.*, 2001, **4**, 177–179.
38 Given the catalyst order of 0.8, we believe that the system is primarily catalyzed by mononuclear titanium complexes, although a minor contribution of dimeric species that dissociate during the rate- determining step,

lowering the reaction order, cannot be excluded. In addition, the order in carboxylic acid and alcohol are outside the scope of this research, since the very high concentrations of both reactants makes order determination cumbersome. Moreover, a Brønsted acid-catalyzed (background) reaction also takes place, making both reactant orders non-informative for the titanium-catalyzed reaction, see reference.[24]

39 For all octahedral complexes with a carboxylate and a carboxylic acid group coordinated to titanium, the carboxylic acid group was not observed with mass spectrometry.

40 G. te Velde, F. M. Bickelhaupt, E. J. Baerends, C. Fonseca Guerra, S. J. A. van Gisbergen, J. G. Snijders and T. Ziegler, *J. Comput. Chem.*, 2001, **22**, 931–967.

41 C. Fonseca Guerra, J. G. Snijders, G. Velde and E. J. Baerends, *Theor. Chem. Acc.*, 1998, **99**, 391–403.

42 A. Coenen, *Adv. Chem.*, 1965, **48**, 76–86.

43 Bruker APEX2 software, 2016.

44 G. M. Sheldrick, SADABS, University of Göttingen, Germany, 2008

45 G. M. Sheldrick, *Acta Cryst. A.*, 2015, **71**, 3–8.

46 G. M. Sheldrick, SHELXL2014, University of Göttingen, Germany, 2014.

47 D. Becke, *Phys. Rev. A.*, 1988, **38**, 3098–3100.

48 J. P. Perdew, *Phys. Rev. B.*, 1986, **33**, 8822–8824.

49 E. Van Lenthe and E. J. Baerends, *J. Comput. Chem.*, 2003, **24**, 1142–1156.

50 A. Grimme, S. Antony, J. Ehrlich, S, Krieg, *J. Chem. Phys.*, 2010, **132**, 154104.

Chapter 3

Mechanistic elucidation of monoalkyltin(IV)-catalyzed esterification

Abstract: Monoalkyltin(IV) complexes are well-known catalysts for esterification reactions and polyester formation, yet the mode of operation of these Lewis acidic complexes is still unknown. Here, we report on mechanistic studies of *n*-butylstannoic acid in stoichiometric and catalytic reactions, analyzed by NMR, IR and MS techniques. While the chemistry of *n*-butyltin(IV) carboxylates is dominated by formation of multinuclear tin assemblies, we found that under catalytically relevant conditions only monomeric *n*-BuSn(OAc)$_3$ and dimeric (*n*-BuSnOAc$_2$OEt)$_2$ are present. Density functional theory (DFT) calculations provide support for a mononuclear mechanism, where *n*-BuSn(OAc)$_3$ and dimeric (*n*-BuSnOAc$_2$OEt)$_2$ are regarded as off-cycle species, and suggest that carbon-oxygen bond breaking is the rate determing step.

This work is based on: L.A. Wolzak, J.J. Hermans, F. de Vries, K.J. van den Berg, J.N.H. Reek, M. Tromp, T.J. Korstanje, *Catal. Sci. Technol.*, **2021**, 11, 3326-3332 (front cover).

Introduction

The synthesis of esters from alcohols and carboxylic acids is an important reaction in organic synthesis of small molecules and polymers.[1,2] Although strong Brøndsted acids are efficient esterification catalysts, often the milder Lewis acids are preferred since they provide less unwanted side products.[3] Therefore over the past decades, a variety of Lewis acidic organotin derivatives have been developed and these catalysts are frequently used in industry.[4,5] The inherent Lewis acidity of tin(IV) complexes in combination with facile ligand exchange are considered the origin of their catalytic performance in the esterification reaction.[6] Especially organometallic mono- and dialkyltin(IV) complexes display good catalytic performance and stability in many transesterification, esterification and polyesterification reactions.[7]

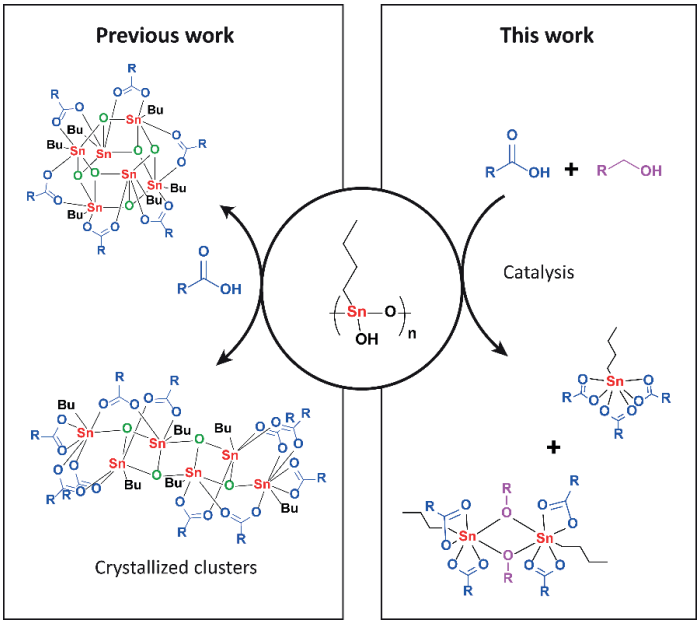

Figure 3.1. Stoichiometric reactions of monoalkyltin complexes with carboxylic acids compared to their behavior under catalytic esterification conditions.

The presence of the alkyl tails, generally *n*-butyl or *n*-octyl, appears to be pivotal for the catalytic behavior of these tin-based catalysts, since strong Lewis acids such as $SnCl_4$ are not considered good esterification catalysts. The dialkyltin(IV) compounds form distinct ladder-like structures, distannoxanes, which can incorporate an alcohol and activate the carbonyl function of the carboxylic acid.[8–11] Although still under debate, the catalytic

activity of these distannoxanes is often attributed to the unique cooperative behavior of the tin atoms in the distannoxanes.[12,13,14] For applications of distannoxanes as catalysts in transesterification reactions see the work of Otera and co-workers.[15,16,17]

Monoalkyltin(IV) catalysts have received far less attention than the distannoxanes. Nevertheless the chemistry of *n*-butyltin(IV) complexes with carboxylic acids has been well studied by X-ray crystallography (Figure 3.1).[18,19] The complex with the highest carboxylate to tin ratio, 3:1, is *n*-butyltin tricarboxylate and is synthesized from *n*-butyltin trichloride and the appropriate silver carboxylate (Figure 3.2).[20]

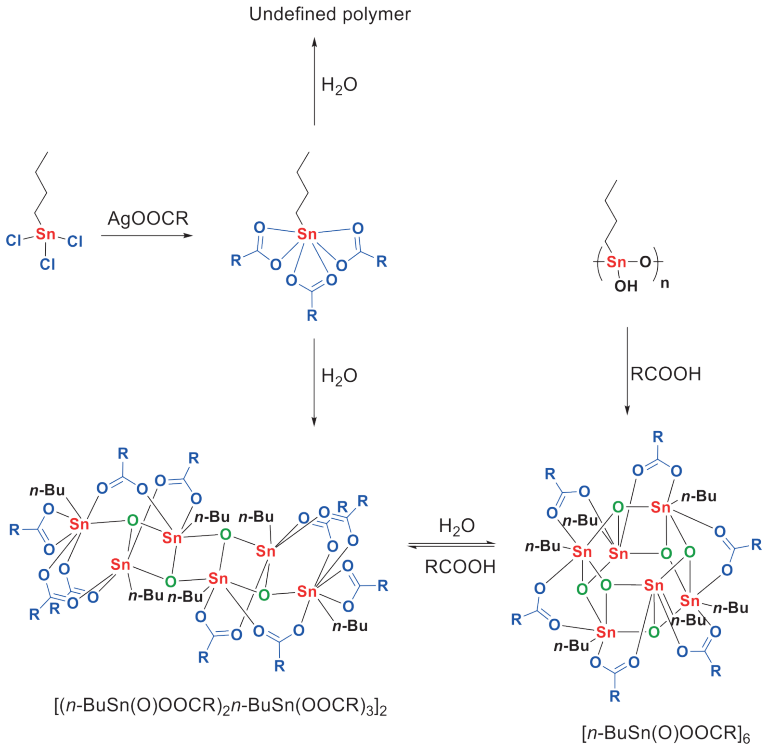

Figure 3.2. Reaction of mono-alkyltin complexes with carboxylic acids.

This hydrolytically unstable complex decomposes in the presence of water to undefined polymeric material or to a ladder-shaped complex, [(*n*-BuSn(O)OOCR)$_2$-*n*-BuSn(OOCR)$_3$]$_2$, with a tin to carboxylate stoichiometry of 3:5.[21] Further hydrolysis results in the formation of a drum-shaped cluster with a tin to carboxylate stoichiometry of 1:1. This [*n*-BuSn(O)OOCR]$_6$ cluster can also be obtained from the reaction of polymeric *n*-

butylstannoic acid with a carboxylic acid in the appropriate ratio.[22,23] Although all of these multinuclear tin complexes have been synthesized and spectroscopically analyzed, their relevance under catalytic conditions remains largely unexplored. It is well possible that under catalytic conditions these tin clusters disintegrate, in contrast to the distannoxanes, and esterification happens via a mononuclear mechanism. Here, we report on our mechanistic investigation of mono-*n*-butyltin(IV)-catalyzed esterification. This class of catalysts was studied under catalytically relevant conditions with a variety of spectroscopic techniques complemented with DFT calculations.

Results and discussion

We started our investigation by establishing the catalytic activity of various tin(IV) compounds. Also *n*-butylstannoic acid and acetic and benzoic acid derivatives thereof were examined in a model esterification reaction between benzoic acid and heptanol (in a 1:10 ratio) in the presence of 1 mol% catalyst (Table 3.1). An excess of alcohol was used in order to exclude the need of dehydrating agents or azeotropic distillation. There is a clear difference in catalytic activity between the tin(IV) compounds and the *n*-butyltin(IV) substituted derivatives, with the latter being more active.

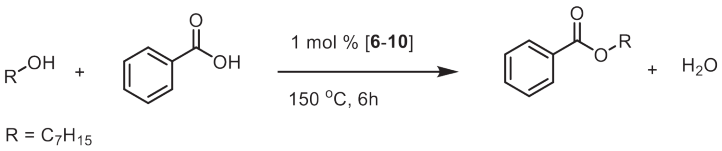

Table 3.1. Catalyst screening in model esterification reaction.

Entry[a]	Complex	Conv. [%] Benzoic acid	Yield [%] Heptylbenzoate
1	no cat.	10	6
2	$Sn(OAc)_4$	23	26
3	$SnCl_4.5H_2O$	31	36
4	*n*-$BuSnCl_3$	52	19
5	(*n*-$BuSnOOH)_n$ (**1**)	82	48
6	[*n*-$BuSn(O)OAc]_6$ (**2**)	87	62
7	*n*-$BuSn(OAc)_3$ (**3**)	63	79
8	*n*-$BuSn(OBz)_3$ (**4**)	89	87

[a] All reactions were performed with benzoic acid (5 mmol), heptanol (50 mmol), and Ti-catalyst (1 mol%, 0.05 mmol), at 150 °C for 6 h. Yield and conversion were determined by GC analysis with pentadecane as internal standard.

The polymeric *n*- butylstannoic acid (**1**), the drum-shaped [*n*-BuSn(O)OAc]$_6$ (**2**) and monomeric *n*-BuSn(OBz)$_3$ (**4**) display the highest activity (Table 3.1, entries 5, 6 and 8). These three compounds have comparable activity, suggesting that catalytic activity is not related to unique properties of the *n*-butylstannoic acid polymer. Counter-intuitively, *n*-BuSn(OAc)$_3$ (**3**) shows inferior performance, which we ascribe to the slow displacement of the tin-bound acetates for benzoate groups. In addition, an order of 0.74 in catalyst (Figure 3.12) was found for **1** (*vide infra* for interpretation).

In order to study the behavior of *n*-butyltin(IV) complexes under catalytically relevant conditions we investigated solutions of **1**, **2** and **3** by NMR spectroscopy. With three NMR-active nuclei with spin ½, ^{119}Sn being the most sensitive, Sn NMR provides a valuable tool for examining the coordination environment of tin complexes in solution.[24] Various organotin complexes retain their geometry in anhydrous organic solvents, as demonstrated by ^{119}Sn NMR experiments.[18,20] In anhydrous $CDCl_3$ a singlet in the ^{119}Sn NMR spectrum at -480 ppm is observed for the cluster **2** and from ^{1}H NMR a 1:1 ratio of the acetate groups and the *n*-butyl tails can be deduced.[22,25] For monomer **3** in anhydrous $CDCl_3$ a signal at -532 ppm is present, which is in the expected range of a seven-coordinate tin complex. The ^{1}H NMR spectrum displays the expected 3:1 ratio of the acetate groups and the *n*-butyl tail. For polymeric **1** no ^{1}H NMR spectra could be obtained due to its insoluble nature in common organic solvents.

After establishing the NMR shifts in $CDCl_3$ we switched to acetic acid-d_4 as solvent and measured the tin precursors at various temperatures (Table 3.2). At 298 K complex **3** shows a singlet at -528 ppm. This minor upfield shift compared to **3** in $CDCl_3$ indicates that the seven-coordinate geometry of *n*-BuSn(OAc)$_3$ is retained in acetic acid (AcOH). Upon increasing the temperature to 363 K a downfield shift to -518 ppm, Δδ 10.5 ppm, is observed which is caused by a decreased temperature-induced shielding (Table 3.2, Column 2).[26] Upon dissolving **2** in AcOD-d_4 at 298 K a singlet at -528 ppm, corresponding to monomer **3**, and a peak at -553 ppm is observed (Table 3.2, Column 3). Upon heating to 363 K we again only observe a singlet at -517 ppm indicative for complex **3**. In addition, this process turned out to be reversible upon lowering the temperature to 298 K. For **1** three peaks at -529, -554 and -592 ppm are present at 298 K (Table 3.2, column 4). Likewise, heating to 363 K resulted in a single signal at -517 ppm. In addition, in ^{1}H and ^{13}C NMR we observed a similar trend with identical spectra for complexes **1**, **2** and **3** (Figure 3.30 – 3.33) at elevated temperatures.

Table 3.2. ^{119}Sn NMR chemical shifts in acetic acid-d_4 at various temperatures[a]

T (K)	*n*-BuSn(OAc)$_3$ (**3**)	[*n*-BuSn(O)OAc]$_6$ (**2**)	(*n*-BuSnOOH)$_n$ (**1**)
298	-528	-528	-529
		-553	-554
			-592
333	-523	-523	-524
		-553	-554
363	-518	-517	-517

[a] ^{119}Sn chemical shifts are given in ppm relative to Sn(CH$_3$)$_4$. All samples are 0.4 M in Sn and measured in AcOD-*d*$_4$.

These results indicate that these precursors in acetic acid at catalytically relevant temperatures (≥363 K) rapidly form a mononuclear tin tricarboxylate *in situ* (Figure 3.3). To obtain more insight into the origin of the two high-field signals around -554 and -591 ppm, which appear upon solvation of **2** and **3** in AcOD-*d*$_4$ at 298 K, we treated complex **1** with various equivalents of D_2O (Figure 3.4). The addition of D_2O resulted in identical ^{119}Sn chemical shifts, which reveals that the formation of these species is dependent on the concentration of water, rather than Sn atoms.

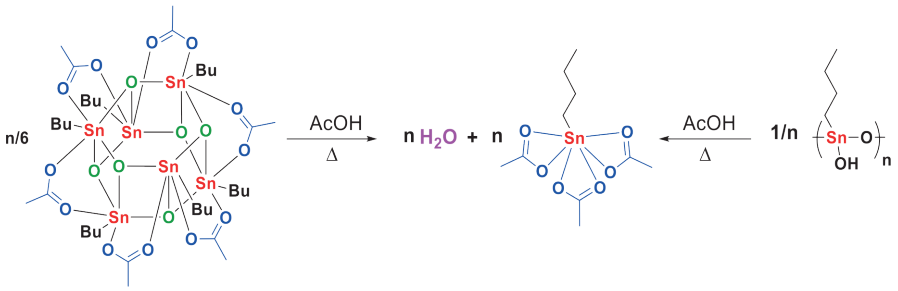

Figure 3.3. Formation of *n*-butyltin triacetate upon dissolution of multimetallic n-butyltin complexes in carboxylic acid at catalytic relevant temperatures.

Upon dissolution in AcOD-d$_4$, the oxo- and hydroxo-moieties in [*n*-BuSn(O)OAc]$_6$ and *n*-butylstannoic acid become protonated and subsequently water is formed *in situ*. Therefore, we propose that these two shifts emerge from **3** with either one (-554 – -556 ppm) or two (-591 – -592 ppm) D_2O molecules coordinated. Similar chemical shifts are

observed for the addition of D_2O to **3** dissolved in a 1:1 mixture of AcOH and EtOH (Figure 3.35).

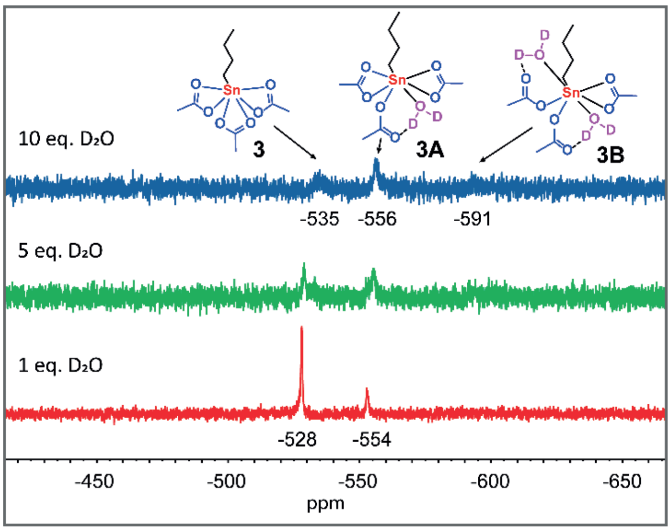

Figure 3.4. $^{119}Sn\{H\}$ NMR spectra (186 MHz, 298 K) of the reaction of **3** (0.4 M) with various equivalents of D_2O in AcOD-d_4 at 298 K. ^{119}Sn chemical shifts are given in ppm relative to $Sn(CH_3)_4$.

More structural information on the formed tin complexes was accessed via ^{119}Sn NMR DFT calculations on a B3LYP/TZVPP all electron level of theory.[27,28] Evaluation of the ^{119}Sn NMR chemical shift of various conformers of **3** with one (Figure 3.14) and two water (Figure 3.15) molecules coordinated to the central tin atom resulted in two structures with a good match between experimental and calculated ^{119}Sn NMR chemical shift (Figure 3.5).

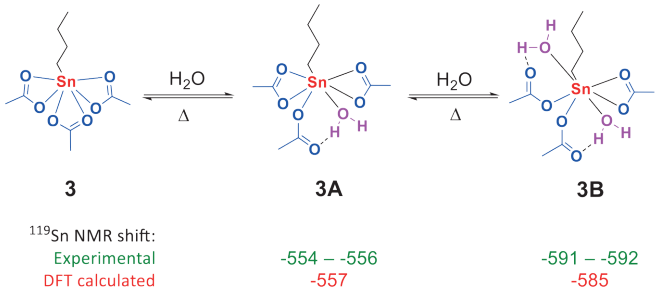

Figure 3.5. Formation of adducts **3A** and **3B** from *n*-BuSn(OAc)$_3$ with H_2O in AcOH. Experimental (green) and calculated (red) ^{119}Sn chemical shifts (in ppm).

For the monohydrate complex **3A**, one water molecule is bound *trans* to the *n*-butyl group and one of the acetate groups has changed coordination mode from bidentate to monodentate in order to accommodate a hydrogen bond between the carbonyl oxygen and the proton of water. For structure **3B** a second water molecule is bound to the central tin core which results in two of the acetate groups adopting a monodentate coordination mode. The coordination of water to structure **3A** and **3B** proved to be reversible upon increasing the temperature, resulting in the sole formation of **3** (Figure 3.36 – 3.37).

The effect of water on **3** in AcOH was further studied by ATR-FTIR spectroscopy via the addition of various equivalents of H_2O to **3** in AcOH. Vibrations at 1588 (vCOO), 660 (vSn-O) and 568 cm^{-1} (vSn-O) appeared to be correlated to the H_2O concentration (Figure 3.38 – 3.39). Similar experiments using $H_2{}^{18}O$ resulted in a small shift in one of the Sn-O vibrational modes from 568 to 554 cm^{-1} (Figure 3.6). This isotope effect further underlines the interaction between **3** and the oxygen atom from the water molecule(s). Furthermore, experiments with D_2O instead of H_2O resulted only in a minor shift in the COO vibrational mode from 1588 to 1575 cm^{-1} (Figure 3.40).

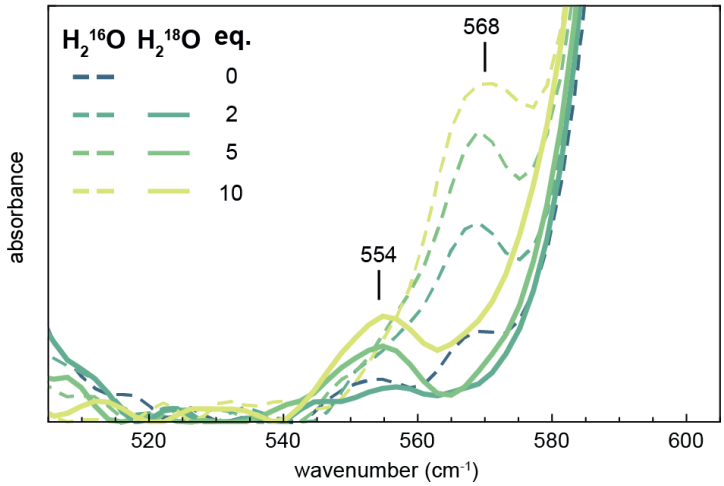

Figure 3.6. ATR-FTIR spectra of **3** in AcOH with 2, 5 and 10 equivalents of $H_2{}^{16}O$ (dashed lines) and $H_2{}^{18}O$ (solid lines).

Knowing its behavior in AcOH in both the presence and absence of water, we turned our attention to the ^{119}Sn NMR spectrum of **3** in anhydrous EtOH at 298 K. Under these conditions two signals at -532 and -541 ppm were observed, revealing the partial conversion of **3** into another seven-coordinate tin complex (Figure 3.41). The structure of this complex was further elucidated with ATR-FTIR which gave a strong vibration at 1020

cm^{-1}, indicative of a C-O stretching vibration (Figure 3.44).[29] In addition, a vibration at 1711 cm^{-1} revealed the presence of uncoordinated AcOH. Only minor isotope effects were observed upon changing EtOH to EtOD-d_6 (Figure 3.45). These findings indicate the exchange of one of the acetate groups for an ethoxy group. Subsequently, an aliquot of this mixture was studied with LIFDI-HRMS which resulted in the detection of the fragments $[SnOAc_3]^+$ and [*n*-BuSnOAc$_2$OEt-*n*-BuSnOAcOEt]$^+$ (Figure 3.46 – 3.47). The *in situ* formation of the dimer (*n*-BuSnOAc$_2$OEt)$_2$ (**5**) is in agreement with a seven-coordinate environment around the tin core as indicated by ^{119}Sn NMR. In addition, the dimer **5** was independently synthesized via the reaction of *n*-BuSn(OAc)$_3$ and *n*-BuSnOEt$_3$, and has a ^{119}Sn NMR chemical shift of -544 ppm in $CDCl_3$.[30] The bridging mode of the ethoxy groups in (*n*-BuSnOAc$_2$OEt)$_2$ (**5**) becomes apparent from the distinct quaternary carbon signal at 182.61 ppm observed for the acetate groups in the ^{13}C NMR spectra at 233 K, indicating that all acetate groups are in a terminal position (Figure 3.48). Discrimination between the different conformers is possible upon comparison of the experimental and DFT-calculated ^{119}Sn NMR chemical shift together with the calculated free energy differences (Figure 3.7).

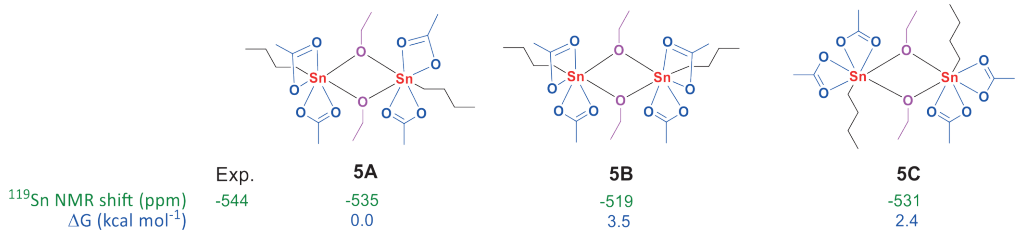

Figure 3.7. Conformers of **5** with their ^{119}Sn NMR chemical shift (green, in ppm) and calculated free energies (blue, in kcal mol^{-1} relative to *n*-BuSn(OAc)$_3$).

These data together point to the formation of the isomer with both *n*-butyl occupying the *trans*-position with respect to the bridging ethoxy groups and *transoid* with respect to the other *n*-butyl group (complex **5A**). Solvation of **5** in AcOH resulted in a ^{119}Sn NMR chemical shift at -529 ppm, which indicates complete conversion to **3** (Figure 3.49). We thus propose the partial formation of the dimer **5A** when **3** is dissolved in EtOH, while addition of AcOH results in the backwards reaction to **3**.

With the knowledge of the behavior of the components under various conditions in hand, we turned our attention to following the catalyst under catalytically relevant conditions. The catalytic esterification of acetic acid and ethanol at 363 K, in the presence of molecular sieves to mimic the azeotropic distillation conditions commonly applied, was monitored over time (18.7 % yield ethyl acetate after 1 h, Figure 3.53). During catalysis, aliquots of

the catalytic reaction mixture were examined by ^{119}Sn NMR spectroscopy. At 363 K a single ^{119}Sn chemical shift is observed which moves upfield from -525 to -539 ppm over a time period of 60 minutes (Figure 3.51), which we attribute to a shift in equilibrium between monomer **3** and dimer **5A**. ^{119}Sn NMR measurements of the same samples at 298 K revealed two broad signals with a chemical shift of -535 and -555 ppm after 5 minutes reaction time (Figure 3.8). These two signals can be assigned to **3** and monohydrated complex **3A** respectively. After 30 minutes reaction time three broad signals at -545, -553 and -590 ppm were observed. The two upfield signals originate from *n*-BuSn(OAc)$_3$ with either one or two water molecules coordinated (structures **3A** and **3B**), while the signal at -545 ppm is consistent with the dimer **5A**. After 60 minutes reaction time two new unidentified signals at -550 and -553 are present but the main contributions are still from structures **3A**, **3B** and **5A**. The adducts of **3** with H_2O (structure **3A** and **3B**) are only observed at 298 K, at elevated temperatures water is expected to be expelled from these complexes and monomeric **3** is formed, *vide supra*.

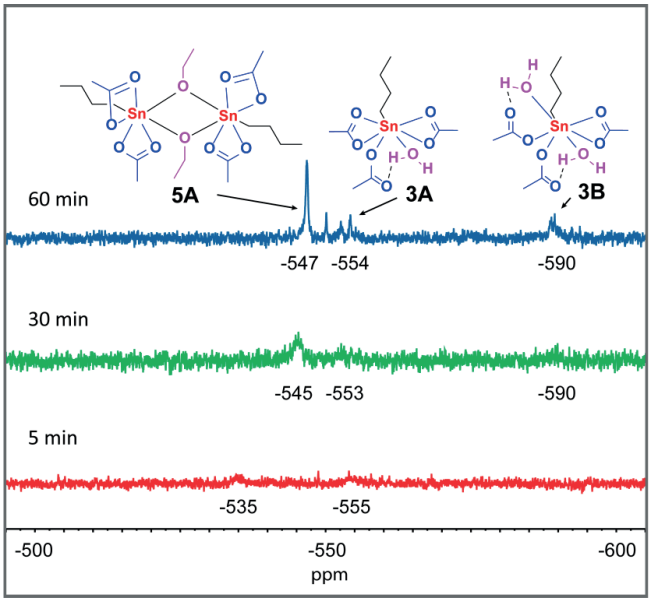

Figure 3.8. Time dependent ^{119}Sn{H} NMR spectra (186 MHz, 298 K) of complex **3** in a 1:1 mixture of AcOH and EtOH. All samples are 0.4 M in Sn and measured unlocked.

To complement our experimental findings under catalytically relevant conditions, we have further examined the reaction mechanism for the *n*-BuSn(OAc)$_3$-catalyzed esterification by DFT calculations at the BP86-D3/def2-TZVP//M06-2X/def2-TZVP/def2-QZVP level of

theory (Figure 3.9).[31] The observed off-cycle resting states, monomer **3** and dimer **5A**, are equal in free energy, and both can lead to the formation of Intermediate **D** (ΔG = 4.5 kcal mol^{-1}) which is the starting points of the catalytic cycle.

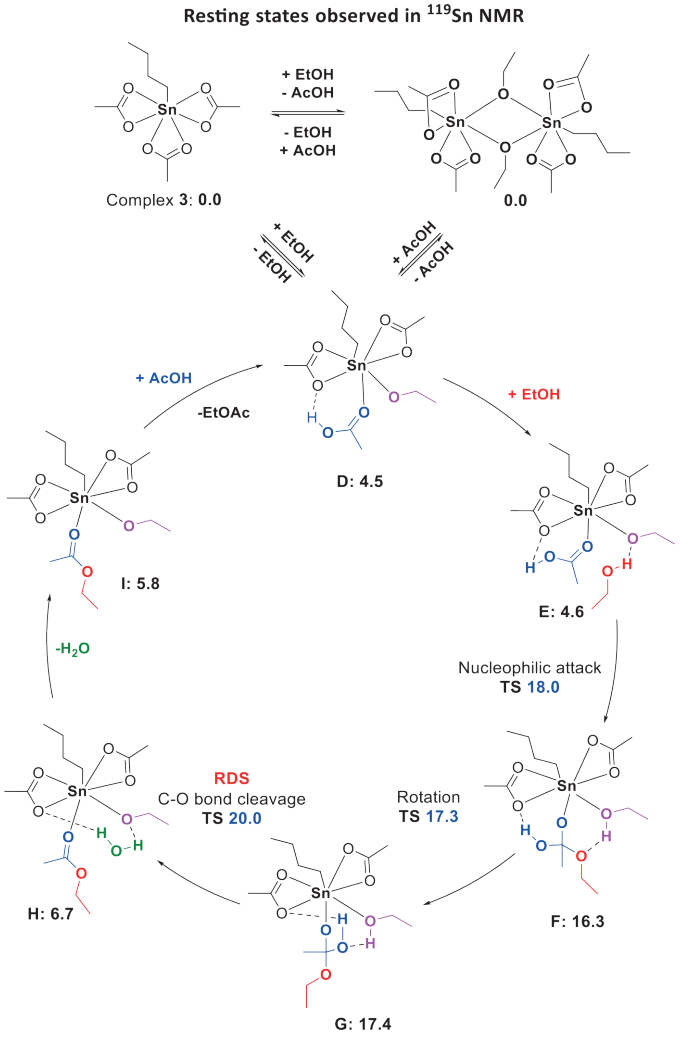

Figure 3.9. Proposed catalytic cycle for the esterification of ethanol and acetic acid catalyzed by **3**. Hydrogen bonds are indicated with black dashed lines and free energy values are given in kcal mol^{-1} relative to **3**.

The tin-bound ethoxy group can subsequently accommodate another ethanol molecule via a hydrogen bond (structure **E**). Next, nucleophilic attack ($\Delta G^{\ddagger}$ = 18.0 kcal mol^{-1}) results

in intermediate **F**, where the hydrogen atom of the ethanol is accepted by the Lewis basic ethoxy group. A rotation ($\Delta G^{\ddagger}$ = 17.3 kcal mol^{-1}), which requires the breakage of a hydrogen bond, pre-organizes intermediate **G** for the carbon-oxygen bond breaking step. The actual carbon-oxygen bond breaking has the highest barrier with $\Delta G^{\ddagger}$ = 20.0 kcal mol^{-1} and can be regarded as the rate determining step. The collapse of the tetrahedral intermediate **G** as turn-over limiting step is consistent with previously reported metal-catalyzed esterification and amidation reactions.[32,33] From structure **H** water is expelled, which was bound via two hydrogen bonds, and finally the ester is replaced by a new acetic acid molecule. Overall the reaction is slightly exergonic with $\Delta\Delta G$ = -1.9 kcal mol^{-1}. The experimentally observed off-cycle resting states **3** and **5A** can both form the amphoteric mixed alkoxide/carboxylate (structure **D**) which is the starting point of the monomeric catalytic cycle. Furthermore, a monomeric catalytic cycle, with two off-cycle resting states one monomeric and the other dimeric in equilibrium with each other, is in agreement with the experimentally determined catalyst order of 0.74, *vide supra*. The *in situ* formation of this amphoteric catalyst is essential since it can act as a Lewis acid to activate the carboxylic acid, and as a Brønsted base to deprotonate the alcohol during nucleophilic attack. The importance of having an amphoteric catalyst in esterification reactions is not only restricted to tin-based catalysts as we have recently demonstrated for titanium-based esterification catalysts.[34] Furthermore, the function of the *n*-butyl tail on the tin catalyst is to enforce a seven-coordinate tin center which remains during the whole catalytic cycle as established by DFT calculations.

Conclusions

We have demonstrated here that *n*-butyl substituted tin(IV) complexes have a unique coordination chemistry which results in a monomeric tin catalyst under catalytic conditions. Although the commonly applied esterification catalyst *n*-butyl stannoic acid is a polymer in the solid state, it transforms to monomeric **3** and dimeric **5A** as off-cycle resting states under catalytically relevant conditions, as proven by NMR, ATR-FTIR and MS measurements. DFT calculations lend support to a monomeric mechanism where structures **3** and **5A** are regarded as off-cycle species. In this mechanism the carbon-oxygen bond breaking step is the rate determining step. Furthermore, water formed during the esterification reaction has limited effect on the active catalyst, since the water adducts **3A** and **3B** where only observed at 298 K. These findings shed new light on the role of the *n*-butyl tail and the nuclearity of the class of mono-*n*-butyl tin esterification catalysts.

Experimental Section

General Experimental Details

Dichloromethane was distilled from CaH_2, *n*-pentane from sodium/benzophenone and toluene from sodium under argon atmosphere. Ethanol was degassed, by bubbling nitrogen through for >30 min, and dried over 3Å molecular sieves. All other chemicals were obtained from Merck and were used without further purification. All air-sensitive materials were manipulated using standard Schlenk techniques or by the use of an argon-filled glovebox (MBraun Unilab). The NMR solvent $CDCl_3$ was dried over molecular sieves and degassed via three cycles of freeze-pump-thaw. Acetic acid-d_4 and Ethanol-d_6 were used without further purification. ^{1}H (500 or 400 MHz) and ^{13}C (125 or 100 Mhz) spectra were recorded on a Bruker DRX 500 MHz or a Bruker AVANCE 400 MHz spectrometer. ^{119}Sn NMR spectra were recorded on a Bruker DRX 500 MHz at 186 MHz and measured in the range of 100 to -700 ppm. ^{1}H and ^{13}C spectra were referenced against residual solvent signal, while ^{119}Sn spectra were externally calibrated against an 5% (v/v) solution of $SnMe_4$ in acetone. 2D ^{1}H DOSY spectra were recorded on a Bruker DRX 300 MHz spectrometer. FD-HRMS spectra were collected on an AccuTOF GC v 4g, JMS-T100GCV Mass spectrometer (JEOL, Japan) equipped with a Carbotec emitter or a LiFDi probe (FD) equipped with an FD Emitter, Linden CMS GmbH. A typical current rate of 51.2 mA/min over 1.2 min and a flashing current 40 mA on every spectra of 30 ms was used. ATR-FTIR spectra were recorded on a Bruker Alpha-P. GC analysis for heptylbenzoate and benzoic acid was performed on a Thermo Scientific Trace GC Ultra equipped with a Restek Stabilwax-DA column (30 m x 0.25 mm x 0.25 µm). Temperature program: initial temperature 50 °C, heat to 200 °C with 20 °C min^{-1}, hold for 10 min, heat to 250°C with 50 °C min^{-1}, hold for 3 minutes. Inlet temperature 250 °C, split ratio of 30, 1.0 mL min^{-1} helium flow, FID temperature 250 °C. Esterification reactions were performed in a Radley Discoveries 12 plus reaction station allowing a maximum of 12 simultaneous reactions under a nitrogen atmosphere.

Synthesis and Catalysis

The tin complexes: $[n\text{-BuSn(O)OAc}]_6$, *n*-$BuSnOAc_3$ and $(n\text{-BuSnOEt}_3)_4$ were synthesized according to literature procedures.[18,20,35]

Complex **1**: $[n\text{-BuSn(O)OAc}]_6$

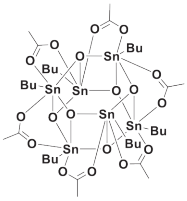

^{1}H NMR (500 MHz, $CDCl_3$): δ 2.09 (s, 3H, $OOCC\underline{H}_3$), 1.67 (m, 2H, $C\underline{H}_2CH_3$), 1.36 (m, 2H, $C\underline{H}_2CH_2$), 1.24 (m, 2H, $SnC\underline{H}_2$), 0.91 (t, *J* = 7.4 Hz, 3H, $CH_2C\underline{H}_3$). ^{13}C NMR (125 MHz, $CDCl_3$): δ 179.88 ($CH_3\underline{C}OO$), 27.24 (^{3}J ^{13}C - $^{119/117}Sn$ = 57.5 Hz, $\underline{C}H_2CH_3$), 26.93 (^{1}J ^{13}C - ^{119}Sn = 1185.0 Hz, ^{1}J ^{13}C - ^{117}Sn = 1131.3 Hz, $Sn\underline{C}H_2CH_2$), 26.73 (^{2}J ^{13}C - $^{119/117}Sn$ = 191.3 Hz, $\underline{C}H_2CH_2$), 24.48 ($OOC\underline{C}H_3$), 13.72 ($CH_2\underline{C}H_3$). $^{119}Sn\{H\}$ NMR (186 MHz, $CDCl_3$): δ -484.91. IR-ATR (cm^{-1}): 1595, 1593, 1448, 1421, 608. FD-HRMS (*m/z, pos*): Calculated for $[C_{31}H_{75}O_{18}Sn_6]$ 1446.9101; found 1446.8201 $[M\text{-}C_4H_9]^+$

Complex **3**: *n*-BuSnOAc$_3$

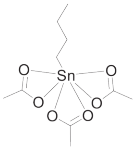

^{1}H NMR (500 MHz, $CDCl_3$): δ 2.15 (s, 9H, OOCC$\underline{H}_3$), 1.77 (m, 2H, C$\underline{H}_2$CH$_3$), 1.66 (m, 2H, SnC$\underline{H}_2$), 1.39 (s, 2H, C$\underline{H}_2$CH$_2$), 0.90 (t, *J* = 7.4 Hz, 3H, CH$_2$C$\underline{H}_3$). ^{13}C NMR (125 MHz, $CDCl_3$): δ 184.16 (CH$_3$$\underline{C}$OO), 29.19 ($^3J$ ^{13}C - $^{119/117}$Sn = 61.3 Hz, $\underline{C}$H$_2$CH$_3$), 26.53 (^1J ^{13}C - ^{119}Sn = 1001.3 Hz, ^1J ^{13}C - ^{117}Sn = 957.5 Hz, Sn$\underline{C}$H$_2$CH$_2$), 25.64 (^2J ^{13}C - $^{119/117}$Sn = 166.3 Hz, $\underline{C}$H$_2$CH$_2$), 18.93 (OOC$\underline{C}$H$_3$), 13.67 (CH$_2$$\underline{C}H_3$). ^{119}Sn{H} NMR (186 MHz, $CDCl_3$): δ -531.51. IR-ATR (cm^{-1}): 1565, 1542, 1428, 1395, 1349, 699, 627.

[*n*-BuSn(O)(OAc)$_2$*n*-BuSn(OAc)$_3$]$_2$

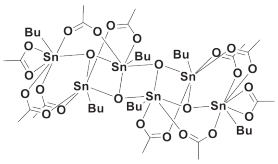

Efforts to synthesize [(*n*-BuSn(O)OAc)$_2$*n*-BuSn(OAc)$_3$]$_2$ via a literature procedure[21] did not result in the isolation of [(*n*-BuSn(O)OAc)$_2$*n*-BuSn(OAc)$_3$]$_2$ but rather [*n*-BuSn(O)OAc]$_6$. Instead, freeze drying of a solution of [*n*-BuSn(O)OAc]$_6$ (100 mg, 0.066 mmol) in 1 mL acetic acid gave [(*n*-BuSn(O)OAc)$_2$*n*-BuSn(OAc)$_3$]$_2$ (113 mg, quantitative).

^{1}H NMR (400 MHz, $CDCl_3$): δ 2.17 – 1.92 (m, 30H, OOCC$\underline{H}_3$), 1.81 – 1.15 (m, 34H , C$\underline{H}_2$), 0.96 – 0.79 (m, 18H, CH$_3$). ^{119}Sn{H} NMR (186 MHz, $CDCl_3$): δ -521.72, -554.17, -640.64. These ^{119}Sn NMR signals do not correspond to the -486, -522, -533 and -549 ppm reported in literature.[21] However, the signals at -486 and -533 ppm should not be assigned to [(*n*-BuSn(O)OAc)$_2$*n*-BuSn(OAc)$_3$]$_2$ but rather to [*n*-BuSn(O)OAc]$_6$ and *n*-BuSnOAc$_3$, which are decomposition products. Due to this decomposition a pure ^{13}C NMR spectrum could not be recorded. In the ^{119}Sn{H} NMR spectrum obtained after the ^{13}C NMR measurement, additional peaks corresponding to decomposition products [*n*-BuSn(O)OAc]$_6$ (-484.84 ppm) and *n*-BuSnOAc$_3$ (-532.16 ppm) were observed.

Complex **4**: *n*-BuSnOBz$_3$

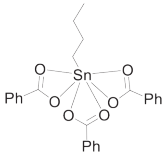

Under a nitrogen atmosphere AgOBz (6.48 g, 28.3 mmol) was suspended in 20 mL anhydrous DCM. Subsequently *n*-BuSnCl$_3$ (1.2 mL, 7.1 mmol) was slowly added and the reaction mixture was brought to reflux for 24 h. Filtration over celite and evaporation of the solvent resulted in a white solid material which was recrystallized from toluene/pentane to afford *n*-BuSnOBz$_3$ (3.15 g, 82% yield).

^{1}H NMR (400 MHz, $CDCl_3$): δ 8.17 (d, *J* = 7.5 Hz, 6H, Ar$\underline{H}$), 7.61 (t, *J* = 7.4 Hz, 3H, Ar$\underline{H}$), 7.45 (t, *J* = 7.4 Hz, 6H, Ar$\underline{H}$), 2.04 (m, 2H, C$\underline{H}_2$), 1.83 (m, 2H, C$\underline{H}_2$), 1.45 (sext, *J* = 7.4 Hz, 2H, C$\underline{H}_2$), 0.90 (t, *J* = 7.3 Hz, 3H, CH$_2$C$\underline{H}_3$). ^{13}C NMR (100 MHz, $CDCl_3$): δ 178.50 (C$_6$H$_5$$\underline{C}$OO), 134.02 ($\underline{C}_6H_5$), 131.26 ($\underline{C}_6H_5$), 128.37 ($\underline{C}_6H_5$), 127.58 ($\underline{C}_6H_5$) 29.58 ($\underline{C}H_2$), 26.47 ($\underline{C}H_2$), 25.56 ($\underline{C}H_2$), 13.48 ($\underline{C}H_3$). ^{119}Sn-^{13}C couplings were not well resolved. ^{119}Sn{H} NMR (186 MHz, $CDCl_3$): δ -535.56. IR-ATR (cm^{-1}): 1596, 1539, 1509, 1450, 1397, 1162, 1068, 1021, 827, 717, 681. FD-HRMS (*m/z, pos*): Calculated for [$C_{18}H_{19}O_4Sn_1$] 419.0309; found 419.0349 [M-OBz]$^+$; Calculated for [$C_{21}H_{15}O_6Sn_1$] 482.9895; found 482.9856 [M-C_4H_9]$^+$.

Single crystals suitable for XRD analysis were obtained via the slow vapor diffusion of *n*-hexane in a toluene solution. $C_{25}H_{24}O_6Sn$, Fw = 539.17, colorless block, 0.565×0.299×0.116 mm, orthorhombic, Pbca (No: 61)), a = 11.9618(3), b = 16.8603(4), c = 23.0411(6) Å, V = 4646.9(2) Å3, Z = 8, Dx = 1.541 g/cm3, m = 1.138 mm-

1. 54938 Reflections were measured up to a resolution of (sin q/l)max = 0.63 Å-1. 4751 Reflections were unique (Rint = 0.0813), of which 3599 were observed [I>2s(I)]. 290 Parameters were refined without any restraints. R1/wR2 [I > 2s(I)]: 0.0277/0.0497. R1/wR2 [all refl.]: 0.0478/ 0.0553. S = 1.049. Residual electron density between -0.362 and 0.517 e/Å3. CCDC 2049109 contains the supplementary crystallographic data for this paper. These data can be obtained free of charge from The Cambridge Crystallographic Data Centre via www.ccdc.cam.ac.uk/data_request/cif.

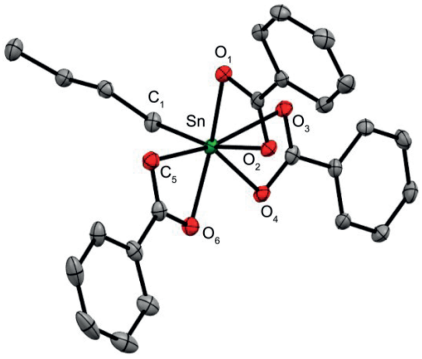

Figure 3.10. ORTEP view of solid state structure of *n*-BuSnOBz$_3$. Ellipsoids are given at 50% probability level. H atoms are omitted for clarity. Selected bond distances (Å): Sn-O$_1$ = 2.373(2) , Sn-O$_2$ = 2.133(2) , Sn-O$_3$ = 2.242(2) , Sn-O$_4$ = 2.135(2) , Sn-O$_5$ = 2.328(2) , Sn-O$_6$ = 2.156(2) , Sn-C$_1$ = 2.118(3). Selected angles (°): C$_1$-Sn-O$_1$ = 93.94(8), C$_1$-Sn-O$_5$ = 96.39(8). Colors correspond to tin (green), oxygen (red) and carbon (gray).

Complex **5**: (n-BuSnOAc$_2$OEt)$_2$

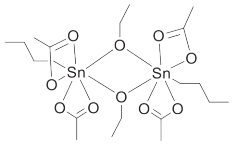

Under a nitrogen atmosphere *n*-BuSnOAc$_3$ (345 mg, 0.987 mmol) and (*n*-BuSnOEt$_3$)$_4$ (42 mg, 0.122 mmol) were both dissolved in 2.5 mL anhydrous DCM. Afterwards the *n*-BuSnOEt$_3$ solution was transferred via a syringe and slowly added to the *n*-BuSnOAc$_3$ solution. After stirring for 1h the solvent was removed in *vacuo*, providing a yellowish oil (512 mg, quant.). Since the complex slowly decomposes at room temperature the ^{13}C NMR spectrum was recorded at 233 K.

^{1}H NMR (500 MHz, CDCl$_3$): δ 3.99 (br s, 4H, CH$_3$C**H**$_2$O), 2.10 (s, 12H, C**H**$_3$COO), 1.61 (m, 8H, C**H**$_2$C**H**$_2$), 1.34 (sext, *J* = 6.9 Hz, 4H, C**H**$_2$), 1.18 (t, *J* = 6.8 Hz, 6H, OCH$_2$C**H**$_3$), 0.89 (t, *J* = 7.3 Hz, 6H, OC**H**$_2$C**H**$_3$). ^{13}C NMR 233 K (125 MHz, CDCl$_3$): δ 182.61 (CH$_3$**C**OO), 61.37 (O**C**H$_2$CH$_3$), 27.74 (**C**H$_2$), 27.06 (**C**H$_2$), 26.27 (**C**H$_2$), 20.06 (**C**H$_3$COO), 18.44 (**C**H$_3$CH$_2$O), 14.03 (**C**H$_3$CH$_2$CH$_2$). ^{119}Sn-^{13}C couplings were not well resolved. ^{119}Sn{H} NMR (186 MHz, CDCl$_3$): δ -543.73. IR-ATR (cm^{-1}): 1560, 1411, 1048, 1021, 877, 662, 613, 546. LIFDI-HRMS (*m/z, pos*): Calculated for [C$_{16}$H$_{31}$O$_{10}$Sn$_2$] 620.9963; found 620.9983 [M-C$_4$H$_9$]$^+$.

Procedure for esterification of benzoic acid and heptanol

In a carousel reaction station under a nitrogen atmosphere benzoic acid (610.6 mg, 5 mmol) was suspended in heptanol (7.14 mL, 50 mmol). Subsequently, the catalyst (1 mol%) and pentadecane (0.41 mL, 1.5 mmol) as internal standard were added. After 6h (at 150 °C) the conversion and yield were determined with GC analysis via the integration of the peak area of benzoic acid and heptylbenzoate.

Procedure for determination of the catalyst order

In a carousel reaction station under a nitrogen atmosphere benzoic acid (600 mg, 4.9 mmol) was suspended in heptanol (7 mL, 49 mmol). Subsequently, *n*-BuSnOOH (0.5, 1, 2 or 3 mol%), o-xylene (2 mL) and pentadecane (0.40 mL, 1.45 mmol) as internal standard were added. After 15, 30, 45 and 60 min (at 150 °C) samples were taken for GC analysis. The rate (K) was determined via a tangent line of the heptyl benzoate concentrations.

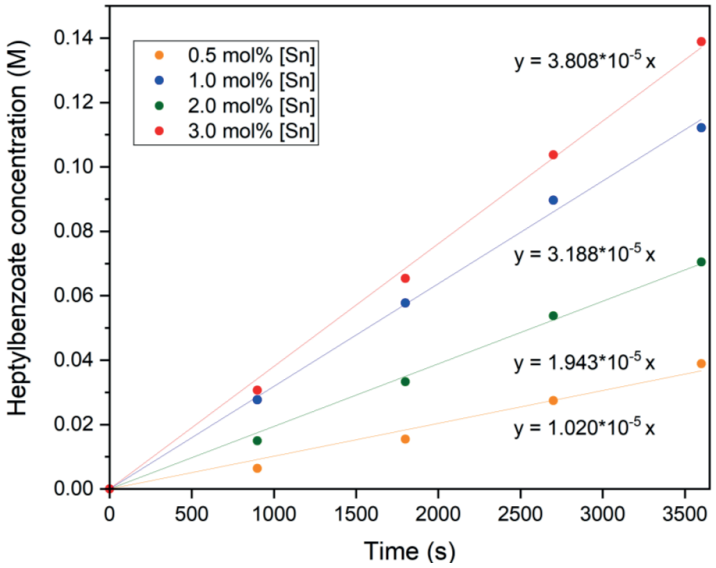

Figure 3.11. Initial rate at different catalyst loadings (*n*-BuSnOOH [**1**]).

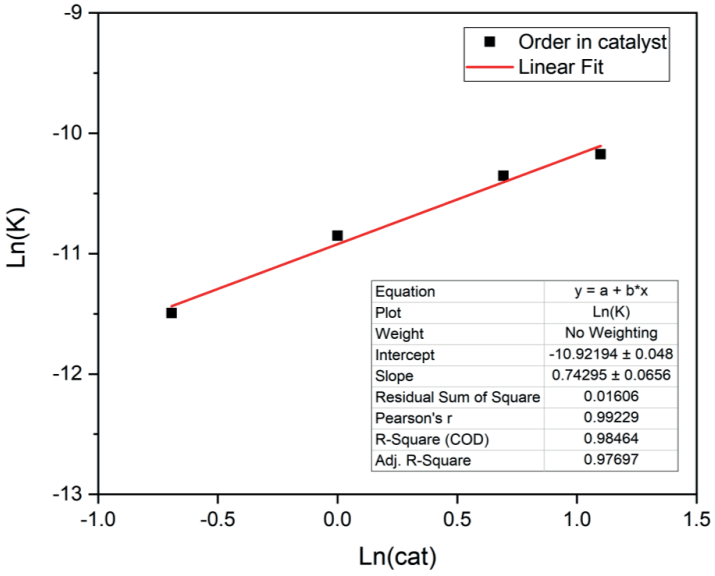

Figure 3.12. Order in catalyst (*n*-BuSnOOH [**1**]).

Procedure for esterification of acetic acid and ethanol

Activated molecular sieves (3Å, 2.0 g) and 1.2 mmol of tin catalyst (0.4 M) were loaded in a Schlenk reaction tube and placed under a nitrogen atmosphere. Anhydrous EtOH (1.5 mL) and acetic acid (1.5 mL) were added and the reaction mixture was heated to 90 °C in an oil bath. Aliquots (0.5 mL) for NMR analysis were taken after 5, 30 and 60 min and ^{119}Sn NMR spectra were directly measured at 90 °C (in a pre-heated NMR machine) and at 25 °C (sample cooled outside NMR machine). The conversion was monitored by ^{1}H NMR spectroscopy from the relative intensities of the methylene protons of EtOH at 3.68 ppm and ethylacetate at 4.09 ppm.

Computational details

Density functional theory calculations were performed using the TURBOMOLE software package, version 7.3.1,[36] coupled to the PQS Baker optimizer[37] via the BOpt package.[38-40] All structure optimizations were performed at the BP86[41-43]/def2-TZVP[44,45] level of theory on an m5 grid using Grimme's version 3 dispersion corrections (disp3)[46], with the corresponding effective core potential (def2-ECP) for Sn. This functional/basis set combination was found to be a good trade-off between accuracy in the geometric parameters of $Sn(OAc)_4$ compared to the known crystal structure[47], and computational costs (Table 3.3). All minima were characterized by no imaginary frequency in the Hessian matrix, while transition states had a single imaginary frequency. Energies were further refined using the M06-2x functional,[48,49] implemented via the XCFun library,[50] in combination with the def2-QZVPP basis set for Sn (with ECP) and def2-TZVP for all other elements, a very fine grid (7) and disp3 dispersion corrections. The M06-2x functional is optimized for main group elements is used for Sn-containing complexes.[51]

Table 3.3. Comparison of average geometric parameters of $Sn(OAc)_4$ versus published crystal structure, using different functionals.

Functional[a]	Deviation in average Sn-O bond length	Absolute deviation in O-Sn-O angles
BP86	0.01839325	1.132
B3LYP	-0.0017655	1.225
M06-L	-0.03221675	0.7425
M06-2x	-0.01011175	0.9652

[a] All calculations were performed with the def2-TZVP basis set and grid size m5.

Isotropic NMR shielding constants were calculated using the Gauge Including Atomic Orbital (GIAO) method[52] as implemented in TURBOMOLE, using the B3LYP functional[53-56] (with grid size 5) in combination with the TZVPPall basis set for Sn and def2-TZVP for all other elements. For comparison to experiment, relative chemical shifts were calculated by referencing to $Sn(CH_3)_4$. The calculated relative chemical shifts were compared to the experimentally obtained chemical shifts for three known compounds, measured at 25 °C in $CDCl_3$: *n*-BuSn(OAc)$_3$, [*n*-BuSn(O)OAc]$_6$ and [(*n*-BuSn(O)OAc)$_2$*n*-BuSn(OAc)$_3$]$_2$. Linear regression was performed to fit the calculated chemical shifts to the experimental values. The B3LYP/TZVPPall combination gave a good fit (R^2 = 0.9933). Using the thus obtained fit parameters, other calculated chemical shifts were compared to the experimental shifts of unknown compounds.

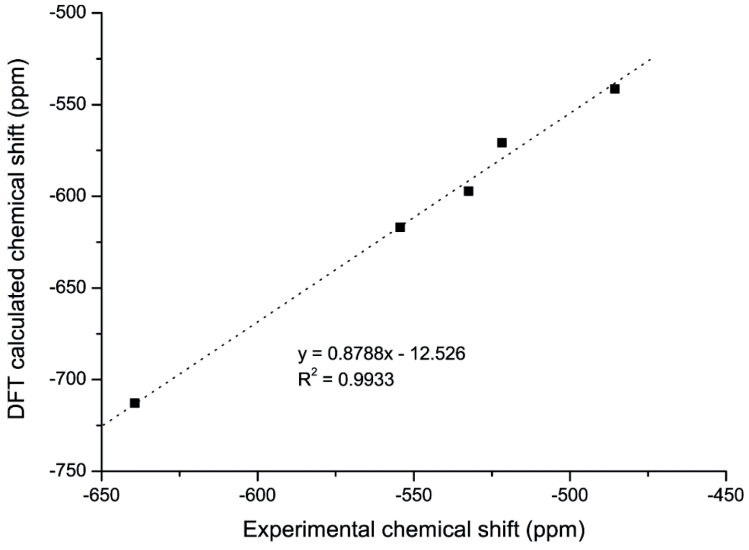

Figure 3.13. Correlation between experimental and calculated ^{119}Sn chemical shifts for B3LYP/TZVPPall.

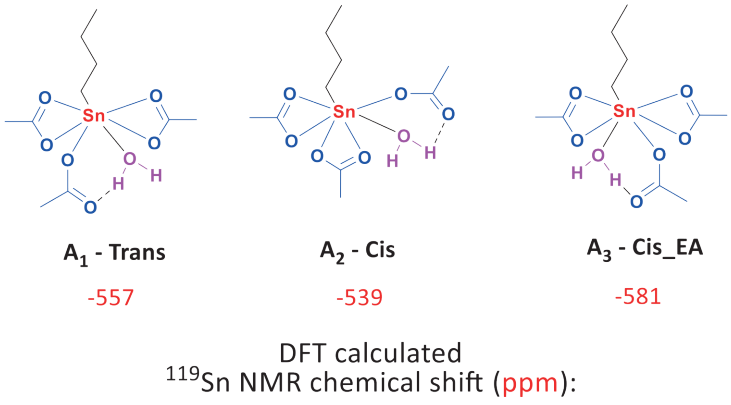

Figure 3.14. DFT calculated ^{119}Sn NMR chemical shifts (in red, in ppm) of adducts of **3** with a single H_2O molecule.

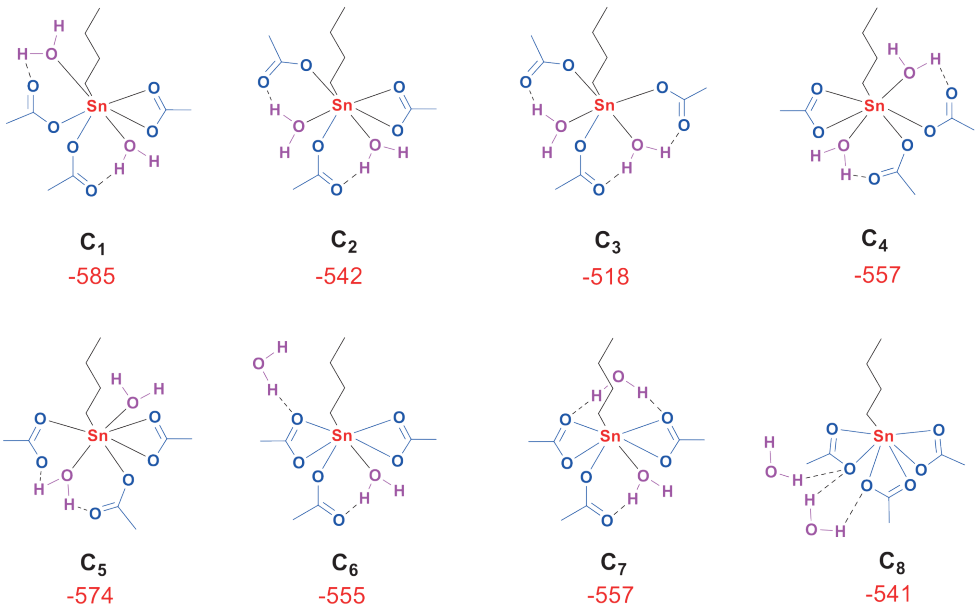

Figure 3.15. DFT calculated ^{119}Sn NMR chemical shifts (red, in ppm) of adducts of **3** with two H_2O molecules.

Spectra

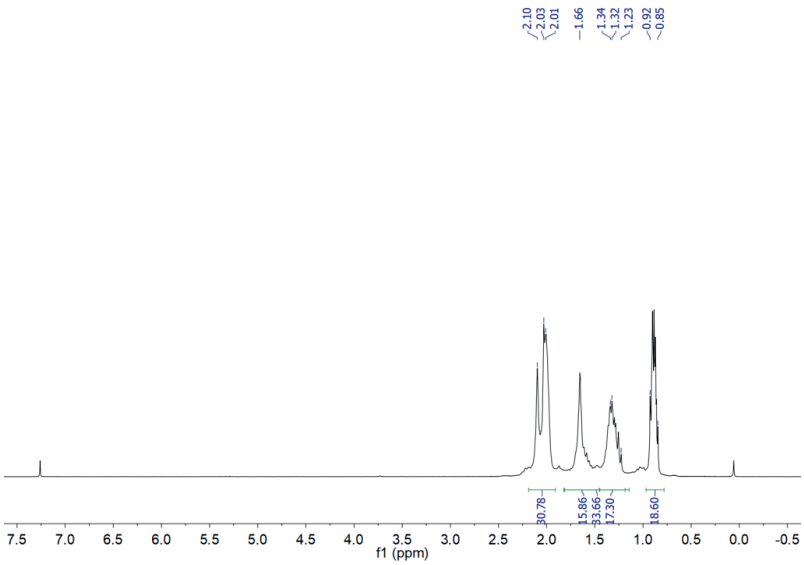

Figure 3.16. ^{1}H NMR of [*n*-BuSn(O)(OAc)$_2$*n*-BuSn(OAc)$_3$]$_2$, $CDCl_3$ at 298 K.

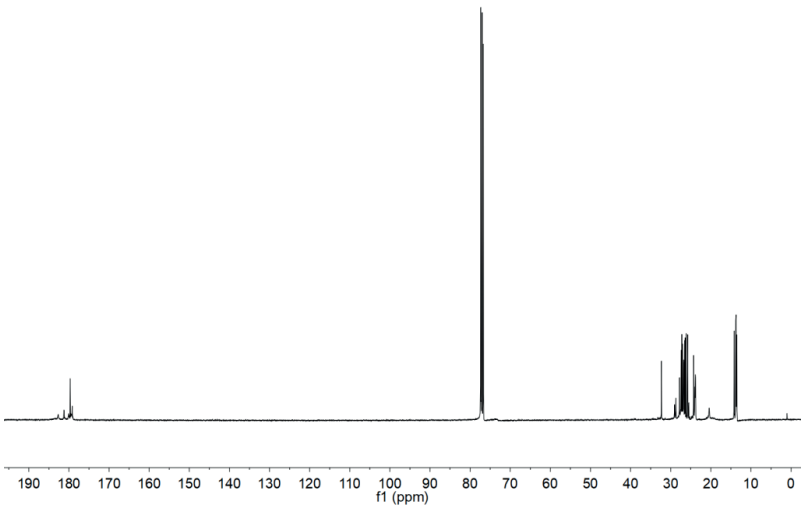

Figure 3.17. ^{13}C NMR of [*n*-BuSn(O)(OAc)$_2$*n*-BuSn(OAc)$_3$]$_2$, $CDCl_3$ at 298 K.

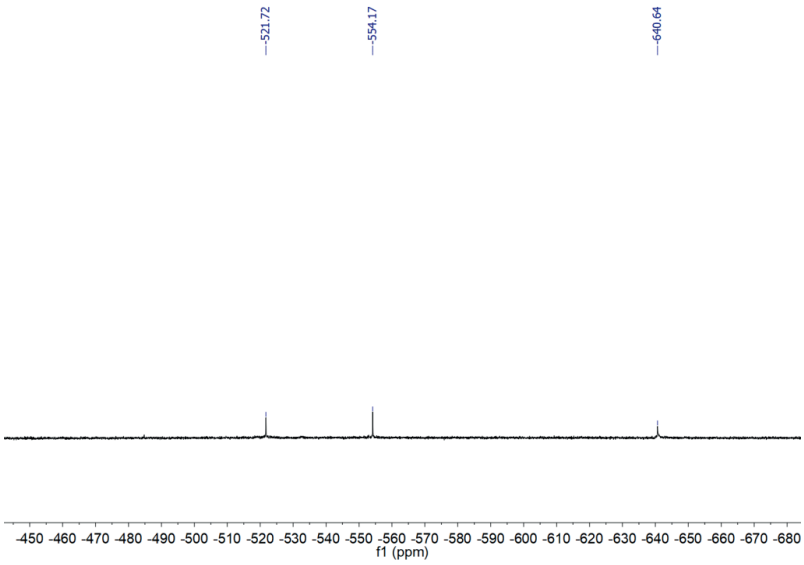

Figure 3.18.[119]Sn NMR of [*n*-BuSn(O)(OAc)$_2$*n*-BuSn(OAc)$_3$]$_2$, $CDCl_3$ at 298 K.

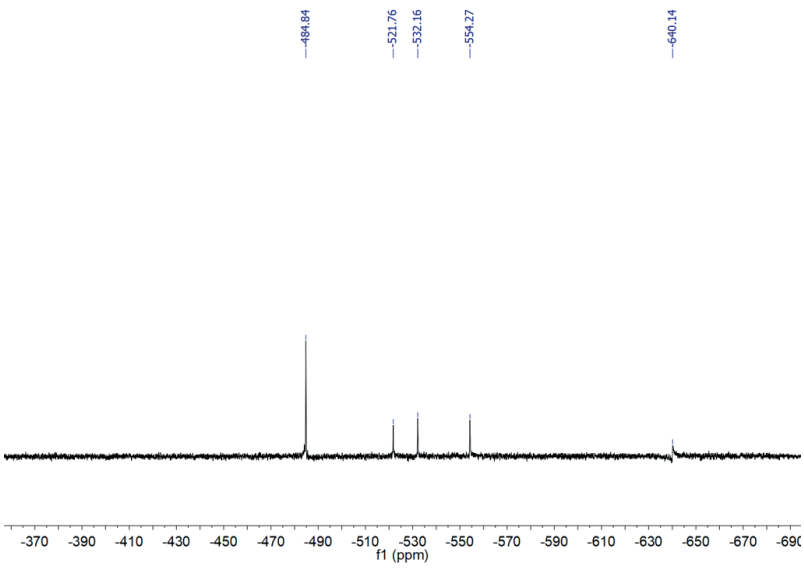

Figure 3.19.[119]Sn NMR of [*n*-BuSn(O)(OAc)$_2$*n*-BuSn(OAc)$_3$]$_2$ after [13]C NMR (Figure 17), $CDCl_3$ at 298 K.

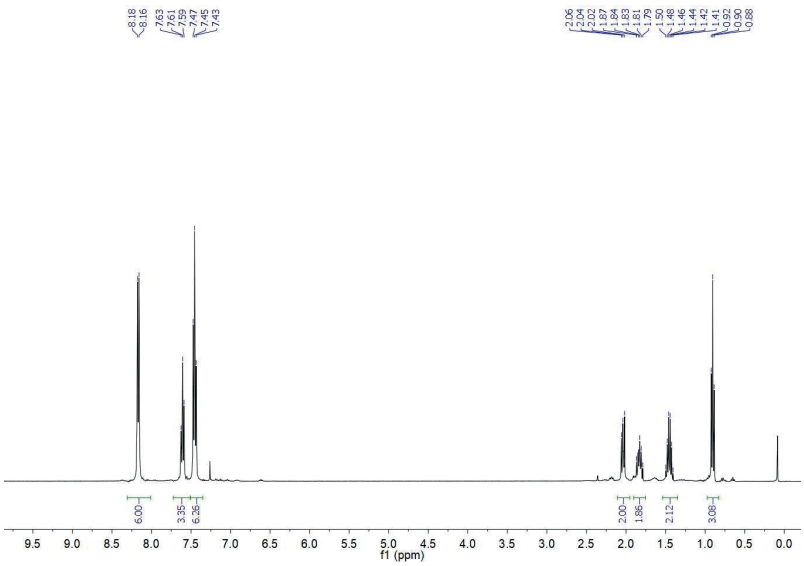

Figure 3.20. ^{1}H NMR of **4** (*n*-BuSnOBz$_3$), $CDCl_3$ at 298 K.

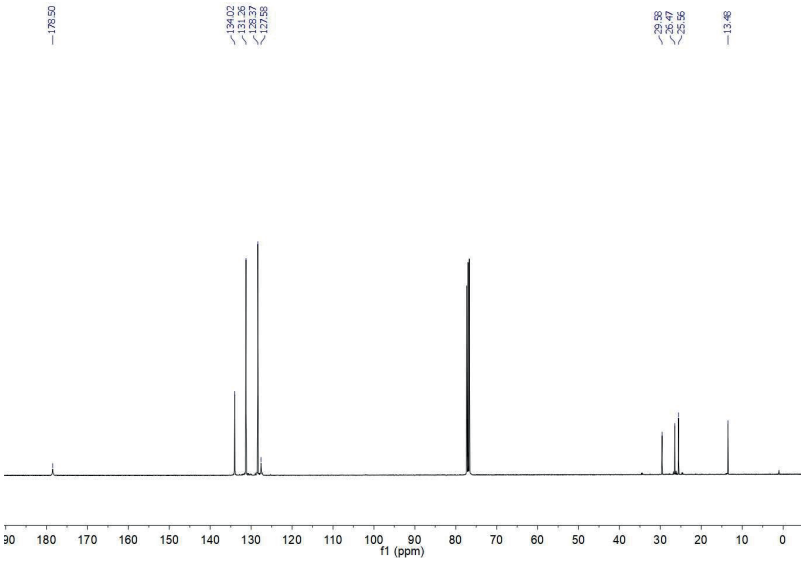

Figure 3.21. ^{13}C NMR of **4** (*n*-BuSnOBz$_3$), $CDCl_3$ at 298 K.

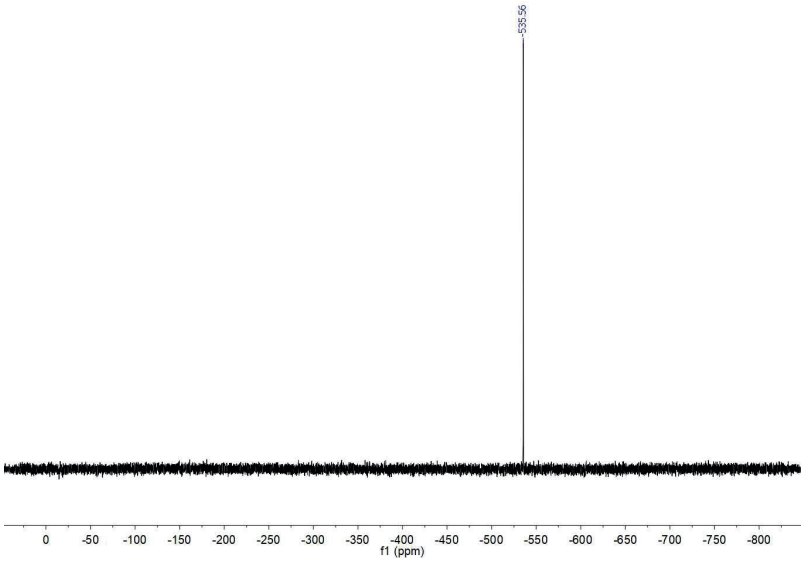

Figure 3.22. ^{119}Sn NMR of **4** (*n*-BuSnOBz$_3$), $CDCl_3$ at 298 K.

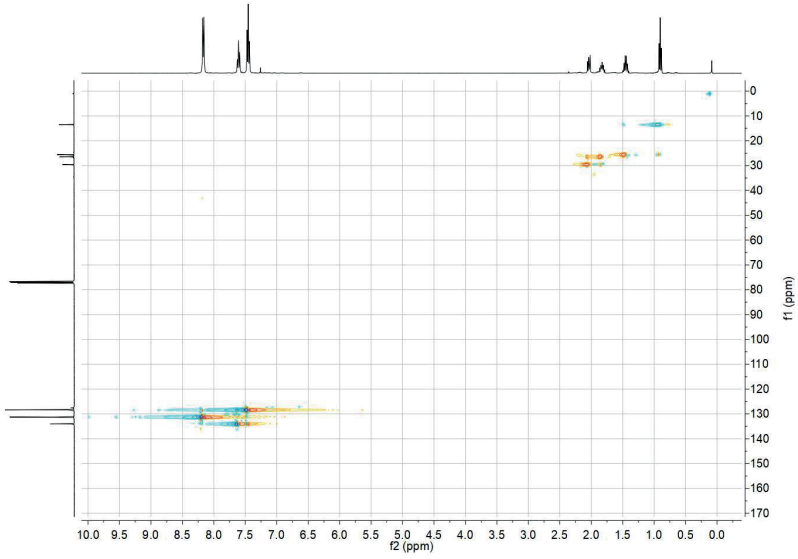

Figure 3.23. ^{1}H-^{13}C HSQC NMR of **4** (*n*-BuSnOBz$_3$), $CDCl_3$ at 298 K.

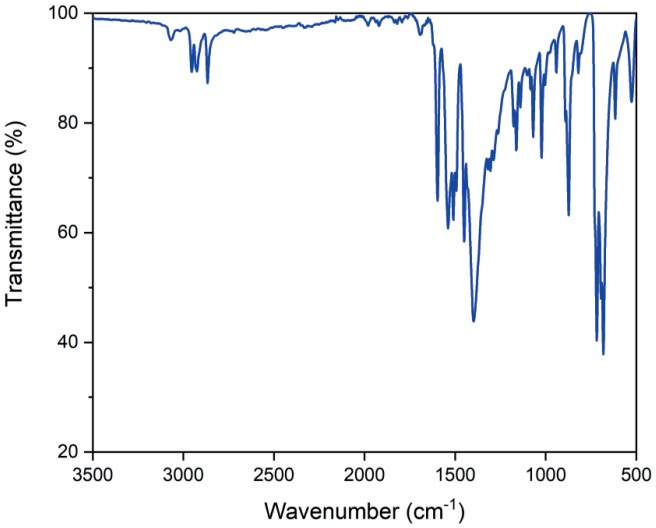

Figure 3.24. IR-ATR spectrum of **4** (*n*-BuSnOBz$_3$).

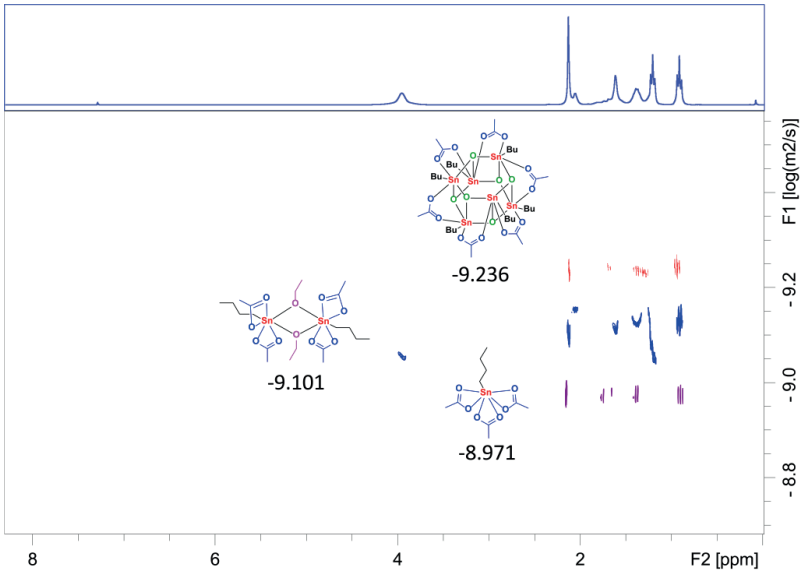

Figure 3.25. 2D ^{1}H DOSY spectrum of monomer **3** (purple trace), dimer **5A** (blue trace, with ^{1}H NMR on horizontal axis) and cluster **2** (red trace) in $CDCl_3$ at 298K.

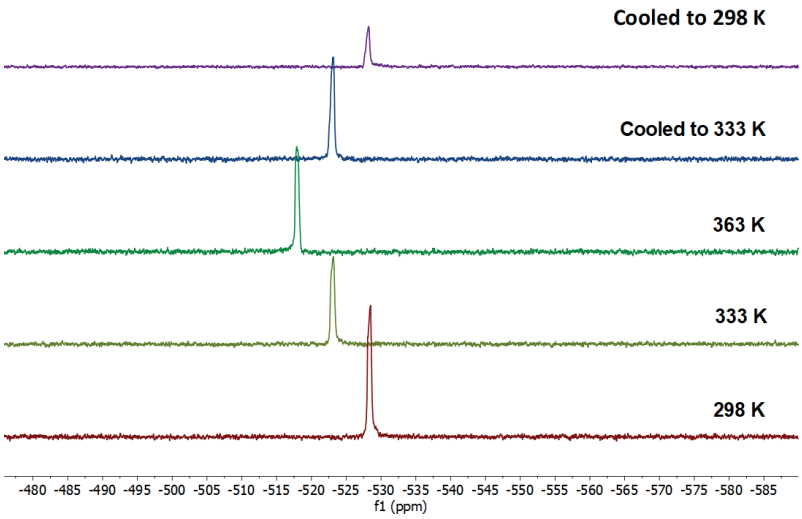

Figure 3.26. VT ^{119}Sn{H} NMR of **3** (0.4 M in Sn), Acetic acid-d_4 at 298 K.

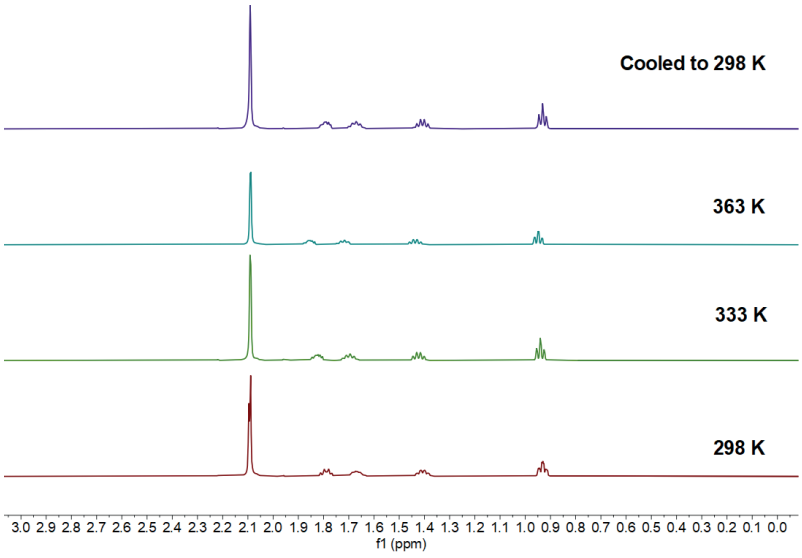

Figure 3.27. VT ^{1}H NMR of **3** (0.4 M in Sn), Acetic acid-d_4.

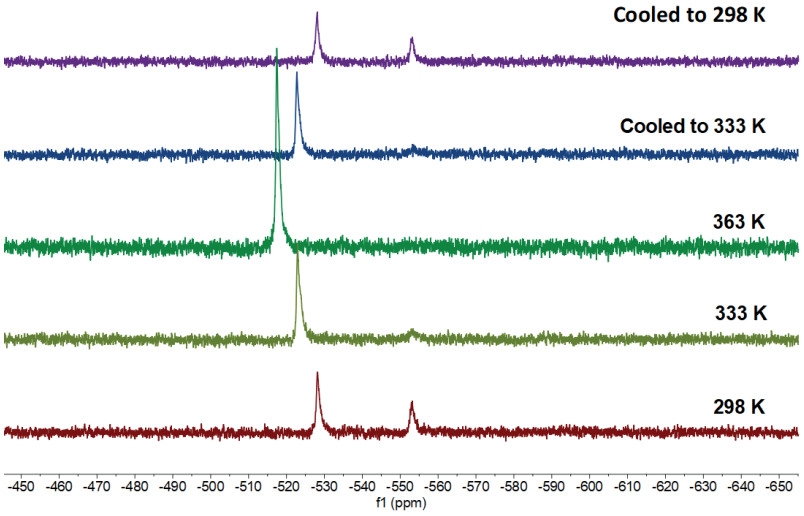

Figure 3.28. VT ^{119}Sn{H} NMR of **2** (0.4 M in Sn), Acetic acid-d_4.

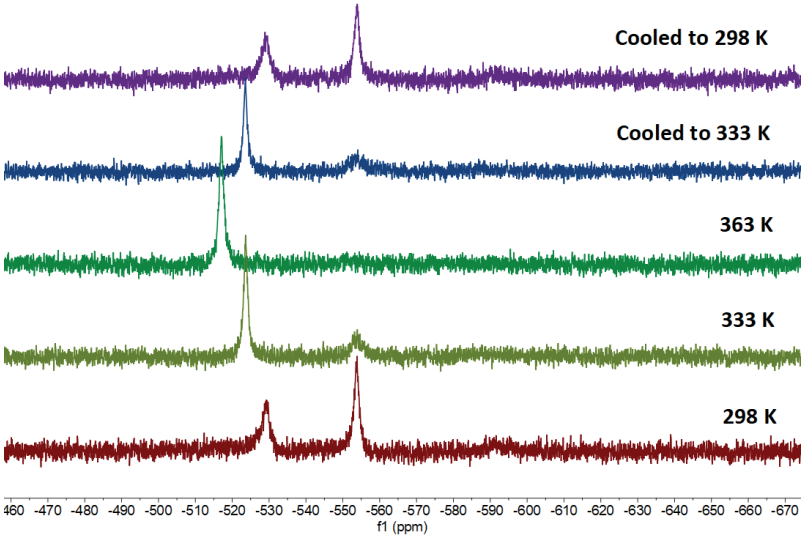

Figure 3.29. VT ^{119}Sn{H} NMR of **1** (0.4 M in Sn), Acetic acid-d_4.

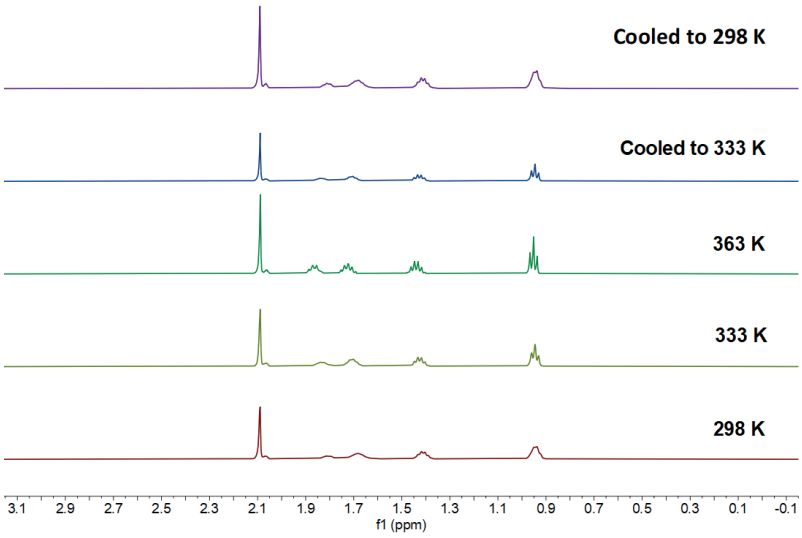

Figure 3.30. VT ^{1}H NMR of **2** (0.4 M in Sn), Acetic acid-d_4.

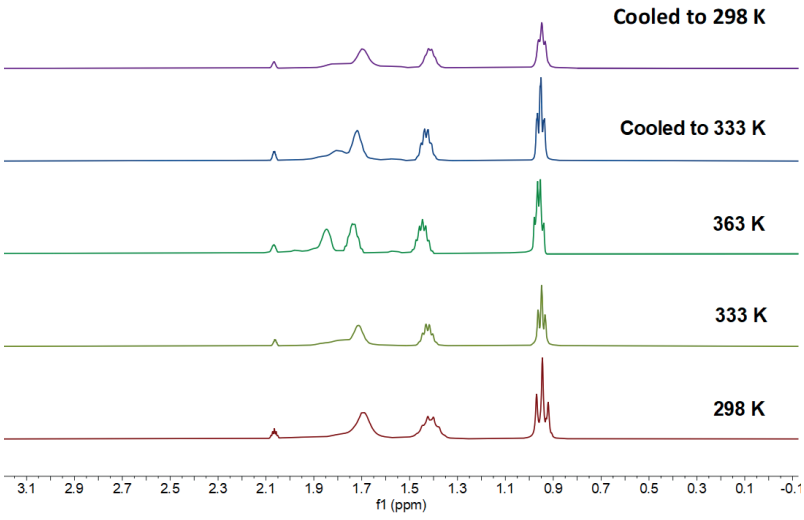

Figure 3.31. VT ^{1}H NMR of **1** (0.4 M in Sn), Acetic acid-d_4.

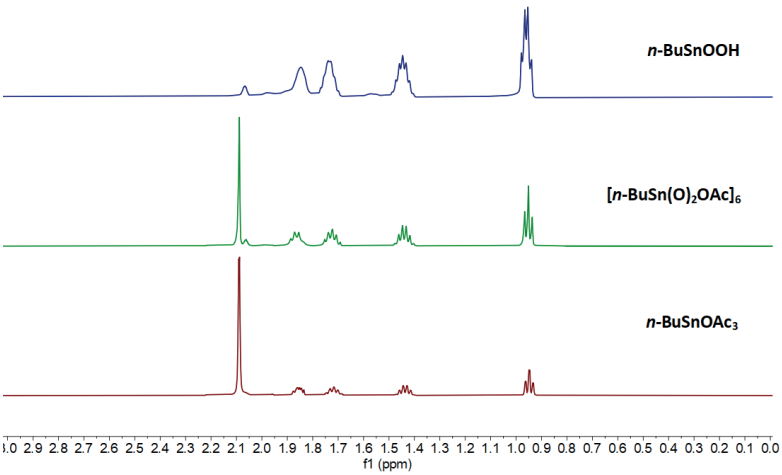

Figure 3.32. ^{1}H NMR of [*n*-BuSn(O)OAc]$_6$, *n*-BuSnOAc$_3$ and BuSnOOH (0.4 M in Sn) at 363 K, Acetic acid-d$_4$.

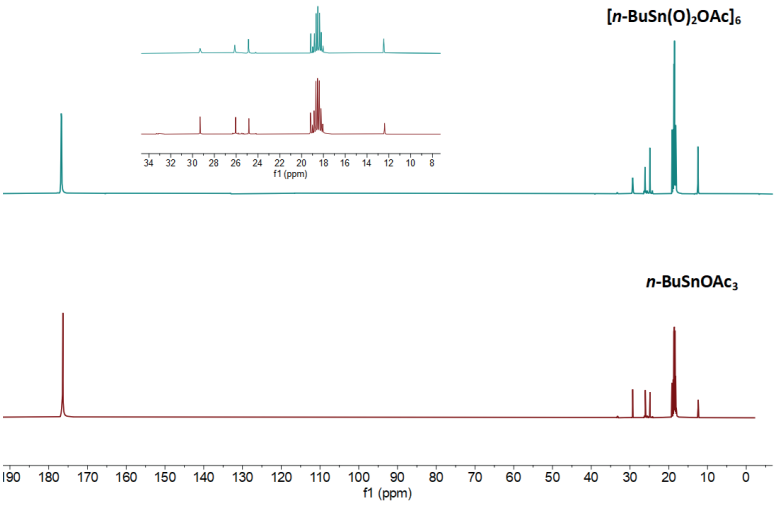

Figure 3.33. ^{13}C NMR of [*n*-BuSn(O)OAc]$_6$ and *n*-BuSnOAc$_3$ (0.4 M in Sn) at 366 K, Acetic acid-d$_4$ at 298 K.

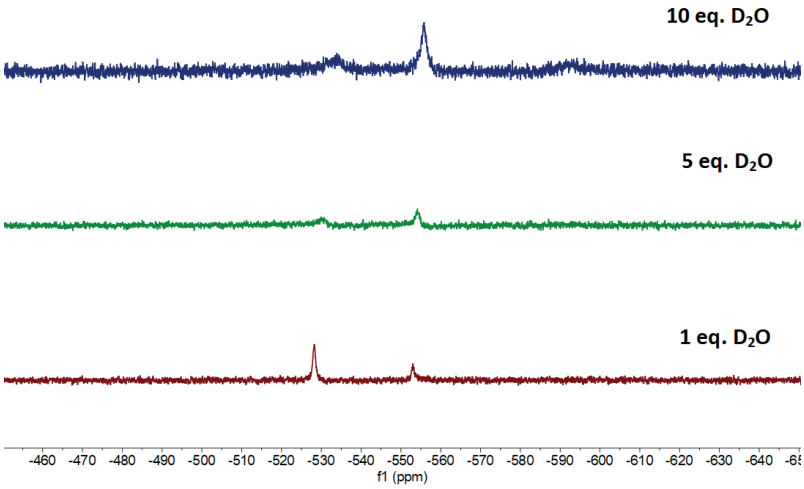

Figure 3.34. ^{119}Sn{H} NMR of **3** (0.4 M in Sn) with 1, 5 and 10 equivalents D_2O at 298K , Acetic acid (measured unlocked).

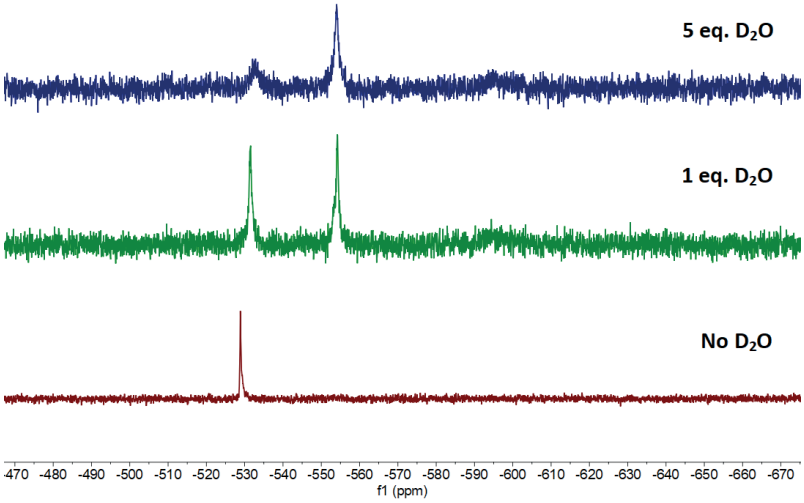

Figure 3.35. ^{119}Sn{H} NMR of **3** (0.4 M in Sn) with no, 1 and 5 equivalents D_2O at 298K , Acetic acid/EtOH 1:1 (measured unlocked)

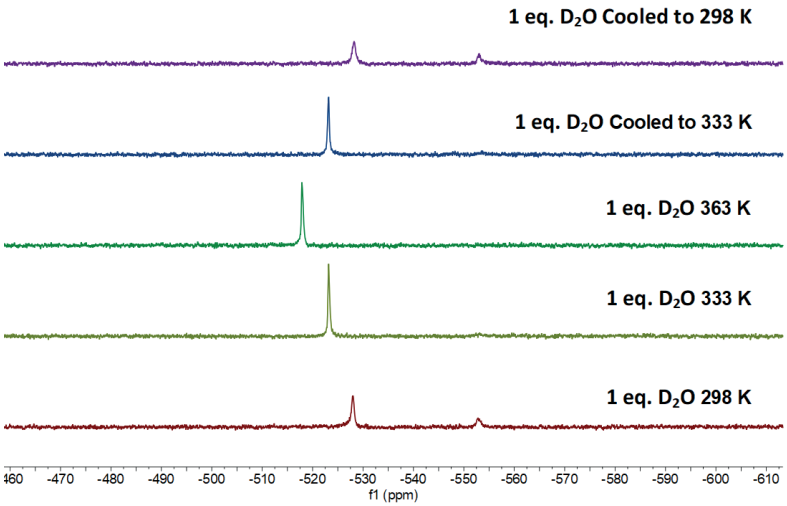

Figure 3.36. ^{119}Sn{H} NMR of **3** (0.4 M in Sn) with 1 equivalent D_2O at 298K, 333K and 363K, in acetic acid (measured unlocked).

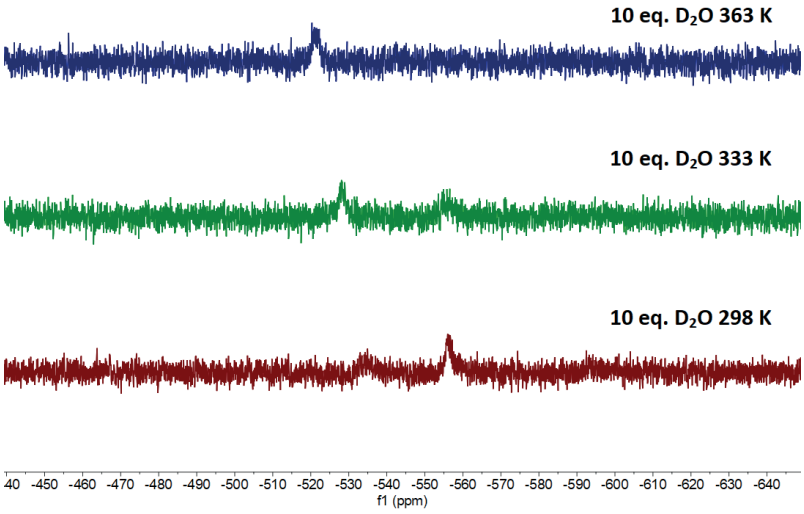

Figure 3.37. ^{119}Sn{H} NMR of **3** (0.4 M in Sn) with 10 equivalents D_2O at 298K, 333K and 363K, Acetic acid (measured unlocked).

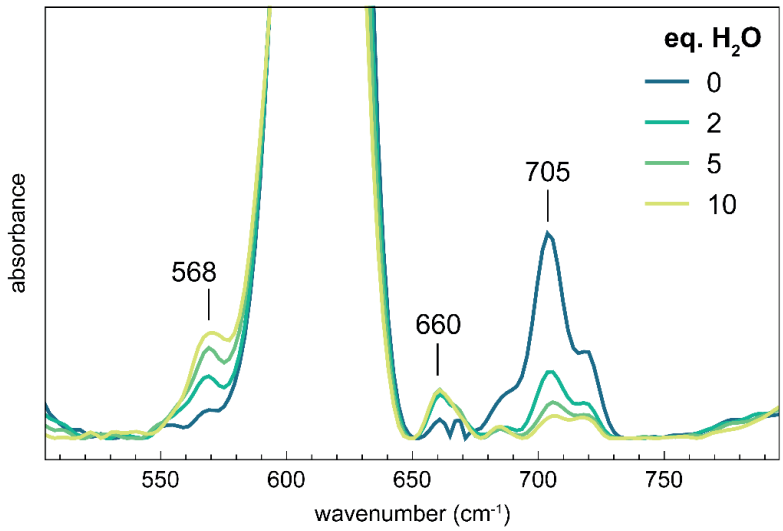

Figure 3.38. IR-ATR spectrum of **3** with 0, 2, 5 and 10 equivalents of H_2O.

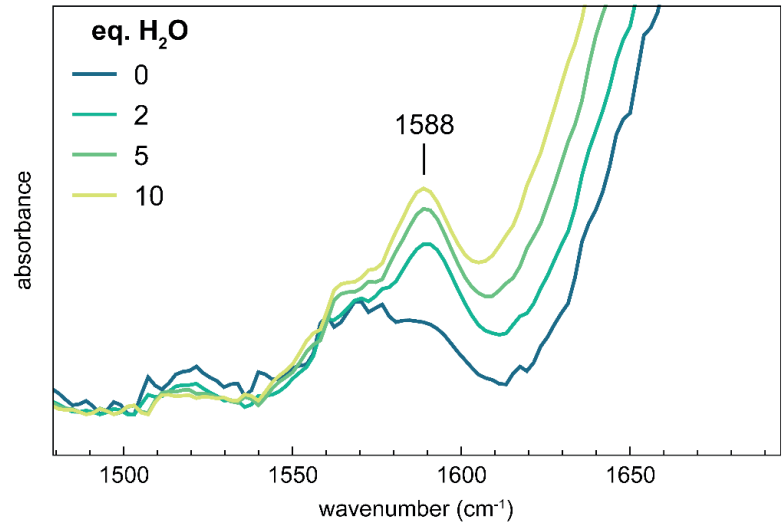

Figure 3.39. IR-ATR spectrum of **3** with 0, 2, 5 and 10 equivalents of H_2O.

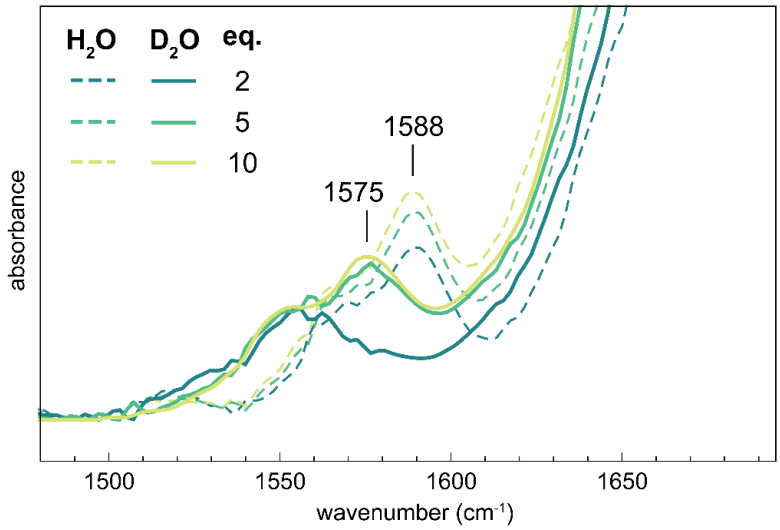

Figure 3.40. IR-ATR spectrum of **3** with 0, 2, 5 and 10 equivalents of H_2O or D_2O

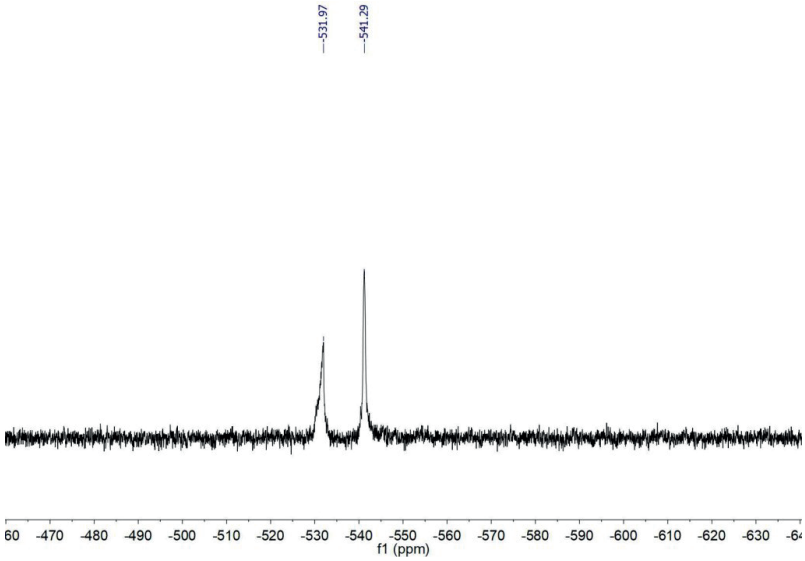

Figure 3.41. $^{119}Sn\{H\}$ NMR of **3** (0.4 M in Sn) in EtOH at 298 K (measured unlocked).

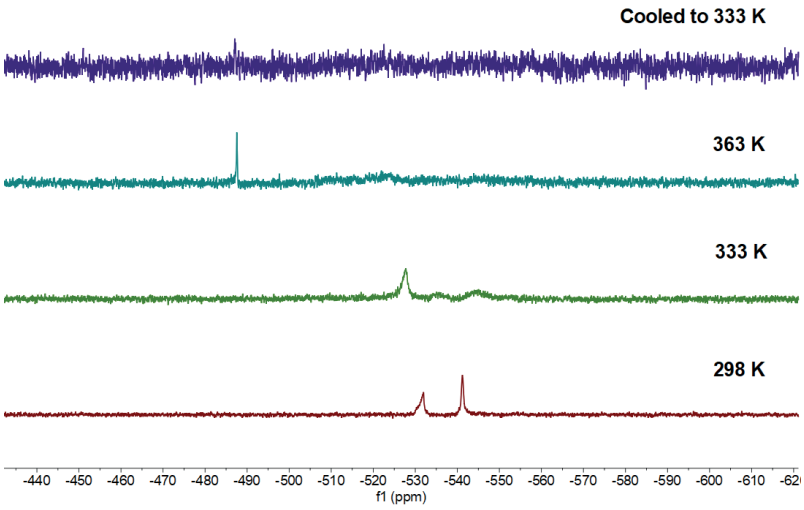

Figure 3.42. ^{119}Sn{H} NMR of **3** (0.4 M in Sn) in EtOH at 298, 333 and 363 K (measured unlocked).

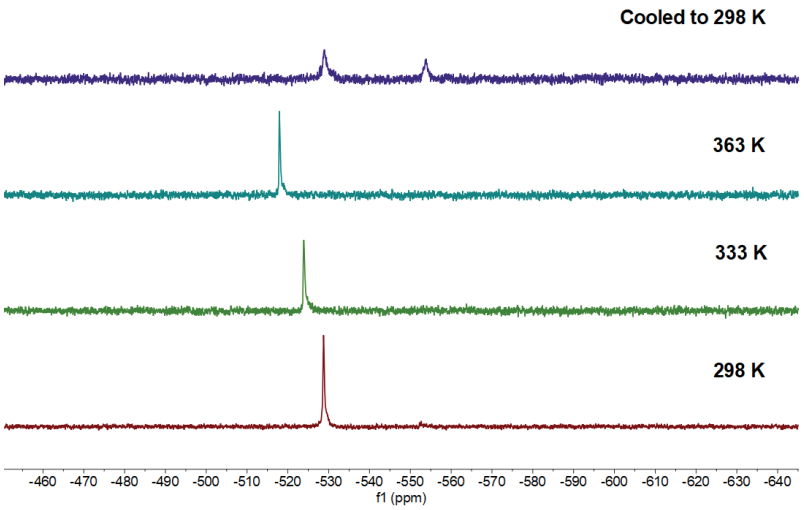

Figure 3.43. ^{119}Sn{H} NMR of **3** (0.4 M in Sn) in AcOH:EtOH 1:1 at 298, 333 and 363 K (measured unlocked).

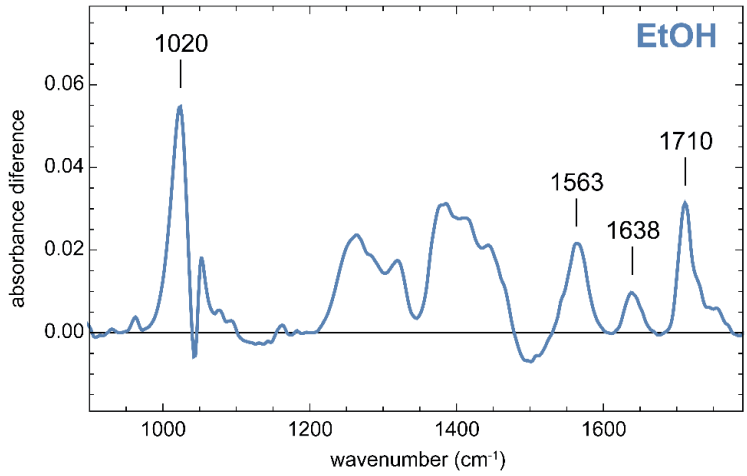

Figure 3.44. IR-ATR difference spectrum of **3** in EtOH (minus EtOH).

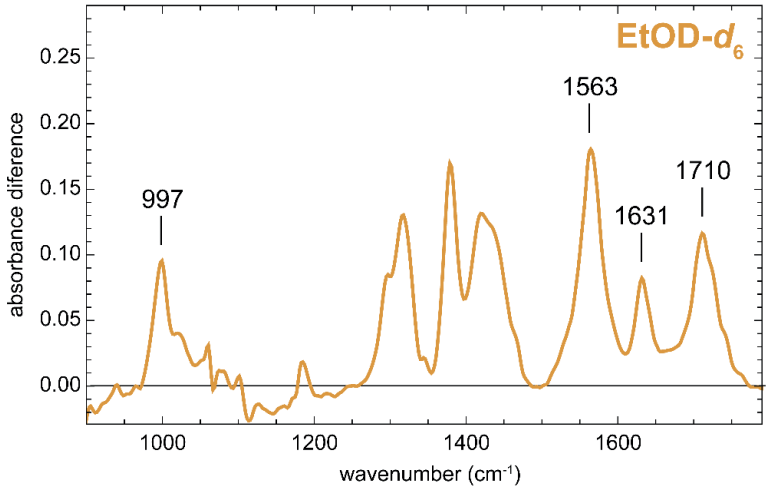

Figure 3.45. IR-ATR difference spectrum of **3** in EtOD-d_6 (minus EtOD-d_6).

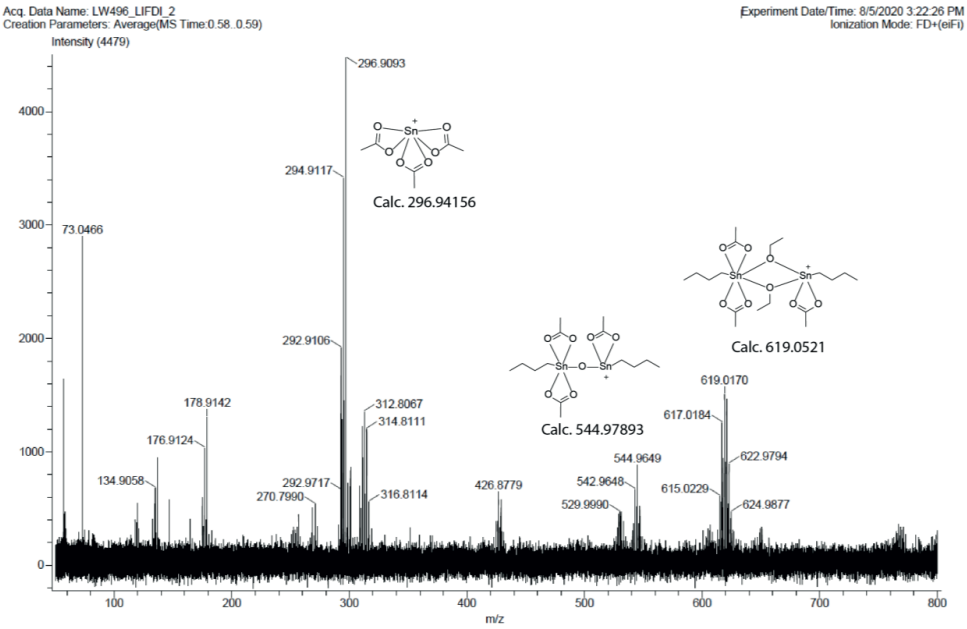

Figure 3.46. LIFDI-HRMS spectrum of **3** in EtOH.

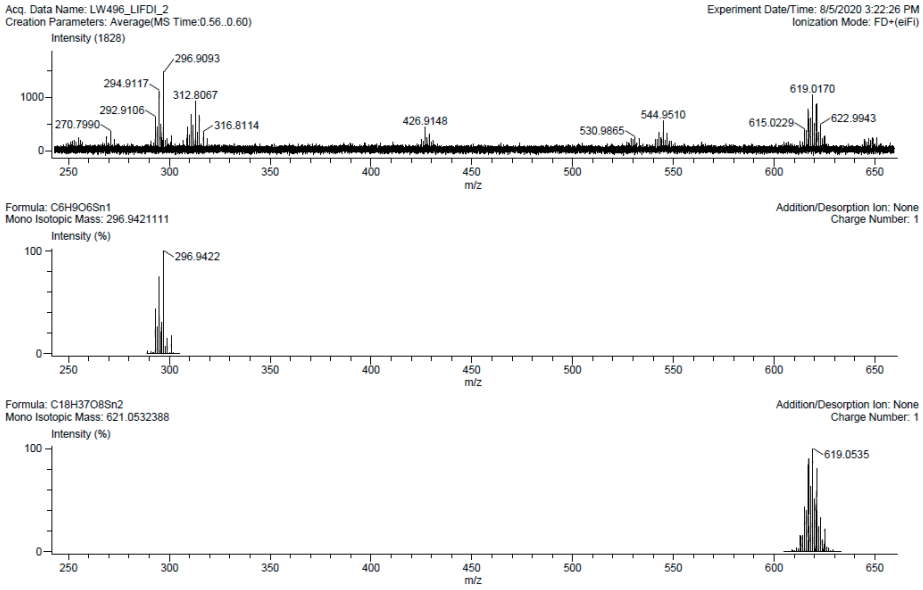

Figure 3.47. LIFDI-HRMS spectrum of **3** in EtOH.

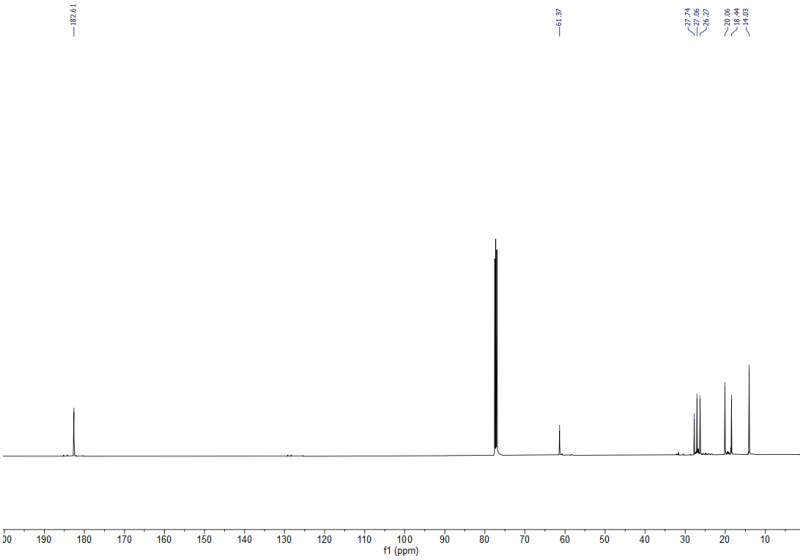

Figure 3.48. ^{13}C NMR of $(n\text{-BuSnOAc}_2\text{EtO})_2$, $CDCl_3$ at 233 K.

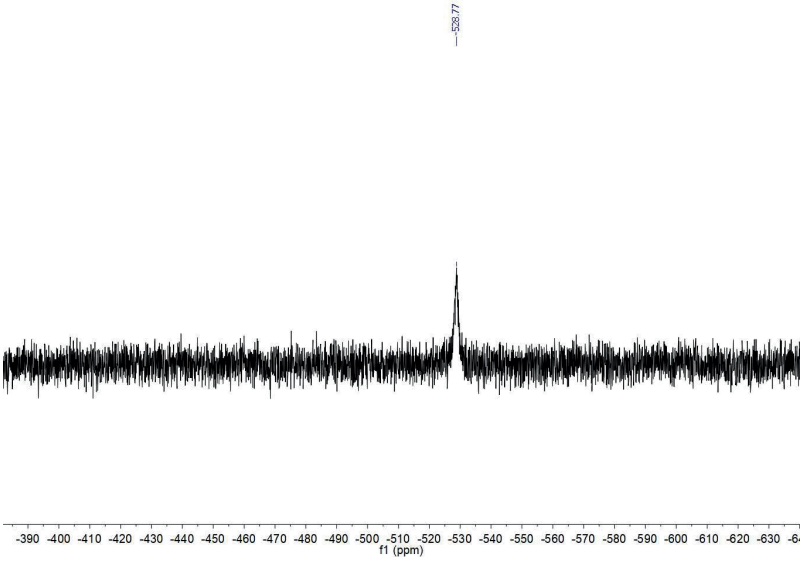

Figure 3.49. $^{119}Sn\{H\}$ NMR of **5A** in acetic acid (measured unlocked) at 298 K.

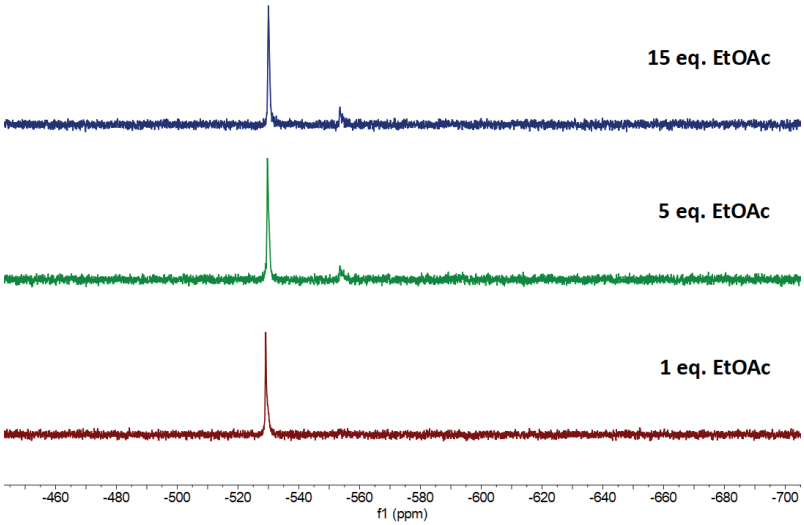

Figure 3.50. ^{119}Sn{H} NMR of **3** (0.4 M in Sn) with 1, 5 and 10 equivalents EtOAc at 298K , Acetic acid/EtOH 1:1 (measured unlocked).

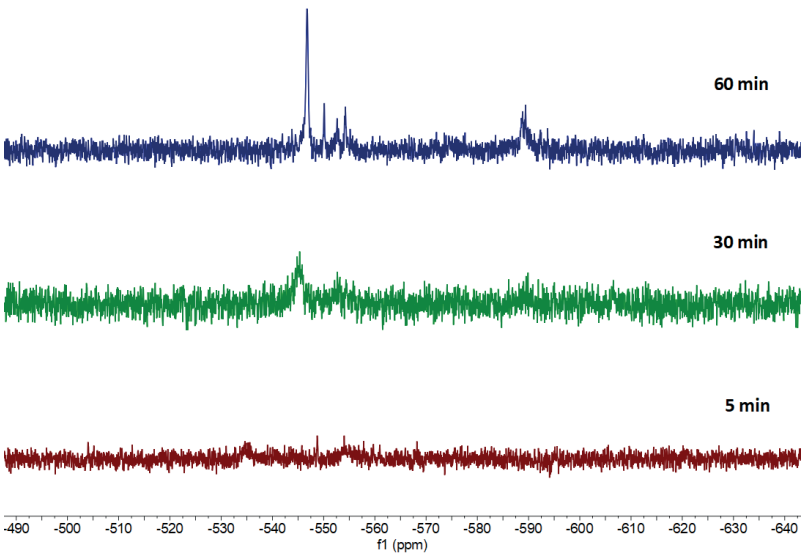

Figure 3.51. ^{119}Sn{H} NMR of esterification reaction catalyzed by **3** (0.4 M in Sn) at 5, 30 and 60 min., Acetic acid/Ethanol ratio 1:1 (measured unlocked at 363 K).

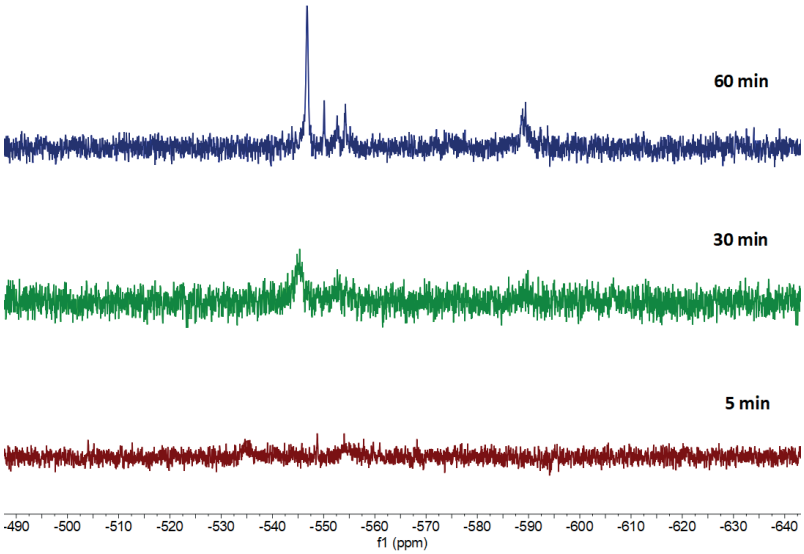

Figure 3.52. ^{119}Sn{H} NMR of esterification reaction catalyzed by **3** (0.4 M in Sn) at 5, 30 and 60 min., Acetic acid/Ethanol ratio 1:1 (measured unlocked at 298 K).

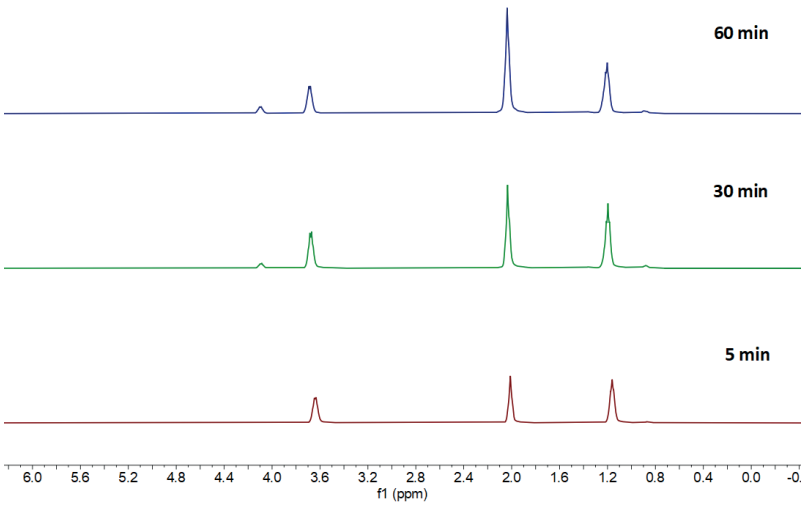

Figure 3.53. ^{1}H NMR of esterification reaction catalyzed by **3** (0.4 M in Sn) at 5, 30 and 60 min, $CDCl_3$ at 298 K.

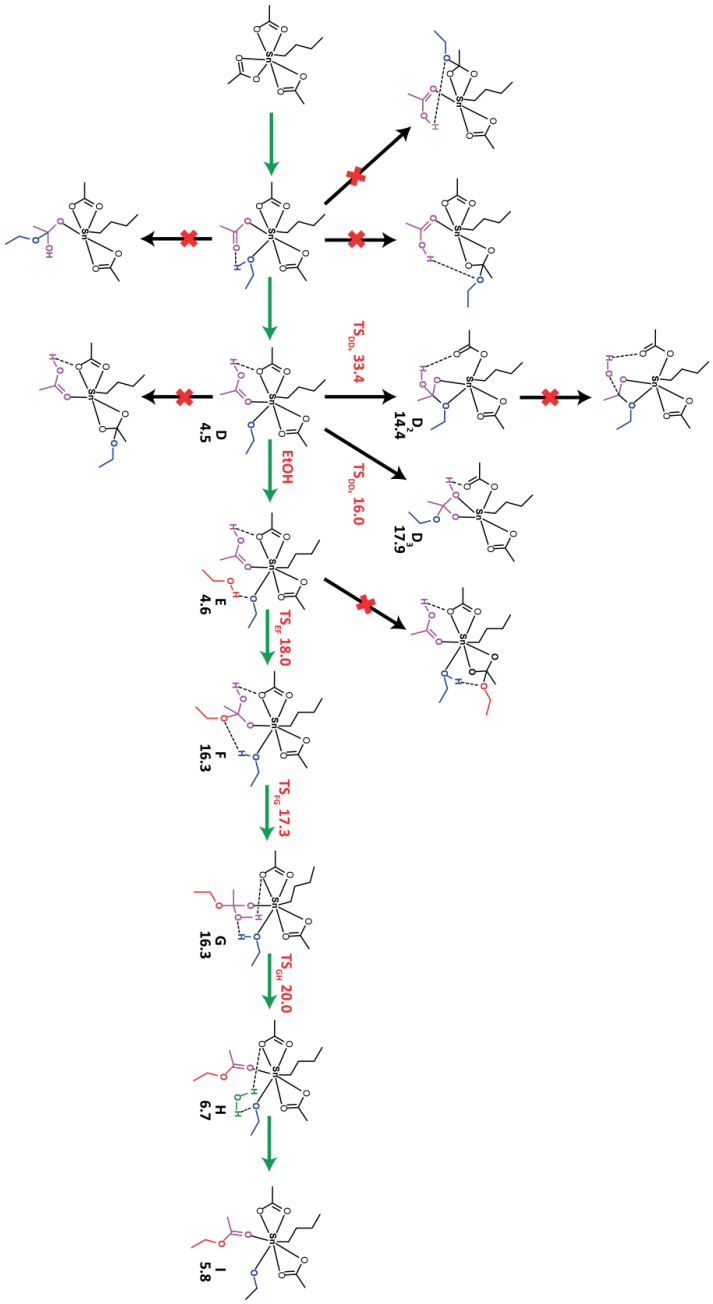

Figure 3.54. Alternative pathways and structures from catalytic cycle. Free energy values are given in kcal mol^{-1} relative to *n*-BuSn(OAc)$_3$.

References

1 J. Otera, J. Nishikido, *Esterification. Methods, Reactions, and Applications*, Wiley-VCH Verlag GmbH & Co., Weinheim, 2nd edn., 2010.

2 J. Clayden, N. Greeves and S. Warren, *Organic Chemistry*, Oxford University press, Oxford, 2nd edn., 2012.

3 J. J. Li, *Fischer-Speier esterification. In: Name Reactions*, Springer, Berlin, Heidelberg, 2002.

4 A. G. Davies, *J. Chem. Res.*, 2010, **34**, 181–190.

5 WO2017/091437 A1, 2013, 21.

6 M. R. Meneghetti and S. M. P. Meneghetti, *Catal. Sci. Technol.*, 2015, **5**, 765–771.

7 M. A. Hossain, M. A. Mohamed Iqbal, N. M. Julkapli, P. San Kong, J. J. Ching and H. V. Lee, *RSC Adv.*, 2018, **8**, 5559–5577.

8 J. Otera, N. Dan-oh and H. Nozaki, *Tetrahedron*, 1993, **49**, 3065–3074.

9 J. Otera, N. Dan-oh and H. Nozaki, *J. Org. Chem.*, 1991, **56**, 5307–5311.

10 T. Yano, K. Nakashima, J. Otera and R. Okawara, *Organometallics*, 1985, **4**, 1501–1503.

11 J. Bonetti, C. Gondard, R. Petiaud and A. Michel, *J. Organomet. Chem.*, 1994, **481**, 7–11.

12 J. Otera, N. Dan-oh and H. Nozaki, *J. Org. Chem.*, 1991, **56**, 5307–5311.

13 E. Crawford, T. Lohr, E. M. Leitao, S. Kwok and J. S. McIndoe, *Dalt. Trans.*, 2009, 9110–9112.

14 B. Jousseaume, C. Laporte, M. C. Rascle and T. Toupance, *Chem. Commun.*, 2003, **3**, 1428–1429.

15 J. Otera, *Chem. Rev.*, 1993, **93**, 1449–1470.

16 J. Otera, *Acc. Chem. Res.*, 2004, **37**, 288–296.

17 D. L. An, Z. Peng, A. Orita, A. Kurita, S. Man-E, K. Ohkubo, X. Li, S. Fukuzumi and J. Otera, *Chem. - A Eur. J.*, 2006, **12**, 1642–1647.

18 V. Chandrasekhar, C. G. Schmid, S. D. Burton, J. M. Holmes, R. O. Day and R. R. Holmes, *Inorg. Chem.*, 1987, **26**, 1050–1056.

19 V. Chandrasekhar, S. Nagendran and V. Baskar, *Coord. Chem. Rev.*, 2002, **235**, 1–52.

20 H. H. Anderson, *Inorg. Chem.*, 1964, **3**, 912–914.

21 R. R. Holmes, C. G. Schmid, V. Chandrasekhar, R. O. Day and J. M. Holmes, *J. Am. Chem. Soc.*, 1987, **109**, 1408–1414.

22 V. B. Mokal, V. K. Jain and R. T. Tiekink, *J. Organomet. Chem.*, 1991, **407**, 173–180.

23 M. C. Sharps, D. A. Marsh, L. N. Zakharov, J. E. Hutchison and D. W. Johnson, *Cryst. Res. Technol.*, 2017, **52**, 1–7.

24 J. C. Martins, M. Biesemans and R. Willem, *Prog. Nucl. Magn. Reson. Spectrosc.*, 2000, **36**, 271–322.

25 G. Prabusankar and R. Murugavel, *Organometallics*, 2004, **23**, 5644–5647.

26 J. D. Kennedy, *J. Chem. Soc., Perkin Trans.*, 1977, **2**, 242–248.

27 G. Casella, F. Ferrante and G. Saielli, *Inorg. Chem.*, 2008, **47**, 4796–4807.

28 P. Avalle, R. K. Harris and R. D. Fischer, *Phys. Chem. Chem. Phys.*, 2002, **4**, 3558–3561.

29 C. T. Lynch, K. S. Mazdiyasni, J. S. Smith and W. J. Crawford, *Anal. Chem.*, 1964, **36**, 2332–2337.

30 D. P. Gaur, G. Srivastava and R. C. Mehrotra, *J. Org. Chem.*, 1973, **63**, 221–231.

31 C. Müller, D. M. Andrada, I. A. Bischoff, M. Zimmer, V. Huch, N. Steinbrück and A. Schäfer, *Organometallics*, 2019, **38**, 1052–1061.

32 P. Villo, O. Dalla-Santa, Z. Szabó and H. Lundberg, *J. Org. Chem.*, 2020, **85**, 6959–6969.

33 H. Lundberg, F. Tinnis, J. Zhang, A. G. Algarra, F. Himo and H. Adolfsson, *J. Am. Chem. Soc.*, 2017, **139**, 2286–2295.

34 L. A. Wolzak, J. I. van der Vlugt, K. J. van den Berg, J. N. H. Reek, M. Tromp and T. J. Korstanje, *ChemCatChem*, 2020, **12**, 5229–5235.

35 J. D. Kennedy, W. Mcfarlane, P. J. Smith, F. Raymond and L. Smith, *J. Chem. Soc. Perkin Trans. 2*, 1973,

1785–1788.
36 TURBOMOLE Version 7.3.1 (TURBOMOLE Gmbh, Karlsruhe, Germany).
37 R. Baer, M. Haeser, M. Horn and H. Koelmel, C. *Chem. Phys. Lett.* 1989, **162**, 165 – 169.
38 PQS version 2.4, 2001, Parallel Quantum Solutions, Fayetteville, Arkansas, USA (the Baker optimizer is available separately from PQS upon request);
39 J. Baker, *J. Comput. Chem.* 1986, **7**, 385 – 395.
40 P. H. M. Budzelaar, *J. Comput. Chem.* 2007, **28**, 2226 – 2236.
41 A. D. Becke*, Phys. Rev. A*. 1988, **38**, 3098–3110.
42 J. P. Perdew, *Phys. Rev. B.* 1986, **33**, 8822–8824.
43 J. P. Perdew, *Phys. Rev. B.* 1986, **34**, 7406–7406.
44 F. Weigend and R. Ahlrichs, *Phys. Chem. Chem. Phys.* 2005, **7**, 3297−3305.
45 F. Weigend, M. Haser, H. Patzelt and R. Ahlrichs, *Phys. Lett.* 1998, **294**, 143−152.
46 S. Grimme, J. Antony, S. Ehrlich and J. Krieg, *J. Chem. Phys.* 2010, **132**, 154104−154119.
47 B. Kamenar and M. Bruvo, Izv. Jug. Cent. Krist., Ser. A **1967**, 2, 60, CCDC 1100657
48 Y. Zhao and D. G. Truhlar*, Theor. Chem. Acc.* 2008, **120**, 215−241.
49 Y. Zhao and D.G. Truhlar, *Acc. Chem. Res.* 2008, **41**, 157−167.
50 U. Ekstrom, L. Visscher, R. Bast, A.J. Thorvaldsen and K.J. Ruud, *Chem. Theor. Comp.* 2010, **6**, 1971–1980.
51 C. Müller, D. M. Andrada, I. Bischoff, M. Zimmer, V. Huch, N. Steinbrück and A. Schäfer, *Organometallics*, 2019, **38**, 1052-1061.
52 M. Haser, R. Ahlrichs, H.P. Baron, P. Weis and H. Horn, *Theoret. Chim. Acta*, 1992, **83**, 455 – 470.
53 A.D. Becke, *J. Chem. Phys*. 1993, **98**, 5648 – 5652.
54 C. Lee, W. Yang and R.G. Parr, *Phys. Rev. B*, **1988**, 37, 785 – 789.
55 S.H. Vosko, L. Wilk and M. Nusair, *Can. J. Phys.* 1980, **58**, 1200 – 1211.
56 P.J. Stephens, F.J. Devlin, C.F. Chabalowski and M.J. Frisch, *Phys. Chem.* 1994, **98**, 11623 – 11627.

Chapter 4

Kinetic Studies on Lewis Acidic Metal Polyesterification Catalysts – Hydrolytic degradation is a Key Factor for Catalytic Performance

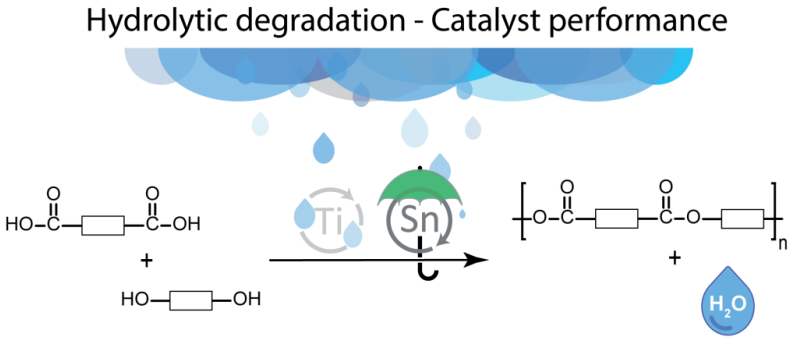

Abstract: Kinetic analysis of polyesterification reactions using Lewis-acidic metal catalysts have been performed. While Sn-based catalysts are superior to Ti-based catalysts under neat polycondensation conditions (high [H_2O]), the result is inverted under azeotropic conditions (low [H_2O]). These findings show that the catalytic activity is crucially determined by the robustness of the catalyst against hydrolytic degradation.

This work is based on: L.A. Wolzak, R. van Gemert, K.J. van den Berg, J.N.H. Reek, M. Tromp, T.J. Korstanje, *Catal. Sci. Technol.* **2022**, 12, 2056-2060.

Introduction

In the past decades, extensive advances in the production of monomers for polyesters, derived from renewable resources, have been made.[1–7] Nevertheless, the synthesis of polyesters itself still heavily relies on well-known condensation reactions, such as the direct esterification of alcohols and carboxylic acids. This route remains a highly sustainable method to obtain polyesters, given the high atom efficiency and water being the only by-product.[8] However, due to the harsh reaction conditions required for this reaction, the use of a catalyst that can reduce the reaction temperature is preferred. High-valent Lewis acidic metal catalysts based on group 4 metals (Ti, Zr and Hf), Sn and Sb have displayed distinct activity in direct polyesterification reactions.[9–13] Yet, potent Lewis acidic metal catalysts based on abundant and non-toxic metals, that are active in direct polyesterification are still highly desired. Next to the ability to lower the activation energy of a reaction, an effective catalyst should be fairly robust, since deactivation of the catalyst can dominate the observed activity. Lewis acidic metal catalysts are typically deactivated by water, which is formed during the initial esterification step. The reaction with water affords the formation of metal-oxo-clusters with reduced catalytic activity (Figure 4.1).

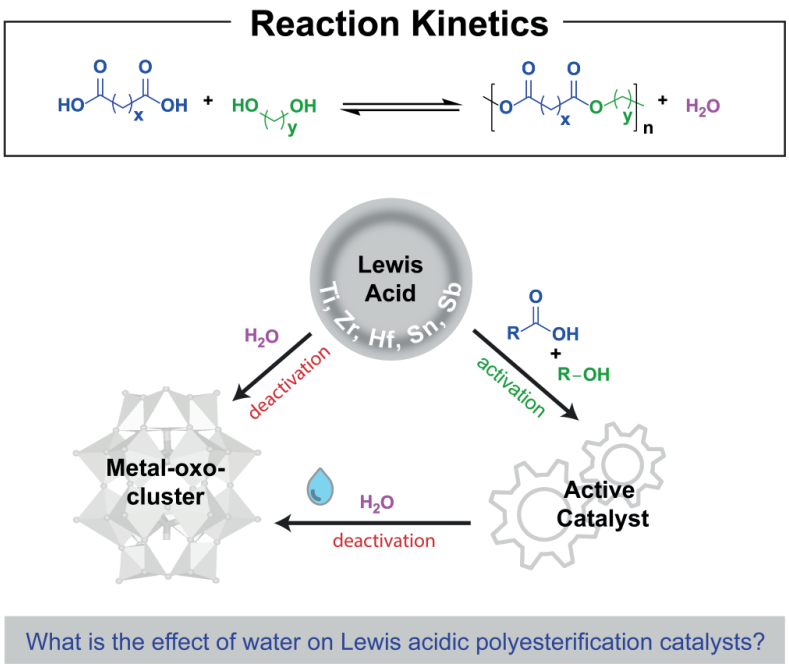

Figure 4.1. The effect of water on Lewis acidic polyesterification catalysts.

Hydrolysis of both group 4 metal alkoxides, and mono- and di-alkyl tin(IV) complexes is well-known and results in the formation of a wide variety of metal-oxo-clusters.[14–18] It remains however unclear to date to what extent these metal-oxo-clusters also form during polyesterification reactions. Polyesterification reactions catalyzed by group 4 metals are predominantly reported under azeotropic conditions in combination with removal of water by a scavenger.[19,20] Such dehydrating agents drive the equilibrium towards the ester product, and prevent prolonged exposure of the catalyst to water formed during polyesterification. Furthermore, multidentate ligands are employed to reduce the number of hydrolysable terminal ligands, which hampers uncontrolled cluster formation.[21–25] Although it is clear that hydrolytic degradation of Lewis acidic catalysts can be problematic, the degree of deactivation will depend on the applied reaction conditions such as polarity of the reaction mixture, reaction temperature, use of solvent and reduced pressure.[26–29] This prompted us to investigate the robustness of different commercially applied polyesterification catalysts through analysis of the reaction profile.[29] Herein, we report our kinetic investigations on titanium- and *n*-butylstannoic acid-catalyzed polyesterification reactions under neat polycondensation and azeotropic conditions.

Results and discussion

We started our investigation with the neat polyesterification of 1,6-hexanediol, in excess, and adipic acid in the presence of 0.1 mol% catalyst (relative to -OH groups) at 170 °C to synthesize polyester-diols. All formed water was collected in a Dean-Stark apparatus (Figure 4.5). In order to obtain kinetic profiles, the reaction progress was followed via the Acid Value (AV) determined by titration. Three different catalysts were selected: *n*-BuSnOOH, $Ti(O^iPr)_4$ and titanium(triethanolaminato)acetate (Ti-atrane) (Figure 4.2). In general, catalysts were added after 1 hour reaction time at 170 °C to ensure effective removal of formed reaction water before catalyst addition. Under neat conditions, *n*-BuSnOOH (Figure 4.2A, blue trace) displays catalytic activity, with an AV = 13.3 mg KOH g^{-1} after 6 hours. This in contrast to $Ti(O^iPr)_4$ (Figure 4.2A, green trace) and Ti-atrane (Figure 4.2A, orange trace) which are not catalytically active, and perform comparable to the reaction without metal catalyst (blank reaction). To obtain insight in the robustness of *n*-BuSnOOH under neat polycondensation conditions we turned to Reaction Progress Kinetic Analysis (RPKA).[30] More specifically, same-excess experiments can help to disclose deactivation of the catalysts via the overlay of kinetic reaction profiles.

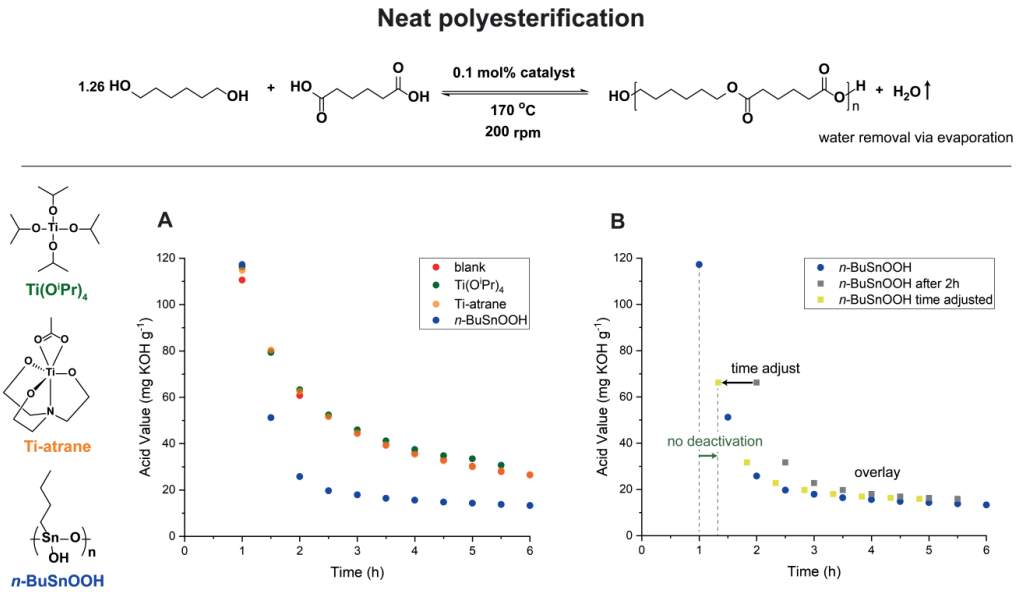

Figure 4.2. (A) Neat polyesterification of 1,6-hexanediol and adipic acid in the presence of 0.1 mol% catalyst (relative to -OH groups) at 170 °C. (B) Time adjusted kinetic profile of *n*-BuSnOOH-catalyzed reaction.

Because the polyesterification reaction is also catalyzed by the carboxylic acid, which results in a background reaction, catalyst deactivation via same-excess conditions can be determined via the addition of catalyst at a later reaction point in time (Figure 4.2B). Next to the initial *n*-BuSnOOH-catalyzed polyesterification (Figure 4.2B, blue trace), a similar reaction was performed, but now with addition of *n*-BuSnOOH after 2 hours reaction time (Figure 4.2B, grey trace). Upon catalyst addition, a clear increase in rate is observed and within 5 hours the AV resembles the value observed in the initial *n*-BuSnOOH catalyzed reaction (Figure 4.6A).

The time-adjusted profile of the second experiment (Figure 4.2B, yellow trace) gives a good overlay with the initial experiment and is indicative for the absence of catalyst deactivation. Next, we turned to the neat polyesterification of oligomers analogue to a two-step polycondensation method (Figure 4.3). Starting from oligomers (AV = 105 mg KOH g^{-1}) the high water concentrations present in the initial stage of the polyesterification reaction were circumvented. Under these reaction conditions the $Ti(O^iPr)_4$ (Figure 4.3A, green trace) catalyst still performed comparable to the blank reaction (Figure 4.3A, red trace). For the Ti-atrane (Figure 4.3A, orange trace) catalyst minor catalytic activity is observed. In order to obtain a more apolar reaction mixture, oligomers based on adipic

and pripol 1009, instead of 1,6-hexanediol, were synthesized. However, also the application of these oligomers (AV = 60 mg KOH g^{-1}) resulted only in minimal activity for the titanium-based catalysts (Figure 4.3B).

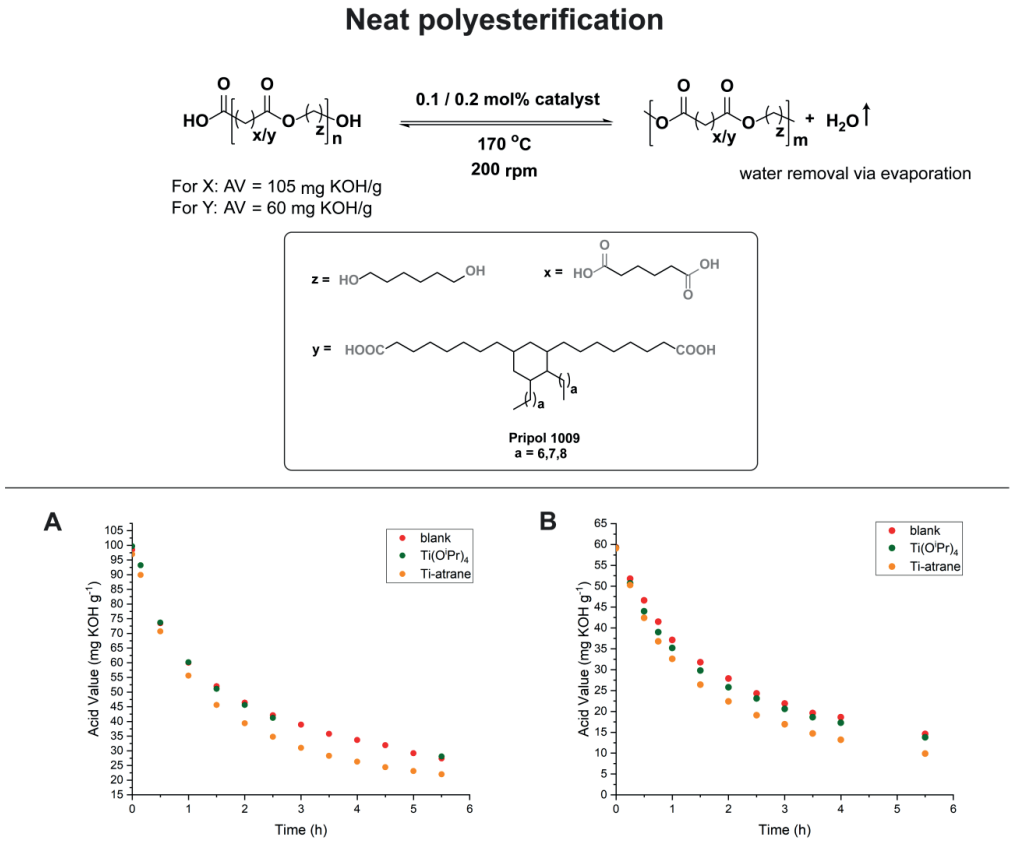

Figure 4.3. (A) Polyesterification of oligomers (AV = 105 mg KOH g^{-1}) of 1,6-hexanediol and adipic acid in the presence of 0.1 mol% catalyst (relative to -OH groups) at 170 °C. (B) Polyesterification of oligomers (AV = 60 mg KOH g^{-1}) of 1,6-hexanediol and Pripol 1009 in the presence of 0.2 mol% catalyst (relative to -OH groups) at 170 °C.

We hypothesize that the lack of catalytic activity for the titanium-based catalysts results from deactivation by water, hence a harmful water concentration is present in the reaction mixture (Table 4.1). We therefore turned to azeotropic reaction conditions, which enable the effective continuous removal of stoichiometrically formed water. Under these conditions, the polyesterification of 1,6-hexanediol and adipic acid was performed

with the inclusion of xylene as high-boiling solvent, in the presence of 0.25 mol% (relative to -OH groups) of catalyst (Figure 4.4). The course of the reaction was followed with *in-situ* infrared spectroscopy via the decrease of the $\nu_{C=O}$ vibration of the carboxylic acid over time (Figure 4.4A), which correlates well with determined Acid Values (Figures 4.13). We observed that under azeotropic reaction conditions at 140 ^{o}C, *n*-BuSnOOH (Figure 4B, blue trace) still has the highest activity after 6 hours.

However, the Ti-atrane (Figure 4.4B, orange trace) and Ti($O^{i}Pr$)$_4$ (Figure 4.4B, green trace) catalysts perform significantly better than the blank reaction (Figure 4.4B, red trace). Remarkably, the Ti-atrane catalyst outperforms *n*-BuSnOOH in the first two hours of the reaction. In addition, after 1 hour the reaction mixture became turbid, which is indicative for the formation of titanium-oxo-clusters and thus the deactivation of Ti($O^{i}Pr$)$_4$ (Figure 4.7). Analysis of the H_2O concentration revealed water levels between 2286 – 4669 ppm after 6 hours reaction time (Table 4.2). An increase in the reaction temperature to 150 ^{o}C proved to be effective to ensure an azeotropic reflux over the whole reaction period, i.e. the water concentrations were significantly diminished to 158 - 523 ppm for all metal-catalyzed reactions (Table 4.2).[31] Performing the reaction at 150 ^{o}C resulted in Ti($O^{i}Pr$)$_4$ (Figure 4.4C, green trace) and Zr($O^{i}Pr$)$_4$-^{i}PrOH (Figure 4.4C, pink trace) being very active catalyst. The improved activity of Group 4 alkoxides encouraged us to investigate the robustness of Ti($O^{i}Pr$)$_4$ under azeotropic reflux conditions at 150 ^{o}C. An additional same excess experiment was performed, with catalyst addition at a later point in time (Figure 4.4D, grey trace). The time-adjusted profile of the second experiment (Figure 4.4B, yellow trace) gives a good overlay with the initial Ti($O^{i}Pr$)$_4$ catalyzed reaction (Figure 4.4B, green trace) which is indicative for the absence of catalyst deactivation.

Overall, the robustness of the catalyst tends to be crucial, which is highlighted by the superior performance of *n*-BuSnOOH, which has the ability to the withstand high water concentrations that accumulate under neat polyesterification conditions. To further test the robustness, against hydrolytic degradation, of the different catalysts we investigated the hydrolysis of a polyester (AV = 24.6 mg KOH g^{-1}) of 1,6-hexanediol and adipic acid.[32-38] After 2 hours reaction time, in an autoclave at 150 ^{0}C (Figure 4.15), an AV of 81.9 mg KOH g^{-1} was found for the *n*-BuSnOOH catalyzed reaction. Whereas the blank reaction and Ti-atrane catalyzed reaction resulted in significantly lower AV's with 35.3 and 33.4 mg KOH g^{-1} (Table 4.3). These results unveil that *n*-BuSnOOH has indeed the ability to the withstand high water concentrations that accumulate under neat polyesterification and polyester hydrolysis conditions.

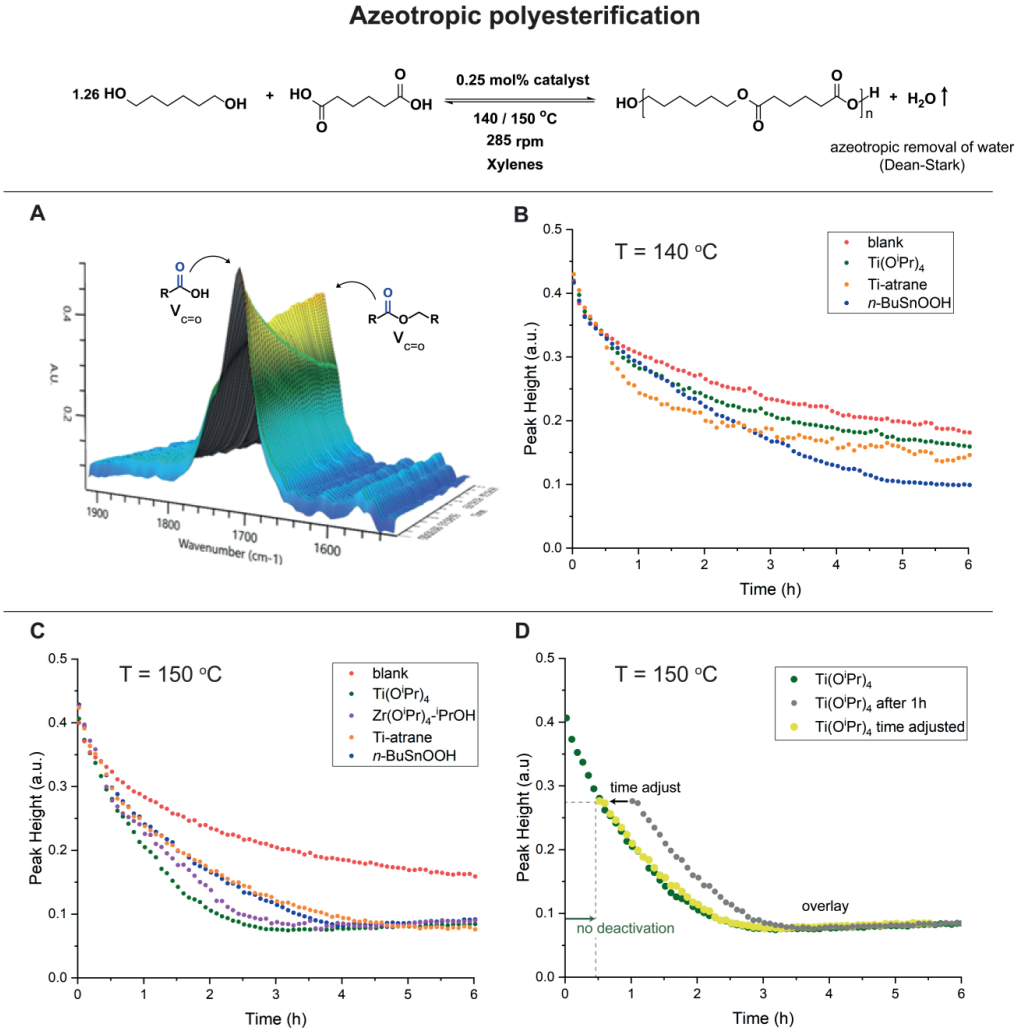

Figure 4.4. Polyesterification of 1,6-hexanediol and adipic acid in the presence of 0.25 mol% catalyst (relative to -OH groups) in the presence of xylene at 150 °C. (A) Peak height of $\nu_{C=O}$ vibration of the carboxylic acid (1712 cm^{-1}) and ester (1736 cm^{-1}) followed over time. (B) Peak height at 1712 cm^{-1} ($\nu_{C=O}$ vibration of the carboxylic acid) and Acid Value (derived from peak height via correlation presented in Figure 13) of catalyzed reactions at 140 °C. (C) Peak height at 1712 cm^{-1} and Acid Value (derived from peak height via correlation presented in Figure 13) of catalyzed reactions at 150 °C. (D) Time adjusted kinetic profile of TiO^iPr_4 catalyzed reaction at 150 °C.

Moreover, these findings are in agreement with our recent spectroscopic study on *n*-BuSnOOH catalyzed esterification, in which we demonstrated that at a relevant reaction temperature (90 °C), the polymeric *n*-BuSnOOH forms a monomeric *n*-butyltintricarboxylate and remains unaffected by water.[39] In contrast to *n*-BuSnOOH, the titanium catalysts greatly suffer from hydrolytic degradation under neat polyesterification conditions. The Ti-atrane complex shows only minor activity for example. However, when the water concentrations are significantly lowered via azeotropic removal, the group 4 metal alkoxides turned out to being very active catalysts, outperforming *n*-BuSnOOH in terms of activity. Nevertheless, deactivation via hydrolytic degradation is facile for all titanium-based catalysts as demonstrated by the azeotropic experiments at 140 °C. The utilization of a multidentate ligand, i.e. in the Ti-atrane complex, resulted in a slightly improved water tolerance. On the other hand, the Ti-atrane performs worse than $Ti(O^iPr)_4$ under optimal azeotropic conditions (150 °C), presumably because the ligand effectively shields the active metal center which hampers catalysis.

Conclusions

We have demonstrated, that *n*-BuSnOOH is an active and robust catalyst under neat polyesterification conditions. This is in contrast to $Ti(O^iPr)_4$ and Ti-atrane, which only gave minor initial activity. Low water concentrations (<550 ppm), which can be achieved via azeotropic removal, proved to be pivotal for group 4 metal alkoxides to be active and robust catalysts. These findings reveal the detrimental effect of water on titanium-based catalysts, even for complexes that bear multidentate ligands. This demonstrates that the robustness of the Lewis acidic metal catalyst dictates the performance in many polyesterification reactions. We believe that these insights will propel the sustainable production of (biobased) polyesters via catalysis by non-toxic and abundant Lewis acidic metals.

Experimental Section

General Experimental Details

Chemicals were obtained from Merck or Acros Organics and were used without further purification. For experiments with an azeotropic reflux, xylenes (mixture of isomers) 99% ACS with b.p. 136 – 140 °C was applied. Titanium(triethanolaminato)acetate was synthesized following a reported procedure.[40] Acid values (AV) were determined via titration, with samples dissolved in a 1:1 mixture of xylene/ethanol, and titrated with a 0.1 M KOH in MeOH solution on a Metrohm 716 DMS Titrino station. The AV is proportional to the carboxylic acid concentration and is defined as milligrams of potassium hydroxide (KOH) required to neutralize one gram of sample. The AV (in mg KOH g^{-1}) was calculated via the formula:

$$\mathrm{AV} = \frac{5.611 * \mathrm{V}}{\mathrm{m}}$$

where V is the required volume (in mL) of a 0.1 M KOH solution and m the mass of the sample (in g). *In-situ* infrared spectra were collected with a Mettler Toledo ReactIR 15 equipped with an air-cooled Art Photonics FlexiSpec® diamond *in-situ* FTIR-ATR probe for harsh conditions. Conversion was followed by the peak height of the $\nu_{c=o}$ of the carboxylic acid (1712 cm^{-1}) with a two point baseline from 1790 to 1630 cm^{-1}. Water concentrations measurements were performed on a Metrohm 831 KF coulometer without diaphragm.

Neat polyesterification

Polyesterification of 1,6-hexanediol and adipic acid

In a 1 L four-necked round bottom flask, equipped with an overhead stirrer and thermocouple, 1,6-hexanediol (327.77 g, 2.77 mol) and adipic acid (322.22 g, 2.20 mol) were heated to 170 °C while the stirring speed was slowly increased to 200 rpm. Water formed during polyesterification was collected in an empty Dean-Stark receiver. After 1 h reaction time at 170 °C, catalyst (5.5 mmol, 0.1 mol% relative to -OH groups) was slowly added to the reaction mixture and samples for acid value determination were taken every 30 minutes.

Polyesterification of oligomers of 1,6-hexanediol and adipic acid

In a 1 L four-necked round bottom flask, equipped with an overhead stirrer and thermocouple, oligomers (650.00 g, AV = 105 mg KOH g^{-1}) of 1,6-hexanediol (1.26 eq) and adipic acid (1.0 eq) and catalyst (5.5 mmol, 0.1 mol% relative to -OH groups) were heated to 170 °C while the stirring speed was slowly increased to 200 rpm. Water formed during polyesterification was collected in an empty Dean-Stark receiver. Samples for acid value determination were taken every 30 minutes.

Polyesterification of oligomers of 1,6-hexanediol and Pripol 1009

In a 1 L four-necked round bottom flask, equipped with an overhead stirrer and thermocouple, oligomers (589.94 g, AV = 60 mg KOH g^{-1}) of 1,6-hexanediol (1.47 eq) and Pripol 1009 (1.0 eq) and catalyst (2 mmol, 0.2 mol% relative to -OH groups) were heated to 170 °C while the stirring speed was slowly increased to 200 rpm. Water formed during polyesterification was collected in an empty Dean-Stark receiver. Samples for acid value determination were taken every 30 minutes.

Azeotropic polyesterification

Polyesterification of 1,6-hexanediol and adipic acid

In a 250 mL five-necked round bottom flask, equipped with an overhead stirrer, thermocouple and *in-situ* ATR-IR probe, 1,6-hexanediol (49.62 g, 0.42 mol), adipic acid (48.71, 0.33 mol) and xylene (80 mL) were heated to 140 °C or 150 °C while the stirring speed was slowly increased to 285 rpm. When the reaction mixture reached 130 °C, catalyst (2.1 mmol, 0.25 mol% relative to -OH groups) was slowly added and the ATR-IR measurement was started (5 minutes waiting time, 250 spectra averaged). Water formed during polyesterification was collected in a pre-filled (10 mL of xylene) Dean-Stark receiver.

Figure 4.5. (A) Reaction set-up for neat polyesterification. (B) Reaction set-up for azeotropic polyesterification and in-situ FTIR-ATR.

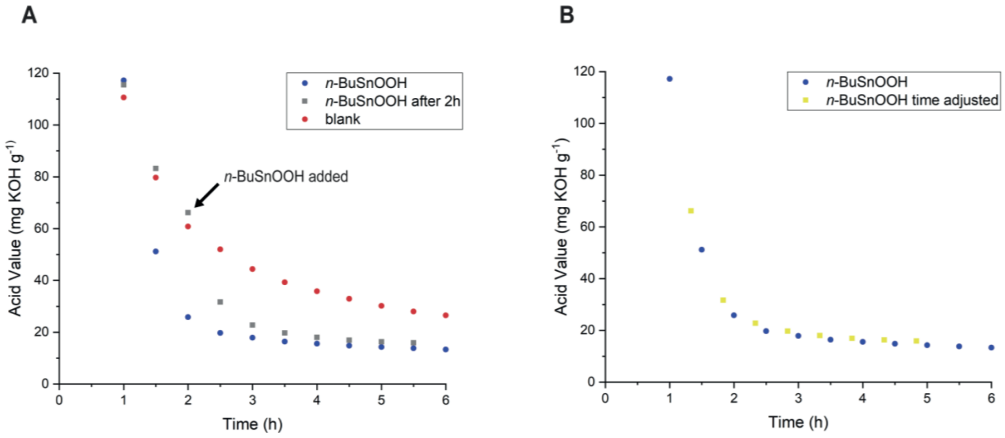

Figure 4.6. (A) Polyesterification of 1,6-hexanediol and adipic acid in the presence of 0.1 mol% *n*-BuSnOOH (on -OH groups) at 170 °C with *n*-BuSnOOH added after 1 h (blue trace) and 2 h (grey trace). (B) Time adjusted kinetic profile (yellow trace).

Table 4.1. Water concentrations of neat polyesterification reactions.

Entry[a]		H_2O concentration (ppm) Polyesterification of 1,6-hexanediol and adipic acid	H_2O concentration (ppm) Polyesterification of oligomers of 1,6-hexanediol and Pripol 1009
1	blank	15077	5320
2	$Ti(O^iPr)_4$	8378	4308
3	*n*-BuSnOOH	1527	-
4	Ti-atrane	5523	3870

[a] Water concentrations of the reaction mixture after 6 h reaction time.

Table 4.2. Water concentrations of azeotropic polyesterification reactions.

Entry[a]		H_2O concentration (ppm) Polyesterification of 1,6-hexanediol and adipic acid at 140 °C	H_2O concentration (ppm) Polyesterification of 1,6-hexanediol and adipic acid at 150 °C
1	blank	4669	1866
2	$Ti(O^iPr)_4$	4382	523
3	*n*-BuSnOOH	3772	514
4	Ti-atrane	2286; 2690[b]	158
5	$Zr(O^iPr)_4$-^{i}PrOH	-	293

[a] Water concentrations of the reaction mixture after 6 h reaction time. [b] Duplo experiment.

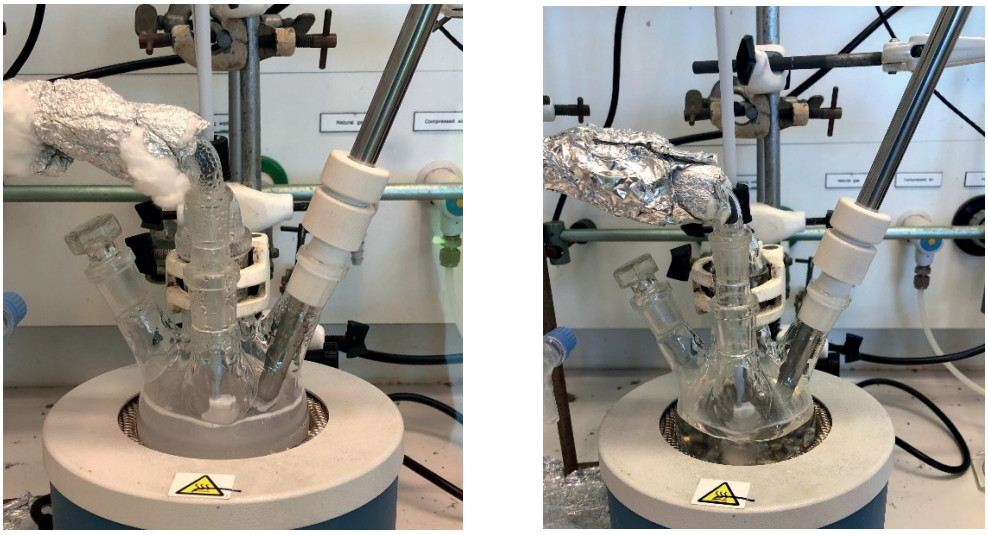

Figure 4.7. Polyesterification of 1,6-hexanediol and adipic acid in the presence of 0.25 mol% $Ti(O^iPr)_4$ (relative to -OH groups) at 140 °C (left) and 150 °C (right) with xylene after 2 h.

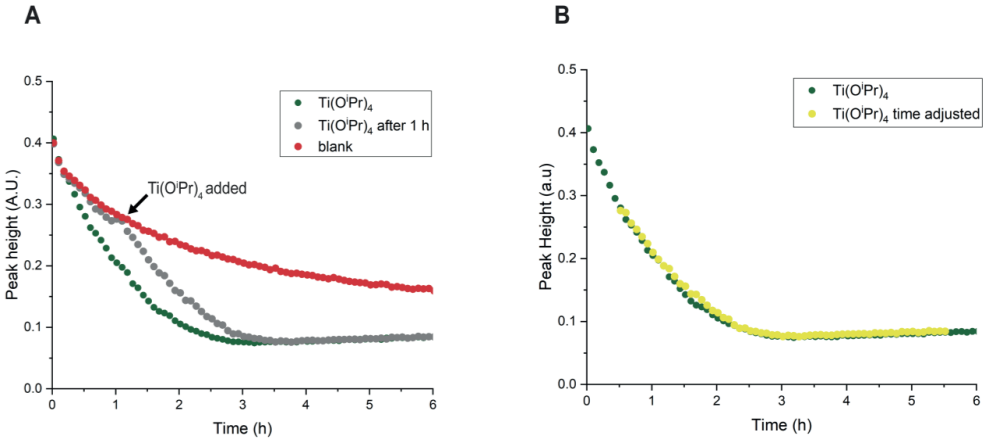

Figure 4.8. Kinetic profile of polyesterification of 1,6-hexanediol and adipic acid in the presence of 0.25 mol% $Ti(O^iPr)_4$ (relative to -OH groups) at 150 °C (green trace), $Ti(O^iPr)_4$ added after 1 h (grey trace) and black (red). (B) Time adjusted kinetic profile (yellow trace). (Peak height given is by peak height of $\nu_{c=o}$ vibration of the carboxylic acid (1712 cm^{-1})).

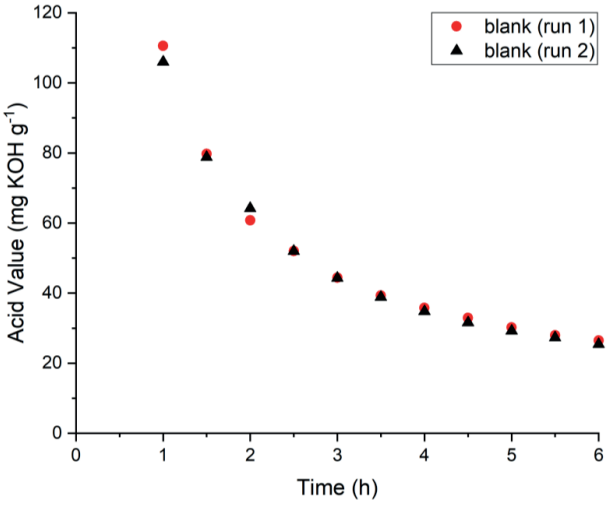

Figure 4.9. Reproducibility of polyesterification of reaction of 1,6-hexanediol and adipic acid of blank reaction (in the absence of a Lewis acidic metal catalyst) at 170 °C.

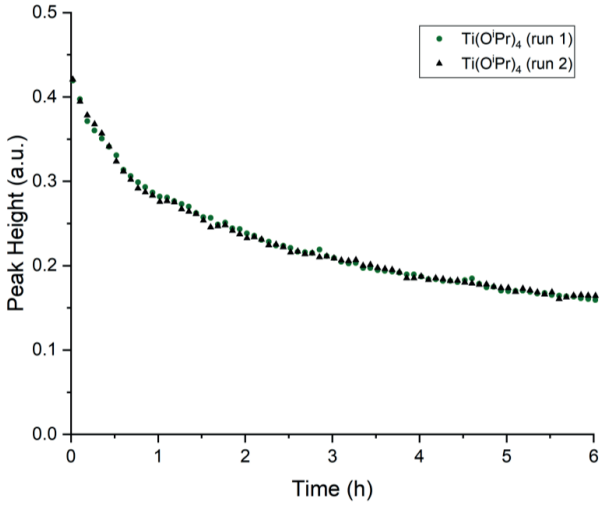

Figure 4.10. Reproducibility of polyesterification reaction of 1,6-hexanediol and adipic acid in the presence of 0.25 mol% $Ti(O^iPr)_4$ (relative to -OH groups) with xylene at 140 °C. Peak height at 1712 cm^{-1} ($\nu_{C=O}$ vibration of the carboxylic acid).

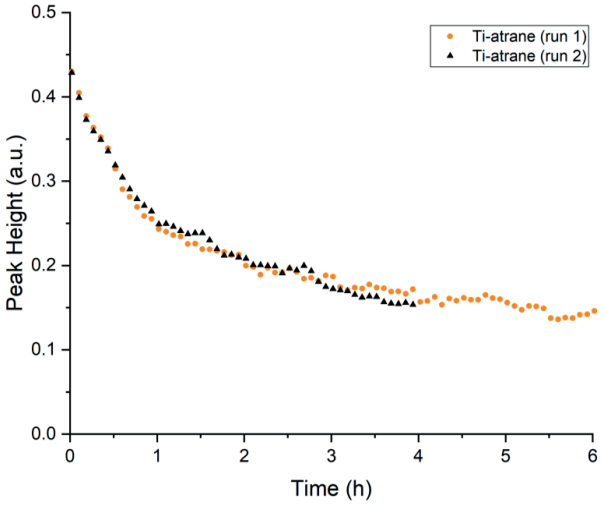

Figure 4.11. Reproducibility of polyesterification reaction of 1,6-hexanediol and adipic acid in the presence of 0.25 mol% Ti-atrane complex (relative to -OH groups) with xylene at 140 °C. Peak height at 1712 cm^{-1} ($\nu_{c=o}$ vibration of the carboxylic acid).

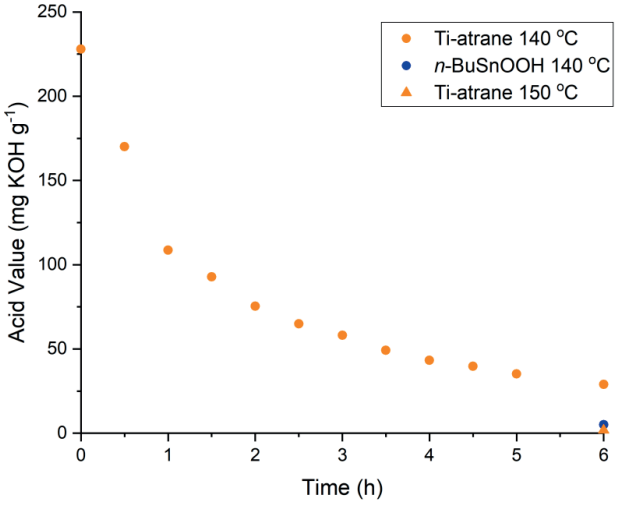

Figure 4.12. Acid Values of azeotropic polyesterification reactions of 1,6-hexanediol and adipic acid in the presence of 0.25 mol% catalyst (relative to -OH groups).

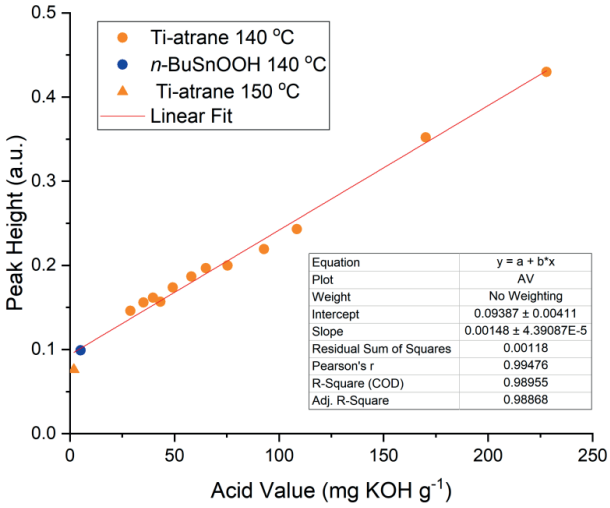

Figure 4.13. Correlation between peak height at 1712 cm^{-1} ($\nu_{c=o}$ vibration of the carboxylic acid) and Acid Value.

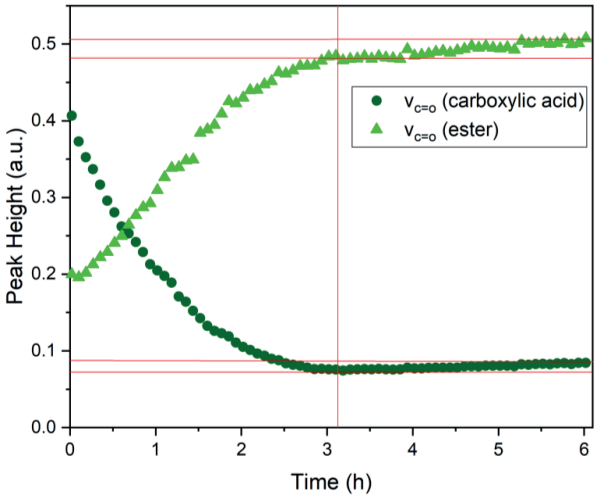

Figure 4.14. Peak height at 1712 cm^{-1} ($\nu_{c=o}$ vibration of the carboxylic acid) and peak height at 1736 cm^{-1} ($\nu_{c=o}$ vibration of the ester) of $TiO^{i}Pr_4$ catalyzed reactions at 150 °C.

The intensity (peak height) of the $\nu_{c=o}$ vibration of the carboxylic acid (at 1712 cm^{-1}) has a minimum at 3.12 hours. However, the increase in peak height, after this point in time is caused by an increase in the intensity of the 1736 cm^{-1} vibration ($\nu_{c=o}$ vibration of the ester) (see Figure 4.4A for the overlap between the $\nu_{c=o}$

vibration of the carboxylic acid and ester). Since this effect is rather small, we performed analysis on the peak height at 1712 cm^{-1} ($\nu_{C=O}$ vibration of the carboxylic acid) without peak deconvolution.

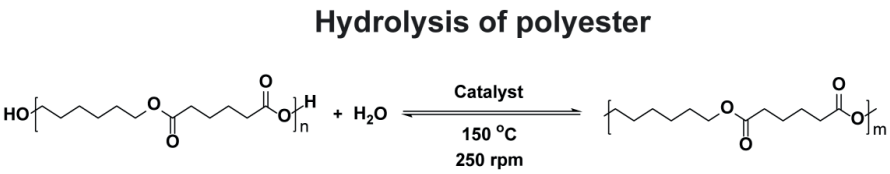

Table 4.3. Hydrolysis of polyester of 1,6-hexanediol and adipic acid.

Entry[a]		Acid Value[b] (mg KOH g^{-1})
1	blank	35.3
2	Ti-atrane	33.4
3	*n*-BuSnOOH	81.9

[a] Acid value of the reaction mixture at 0 h was 20.5 mg KOH g^{-1}. [b] Acid value of the reaction mixture after 2 h reaction time.

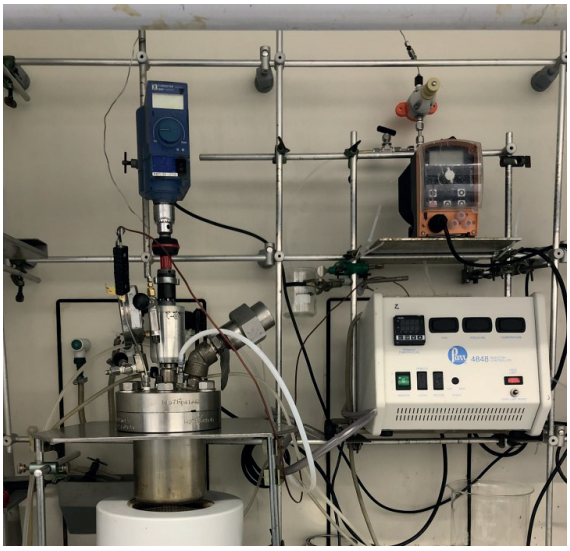

Figure 4.15. Reaction set-up for hydrolysis of polyester experiments.

References

1 H. Sardon, D. Mecerreyes, A. Basterretxea, L. Avérous and C. Jehanno, *ACS Sustain. Chem. Eng.*, 2021, **9**, 10664–10677.

2 O. Gómez-Jiménez-Aberasturi and J. R. Ochoa-Gómez, *J. Chem. Technol. Biotechnol.*, 2017, **92**, 705–711.

3 K. Lang, R. J. Sánchez-Leija, R. A. Gross and R. J. Linhardt, *Polymers (Basel).*, 2020, **12**, 1–25.

4 I. Hevus, N. G. Ricapito, S. Tymoshenko, S. N. Raja and D. C. Webster, *ACS Sustain. Chem. Eng.*, 2020, **8**, 5750–5762.

5 A. F. Sousa, C. Vilela, A. C. Fonseca, M. Matos, C. S. R. Freire, G. J. M. Gruter, J. F. J. Coelho and A. J. D. Silvestre, *Polym. Chem.*, 2015, **6**, 5961–5983.

6 Q. Zhang, M. Song, Y. Xu, W. Wang, Z. Wang and L. Zhang, *Prog. Polym. Sci.*, 2021, **120**, 101430.

7 J. Iglesias, I. Martínez-Salazar, P. Maireles-Torres, D. Martin Alonso, R. Mariscal and M. López Granados, *Chem. Soc. Rev.*, 2020, **49**, 5704–5771.

8 J. Otera, J. Nishikido, *Esterification. Methods, Reactions, and Applications*, Wiley-VCH Verlag GmbH & Co., Weinheim, 2nd edn., 2010.

9 K. Ishihara, *Tetrahedron*, 2009, **65**, 1085–1109.

10 U. K. Thiele, *Int. J. Polym. Mater.*, 2001, **50**, 387–394.

11 W. A. MacDonald, *Polym. Int.*, 2002, **51**, 923–930.

12 L. Papadopoulos, A. Zamboulis, N. Kasmi, M. Wahbi, C. Nannou, D. A. Lambropoulou, M. Kostoglou, G. Z. Papageorgiou and D. N. Bikiaris, *Green Chem.*, 2021, **23**, 2507–2524.

13 M. R. Meneghetti and S. M. P. Meneghetti, *Catal. Sci. Technol.*, 2015, **5**, 765–771.

14 V. G. Kessler, *The Synthesis and Solution Stability of Alkoxide Precursors. In: Klein L., Aparicio M., Jitianu A. (eds) Handbook of Sol-Gel Science and Technology.*, Springer, Cham., 2018.

15 U. Schubert, *J. Mater. Chem.*, 2005, **15**, 3701–3715.

16 U. Schubert, *Acc. Chem. Res.*, 2007, **40**, 730–737.

17 T. J. Boyle, R. P. Tyner, T. M. Alam, B. L. Scott, J. W. Ziller and B. G. Potter, *J. Am. Chem. Soc.*, 1999, **121**, 12104–12112.

18 V. Chandrasekhar, S. Nagendran and V. Baskar, *Coord. Chem. Rev.*, 2002, **235**, 1–52.

19 K. Ishihara, S. Ohara and H. Yamamoto, *Science*, 2000, **290**, 1140–1142.

20 K. Ishihara, M. Nakayama, S. Ohara and H. Yamamoto, *Tetrahedron*, 2002, **58**, 8179–8188.

21 *US Pat*., US20120316316, 2012.

22 W. M. P. B. Menge and J. G. Verkade, *Inorg. Chem.*, 1991, **30**, 4628–4631.

23 *US Pat*., US20100292449 A1, 2010.

24 *US Pat*., US19814260735, 1981.

25 L. A. Wolzak, J. I. van der Vlugt, K. J. van den Berg, J. N. H. Reek, M. Tromp and T. J. Korstanje, *ChemCatChem*, 2020, **12**, 5229–5235.

26 E. Leverd, F. Fradet, A. Maréchal, *Eur. Polym. J.*, 1987, **23**, 695–698.

27 E. Leverd, F. Fradet, A. Maréchal, *Eur. Polym. J.*, 1987, **23**, 699–704.

28 F. Leverd, A. Fradet and E. Maréchal, *Eur. Polym. J.*, 1987, **23**, 705–709.

29 D. G. Blackmond, *J. Am. Chem. Soc.*, 2015, **137**, 10852–10866.

30 N. Jacquel, F. Freyermouth, F. Fenouillot, A. A. Rousseau, J. Pascault, P. Fuertes and R. Saint-Loup, *J. Polymer Science Part A: Polymer Chemistry*, 2011, **49**, 5301-5312.

31 See Figure 4.14 for discussion on the peak height minimum of the $Ti(O^iPr)_4$-catalyzed reaction in Figure 4.4C and 4.4D.

32 A. Sakakura, S. Nakagawa and K. Ishihara, *Tetrahedron*, 2006, **62**, 422–433.

33 A. Sakakura, Y. Koshikari and K. Ishihara, *Tetrahedron Lett.*, 2008, **49**, 5017–5020.
34 A. Sakakura, H. Watanabe, S. Nakagawa and K. Ishihara, *Chem. - An Asian J.*, 2007, **2**, 477–483.
35 K. Ishihara, S. Nakagawa and A. Sakakura, *J. Am. Chem. Soc.*, 2005, **127**, 4168–4169.
36 A. Sakakura, S. Nakagawa and K. Ishihara, *Nat. Protoc.*, 2007, **2**, 1746–1751.
37 Y. Koshikari, A. Sakakura and K. Ishihara, *Org. Lett.*, 2012, **14**, 3194–3197.
38 A. Sakakura, Y. Koshikari, M. Akakura and K. Ishihara, *Org. Lett.*, 2012, **14**, 30–33.
39 L. A. Wolzak, J. J. Hermans, F. de Vries, K. J. van den Berg, J. N. H. Reek, M. Tromp and T. J. Korstanje, *Catal. Sci. Technol.*,
2021, **11**, 3326-3332.
40 L. A. Wolzak, J. J. Hermans, F. de Vries, K. J. van den Berg, J. N. H. Reek, M. Tromp and T. J. Korstanje, *Catal. Sci. Technol.*, 2021, **11**, 3326-3332.
41 *US Pat.*, US20120316316, 2012.

Chapter 5

Ligand-free Nickel-catalyzed Carboxylate *O*-arylation: Mechanistic insight in Ni^{I}/Ni^{III} cycles

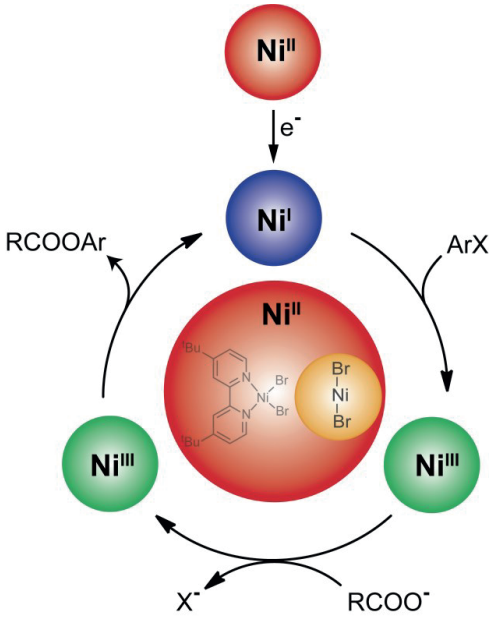

Abstract: Nickel-catalyzed cross-coupling reactions have become a powerful methodology to construct C–heteroatom bonds. However, many protocols suffer from competitive off-cycle reaction pathways and require non-equimolar amounts of coupling partners to suppress them. Here, we report on mechanistic examination of carboxylate *O*-arylation under thermal conditions, in both the presence and absence of an exogeneous bipyridine-ligand. Furthermore, spectroscopic studies of the novel ligand-free carboxylate *O*-arylation reaction unveiled the resting state of the nickel catalyst, the crucial role of the alkylamine base and the formation of a catalytically relevant Ni^{I}–Ni^{II} dimer upon reduction. This study provides insights into the competition between productive catalysis and deleterious pathways (comproportionation and protodehalogenation) that exist for all elementary steps in the commonly proposed self-sustained Ni^{I}/Ni^{III} catalytic cycle. Thereby we show that for productive nickel-catalyzed carboxylate *O*-arylation a choice must be made between either mild conditions or equimolar ratios of substrates.

This work is based on: L.A. Wolzak, F.J. de Zwart, J.H. Oudsen, S.A. Bartlett, B. de Bruin, J.N.H. Reek, M. Tromp, T.J. Korstanje. *Manuscript in preparation*.

Introduction

In recent years, nickel catalysis has enabled the formation of challenging C–heteroatom bonds, resulting in previously elusive cross-coupling reactions that can now be performed under mild conditions.[1–3] An example hereof is the coupling of carboxylic acids and aryl halides to form *O*-aryl esters enabled by (dtbbpy)NiX_2 under photochemical[4–8], electrochemical[9] or thermal reaction conditions[10] (Figure 5.1A). This cross-coupling reaction is notably demanding due to the low nucleophilicity of the carboxylate group. Although analogous *O*-aryl ester bond formation reactions catalyzed by palladium have been reported, these protocols are far from mild and efficient, and are relying on stoichiometric amounts of silver salts.[11,12] Mechanistically, nickel-catalyzed C–heteroatom bond formations under thermal conditions were proposed to proceed via a self-sustained Ni^{I}/Ni^{III} catalytic cycle.[10] In addition, the relevance of this catalytic mechanism was also demonstrated under photochemical[13–17] and electrochemical[14] reaction conditions.

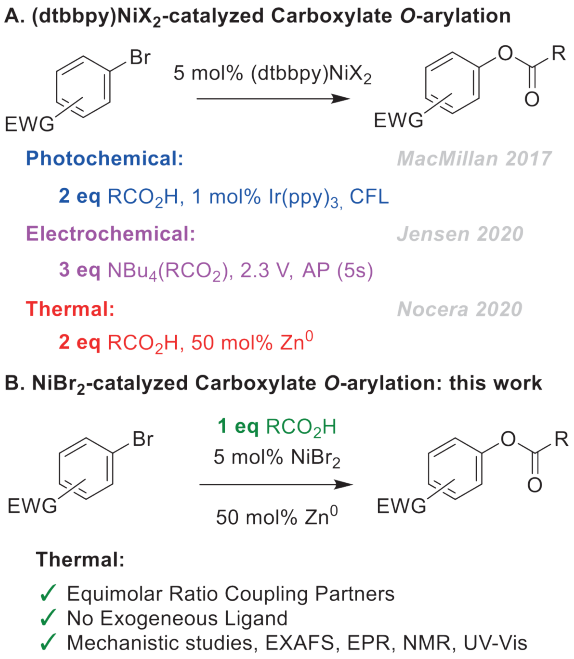

Figure 5.1. Nickel Catalyzed Cross-Coupling between aryl halides and carboxylic acids using: A) (dtbbpy)NiX_2 system or B) Ligand-Free system. (dtbbpy = 4,4'-di-tert-butyl-2,2'-bipyridine, AP = alternating polarity).

From these catalytic studies it became apparent that in order to successfully engage a self-sustained Ni^{I}/Ni^{III} catalytic cycle the continuous reduction of Ni^{II} to Ni^{I} is required, as Ni^{I} is prone to deactivation via an exergonic comproportionation reaction with Ni^{III} forming inactive Ni^{II}. Besides catalytic studies, another important approach to elucidate catalytic pathways has been provided by the synthesis, characterization and *in situ* generation of Ni^{I} complexes and the study of their reactivity. Investigations have unveiled that specific Ni^{I} complexes bearing a bipyridine (bpy) based ligand[14,18–20] are indeed able to activate aryl halides[14,19] and that the required Ni^{III} state can be accessed via oxidative addition of a Ni^{I} complex.[21,22] So far mechanistic insights through catalytic studies and stoichiometric reactions have demonstrated the validity of the elementary steps proposed in the self-sustained Ni^{I}/Ni^{III} catalytic cycle. However, they do not account for the non-equimolar ratios of substrates often required for productive C **–** heteroatom bond formations. Therefore, to further develop the field of nickel cross-coupling and enable more efficient reactions, a better understanding of the competition between productive fundamental elementary steps and off-cycle reaction pathways is required.

Here, we report on a detailed mechanistic study, where carboxylate *O*-arylation is performed under thermal and photocatalytic conditions in both the presence and absence of a dtbbpy-ligand and show ligand-free conditions (i.e. no exogeneous dtbbpy-ligand) enable an equimolar ratio of coupling partners (Figure 5.1B). In addition, the nickel complexes prior and after reduction have been studied with a variety of spectroscopic techniques, which show the first observation of a Ni^{I}–Ni^{II} dimer after reduction under ligand-free conditions. Moreover, a scope of coupling of carboxylic acids with aryl bromides is displayed using substoichiometric amounts of earth-abundant zinc as reductant and nickel(II) bromide as catalyst. Overall, we provide insight into self-sustained Ni^{I}/Ni^{III} catalytic cycles including deleterious off-cycle reaction pathways and show that for nickel-catalyzed carboxylate *O*-arylation a choice must be made between either mild conditions or equimolar ratios of substrates.

Results and discussion

Approach. Ligand-free protocols have been reported for nickel-catalyzed C**–**N cross-coupling reactions,[23,24] and therefore a similar approach to carboxylate *O*-arylation could be feasible. After initial optimization (Table 5.2–5.5) we arrived at optimal reaction conditions furnishing *O*-aryl ester, 4'-benzoyloxyacetophenone (**2**) in 81% yield without use of an exogeneous ligand (Table 5.1, entry 1). First, a hypothesis (Figure 5.2) on the mechanism of this reaction and the structure of nickel complexes relevant to it was developed through catalytic studies as described in the

following section, after which the proposed mechanism was corroborated through spectroscopic studies (Figure 5.3) in the last section.

Catalytic studies. To establish that ligand-free carboxylate *O*-arylation indeed operates via a self-sustained Ni^{I}/Ni^{III} catalytic cycle, dependency on photons was excluded (Table 5.1, entry 2). Furthermore, the bulk of nickel is proposed to remain in a dormant Ni^{II} oxidation state (precatalyst, Figure 5.2) which was supported experimentally by a dependency of the rate of product formation on the reduction by zinc (Figure 5.6).

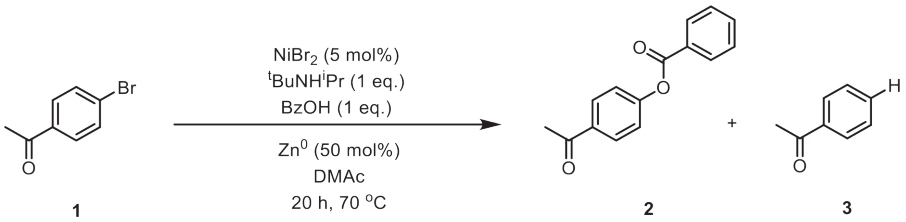

Table 5.1. Nickel-catalyzed carboxylate *O*-arylation.

Entry[a]	Change in condition	1[a] Conv. [%]	2[a] Yield [%]	3[a] Yield [%]
1	-	100	81	9
2	In dark	100	76	13
3	2 eq. BzOH + 2eq. ^{t}BuNH^{i}Pr	100	89	6
4	5 mol% dtbbpy	100	61	38
5	40 °C	15	12	2
6	$Ni(OBz)_2$	100	83	15
7	DMF as solvent	21	19	2
8	Bu_4NOBz as substrate	21	7	5
9	2 eq. ^{t}BuNH^{i}Pr	100	90	10

Conditions: Bromoacetophenone (200 mM) Benzoic Acid (200 mM), ^{t}BuNH^{i}Pr (200 mM) Nickel(II)bromide (5 mol%), Zinc (50 mol%), DMAc (6 mL), 20 hours, 70 °C. [a] Determined by GC analysis.

To indicate oxidative addition as an elementary step in the mechanism a strong rate dependency on the electronic parameter of the aryl bromides (Hammett Plot, Figure 5.7) was found, similar to (dtbbpy)$NiBr_2$-catalyzed reactions. Interestingly, increasing the equivalents of BzOH and ^{t}BuNH^{i}Pr only gave a slight increase in the yield for ester **2** to 89% (Table 5.1, entry 3), in fair contrast to (dtbbpy)$NiBr_2$-catalyzed reactions which require non-equimolar ratios of carboxylic acid, base and aryl halide.[4,5,7,8,10,25–27] Addition of dtbbpy-ligand under optimized conditions showed a declined yield of ester **2** and an increased yield in acetophenone (**3**) as byproduct

(Table 5.1, entry 4). Therefore, it is proposed that the addition of ligand slows down ligand exchange as elementary step causing the formation of protodehalogenated side product **3** (Figure 5.2, LE $k_{dtbbpy} < k_{LF}$). Nickel catalyzed carboxylate *O*-arylation using dtbbpy as ligand operate at mild temperatures (25–40 °C), but for the ligand-free reaction lowering the temperature to 40 °C had a detrimental effect on the formation of ester **2** (Table 5.1, entry 5), presumably due to the slower oxidative addition at a less electron-rich nickel center (Figure 5.2, OA: $k_{dtbbpy} > k_{LF}$). Further attempts to enable equimolar substrate ratios using the (dtbbpy)$NiBr_2$ system by changing the ligand (Table 5.6) or conditions (Table 5.9) were unproductive and lead us to pursue investigation of the ligand-free system. To gain structural insight into the complexes relevant to catalysis, the precursor was exchanged for nickel(II) benzoate, resulting in a comparable yield for ester product **2** (Table 5.1, entry 6), indicating that at least for the initial reduction and oxidative addition a bromide ligand is not essential. Moreover, when DMAc (*N,N*-dimethylacetamide) as solvent is exchanged for DMF (*N,N*-dimethylformamide), greatly diminished yields are obtained (Table 5.1, entry 7). Due to the slight increase in steric bulk of DMAc, nickel halide systems in this solvent are significantly more dynamic than in DMF.[28] Furthermore, the pivotal role of an aliphatic alkylamine base in catalysis, especially $^{t}BuNH^{i}Pr$, was demonstrated by the use of other nitrogen-containing bases, which all provide inferior results with yields under 10% (Table 5.3, entries 4-6).

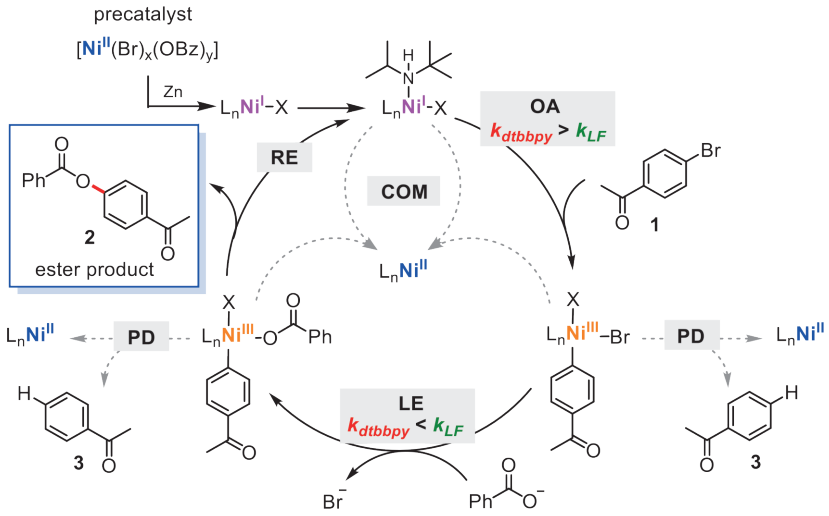

Figure 5.2. Mechanistic hypothesis of productive catalysis, protodehalogenation (side product formation) and comproportionation. OA, oxidative addition; LE, ligand exchange; RE, reductive elimination; PD, protodehalogenation; COM, comproportionation; *k*, rate; dtbbpy, 4,4'-di-tert-butyl-2,2'-bipyridine; LF, ligand-free.

Likewise, the use of tetrabutylammonium benzoate (Bu_4NOBz), rather than $^tBuNH^iPr$ and benzoic acid, gave only 7 % yield for ester **2** (Table 5.1, entry 8). This result varies from (dtbbpy)$NiBr_2$-catalyzed reaction, with zinc as reducing agent, which does tolerate this substrate.[10] Adding an additional equivalent of $^tBuNH^iPr$ increased the yield of ester **2** to 90% (Table 5.1, entry 9).

These results clearly indicate a more elaborate role for $^tBuNH^iPr$ than solely functioning as a Brønsted base, and therefore the catalytically active complex is proposed to be of the form $[(^tBuNH^iPr)Ni^I(L)_n]$ (Figure 5.2, where L = Br^-, BzO^-, DMAc). Summarizing the catalytic experiments, we propose that in absence of the dtbbpy-ligand, protodehalogenation and deleterious comproportionation reactions are prevented because of facile ligand exchange and reductive elimination steps (Figure 2). This enables the formation of *O*-aryl esters from equimolar amounts of coupling partners. In contrast, for the (dtbbpy)$NiBr_2$-catalyzed reaction an excess of carboxylate substrate is required to enhance the rate of ligand exchange and prevent unproductive comproportionation of Ni^I and Ni^{III}. However, for this reaction the rate of oxidative addition is expected to be higher due to the electron-donating effect of the dtbbpy ligand, and hence catalysis can be performed at a lower reaction temperature (Table 5.9).[10] Therefore, the ligand-free system shows diminished activity at 40 °C (Table 5.1, entry 2) whereas the (dtbbpy)$NiBr_2$-catalyzed reaction is less effective at elevated temperatures.

Spectroscopic investigation. To elucidate the nature of the Ni^{II} precatalyst and catalytic intermediates under ligand-free conditions we performed spectroscopic studies. UV-Vis spectra of the catalytic reaction mixture (Figure 5.3A, orange trace) and a DMAc solution containing $NiBr_2$, $^tBuNH^iPr$ and BzOH (Figure 5.3A, green trace) proved to be identical, disclosing a Ni^{II} resting state. Additionally, a DMAc solution containing $NiBr_2$ and tetrabutylammonium benzoate (Bu_4NOBz) also gave a fairly similar UV-Vis spectrum (Figure 5.3A, purple trace), indicating the amine base does not coordinate to nickel. That the amine base primarily exists in the protonated, and the benzoic acid in the deprotonated form was further demonstrated via ^1H and ^{13}C NMR studies using ^{13}C-labeled benzoic acid (Figure 5.18, 5.19 and Figure 5.4B). Comparison of the chemical shifts of BzOH-α-^{13}C (167.0 ppm), BzO^--α-^{13}C (168.9 ppm) and a mixture of $NiBr_2$, $^tBuNH^iPr$ and BzOH in DMAc (~169.2 ppm) indicates that during catalysis the nucleophile is present as benzoate (Figure 5.3B; I, III and IV). The line broadening of the signal at ~169.2 ppm can be explained by the benzoate molecule being in close proximity to the paramagnetic Ni^{II} center and/or exchange between free and coordinated benzoate (Figure 5.3B; IV). Additionally, the chemical shift of the DMAc-α-C provides information about the role of DMAc as a ligand.

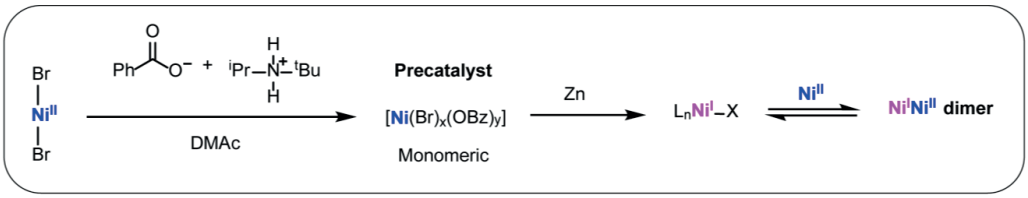

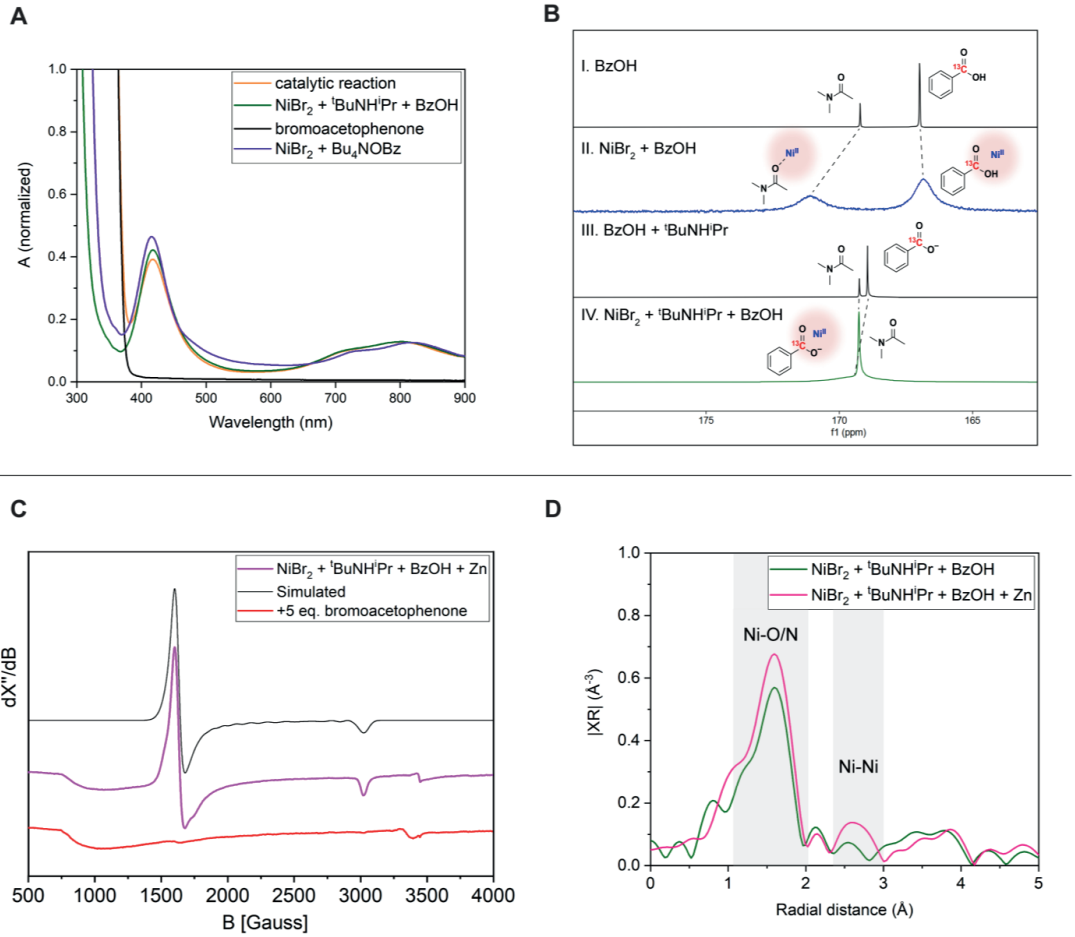

Figure 5.3. Spectroscopic investigations on the nickel system. [A] UV-Vis spectra in DMAc, catalytic reaction after 2h (at 9% yield of 2). [B] ^{13}C NMR spectra in DMAc. [C] X-Band EPR spectra at 10K. [D] Ni K-edge k^2-weighted Fourier transform EXAFS spectrum of frozen DMAc solution.

While coordination of DMAc was observed for solely $NiBr_2$ (~171 ppm) in DMAc, DMAc serves a minor role as a ligand (169.2 ppm) for the mixture containing all components (Figure 5.3B; II and IV). For further structural characterization we turned to X-ray absorption spectroscopy (XAS), since Ni K-edge XAS has shown to be a valuable spectroscopic tool for the elucidation of the local structure including geometry of molecular coordination complexes as well as their electronic structures.[29–31] For a DMAc solution containing $NiBr_2$, ^{t}BuNH^{i}Pr and BzOH the X-ray absorption near edge structure spectrum (XANES) (Figure 5.22) reveals a distinct pre-edge peak at 8333 eV which can be assigned to a 1s → 3d electronic transition, while the 1s → $4p_z$ electronic transition (expected at 8337 eV) is absent thereby excluding the formation of complexes lacking one or more axial ligands (square planar and square pyramidal geometries).[32] More structural parameters were determined by Extended X-ray absorption fine structure (EXAFS) analysis, with figure 5.3D providing the Fourier Transform (FT) EXAFS function. The absence of any remote nickel shell, as observed for a DMAc solution containing only $NiBr_2$ and ^{t}BuNH^{i}Pr (Figure 5.25), is indicative for monomeric nickel complexes present in solution with 1.9(1) Ni–O/Ni–N at 2.08(2) Å (Figure 5.3D, green trace, for details see S.I.). However, solely based on nickel K-edge EXAFS data an exact coordination number of the bromide shell cannot be determined reliably due to the almost complete anti-phase behavior of different Ni–Br contributions, when present at slightly different distances (Figure 5.26 – 5.28).[33] This means that these EXAFS data suggest that either no Ni–Br contributions are present, or that an even number of Ni–Br contributions (at different distances) are present. In order to provide more detail hereon, follow-up studies could include additional bromine K-edge XAS measurements.[31,34] To summarize, ^{t}BuNH^{i}Pr was found to be essential in catalytic experiments, while our spectroscopic investigations indicate that the Brønsted base primarily exists in the protonated form (^{t}BuNH$_2^i$Pr$^+$). We therefore propose that the bulk of the nickel that forms the precatalyst is present as a mixture of monomeric complexes of the type $[Ni(Br)_x(OBz)_y]$.

More insight into the reduction of the formed Ni^{II} species was obtained stirring a Ni^{II}-precursor solution (a DMAc solution containing $NiBr_2$, ^{t}BuNH^{i}Pr and BzOH) in the presence of excess zinc.[35] The *in situ* reduced Ni^{II}-precursor solution was studied by UV-Vis, EPR and XAS spectroscopy. In the UV-Vis spectrum a new band at 541 nm is observed, as well as a shoulder at ~415 nm originating from non-reduced Ni^{II} (Figure 5.17, pink trace). EPR spectroscopy on this solution provided a spectrum with a characteristic S = $3/2$ signal (Figure 5.3C, pink trace, for simulation details see Figure 5.20). Based on Ni K-edge XANES data the formation of complexes deprived of axial ligands (square pyramidal or square planar geometries) can be excluded (Figure 5.22). EXAFS analysis indicates an increase in the Ni–O/Ni–N shell (3.1(3)) at a bond distance of 2.04(1) Å and, more importantly, the emergence of a Ni–Ni shell at 3.10(3) Å with a coordination number

of 0.6(5) (Figure 5.3D, pink trace, for details see SI). Overall, it can be rationalized that Ni^{II} is reduced by zinc to Ni^{I} which subsequently forms a bimetallic nickel intermediate. The trapping of formed Ni^{I} by excess Ni^{II} in solution leading to a Ni^{I}–Ni^{II} dimer was also reported by Nocera and co-workers in the nickel-catalyzed aryl etherification by (dtbbpy)$NiCl_2$ in the presence of quinuclidine and a photocatalyst or zinc.[14] Dimeric nickel complexes have been identified before as important intermediates in nickel-catalyzed cross-coupling, but this represents the first observation of a Ni^{I}–Ni^{II} dimer under ligand-free conditions.[14,20,21]

Next, the reactivity of the *in situ* formed Ni^{I}–Ni^{II} dimer was examined. Therefore we treated the pink-colored nickel solution, obtained after reduction, with 5 equiv. of 4'-bromoacetophenone and heated to 70 °C which resulted in a yellow-colored reaction mixture after 30 min (no color change was observed at R.T.). UV-Vis and EPR spectroscopy revealed the complete disappearance of the UV-Vis band at 541 nm (Figure 5.17, red trace) and the S = 3/2 signal in the EPR spectrum (Figure 5.3C, red trace). The catalytic relevance of the Ni^{I}–Ni^{II} dimer was further evaluated in an experiment, where $NiBr_2$ in the presence of $^{t}BuNH^{i}Pr$ and BzOH, was first reduced with zinc for 3 hours (see Figure 5.16 for UV-Vis spectrum). Next, this solution was filtered, to remove zinc, and 20 equiv. of bromoacetophenone were supplied and the mixture was stirred at 70 °C for 30 min. Subsequent GC analysis revealed minor formation of *O*-aryl ester **2** (yield <2%). Diminishing the reduction time to 30 min. (see Figure 5.16 for UV-Vis spectrum), resulted in no ester product **2** formation. Moreover, this experiment was repeated but now besides bromoacetophenone also another 0.5 equiv. of zinc was added after filtration. After 20 hours reaction time at 70 °C ester product **2** was obtained in 80% yield. These results are notable since it contrasts with other studies into nickel-catalyzed C-heteroatom bond formations, where: 1) dimeric nickel complexes proved to be unreactive towards aryl halides[19,20] or 2) high concentrations of low-valent nickel had a detrimental effect due to the facile formation of inactive states such as nickel black, Ni^{II} or Ni^{I}–Ni^{I} dimers.[14,24] This is also highlighted by the numerous literature reports on successful marriages between photocatalysis and nickel catalysis, as photocatalytic reduction of nickel ensures a low absolute concentration of Ni^{I}, suppressing deleterious pathways.

To demonstrate the applicability of the developed protocol for ligand-free nickel-catalyzed ester bond formation with equimolar amounts of aryl halide, carboxylic acid and base we examined the scope of this reaction (Figure 5.4). Changing the aryl bromide from **1** (81%) to 4'-iodoacetophenone **5** gave the corresponding ester product **2** in a good yield (87%). Even when using aryl chloride **6**, catalytic product formation was observed albeit with lowered yields (21%). Aryl halides lacking sufficient electron-withdrawing groups show low reactivity (**8, 9, 10**) presumably because of a slow rate for oxidative addition. A variety of electron-poor aryl bromides were found to be effective coupling partners (**11-15**). For the carboxylic acid coupling

partner, sterically hindered pivalic acid and cyclohexanecarboxylic acid (**16, 17**) furnished the corresponding ester efficiently, as well as various aromatic carboxylic acids (**19-21**). Only acetic acid hampered catalysis and afforded the ester product (**18**) in poor yield (<10%).

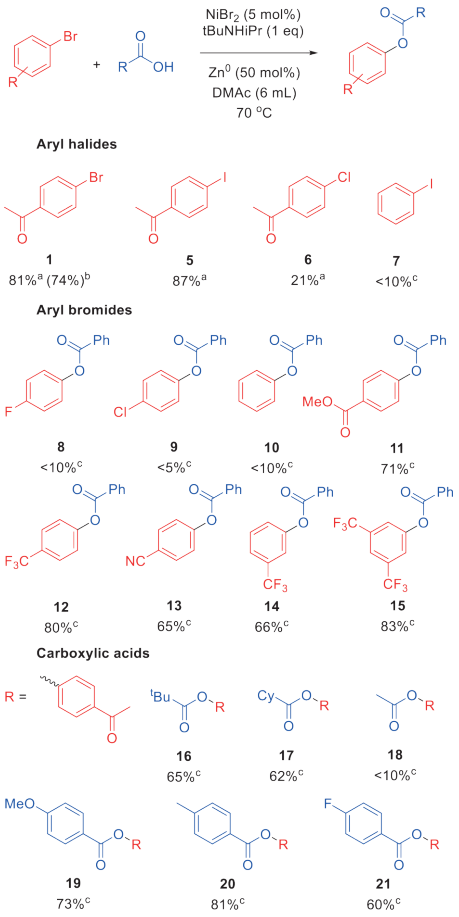

Figure 5.4. Substrate scope of $NiBr_2$-catalyzed esterification of carboxylic acids and aryl bromides. [a] Yield determined by GC with mesitylene as internal standard after 20 hours reaction time. [b] Isolated yield. [c] Yield determined by ^1H NMR with 1,3,5-Tri-tert-butylbenzene as internal standard after 24 hours reaction time.

To provide an opening for future studies into photocatalyzed nickel carboxylate *O*-arylation, we investigated the herein developed ligand-free system under photocatalytic conditions. Zinc was replaced by the competent photocatalyst ($Ir(ppy)_3$) which only furnished ester product **2** in

moderate yields, also for a reaction with excess BzOH and $^{t}BuNH^{i}Pr$ (Table 5.7, entries 1 and 2) which is in contrast to the (dtbbpy)$NiBr_2$-catalyzed reaction (Table 5.7, entry 3).[4] Previous studies showed that in ligand-based systems, (dtbbpy)$NiBr_2$ directly quenches the excited photocatalyst and that $^{t}BuNH^{i}Pr$ has no function in the photocatalysis.[36,37] Moreover, in ligand-free C–N cross-coupling 1,4-diazabicyclo[2.2.2]octane (DABCO) is employed as a base and serves also as a quenching agent for the excited Ir^{III}* photocatalyst, being oxidized to generate Ir^{II} which consecutively reduces Ni^{II}.[17] However, for ligand-free carboxylate *O*-arylation the addition of DABCO diminished the formation of ester product **2** (Table 5.7, entry 4). The incompatibility of DABCO with ligand-free conditions was also displayed in a reaction with zinc as reducing agent, which resulted in no formation of ester product **2** (Table 5.7, entry 5). This is presumably caused by coordination of DABCO inhibiting catalysis, similar to inhibition we observed by addition of COD as poison (Table 5.8, entry 6). Furthermore, photoinitiation with visible light (405 nm) afforded ester **2** only in moderate yields (Table 5.7, entries 6 and 7). These results show that it could be possible to enable equimolar photocatalytic ligand-free nickel-catalyzed carboxylate *O*-arylation, if a compatible quencher which preferably also serves as the base is found.

Conclusions

In summary, the presented mechanistic studies of nickel-catalyzed carboxylate *O*-arylation have uncovered the competition between productive catalysis and off-cycle pathways (comproportionation and protodehalogenation) that exists for all fundamental elementary steps. In the absence of an exogenous dtbbpy-ligand these deleterious reactions where significantly suppressed allowing equimolar amounts of coupling partners. Spectroscopic investigation of the novel ligand-free catalytic system revealed that during catalysis the bulk of Ni^{II} is present in the form of $[Ni(Br)_x(OBz)_y]$, yet for catalysis an alkylamine base was essential. Studies into the reduction of the Ni^{II}-precursor identified a bimetallic pathway resulting in a catalytically relevant Ni^{I}-Ni^{II} dimer under ligand-free conditions. The presented insights into the reaction pathways of the commonly proposed self-sustained Ni^{I}/Ni^{III} catalytic cycle and the *in situ* formed nickel complexes offer valuable knowledge that will be relevant for the design of novel nickel-catalyzed C-heteroatom bond formations under mild conditions.

Experimental Section

General Experimental Details

Chemicals were obtained from Fluorochem or Merck and used without further purification, unless noted otherwise. Anhydrous *N,N*-Dimethylacetamide 99 % (abbreviated DMAc) was degassed by bubbling argon through for > 60 min, and dried over 4Å molecular sieves. All air-sensitive materials were manipulated using standard Schlenk techniques (under argon) or by the use of a nitrogen-filled glovebox (MBraun Unilab). $Ni(OBz)_2 \cdot 3H_2O$ (abbreviated $NiOBz_2$) was synthesized and zinc was activated following literature procedures.[38,39] $NiBr_2$·2-methoxyethylether (abbreviated $NiBr_2$), tetrabutylammoniumbenzoate (Bu_4NOBz) and activated zinc were stored and weighed in a nitrogen-filled glovebox. The NMR solvent C_6D_6 was dried over molecular sieves and degassed via three freeze-pump-thaw cycles. ^1H (500 or 400 MHz) and ^{13}C (125 or 100 MHz) spectra were recorded on a Bruker DRX 500 MHz or a Bruker AVANCE 400 MHz spectrometer and referenced against residual solvent signal. UV-Vis spectra were collected on a double beam Shimadzu UV-2600 spectrometer in a 1.0 cm quartz cuvette with DMAc as reference. GC analysis was performed on a Thermo Scientific Trace GC Ultra equipped with a Rxi-5ms fused silica column (30.0 m x 0.25 mm x 0.25 µm). Temperature program: initial temperature 50 °C, heat to 200 °C with 8.0 °C min^{-1}, heat to 250 °C with 50 °C min^{-1}, hold for 6 minutes. Inlet temperature 250 °C, split ratio of 30, 1.0 mL min^{-1} helium flow, FID temperature 250 °C. For GC measurements mesitylene was used as internal standard and GC calibration curves were composed for 4-'bromoacetophenone (**1**), acetophenone (**3**), 4'-benzoyloxyacetophenone (**2**) and 4'-hydroxyacetophenone (**4**) (Figure 5.38). GC-HRMS (HRMS) measurements were performed on a Jeol AccuTOF GC v 4g, JMS-T100GCV Mass spectrometer equipped with a field desorption (FD) / field ionization (FI) probe, fitted with a 10 µm tungsten FI emitter. Samples were diluted with acetone and mesitylene was used as an internal calibrant. Here, GC analysis was conducted on a Thermo Scientific Trace GC Ultra equipped with an Agilent 19091S-433 column (30.0 m x 0.25 mm x 0.25 µm). Temperature program: initial temperature 50 °C, heat to 315 °C with 15 °C min^{-1}, hold for 5 min. Inlet temperature 230 °C, split ratio of 15:1, 1.0 mL min^{-1} helium flow and GC interface at 250 °C. For the field ionization (FI) a flashing current of 40 mA on every spectrum of 30 ms was applied. EPR measurements were performed in air-tight J.Young quartz tubes in an atmosphere of purified argon. Frozen solution EPR spectra were recorded on a Bruker EMX-plus CW X-band spectrometer equipped with a Bruker ER 4112HV-CF100 helium cryostat. The spectra were obtained on freshly prepared solutions of nickel compounds and simulated using EasySpin[40] via the cwEPR GUI.[41]

General experiment for catalysis

In a nitrogen-filled glovebox, $NiBr_2$ (21.2 mg, 0.06 mmol) and zinc (39.2 mg, 0.6 mmol) were weighed and transferred to a Schlenk flask (20 mL). The flask was removed from the glovebox, the atmosphere changed to argon, and the solids 4-bromoacetophenone (239 mg, 1.2 mmol) and benzoic acid (147 mg, 1.2 mmol) were added. Directly thereafter, DMAc (6 mL) and $^tBuNH^iPr$ (190 µL, 1.2 mmol) were supplied via a syringe and the temperature was increased to 70 °C with stirring at 1400 rpm. After 20 h reaction time, 60 µL mesitylene (internal standard) was added and approximately 10 µL of the reaction mixture was diluted with 2 mL acetone, filtered over a 45 µm syringe filter and analyzed with GC.

General experiment for substrate scope

In a nitrogen-filled glovebox, $NiBr_2$ (21.2 mg, 0.06 mmol) and zinc (39 mg, 0.6 mmol) were weighed and transferred to a Schlenk flask (20 mL). The flask was removed from the glovebox, the atmosphere changed to argon, and the arylhalide (1.2 mmol) and carboxylic acid (1.2 mmol) were added. Directly thereafter, via a syringe DMAc (6 mL) and $^{t}BuNH^{i}Pr$ (190 µL, 1.2 mmol) were supplied and the temperature was increased to 70 °C and stirring speed to 1400 rpm. After 24 h reaction time 1,3,5-Tri-tert-butylbenzene (24.6 mg, 0.1 mmol) was added as internal standard and the reaction was quenched with 5 mL of aqueous LiCl solution (50 % saturated aqueous LiCl, 50 % water). This solution was extracted three times with 10 mL EtOAc. The combined organic phases were dried over Na_2SO_4 and concentrated. Approximately 20 µL of the concentrated reaction mixture was used to determine yield by ^{1}H NMR in $CDCl_3$ (in cases of inhomogeneous ^{1}H NMR samples, 1 mL of DMAc was added to the concentrated reaction mixture). In addition, 10 µL of the ^{1}H NMR sample was taken and diluted with 1.5 mL acetone for GC-HRMS analysis.

Reduction of Ni^{II}

Spectroscopy

Experiment A. In a nitrogen-filled glovebox, $NiBr_2$ (10.6 mg, 0.03 mmol) and zinc (118 mg, 1.80 mmol) were weighed and transferred to a J. Young type Schlenk flask (10 mL). The flask was removed from the glovebox, the atmosphere changed to argon and benzoic (73 mg, 0.6 mmol) was added. Directly thereafter, $^{t}BuNH^{i}Pr$ (95 µL, 0.6 mmol) and 3 mL DMAc were supplied via a syringe. This suspension was vigorously stirred (1400 rpm) at 70 °C for 3 hours to obtain a pink colored solution. The flask was transferred back to the glovebox and zinc was removed via filtration over a 45 µm syringe filter providing samples for UV-Vis, EPR and XAS spectroscopy (Attempts to remove Zn via filtration outside the glovebox all resulted in rapid discoloration).

Experiment B. To study the reactivity, towards aryl halides, of reduced Ni^{II} (described in the experiment above) we supplied bromoacetophenone (29.9 mg, 0.15 mmol) to 3 mL of the pink-colored solution (after filtration) and stirred this for 15 minutes in a glovebox (no color change was observed). Subsequently, the vial was taken outside the glovebox and heated to 70 °C. Over a period of 30 minutes the pink color disappeared and a yellow-colored solution was obtained. Subsequently, samples for UV-Vis and EPR spectroscopy were prepared.

Catalysis

Experiment A: The reduction experiment (A) described above was repeated twice with a reduction time of 30 min. and 3 hours (on a 6 mL scale). Next, in a nitrogen-filled glovebox the obtained solution was filtered over a 45 µm syringe filter and 3 mL was transferred to a 10 mL vial charged with bromoacetophenone (119.5 mg, 0.6 mmol). Outside the glovebox this reaction mixture was stirred for 30 min at 70 °C. Subsequently 30 µL mesitylene (internal standard) was added and approximately 10 µL of the reaction mixture was diluted with 2 mL acetone, filtered over a 45 µm syringe filter and analyzed with GC.

Experiment B: The reduction experiment (A) described above was repeated with a reduction time of 3 hours (on a 6 mL scale). Next, in a nitrogen-filled glovebox the obtained solution was filtered over a 45 µm syringe filter and 3 mL was transferred to a Schlenk flask (20 mL) charged with bromoacetophenone (119.5 mg, 0.6 mmol) and zinc (19.5 mg, 0.3 mmol). Outside the glovebox this reaction mixture was stirred for 20 h at 70 °C. Subsequently 30 µL mesitylene (internal standard) was added and approximately 10 µL of the reaction mixture was diluted with 2 mL acetone, filtered over a 45 µm syringe filter and analyzed with GC.

Catalytic studies

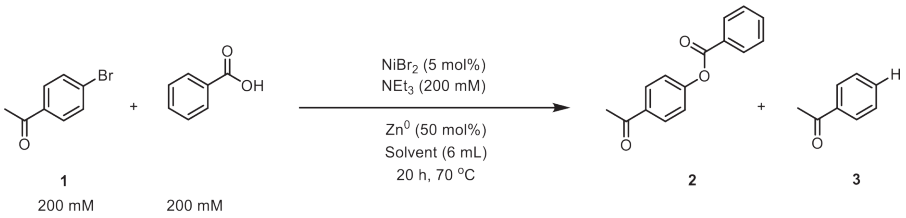

1 (200 mM) + 200 mM → 2 + 3

Table 5.2. Solvent screening

Entry[a]	Solvent	1[a]	2[a]	3[a]
		Conv. [%]	Yield [%]	Yield [%]
1	DMAc	87	68	19
2	DMSO	17	0	2
3	DMF	21	19	2
4	DMI	27	23	4

[a] Determined by GC analysis.

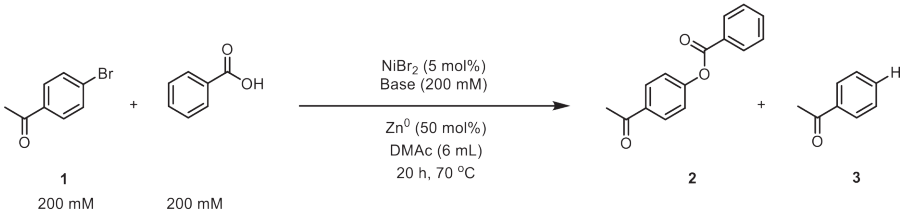

1 (200 mM) + 200 mM → 2 + 3

Table 5.3. Base screening

Entry[a]	Base	1[a]	2[a]	3[a]
		Conv. [%]	Yield [%]	Yield [%]
1	^{t}BuNH^{i}Pr	100	81	9
2	^{t}BuNH^{i}Pr (400 mM)	100	90	10
3	NEt_3	87	68	19
4	DBU	8	n.d.	5
5	DABCO	6	<1	5

6	DMAP	23	10	11
7	K_3PO_4	21	17	4
8	K_3PO_4 + Bu_4NI (200 mM)	16	5	11
9	Bu_4NOBz	21	7	5
10	Bu_4NOBz + $^{t}BuNH^{i}Pr$ (20 mM)	60	27	16

[a] Determined by GC analysis.

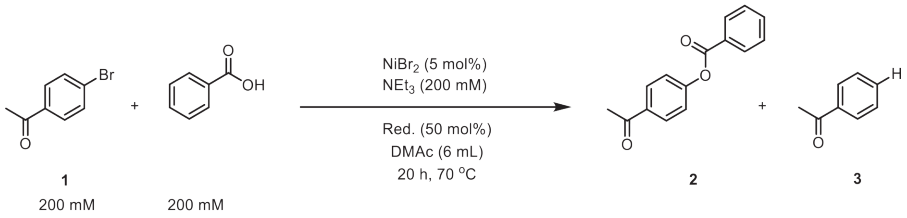

Table 5.4. Reducing agent screening

Entry[a]	**Reducing agent**	**1[a]**	**2[a]**	**3[a]**
		Conv. [%]	**Yield [%]**	**Yield [%]**
1	Zn	87	68	19
2	Mn	42	23	16
3	Mn + Et_4NI (0.5 eq)	64	49	15
4	$CoCp_2$	13	n.d.	12
5	$CoCp^*_2$	9	n.d.	9

[a] Determined by GC analysis.

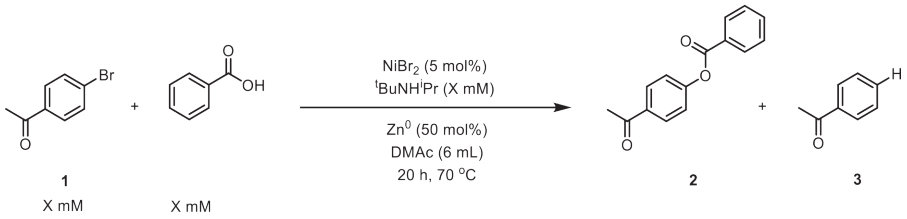

Table 5.5. Concentration screening

Entry[a]	**Conc. [mM]**	**1[a]**	**2[a]**	**3[a]**
		Conv. [%]	**Yield [%]**	**Yield [%]**
1	50	67	53	n.d.
2	100	60	47	2
3	200	100	81	9
4	500	100	72	15
5	1200	100	40	10

[a] Determined by GC analysis.

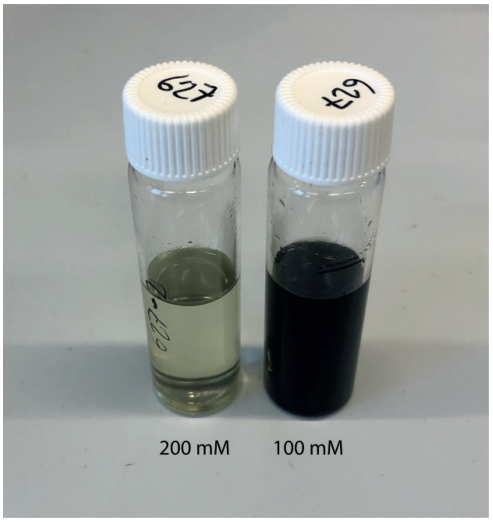

Figure 5.5. Reaction mixtures after 20 h reaction time at a concentration of 200 and 100 and mM. Concentrations below 200 mM resulted in the reaction mixture turning black, indicative for nanoparticle formation.

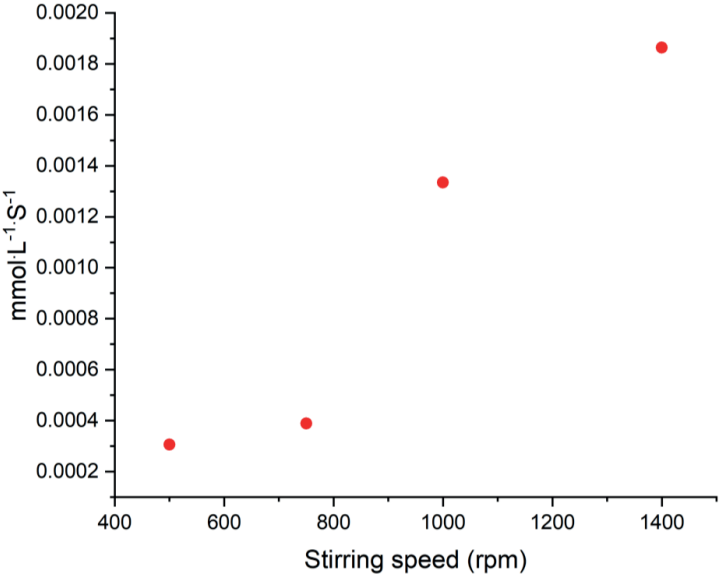

Figure 5.6. Rate dependency of rate on stirring speed for $NiBr_2$-catalyzed reaction (initial rate was determined after 2 hours reaction time).

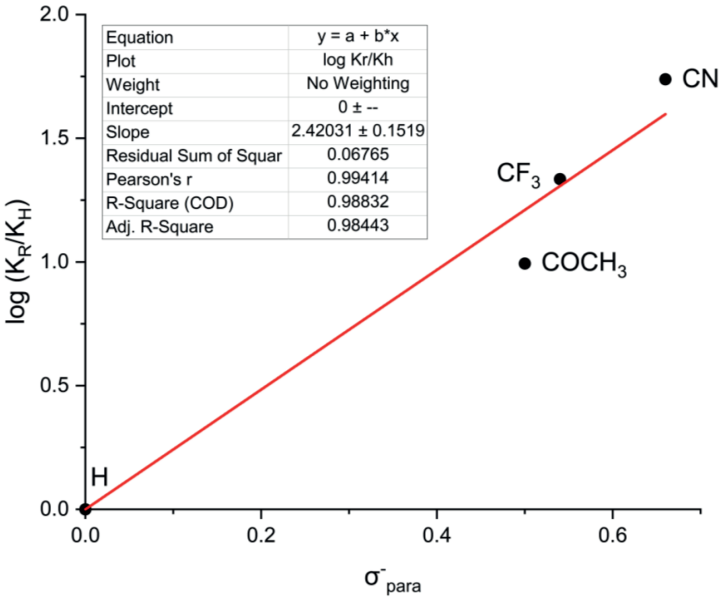

Figure 5.7. Hammett plot for $NiBr_2$-catalyzed esterification of bromobenzene derivatives with benzoic acid (initial rate was determined after 2 h reaction time).

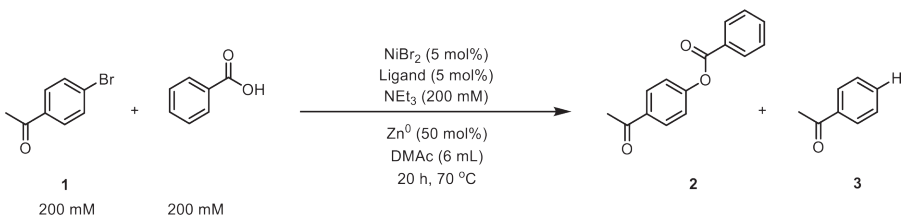

Table 5.6. Ligand screening.

Entry[a]	Ligand	1[a] Conv. [%]	2[a] Yield [%]	3[a] Yield [%]
1	No ligand	100	81	9
2	dtbbpy	85	50	32
3	Bipy	87	68	19
4	6,6 dimethyl-2,2 dipyridyl	8	n.d.	5
5	4,4 dimethoxy-2,2 dipyridine	6	<1	5
6	4,4 trifluoromethyl-2,2 dipyridine	23	10	11
7	Phenantroline	21	17	4
8	Neocuproine	16	5	11

[a] Determined by GC analysis.

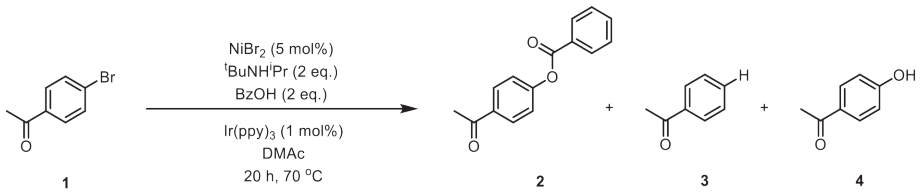

Table 5.7. Photocatalytic nickel-catalyzed carboxylate *O*-arylation.

Entry[a]	Light source	Change in condition	Additive	1[a] Conv. [%]	2[a] Yield [%]	3[a] Yield [%]	4[a] Yield [%]
1	CFL1, 24W	1 eq. BzOH + 1 eq. ^{t}BuNH^{i}Pr	-	35	14	14	n.d.
2	CFL1, 24W	-	-	59	37	15	n.d.
3	CFL1, 24W	BzOH (400 mM) + ^{t}BuNH^{i}Pr (400 mM)	dtbbpy (5 mol%)	92	86	5	
4	LED, 460 nm	Ir[dF(CF$_3$)ppy]$_2$(dtbbpy))PF$_6$	DABCO (1 eq.)	12	n.d.	12	n.d.
5	None	Zn instead of Ir(ppy)$_3$	DABCO (1 eq.)	12	n.d.	12	n.d.
		1 eq. BzOH + 1 eq. ^{t}BuNH^{i}Pr					
6	LED, 405 nm	1 eq. BzOH + 1 eq. ^{t}BuNH^{i}Pr		77	38	26	12
7	LED, 405 nm			89	39	24	22

Conditions: Bromoacetophenone (200 mM) Benzoic Acid (400 mM), tBuNHiPr (400 mM) Nickel(II) bromide (5 mol%), Ir(ppy)$_3$ (1 mol%), DMAc (6 mL), 20 hours, 70 °C. [a] Determined by GC analysis.

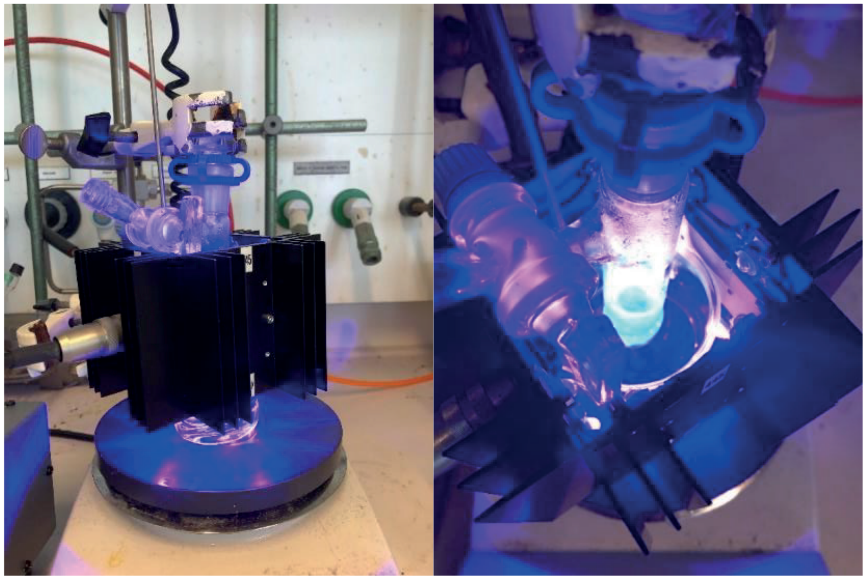

Figure 5.8. Reaction set-up for photoinitiation with 405 nm light at 70 °C.

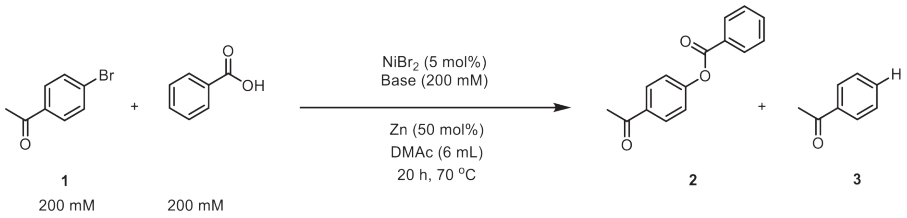

Table 5.8. Control experiments.

Entry[a]	Deviation	Base	1[a] Conv. [%]	2[a] Yield [%]	3[a] Yield [%]
1	Aerobic	^{t}BuNH^{i}Pr	6	n.d.	n.d.
2	No Zn	^{t}BuNH^{i}Pr	1	n.d.	<1
3	No $NiBr_2$	^{t}BuNH^{i}Pr	36	<1	35
4	$NiCOD_2$, no Zn	NEt_3	6	4	2
5	$NiCOD_2$	NEt_3	46	34	6
6	10 mol% COD	NEt_3	42	36	5

[a] Determined by GC analysis.

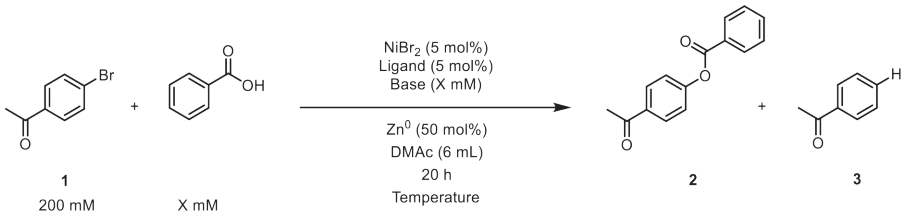

Table 5.9. (dtbbpy)$NiBr_2$- and $NiBr_2$-catalyzed reaction.

Entry[a]	Ligand	Base	Acid : Base Conc. [mM]	Solvent	Temp. [°C]	1[a] Conv. [%]	2[a] Yield [%]	3[a] Yield [%]
1	dtbbpy	NEt_3	200	DMF	40	39	21	18
2	dtbbpy	NEt_3	200	DMAc	40	33	15	18
3	dtbbpy	NEt_3	400	DMAc	40	99	63	27
4	dtbbpy	NEt_3	200	DMAc	70	85	50	32
5	dtbbpy	^{t}BuNH^{i}Pr	200	DMAc	70	100	61	38
6	none	NEt_3	200	DMAc	40	12	10	2
7	none	NEt_3	200	DMF	40	2	2	0
8	none	NEt_3	400	DMAc	40	22	14	8
9	none	NEt_3	200	DMAc	70	87	68	19
10	none	^{t}BuNH^{i}Pr	200	DMAc	70	100	81	9

[a] Determined by GC analysis.

Spectroscopy

UV-Vis Spectroscopy

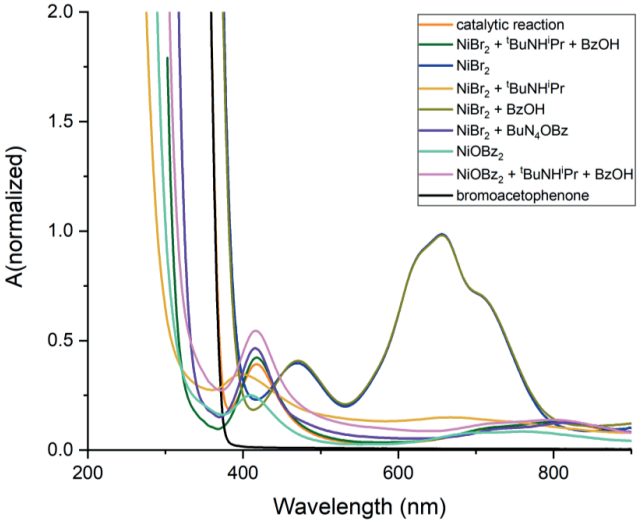

Figure 5.9. UV-Vis spectra of catalytic reaction after 2 h (orange) and DMAc solutions containing: $NiBr_2$ (10 mM), $^tBuNH^iPr$ (200 mM) and BzOH (200 mM) (green); $NiBr_2$ (10 mM) (blue); $NiBr_2$ (10 mM) and $^tBuNH^iPr$ (200 mM) (yellow); $NiBr_2$ (10 mM) and BzOH (200 mM) (light green); $NiBr_2$ (10 mM) and Bu_4NOBZ (200 mM) (purple); $NiOBz_2$ (10 mM) (turquoise); $NiOBz_2$ (10 mM), $^tBuNH^iPr$ (200 mM) and BzOH (200 mM) (pink); bromoacetophenone (200 mM) (black).

Formation of $[NiBr_x(DMAc)_y]$

While single crystals with the formula $[Ni(DMAc)_6][NiBr_4]$ can be obtained from a concentrated DMAc solution containing $NiBr_2$, Isiguro and co-workers demonstrated that in a DMAc solution a variety of complexes of the type $[NiBr_y(DMAc)_x]$ exists depending on the bromide concentration.[28,42] The following species were identified: five coordinated $[NiBr(DMAc)_4]^+$ (460 nm), five coordinated $[NiBr_2(DMAc)_3]$ (490 nm), four coordinated $[NiBr_2(DMAc)_2]$ (600 nm) and four coordinated $[NiBr_3(DMAc)]^-$ (660 nm with a shoulder at ~700 nm). These assigned peaks correlate well with the observed UV-Vis bands at 470 and 656 nm and shoulders at ~625 and ~710 nm for $NiBr_2$ (10 mM) in DMAc (Figure 5.9, blue trace).

UV-Vis Titration of $[NiBr_x(DMAc)_y]$ with $^tBuNH^iPr$ or Bu_4NOBz

Titration of experiments were performed under argon by mixing solutions of $NiBr_2$ (stock solution A) with various equivalents a solution of $NiBr_2$ and $^tBuNH^iPr$ or Bu_4NOBz (stock solution B). For stock solution A: $NiBr_2$ (14.1 mg, 0.04 mmol) was suspended in 4 mL DMAc and stirred at 70 °C at 15 min to obtain a homogeneous solution. For stock solution B: $NiBr_2$ (35.3 mg, 0.1 mmol) was dissolved in 9.7 mL DMAc and stirred at 70 °C at 15 min,

subsequently $^{t}BuNH^{i}Pr$ (317 µL, 2 mmol) or Bu_4NOBz (727.16 mg, 2 mmol) was added forming a yellow solution (this solution was immediately used for titration experiments). From stock solution A, 3 mL was transferred to a 1.0 cm pathlength J. Young type square quartz UV-Vis cuvette with an additional mixing reservoir (total volume 20 mL) and thereafter distinct equivalents of stock solution B were added via syringe (see Table 5.10, for the titration experiment with $^{t}BuNH^{i}Pr$). Before every UV-Vis measurement the solution was extensively mixed in the connected reservoir. For the sample with 20 eq. of $^{t}BuNH^{i}Pr$ or Bu_4NOBz, 3 mL of a freshly prepared stock solution B was transferred to the empty J. Young type UV-Vis cuvette and measured. Over a time period of 30 minutes the sample with 20 eq. of $^{t}BuNH^{i}Pr$ became turbid.

Table 5.10. UV-Vis titration of $NiBr_2$ with 0 to 20 equivalents of $^{t}BuNH^{i}Pr$

Equiv. $^{t}BuNH^{i}Pr$	**Stock solution B (µL)**	**Ni (mmol)**	**$^{t}BuNH^{i}Pr$ (mmol)**
0	-	0.0300	-
0.1	15	0.0302	0.0030
0.2	15	0.0303	0.0060
0.3	16	0.0305	0.0091
0.4	16	0.0306	0.0121
0.5	17	0.0308	0.0153
0.6	17	0.0309	0.0186
0.7	17	0.0311	0.0219
0.8	17	0.0312	0.0249
0.9	17	0.0314	0.0283
1.0	17	0.0316	0.0317
1.5	85	0.0324	0.0487
2.0	89	0.0333	0.0666
3.0	196	0.0353	0.1060
4.0	221	0.0375	0.1500
5.0	250	0.4000	0.2000
7.5	800	0.4800	3.6000
10	1210	0.6010	6.0100
20	Only stock solution B		

Figure 5.10. J. Young type UV-Vis cuvette with additional mixing volume.

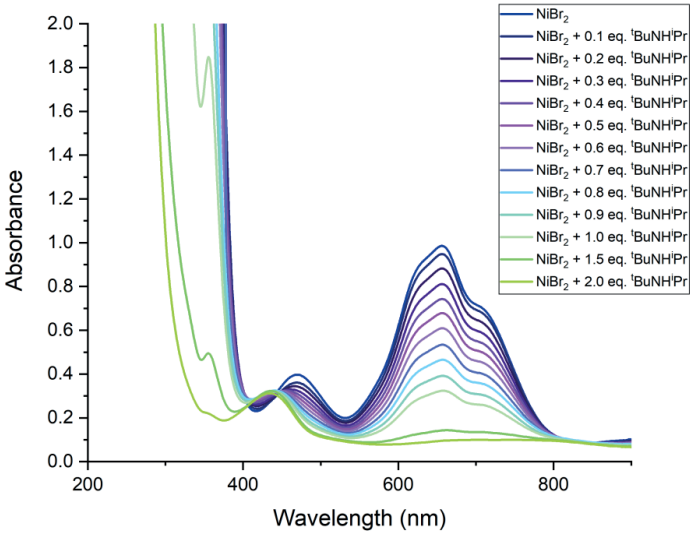

Figure 5.11. UV-Vis titration of a DMAc solution containing $NiBr_2$ (10 mM) with 0 to 2.0 equiv. of $^{t}BuNH^{i}Pr$.

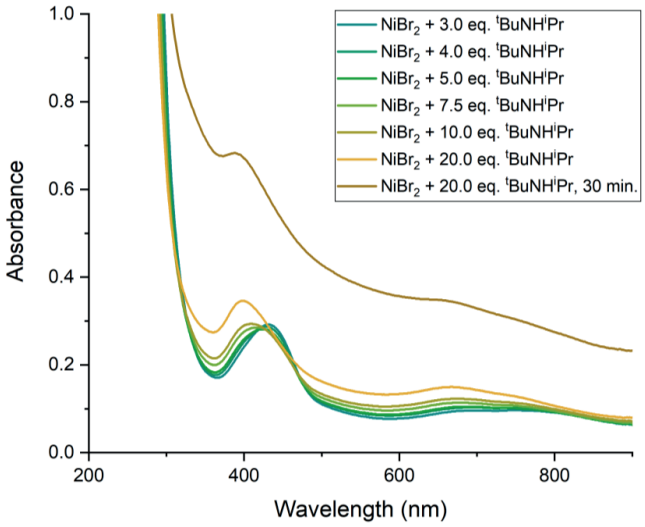

Figure 5.12. UV-Vis titration of a DMAc solution containing $NiBr_2$ (10 mM) with 3.0 to 20.0 equiv. of $^{t}BuNH^{i}Pr$.

UV-Vis titration of a DMAc solution containing $NiBr_2$ with up to 20 equiv. of $^{t}BuNH^{i}Pr$ led to the formation of nickel species with an increasing number of amine as ligand (Figures 5.11 - 5.12). However, at 20 equivalents of $^{t}BuNH^{i}Pr$ the solution slowly turned turbid over a period of 30 minutes (Figure 5.12, brown trace).

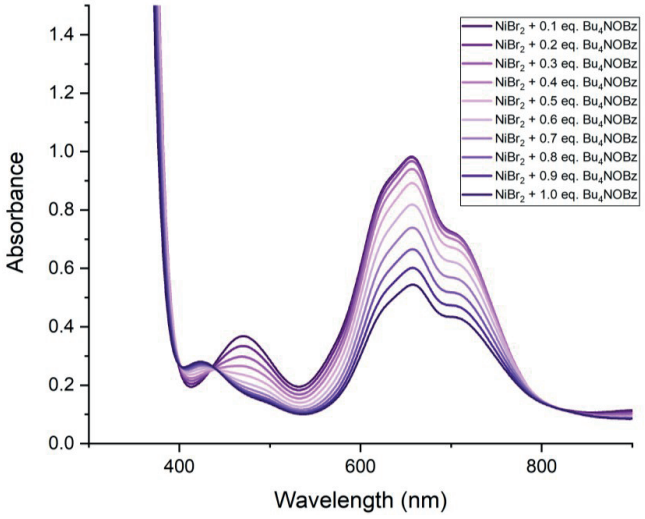

Figure 5.13. UV-Vis titration of a DMAc solution containing $NiBr_2$ (10 mM) with 0 to 1.0 equiv. of Bu_4NOBz.

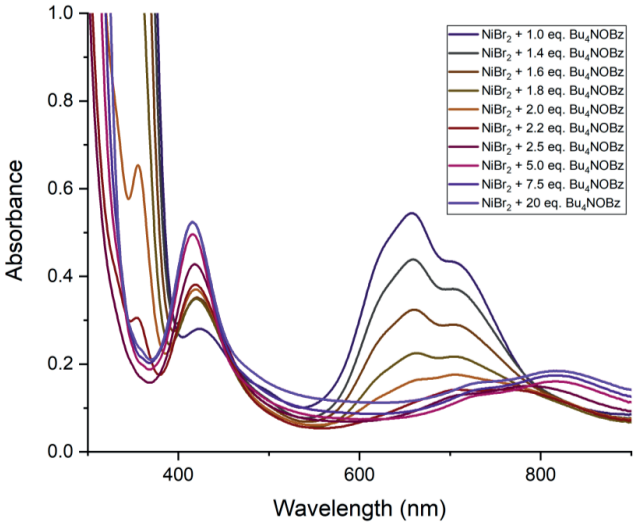

Figure 5.14. UV-Vis titration of a DMAc solution containing $NiBr_2$ (10 mM) with 1.0 to 20.0 equiv. of Bu_4NOBz.

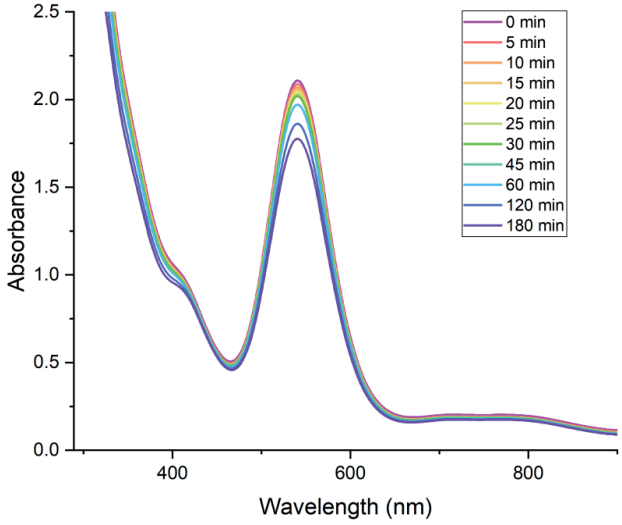

Figure 5.15. UV-Vis spectra of a DMAc solution containing $NiBr_2$ (10 mM), $^{t}BuNH^{i}Pr$ (200 mM), BzOH (200 mM) and zinc (600 mM) stirred at 70 °C for 3 h (filtered to remove zinc). The solution was kept under nitrogen atmosphere in a J. Young type quartz cuvette.

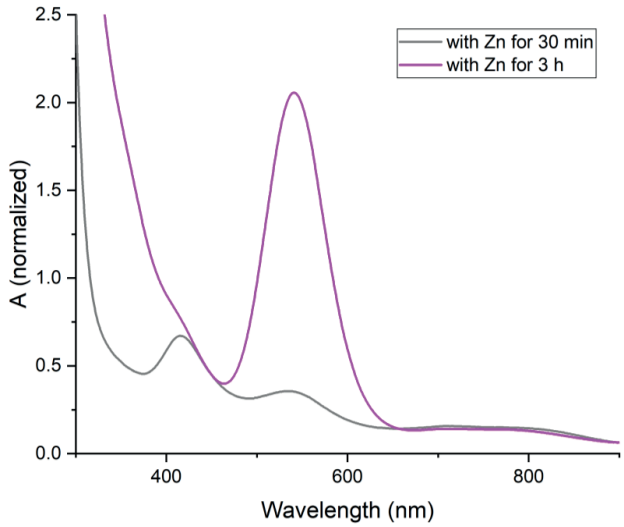

Figure 5.16. UV-Vis spectra of a DMAc solution containing $NiBr_2$ (10 mM), $^{t}BuNH^{i}Pr$ (200 mM), BzOH (200 mM) and zinc (600 mM) stirred at 70 °C for 30 min. (gray) and 3 h (pink) (filtered to remove zinc).

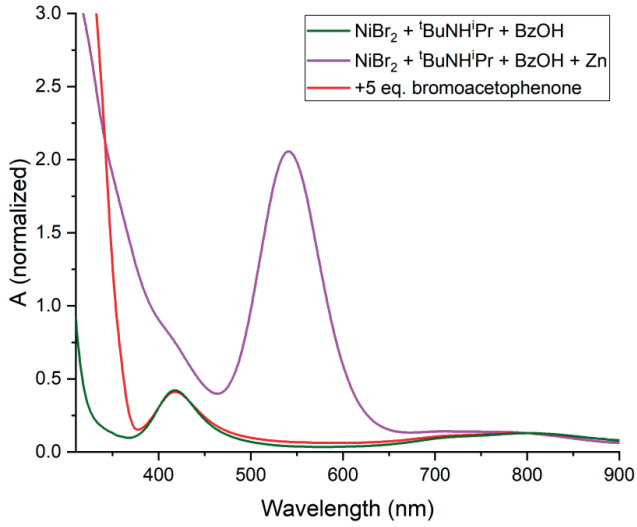

Figure 5.17. UV-Vis spectra of a DMAc solution containing $NiBr_2$ (10 mM), $^{t}BuNH^{i}Pr$ (200 mM) and BzOH (200 mM) (green); $NiBr_2$ (10 mM), $^{t}BuNH^{i}Pr$ (200 mM), BzOH (200 mM) and zinc (600 mM) stirred at 70 °C for 3 h (pink); $NiBr_2$ (10 mM), $^{t}BuNH^{i}Pr$ (200 mM), BzOH (200 mM) and zinc (600 mM) stirred at 70 °C for 3 h then filtered to remove zinc and 5 equivalents bromoacetophenone added.

NMR spectroscopy

In a nitrogen-filled glovebox, $NiBr_2$ (10.6 mg, 0.03 mmol) was weighed and transferred to a Schlenk flask (10 mL). The flask was removed from the glovebox, the atmosphere changed to argon and benzoic acid-α-^{13}C 99% (72 mg, 0.6 mmol) was added. Afterwards, $^{t}BuNH^{i}Pr$ (95 µL, 0.6 mmol) and 3 mL DMAc were supplied via a syringe. This solution was stirred at 70 °C for 15 min. to obtain a homogeneous mixture. For ^{1}H and ^{13}C NMR measurements, 0.05 mL anhydrous C_6D_6 was mixed with 0.45 mL of the reaction mixture in an NMR tube. Additional samples, were prepared in a similar fashion.

^{1}H NMR spectroscopy

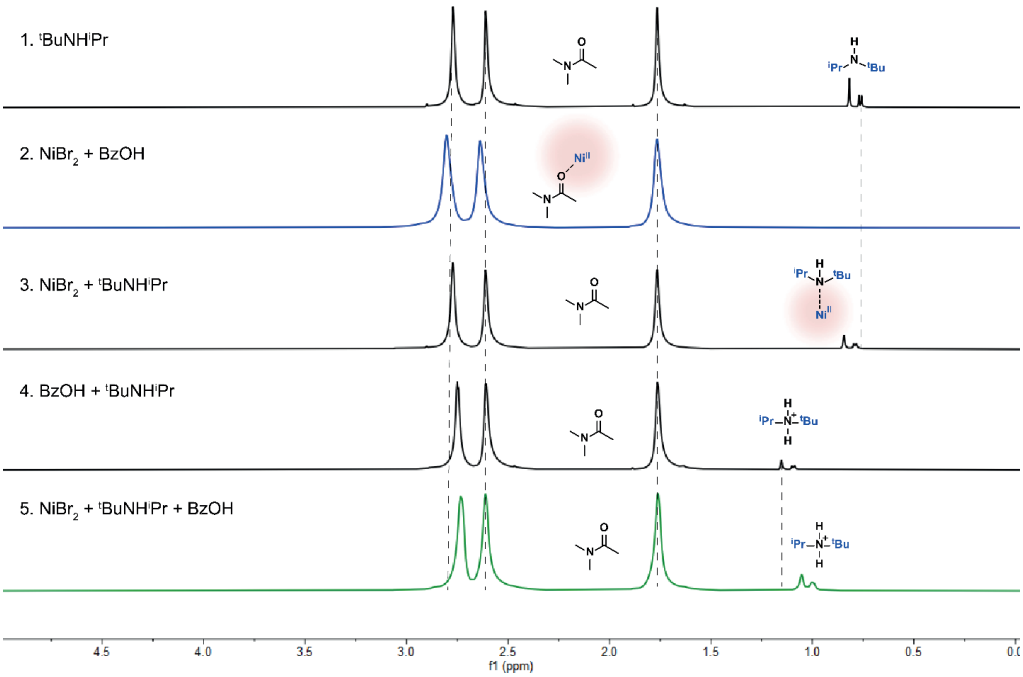

Figure 5.18. ^{1}H NMR spectra (aromatic region) of DMAc solutions containing: [1] BzOH (200 mM); [2] $NiBr_2$ (10 mM) and BzOH (200 mM) (blue); [3] BzOH (200 mM) and $^{t}BuNH^{i}Pr$ (200 mM); [4] $NiBr_2$ (10 mM); $^{t}BuNH^{i}Pr$ (200 mM) and BzOH (200 mM) (green).

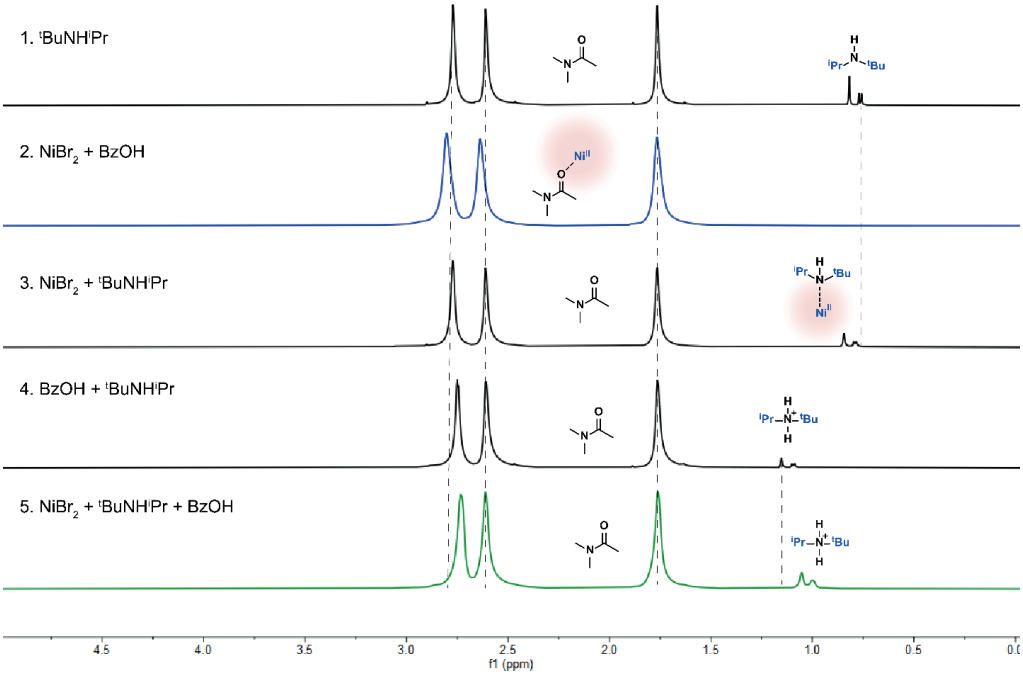

Figure 5.19. ^{1}H NMR spectra (0 to 5 ppm) of DMAc solutions containing: [1] $^{t}BuNH^{i}Pr$ (200 mM); [2] $NiBr_2$ (10 mM) and BzOH (200 mM) (blue); [3] $NiBr_2$ (10 mM) and $^{t}BuNH^{i}Pr$ (200 mM); [4] BzOH (200 mM) and $^{t}BuNH^{i}Pr$ (200 mM); [5] $NiBr_2$ (10 mM), $^{t}BuNH^{i}Pr$ (200 mM) and BzOH (200 mM) (green).

EPR Spectroscopy

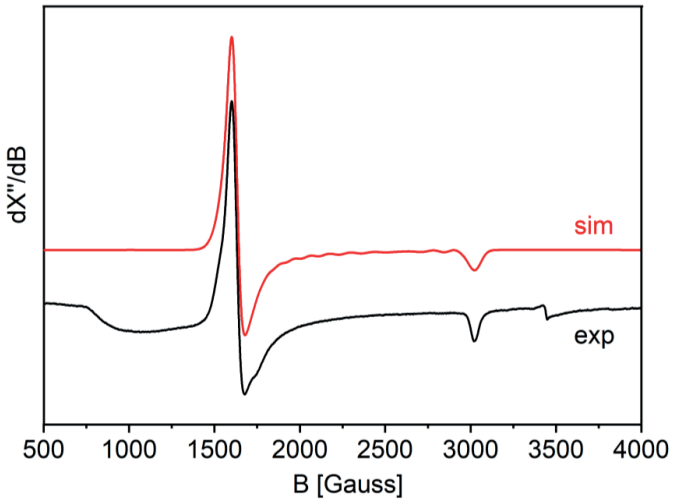

Figure 5.20. Experimental and simulated X-band EPR spectra of a frozen (9 K) DMAc solution containing $NiBr_2$ (10 mM), $^{t}BuNH^{i}Pr$ (200 mM) and BzOH (200 mM) that was reduced with zinc (600 mM) (black trace) and simulated spectrum (red trace). S=3/2, g=[2.18 2.09 2.28], lw=10, D= 10^5 MHz, E/D = 0.032, gStrain=[0.139 0.0496 0.0367]. (MW freq.=9.65, MW power=3.170 mW, Mod. amp.=8 G).

X-ray Absorption Spectroscopy

Ni K-edge XAS measurements were performed at B18 (Diamond) in Didcot, United Kingdom. Measurements were conducted with a Si(111) double crystal monochromator in fluorescence mode, where fluorescence from the sample was detected with a 36 element Ge solid State detector. A typical measurement required 3 minutes and 25 scans were required to obtain good signal-to-noise. Samples (10 mM in Ni) were measured as frozen DMAc solutions in a 5 mm Kapton® tube, and kept frozen with a Cryojet which was set at 100 K during the measurement. All spectra were calibrated to a Ni foil. The amplitude redaction factor was determined using the Ni foil and found to be 0.8. XAS data processing was performed in Athena, and EXAFS analysis was conducted in Artemis.[43]

XANES

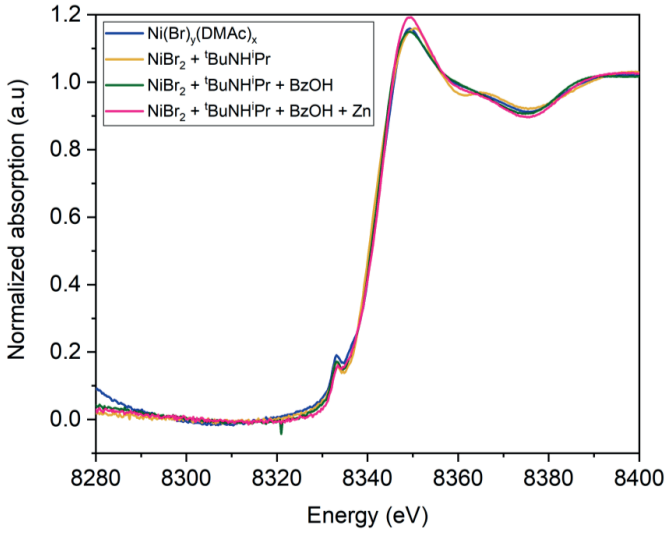

Figure 5.21. Ni K-edge XANES spectrum for DMAc solutions containing: $NiBr_2$ (10 mM) (blue), $NiBr_2$ (10 mM) and $^{t}BuNH^{i}Pr$ (200 mM) (yellow); $NiBr_2$ (10 mM), $^{t}BuNH^{i}Pr$ (200 mM) and BzOH (200 mM) (green); $NiBr_2$ (10 mM), $^{t}BuNH^{i}Pr$ (200 mM) and BzOH (200 mM) reduced with zinc (600 mM) (pink).

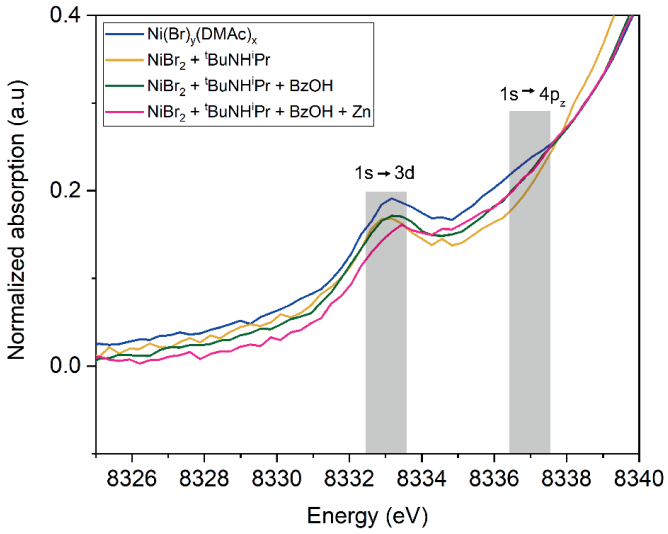

Figure 5.22. Ni K-edge XANES spectrum (pre-edge region) for DMAc solutions containing: $NiBr_2$ (10 mM) (blue), $NiBr_2$ (10 mM) and $^{t}BuNH^{i}Pr$ (200 mM) (yellow); $NiBr_2$ (10 mM), $^{t}BuNH^{i}Pr$ (200 mM) and BzOH (200 mM) (green); $NiBr_2$ (10 mM), $^{t}BuNH^{i}Pr$ (200 mM) and BzOH (200 mM) reduced with zinc (600 mM) (pink).

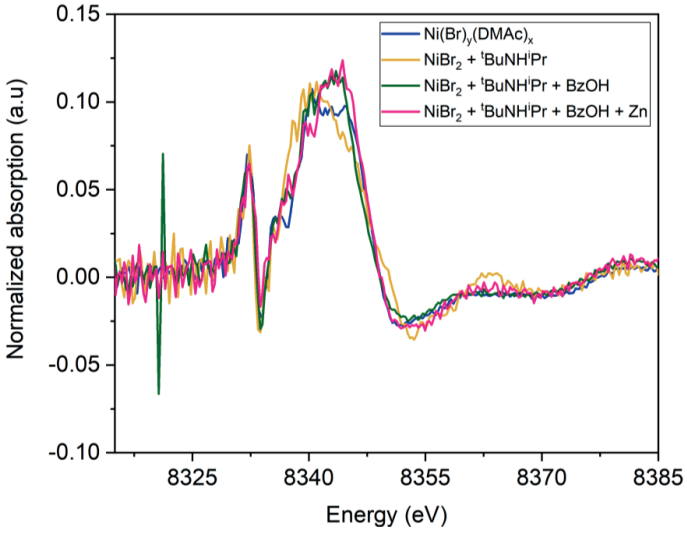

Figure 5.23. First derivatives of the Normalized Ni K-edge XANES spectra.

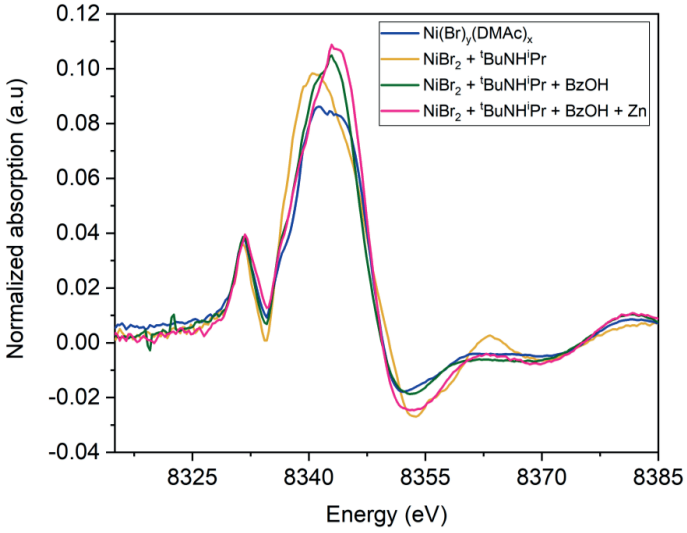

Figure 5.24. First derivatives of the Normalized Ni K-edge XANES spectra for (with a moving average (size 4)).

EXAFS

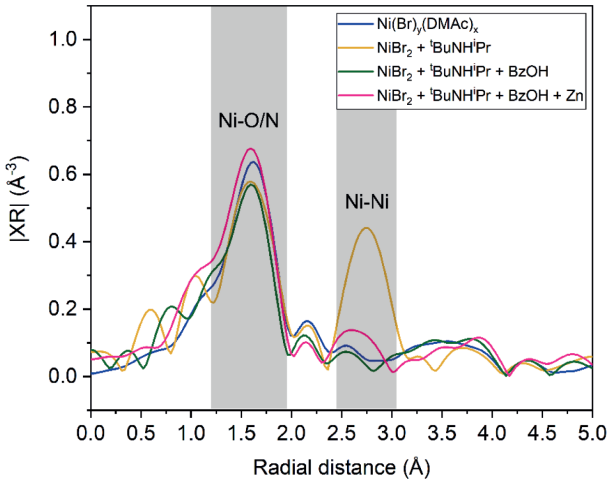

Figure 5.25. Ni K-edge k^2 weighted Fourier transform EXAFS for DMAc solutions containing: $NiBr_2$ (10 mM) (blue), $NiBr_2$ (10 mM) and $^{t}BuNH^{i}Pr$ (200 mM) (yellow); $NiBr_2$ (10 mM), $^{t}BuNH^{i}Pr$ (200 mM) and BzOH (200 mM) (green); $NiBr_2$ (10 mM), $^{t}BuNH^{i}Pr$ (200 mM) and BzOH (200 mM) reduced with zinc (600 mM) (pink).

Ni K-edge EXAFS fitting parameters

For a DMAc solution containing solely $NiBr_2$ required one oxygen shell with a coordination number of 2.50(17) at a corresponding distance of 2.05(1)Å (Table 5.11, entry 1). For a DMAc solution containing $NiBr_2$ and $^{t}BuNH^{i}Pr$ (Figure 5.25, yellow trace), two independent shells are required to obtain a satisfactory fit for the data. The first shell, composing of a indistinguishable, nitrogen or oxygen shell has a coordination number of 1.79(17) at a distance of 2.05(1)Å. The second shell is a nickel shell, containing 1.65(50) atoms at 3.10(1)Å (Table 5.11, entry 2). Entries 3 and 4 of Table 5.11 are discussed in the main text.

Table 5.11. Ni K-edge EXAFS fitting parameters for all components with N = coordination number, σ^2 = Debye Waller factor [$Å^2$], R_{Fit} = fitted bond length [Å].

Entry[a]	Sample	Shell	N	σ^2 ($Å^2$)	R_{Fit} (Å)	σ^2 ($Å^2$)
1	$Ni(Br)_x(DMAc)_y$[a]	Ni-O	2.50(17)	0.0066(8)	2.05(1)	2.05(1)
2	$NiBr_2$ + $^{t}BuNH^{i}Pr$ [b]	Ni-O/N	1.79(17)	0.005(2)	2.05(1)	2.05(1)
		Ni-Ni	1.65(50)	0.006(2)	3.10(1)	3.10(1)
3	$NiBr_2$ + $^{t}BuNH^{i}Pr$ + BzOH[c]	Ni-O/N	0.95(10)	0.006(6)	2.054(6)	2.054(6)
		Ni-O/N	0.95(10)	0.001(1)	2.10(2)	2.10(2)
4	$NiBr_2$ + $^{t}BuNH^{i}Pr$ + BzOH + Zn[d]	Ni-O/N	3.0(3)	0.006(1)	2.04(1)	2.04(1)
		Ni-Ni	0.6(5)	0.009(9)	3.10(3)	3.10(3)

[a] k range = 3–13 $Å^{-1}$, R range = 1–3 Å; k-weighted fit = 1,2,3 E_0 = 2.8(7) eV, S_0^2 = 0.80 R-factor fit: 0.006.
[b] k range = 3–11.6 $Å^{-1}$, R range = 1–3 Å; k-weighted fit = 1,2,3 E_0 = 1(1) eV, S_0^2 = 0.80 R-factor fit: 0.016.
[c] k range = 3–12 $Å^{-1}$, R range = 1–2.9 Å; k-weighted fit = 1,2,3 E_0 = -6(1) eV, S_0^2 = 0.80 R-factor fit: 0.005.
[d] k range = 3–13.25 Å, R range = 1–3.1 Å; k-weighted fit = 1,2,3 E_0 = -4(1) eV, S_0^2 = 0.80 R-factor fit: 0.021.

Formation of Ni clusters

For a DMAc solution containing $NiBr_2$ and 20 equivalents of $^tBuNH^iPr$ a prominent contribution of a back scatterer emerges in the FT EXAFS spectrum (Figure 5.25, yellow trace). This coordination shell can be assigned to a Ni-Ni interaction and is indicative for the formation of Ni clusters. Moreover, this result is in agreement with the turbid solution obtained during at the end of the UV-Vis titration experiment (Figure 5.12). Formation of multinuclear species is indicative for a more elaborate ligand exchange process than only associative coordination of the amine substrate. The displacement of the bromide ligand, for the amine base, is a potential pathway. This ligand exchange reaction was also proposed as protodehalogenation pathway in energy transfer mediated photocatalytic *O*-arylation with (dtbbpy)$NiBr_2$ and diisopropylamine (DIPA) as base.[8]

Determination of coordination number of the bromide shell

The Ni-Br contributions were surprisingly difficult to fit. We expected anti-phase behavior could play a role, as previously observed for Cu organometallic compounds.[30] To study this, simulations of a Ni-Br bond were performed within Artemis (Parameters: $S_0^2 = 0.80$ fixed, $\sigma^2 = 0.003$ fixed and $E_0 = 0$ fixed). In figures 5.26 – 5.28 the simulated Ni K-edge EXAFS data (chi, for different k-weightings) for a Ni-Br contribution as a function of Ni-Br bond length is plotted (starting from a Ni-Br bond length of 2.40 Å). It is clear from these simulations that, in all k-weightings, the Ni-Br contributions are strong. However, from about a difference of 0.1-0.15 Å in Ni-Br bond length, the paths are completely in anti-phase, cancelling each other out when they are both present in equal amounts (i.e. similar coordination number). This anti-phase behavior is very similar for all k-weightings, such that a careful plot in different k-weighting, as was performed for Cu[30], does not solve the problem. Therefore, if in single nickel complex or a mixture of nickel complexes, multiple Ni-Br contribution are present at different distances, the antiphase behavior of the different paths, can result in a seemingly absence of Ni-Br at all; or in fact, only part of the Ni-Br contributions are analyzed (i.e. the Ni-Br contributions are underestimated). For the data in this paper, we therefore can only say with confidence that either no Ni-Br contributions are present, or that a similar amount of Ni-Br contributions are present at different distances, resulting in an even number of Ni-Br contributions.

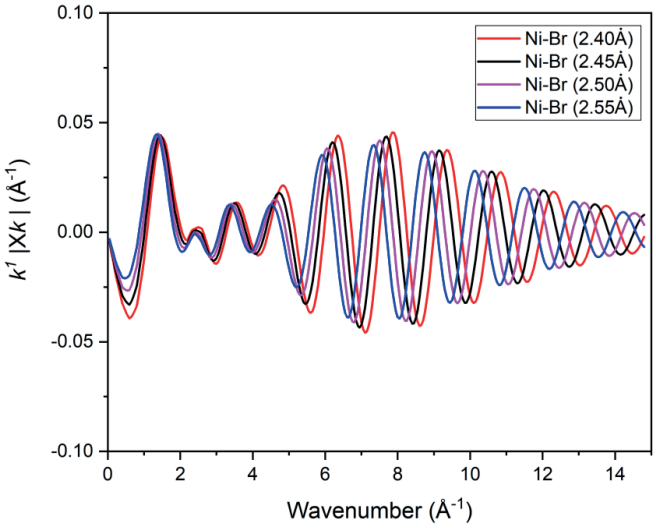

Figure 5.26. *k*-weighted Fourier transforms of the EXAFS data of the Ni-Br bond, starting from 2.40 Å.

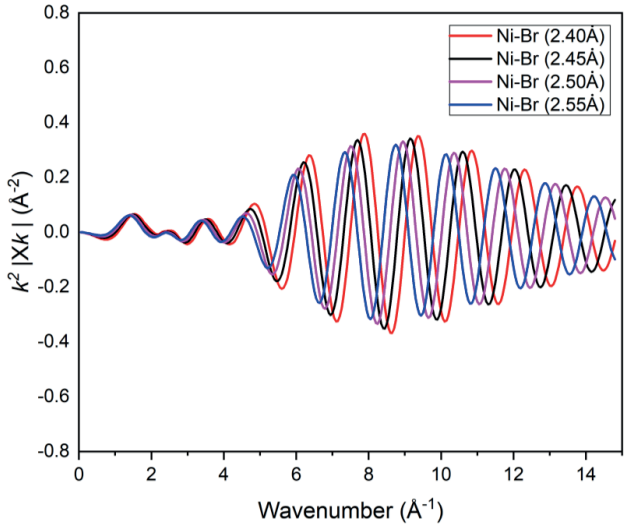

Figure 5.27. k^2-weighted Fourier transforms of the EXAFS data of the Ni-Br bond, starting from 2.40 Å.

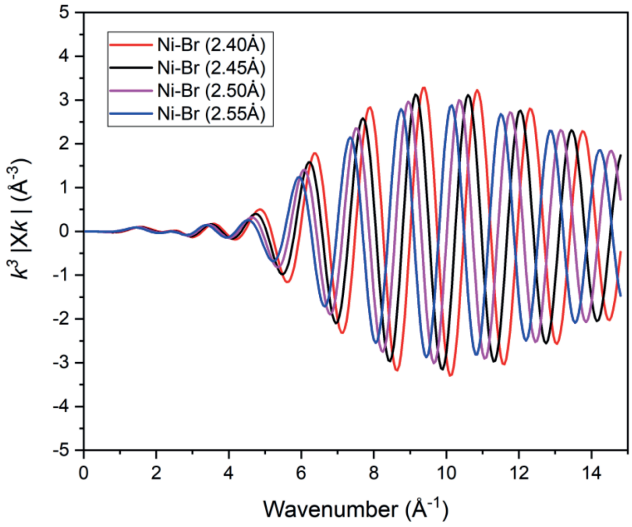

Figure 5.28. k^3-weighted Fourier transforms of the EXAFS data of the Ni-Br bond, starting from 2.40 Å.

EXAFS fits

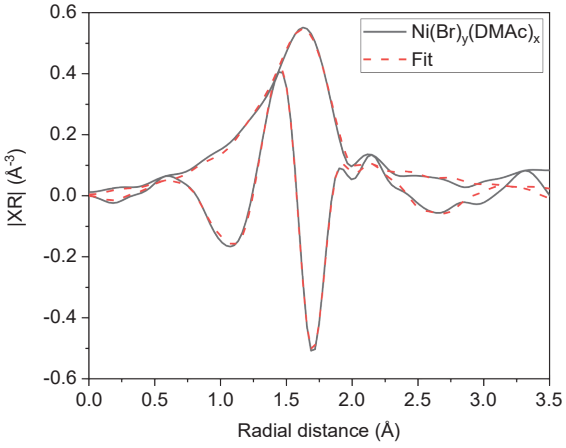

Figure 5.29. k^2 -weighted Fourier transforms of the EXAFS data of a DMAc solution containing $NiBr_2$ (10 mM). The data is represented by the solid trace (black), whereas the corresponding fit is the dotted line (red).

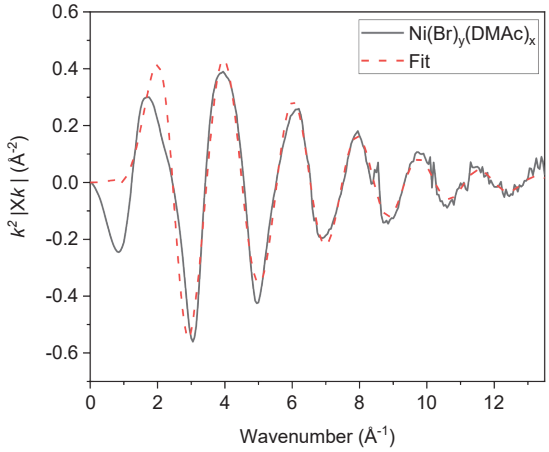

Figure 5.30. k^2 -weighted EXAFS data of a DMAc solution containing $NiBr_2$ (10 mM). The data is represented by the solid trace (black), whereas the corresponding fit is the dotted line (red).

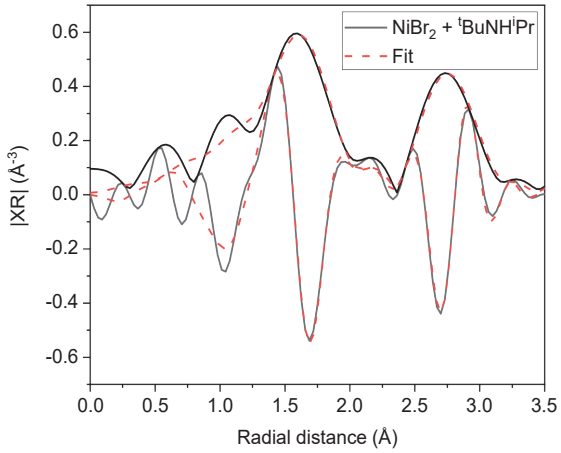

Figure 5.31. k^2 -weighted Fourier transforms of the EXAFS data of a DMAc solution containing $NiBr_2$ (10 mM) and $^{t}BuNH^{i}Pr$ (200 mM). The data is represented by the solid trace (black), whereas the corresponding fit is the dotted line (red).

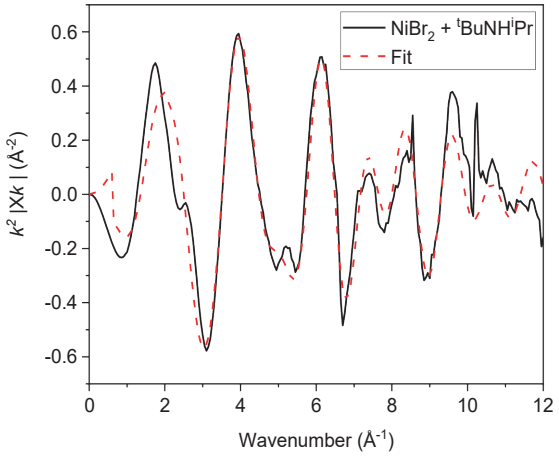

Figure 5.32. k^2 -weighted EXAFS data of a DMAc solution containing $NiBr_2$ (10 mM) and $^tBuNH^iPr$ (200 mM)H^iPr. The data is represented by the solid trace (black), whereas the corresponding fit is the dotted line (red).

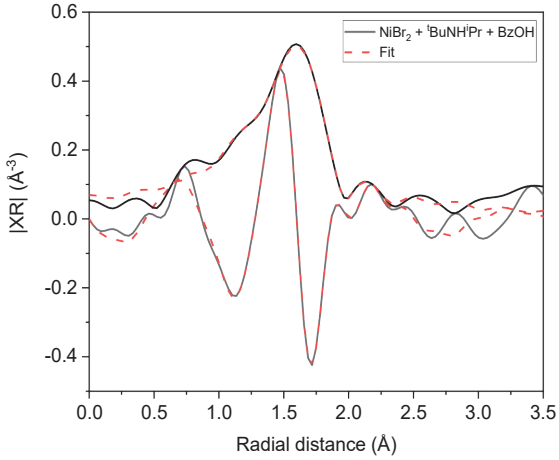

Figure 5.33. k^2 -weighted Fourier transforms of the EXAFS data of a DMAc solution containing $NiBr_2$ (10 mM), $^tBuNH^iPr$ (200 mM) and BzOH (200 mM). The data is represented by the solid trace (black), whereas the corresponding fit is the dotted line (red).

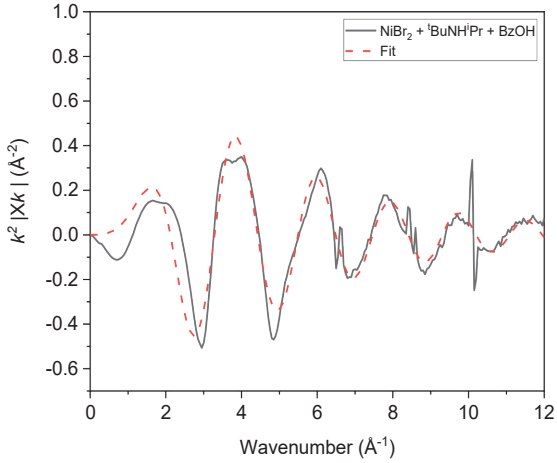

Figure 5.34. k^2 -weighted EXAFS data of a DMAc solution containing $NiBr_2$ (10 mM), $^{t}BuNH^{i}Pr$ (200 mM) and BzOH (200 mM). The data is represented by the solid trace (black), whereas the corresponding fit is the dotted line (red).

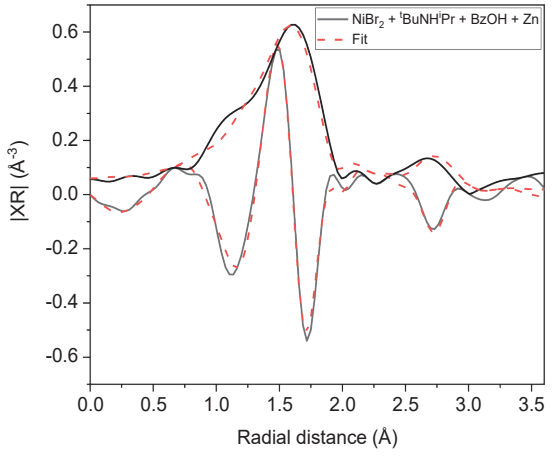

Figure 5.35. k^2 -weighted Fourier transforms of the EXAFS data of a DMAc solution containing $NiBr_2$ (10 mM), $^{t}BuNH^{i}Pr$ (200 mM) and BzOH (200 mM) reduced with zinc (600 mM). The data is represented by the solid trace (black), whereas the corresponding fit is the dotted line (red).

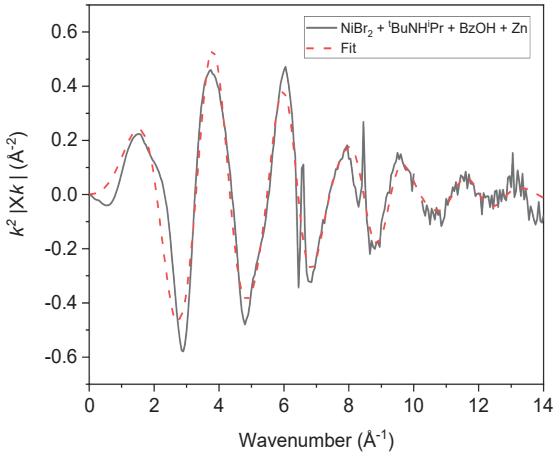

Figure 5.36. k^2 -weighted EXAFS data of a DMAc solution containing $NiBr_2$ (10 mM), $^tBuNH^iPr$ (200 mM) and BzOH (200 mM) reduced with zinc (600 mM). The data is represented by the solid trace (black), whereas the corresponding fit is the dotted line (red).

GC analysis

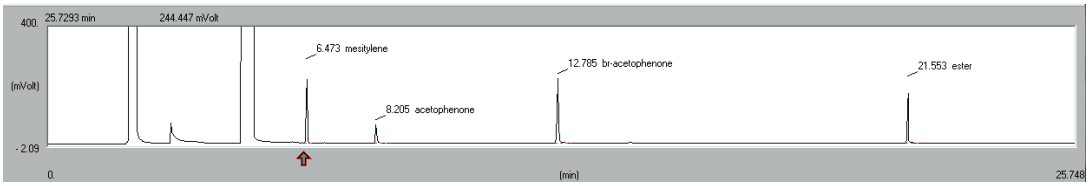

Figure 5.37. Typical GC-trace for cross-coupling of bromoacetophenone with benzoic acid.

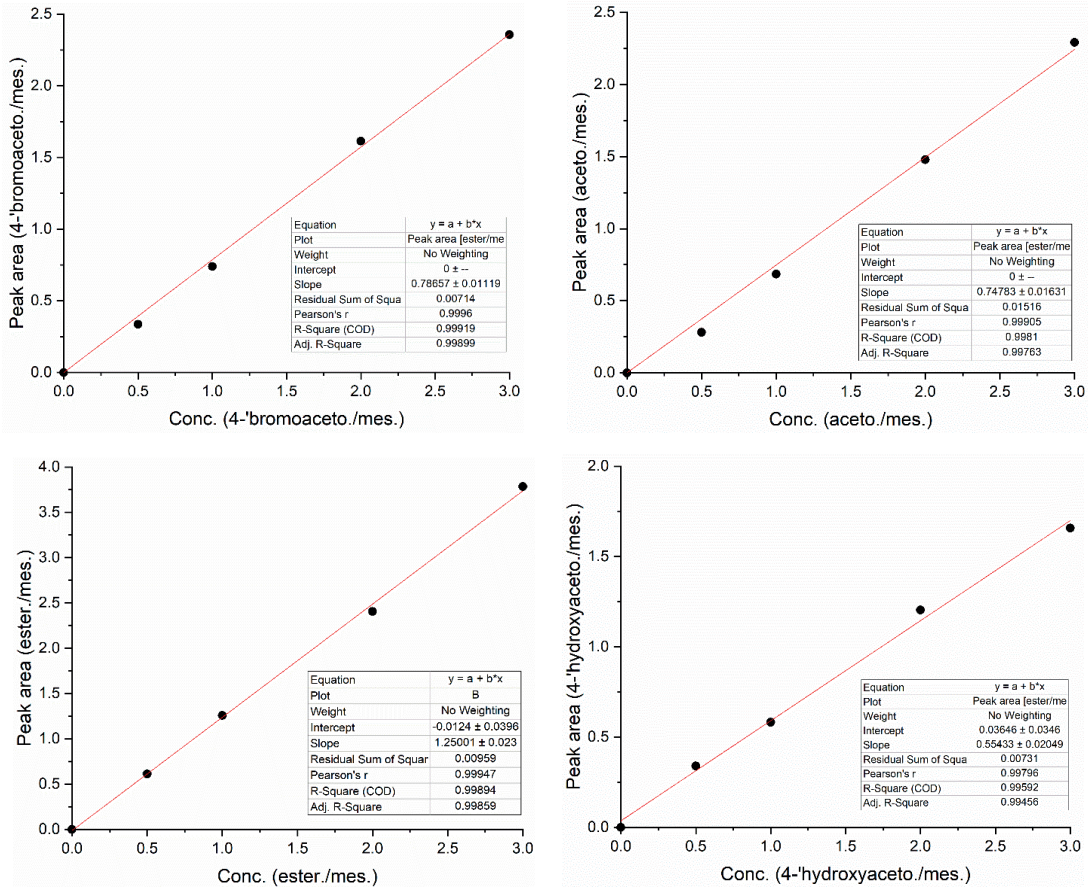

Figure 5.38. GC calibration curves for 4'-bromoacetophenone (**1**), acetophenone (**3**), 4'-benzoyloxyacetophenone (**2A**) and 4'-hydroxyacetophenone (**4**).

References

1 O. S. Wenger, *Chem. - A Eur. J.*, 2021, **27**, 2270–2278.
2 C. Zhu, H. Yue, J. Jia and M. Rueping, *Angew. Chemie - Int. Ed.*, 2021, **60**, 17810–17831.
3 J. B. Diccianni and T. Diao, *Trend Chem.*, 2019, 1–15.
4 E. R. Welin, C. Le, D. M. Arias-Rotondo, J. K. McCusker and D. W. C. MacMillan, *Science*, 2017, **355**, 380–385.
5 M. He, S. Yang, X. Yu and M. Bao, *Synlett*, 2021, **32**, A-E.
6 D. L. Zhu, H. X. Li, Z. M. Xu, H. Y. Li, D. J. Young and J. P. Lang, *Org. Chem. Front.*, 2019, **6**, 2353–2359.
7 B. Pieber, J. A. Malik, C. Cavedon, S. Gisbertz, A. Savateev, D. Cruz, T. Heil, G. Zhang and P. H. Seeberger, *Angew. Chemie - Int. Ed.*, 2019, **58**, 9575–9580.
8 J. Lu, B. Pattengale, Q. Liu, S. Yang, S. Li, J. Huang and J. Zhang, *J. Am. Chem. Soc.*, 2018, **140**, 13719–13725.
9 Y. Mo, Z. Lu, G. Rughoobur, P. Patil, N. Gershenfeld, A. I. Akinwande, S. L. Buchwald and K. F. Jensen, *Science*, 2020, **368**, 1352–1357.
10 R. Sun, Y. Qin and D. G. Nocera, *Angew. Chemie - Int. Ed.*, 2020, **59**, 9527–9533.
11 H. Kitano, H. Ito and K. Itami, *Org. Lett.*, 2018, **20**, 2428–2432.
12 L. Li, F. Song, X. Zhong, Y. D. Wu, X. Zhang, J. Chen and Y. Huang, *Adv. Synth. Catal.*, 2020, **362**, 126–132.
13 B. J. Shields, B. Kudisch, G. D. Scholes and A. G. Doyle, *J. Am. Chem. Soc.*, 2018, **140**, 3035–3039.
14 R. Sun, Y. Qin, S. Ruccolo, C. Schnedermann, C. Costentin and D. G. Nocera, *J. Am. Chem. Soc.*, 2019, **141**, 89–93.
15 Y. Qin, R. Sun, N. P. Gianoulis and D. G. Nocera, *J. Am. Chem. Soc.*, 2021, **143**, 2005–2015.
16 L. Yang, H. H. Lu, C. H. Lai, G. Li, W. Zhang, R. Cao, F. Liu, C. Wang, J. Xiao and D. Xue, *Angew. Chemie - Int. Ed.*, 2020, **59**, 12714–12719.
17 N. A. Till, L. Tian, Z. Dong, G. D. Scholes and D. W. C. MacMillan, *J. Am. Chem. Soc.*, 2020, **142**, 15830–15841.
18 Y. Kawamata, J. C. Vantourout, D. P. Hickey, P. Bai, L. Chen, Q. Hou, W. Qiao, K. Barman, M. A. Edwards, A. F. Garrido-Castro, J. N. Degruyter, H. Nakamura, K. Knouse, C. Qin, K. J. Clay, D. Bao, C. Li, J. T. Starr, C. Garcia-Irizarry, N. Sach, H. S. White, M. Neurock, S. D. Minteer and P. S. Baran, *J. Am. Chem. Soc.*, 2019, **141**, 6392–6402.
19 N. A. Till, S. Oh, D. W. C. MacMillan and M. J. Bird, *J. Am. Chem. Soc.*, 2021, **143**, 9332–9337.
20 M. Mohadjer Beromi, G. W. Brudvig, N. Hazari, H. M. C. Lant and B. Q. Mercado, *Angew. Chemie - Int. Ed.*, 2019, **58**, 6094–6098.
21 S. I. Ting, W. L. Williams and A. G. Doyle, *ChemRxiv 2022.*, DOI:10.26434/chemrxiv-2022-m8xj2.
22 H. Na and L. Mirica, *Chemrxiv 2022*, DOI:10.33774/chemrxiv-2021-cwk2r.
23 E. B. Corcoran, M. T. Pirnot, S. Lin, S. D. Dreher, D. A. Dirocco, I. W. Davies, S. L. Buchwald and D. W. C. Macmillan, *Science*, 2016, **353**, 279–283.
24 S. Gisbertz, S. Reischauer and B. Pieber, *Nat. Catal.*, 2020, **3**, 611–620.
25 D. L. Zhu, H. X. Li, Z. M. Xu, H. Y. Li, D. J. Young and J. P. Lang, *Org. Chem. Front.*, 2019, **6**, 2353–2359.
26 E. O. Bortnikov and S. N. Semenov, *J. Org. Chem.*, 2021, **86**, 782–793.
27 W. Zu, C. Day, L. Wei, X. Jia and L. Xu, *Chem. Commun.*, 2020, **56**, 8273–8276.
28 M. Koide, H. Suzuki and S. ichi Ishiguro, *J. Solution Chem.*, 1994, **23**, 1257–1270.
29 W. Hao, Y. Sha, Y. Deng, Y. Luo, L. Zeng, S. Tang, Y. Weng, C. W. Chiang and A. Lei, *Chem. - A Eur. J.*, 2019, **25**, 4931–4934.
30 J. Rabeah, J. Radnik, V. Briois, D. Maschmeyer, G. Stochniol, S. Peitz, H. Reeker, C. La Fontaine and A. Brückner, *ACS Catal.*, 2016, **6**, 8224–8228.
31 M. P. Feth, A. Klein and H. Bertagnolli, *Eur. J. Inorg. Chem.*, 2003, 839–852.
32 G. J. Colpas, M. J. Maroney, C. Bagyinka, M. Kumar, W. S. Willis, S. L. Suib, N. Baidya and P. K. Mascharak, *Inorg. Chem.*, 1991, **30**, 920–928.
33 M. Tromp, J. A. Van Bokhoven, A. M. Arink, J. H. Bitter, G. Van Koten and D. C. Koningsberger, *Chem. - A Eur. J.*, 2002, **8**, 5667–5678.
34 J. Evans, W. Levason and R. J. Perry, *J.Chem. Soc. Dalt. Trans.*, 1992, 1497–1501.
35 Q. Lin and T. Diao, *J. Am. Chem. Soc.*, 2019, **141**, 17937–17948.
36 L. Tian, N. A. Till, B. Kudisch, D. W. C. MacMillan and G. D. Scholes, *J. Am. Chem. Soc.*, 2020, **142**, 4555–4559.
37 S. I. Ting, S. Garakyaraghi, C. M. Taliaferro, B. J. Shields, G. D. Scholes, F. N. Castellano and A. G. Doyle, *J. Am. Chem. Soc.*, 2020, **142**, 5800–5810.

38 A. Vráblová, L. R. Falvello, J. Campo, J. Miklovič, R. Boča, J. Černák and M. Tomás, *Eur. J. Inorg. Chem.*, 2016, 928–934.
39 C. R. Smith, *Synlett*, 2009, 1522–1523.
40 S. Stoll and A. Schweiger, *J. Magn. Reson.*, 2006, **178**, 42–55.
41 T. Casey, cwEPR (https://www.mathworks.com/matlabcentral/fileexchange/73292-cwepr), MATLAB Central File Exchange. Retrieved December 13, 2021.
42 M. Kudisch, C. H. Lim, P. Thordarson and G. M. Miyake, *J. Am. Chem. Soc.*, 2019, **141**, 19479–19486.
43 B. Ravel and M. Newville, *J. Synchrotron Radiat.*, 2005, **12**, 537–541.

Summary

The ester bond is an important structural motif in organic molecules, that among others find application as pharmaceuticals, fragrances or coatings. Although the direct coupling of carboxylic acids and alcohols is known for more than a century, it is still the most prominent route to synthesize the ester moiety. This chemical transformation affords the desired ester bond and water as the only by-product. However, the unfavorable equilibrium conditions of this reaction require a non-equimolar stoichiometry of substrates or a dehydration technique to drive the reaction to completion. Dehydration via evaporation or azeotropic distillation is often, especially at an industrial scale, the preferred route to obtain (poly)esterification products. This method allows equimolar ratios of substrates, but high reaction temperatures are still required. Therefore, the use of a catalyst that can lower the reaction temperature and enable mild reaction conditions is highly desirable. Strong Brønsted acids are well-known to efficiently catalyze the direct esterification reaction, but their application has several disadvantages since they are highly corrosive and facilitate unwanted side reactions. In contrast, Lewis acidic metals are less corrosive and exclusively catalyze the desired esterification reaction. As a result, Lewis acidic metals have been intensively explored as catalysts in the direct esterification reaction. Although a wide variety of different metal salts were found to be effective catalysts, understanding the origin of their catalytic activity is still limited. Mechanistic studies are severely complicated due to *in situ* transformation of the catalyst, since all reaction components (carboxylic acid, alcohol and ester) have the ability to coordinate to the Lewis acidic metal center. This transformation does not exclusively lead to monomeric species but also dimeric and multinuclear complexes have been identified.
Besides the direct (poly)esterification, many other ester-forming reactions have been explored by chemists. One notable example is the nickel-catalyzed carbon-oxygen bond forming reaction between an organic (pseudo)halide and a carboxylic acid, which has received much attention in recent years. Also here, mechanistic understanding of the catalytic cycle is hindered by many side reactions, either by reaction with one of the reaction components, or by other (deactivation) reactions.

In this thesis, we have shed light on the structure of various *in situ* formed catalysts, potential intermediates and have provided deeper mechanistic understanding of the catalytic cycle. This knowledge contributes to the development of novel efficient esterification catalysts based on abundant and non-toxic metals.

In ***Chapter 1*** an overview of different Lewis acidic homogeneous catalysts applied in the direct (poly)esterification reactions is provided. Studies that have attempted to elucidate the structure of the *in situ* formed catalytically active complex and investigations that provide mechanistic insights are discussed. Moreover, new routes for ester synthesis are reviewed with a focus on the nickel-catalyzed cross-coupling of aryl halides and carboxylic acids.

In ***Chapter 2*** a mechanistic study into titanium(IV)-catalyzed direct esterification reactions is described. Since mechanistic investigations into common titanium alkoxides (poly)esterification catalysts are troublesome due to uncontrolled ligand exchange reactions, we selected the class of titanium-aminotriphenolate complexes for our investigations. The combination of the tetradentate aminotriphenolate ligand and $Ti(^{i}OPr)_4$ afforded a variety of robust C_3-symmetric titanium complexes with only an exchangeable isopropoxide group in the apical position (Figure S1). During catalytic studies we found that steric bulk in the *ortho*-position was hampering catalysis. As a result, the titanium-aminotriphenolate complex lacking steric bulk in this position was found to be the most active catalyst, albeit with a lower activity than $Ti(^{i}OPr)_4$. Based on *in situ* and stoichiometric experiments, we concluded that the amphoteric octahedral titanium-aminotriphenolate acetic acid/acetate complex is the resting state during catalysis. With the help of kinetic experiments and DFT calculations a mononuclear reaction mechanism was proposed, which revealed three essential prerequisites for an active catalyst: Lewis acidity of the titanium(IV) metal, favorable hydrogen bonding interactions between both reactants and the ligand, and a Brønsted basic group to facilitate proton transfer.

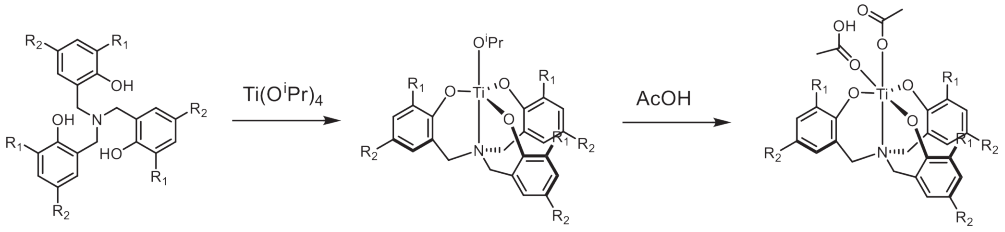

Figure S1. Synthesis of titanium aminotriphenolate complexes.

In ***Chapter 3***, we have investigated *n*-butyltin(IV) complexes using a variety of spectroscopic techniques (ATR-FTIR, ^{119}Sn NMR, ^{1}H NMR) under catalytically relevant conditions. The profound activity of this class of (poly)esterification catalyst was demonstrated in a model esterification reaction. Here, the mono-alkylated tin(IV)

complexes readily outperformed other tin(IV)-based catalysts (e.g. $SnCl_4$ and $Sn(OAc)_4$). In order to elucidate the structure of various mono-alkylated tin(IV) complexes (polymeric *n*-BuSnOOH and hexameric [*n*-BuSn(O)OAc]$_6$) in solution we studied their transformation in acetic acid at various temperatures. At an elevated temperature (90 °C), all complexes formed monomeric *n*-BuSn(OAc)$_3$ (Figure S2), while at reduced temperatures also water adducts of this complex were detected. In ethanol monomeric *n*-BuSn(OAc)$_3$ was partially converted into dimeric (*n*-BuSnOAc$_2$OEt)$_2$ (Figure S2). During catalytic experiments using a 1:1 mixture of acetic acid and ethanol, an equilibrium between the previously identified monomeric *n*-BuSn(OAc)$_3$ and dimeric (*n*-BuSnOAc$_2$OEt)$_2$ emerged. These findings reveal that while the stoichiometric chemistry of *n*-butyltin(IV) carboxylates is dominated by the formation of multinuclear tin assemblies, during catalysis only monomeric and dimeric complexes are present. Additional DFT calculations provided support for a mononuclear mechanism, where *n*-BuSn(OAc)$_3$ and dimeric (*n*-BuSnOAc$_2$OEt)$_2$ are regarded as off-cycle species, and suggested that carbon-oxygen bond breaking is the rate determining step.

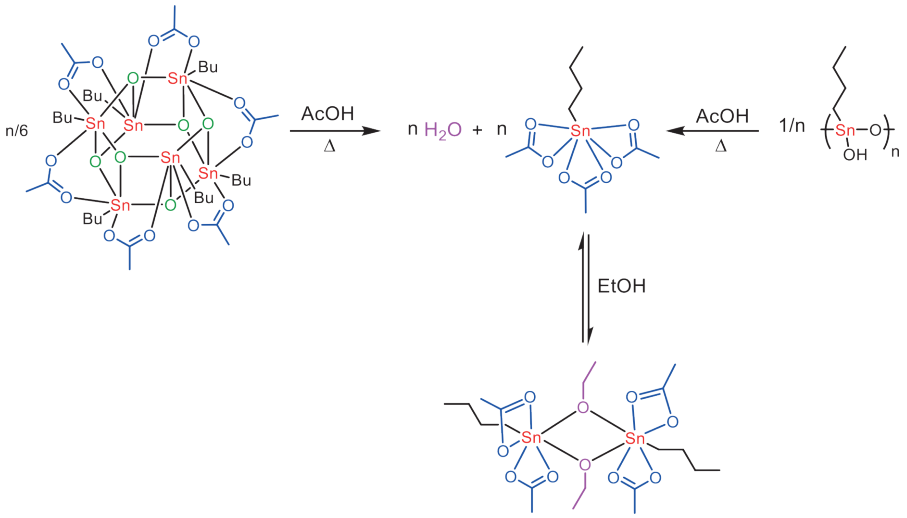

Figure S2. Reaction of mono-alkyltin complexes with acetic acid and ethanol.

In ***Chapter 4***, the reaction kinetics of titanium- and tin-catalyzed polyesterification are studied under different reaction conditions. Under neat conditions (polyesterification of 1,6-hexanediol and adipic acid at 170 °C, with removal of water via evaporation) the *n*-BuSnOOH catalyst displayed remarkable activity. Moreover, under these reaction conditions catalyst deactivation was not observed for *n*-BuSnOOH. In contrast, both the titanium-based catalysts (Ti(O^{i}Pr)$_4$ and Ti-atrane complex) performed comparable to the

reaction without metal catalyst. We also performed the same polyesterification reaction under azeotropic conditions (via the addition of xylene). At a reaction temperature of 140 °C, *n*-BuSnOOH still has the highest activity, but is outperformed in the initial phase of the reaction (first 2 hours) by the Ti-atrane complex. Further elevation of the temperature (to 150 °C) provided an effective azeotropic reflux over the whole reaction period and the water concentrations were significantly diminished. Under these conditions, $Ti(OiPr)_4$ was the most active catalyst and no catalyst deactivation was observed. These findings show that the catalytic performance is crucially determined by the robustness of the catalyst against hydrolytic degradation.

In ***Chapter 5***, we focused on the cross-coupling reaction of aryl halides and carboxylic acids. This reaction is a prime example of a challenging C-heteroatom bond formation that has been enabled by nickel catalysis. Similar to other nickel-catalyzed protocols for the synthesis of C-heteroatom bonds also this reaction is hampered by off-cycle pathways. In order to suppress these unwanted side reactions non-equimolar ratios of coupling partners are typically required. To gain mechanistic insight, including off-cycle pathways, we performed the nickel-catalyzed carboxylate *O*-arylation reaction in the presence and absence of an exogeneous 2,2'-bipyridine-ligand. We demonstrate that for the reaction in the absence of an exogeneous ligand, facile ligand exchange and reductive elimination steps exists (Figure S3).

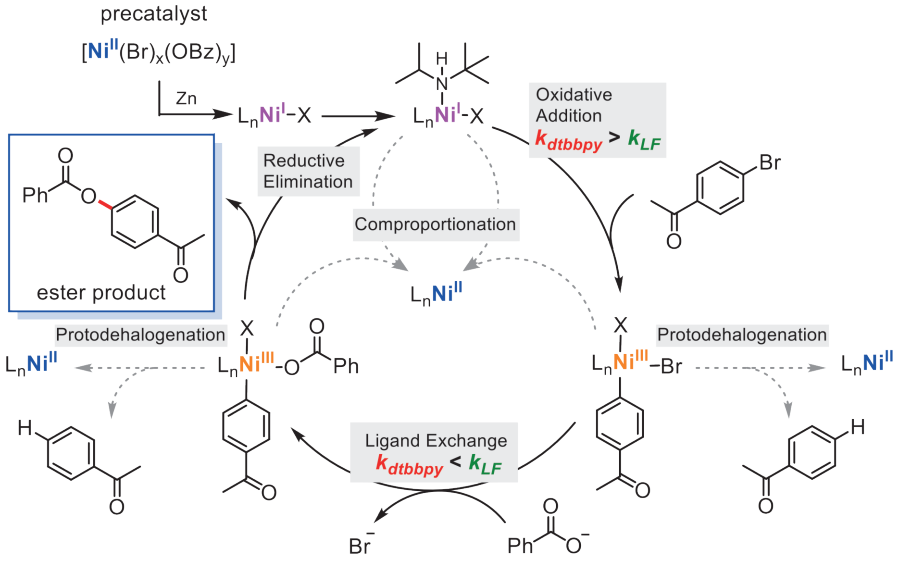

Figure S3. Mechanistic hypothesis for nickel-catalyzed carboxylate *O*-arylation.

Moreover, deleterious off-cycle protodehalogenation and comproportionation pathways are circumvented. Thereby this strategy enabled the formation of *O*-aryl esters from equimolar amounts of carboxylic acid and aryl halides. In contrast, for the (dtbbpy)$NiBr_2$-catalyzed reaction an excess of the carboxylic acid substrate is required to enhance the rate for ligand exchange and prevent unproductive comproportionation of Ni^{I} and Ni^{III}. Our subsequent spectroscopic investigation of the novel ligand-free (no exogeneous dtbbpy-ligand) catalytic system revealed that during catalysis the bulk of Ni^{II} is present in the form of $[Ni(Br)_x(OBz)_y]$, yet for catalysis an alkylamine base was essential. Therefore the catalytically active complex is likely a minor nickel complex where the base functions as ligand. For the reduction of the Ni^{II}-precursor, in the absence of aryl halides, we identified a Ni^{I}-Ni^{II} dimer as the reaction product. Moreover, this bimetallic complex was found to be reactive towards aryl bromides.

In ***Chapters* 2**, ***3*** and ***4*** we performed spectroscopic, computational and kinetic studies to unveil the relationship between catalytic activity and structure of the *in situ* formed catalyst in direct esterification reactions. Our investigations show that catalytic performance is not solely determined by the Lewis acidity of the metal center. Ligands proved to play an important role in catalysis since they were found to function as an internal base and to form hydrogen bonds with substrates. Even ligands that are considered spectators have a distinct effect on the *in situ* formation of the active catalyst, as was demonstrated for the *n*-butyltin(IV) complexes, where the alkyl tail enforces a favorable seven-coordinate environment around the tin center. In the case of the titanium-based catalyst, the application of a multidentate ligand affords a catalyst that has a slight improved ability to withstand hydrolytic degradation. However, for these type of complexes the catalytic activity was generally lower because the ligand effectively shields the active metal center. Although it remains challenging to provide clear design rules for the development of novel Lewis acid catalyst based on abundant and non-toxic materials, we identified the following factors as requisite: 1) Lewis acidity of the metal center; 2) Facile ligand exchange reactions, hence a sterically uncongested metal center; 3) Robustness of the catalyst, particularly the ability to withstand hydrolytic degradation. Similar to the preceding chapters, ***Chapter 5*** provides fundamental insight into the catalytic cycle of an esterification reaction. Our studies uncover the competition between productive catalysis and deleterious off-cycle reaction pathways that exist for all fundamental elementary steps. These findings provide a better understanding of the commonly proposed self-sustained Ni^{I}/Ni^{III} catalytic cycle and are therefore relevant to many nickel-catalyzed C-heterobond formation reactions.

Samenvatting

De esterbinding is een belangrijke binding in organische moleculen die toepassing vinden als medicijnen, geurstoffen of plastics. Ondanks dat de directe koppelingsreactie van carbonzuren en alcoholen al meer dan een eeuw bekend is , is dit nog steeds de meeste gebruikte manier om de esterfunctionaliteit te synthetiseren. Deze chemische transformatie levert naast de gewenste esterbinding alleen water als bijproduct op. Echter, de ongunstige evenwichtscondities van deze reactie vragen om een overmaat van een van de reactanten of om dehydratatie van het reactiemengsel. Om (poly)esterificatieproducten te verkrijgen, vooral op industriële schaal, heeft dehydratatie via verdamping of azeotropische distillatie de voorkeur. Deze methode maakt het mogelijk om equimolaire reactanten te gebruiken maar vereist nog wel een hoge reactie temperatuur. Daarom is het gebruik van een katalysator, die de reactietemperatuur kan verlagen en daarmee milde reactieomstandigheden mogelijk maakt, zeer gewenst. Sterke Brønstedzuren zijn goede katalysatoren in de directe esterificatiereactie, maar hun toepassing heeft ook nadelen omdat deze zuren zeer corrosief zijn en ongewenste zijreacties kunnen katalyseren. De Lewiszuren daarentegen zijn milder en katalyseren enkel de koppeling van alcoholen en carbonzuren. Vanwege deze gunstige eigenschappen zijn Lewiszure metalen intensief onderzocht als katalysatoren in de directe esterificatiereactie. Ondanks dat vele metaalzouten effectieve katalysatoren zijn, blijft het begrip van hun katalytische activiteit beperkt. Mechanistische studies worden bemoeilijkt door de transformatie die de katalysator ondergaat in het reactiemengsel doordat alle reactiecomponenten (carbonzuur, alcohol en ester) kunnen coördineren aan het Lewiszure metaal. Deze verandering van de katalysator resulteert niet alleen in metaalcomplexen met een monomere structuur maar ook dimeren en clusters zijn bekend. Naast de directe (poly)esterificatiereactie hebben chemici een verscheidenheid aan reacties verkend die de esterbinding kunnen vormen. Een voorbeeld hiervan is de nikkel-gekatalyseerde vorming van een koolstof-zuurstofbinding uit een organische (pseudo)halide en een carbonzuur. Ook voor dit type reactie wordt het begrip van de katalytische cyclus gehinderd door vele zijreacties, bijvoorbeeld met de substraten, of (deactivatie)reacties.

In dit proefschrift hebben we de structuur van verschillende katalysatoren opgehelderd en intermediairen bestudeerd om zo een beter begrip van de katalytische cyclus te krijgen. Deze kennis draagt bij aan de ontwikkeling van nieuwe efficiënte esterificatiekatalysatoren gebaseerd op veelvoorkomende en niet-giftige metalen.

In ***hoofdstuk 1*** wordt een overzicht gegeven van verschillende Lewiszure homogene metaalkatalysatoren die in (poly)esterificatiereacties worden toegepast. Studies waarin getracht is de structuur van de katalysator op te helderen en onderzoeken die inzicht hebben geven in de katalystische cyclus worden besproken. Daarnaast worden nieuwe routes voor de synthese van de esterbinding behandeld met de nadruk op de nikkel-gekatalyseerde koppelingsreactie tussen arylhalides en carbonzuren.

In ***hoofdstuk 2*** wordt een mechanistische studie naar titanium(IV)-gekatalyseerde directe esterificatiereacties beschreven. Doordat onderzoek naar de veelgebruikte titaniumalkoxides bemoeilijkt wordt door ongecontroleerde ligand-uitwisselingsreacties, hebben wij voor deze studie de titanium-aminotrifenolaat complexen geselecteerd. De combinatie van een tetradentaat ligand en Ti(^{i}OPr)$_4$ resulteerde in verschillende robuuste C_3-symmetrische titaniumcomplexen met enkel een uitwisselbare isopropoxide groep in de apicale positie (Figuur 1). Tijdens de katalytische studie vonden we dat sterische hinder in de *ortho*-positie de katalyse vertraagd.

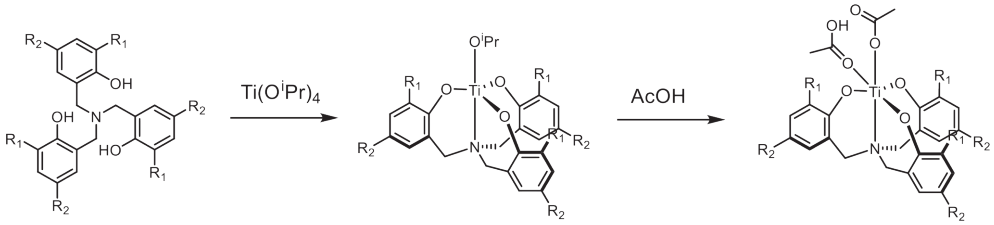

Figuur S1. Synthese van titanium aminotrifenolaat complexen.

Hierdoor is het titaniumaminotrifenolaat complex zonder sterische groep in deze positie de meest actieve katalysator, maar nog wel met een lagere activiteit dan Ti(^{i}OPr)$_4$. Op basis van *in situ* en stoichiometrische experimenten, concluderen we dat een amfoterische octahedraal titanium-aminotrifenolaat zuur/acetate complex de rusttoestand is tijdens katalyse. Op basis van kinetische experimenten en dichtheidsfunctionaaltheorie (DFT) berekeningen wordt een mononucleair reactiemechanisme voorgesteld. In dit mechanisme komen drie vereisten voor een actieve katalysator naar voren: de Lewiszuurgraad van het titanium(IV) metaal, gunstige waterstofbruginteracties tussen de reactanten en het ligand, en een Brønstedbasische groep die kan faciliteren bij protonoverdracht.

In ***hoofdstuk 3***, hebben we *n*-butyltin(IV) complexen onderzocht onder katalytisch relevante condities met behulp van verschillende spectroscopische technieken (ATR-FTIR, ^{119}Sn NMR, ^{1}H NMR). De uitzonderlijke activiteit van deze groep van (poly)esterificatiekatalysatoren wordt getoond in een modelesterificatiereactie. Hier hebben de mono-alkyl tin(IV) complexen een veel hogere activiteit dan andere op tin(IV) gebaseerde katalysatoren (zoals $SnCl_4$ of $Sn(OAc)_4$). Om de structuur in oplossing, van verschillende mono-alkyl tin(IV) complexen (polymerisch *n*-BuSnOOH en hexamerisch [*n*-$BuSn(O)OAc]_6$) op te helderen hebben we hun transformatie in azijnzuur bij verschillende temperaturen bestudeerd. Bij een verhoogde temperatuur (90 °C) vormen alle complexen het monomerische *n*-$BuSn(OAc)_3$ (Figuur S2), terwijl bij een lagere temperatuur ook wateradducten van dit complex werden gevonden. In ethanol wordt het monomerische *n*-$BuSn(OAc)_3$ complex gedeeltelijk omgezet in het dimerische (*n*-$BuSnOAc_2OEt)_2$ complex (Figuur S2). Voor een equimolair mengsel van azijnzuur en ethanol, ontstond er een evenwicht tussen het monomerische *n*-$BuSn(OAc)_3$ en dimerische (*n*-$BuSnOAc_2OEt)_2$. Deze bevindingen laten zien, dat ondanks dat de stoichiometrische chemie van *n*-butyltin(IV) carboxylaten wordt gedomineerd door de vorming van multinucleaire tin clusters, tijdens katalyse enkel monomerische en dimerische complexen aanwezig zijn in het reactiemengsel. Aanvullende DFT-berekeningen ondersteunen een mononucleair mechanisme, waar *n*-$BuSn(OAc)_3$ en (*n*-$BuSnOAc_2OEt)_2$ complexen zijn die buiten de katalytische cyclus liggen, en het breken van de koolstof-zuurstofbinding de reactiesnelheidsbepalende stap is.

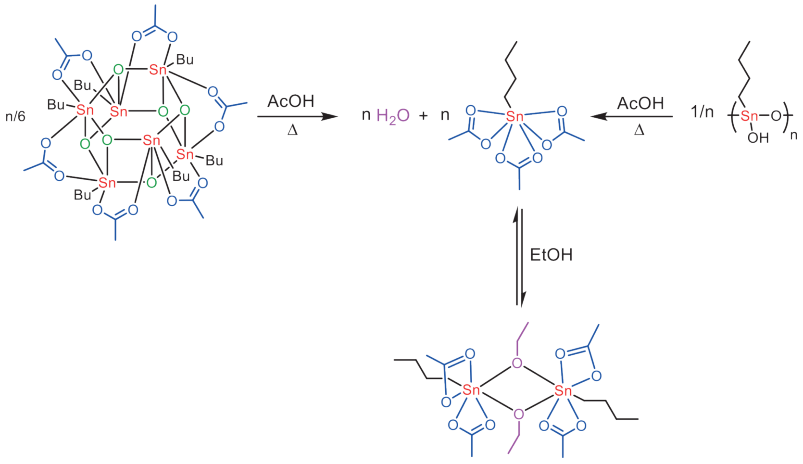

Figuur S2. Reactie van mono-alkyltin complexen met azijnzuur en ethanol.

In ***hoofdstuk 4*** wordt de reactiekinetiek van titanium en tin gekatalyseerde polyesterificatiereacties beschreven bij verschillende reactieomstandigheden. Bij oplosmiddelvrije condities (polyesterificatie van 1,6-hexaandiol en adipinezuur bij 170 ^{o}C met dehydratatie via verdamping) is de *n*-BuSnOOH katalysator bijzonder actief. Ook is er onder deze reactiecondities geen sprake van deactivatie van de *n*-BuSnOOH katalysator. Dit in tegenstelling tot de beide op titanium gebaseerde katalysatoren (Ti($O^{i}Pr$)$_4$ en Ti-atrane complex) welke een vergelijkbare activiteit hadden als de reactie zonder metaalkatalysator. Naast onder oplosmiddelvrije condities hebben we dezelfde reactie uitgevoerd onder azeotropische condities (door de toevoeging van xyleen). Bij een reactietemperatuur van 140 ^{o}C heeft *n*-BuSnOOH nog steeds de hoogste activiteit maar in de initiële fase van de reactie (eerste 2 uur) heeft het Ti-atrane complex een hogere activiteit. Verhoging van de reactietemperatuur (naar 150 ^{o}C) gaf een effectieve azeotropische reflux over de gehele reactie waardoor de waterconcentratie in het reactiemengsel significant werd verlaagd. Onder deze condities was Ti(OiPr)$_4$ de meest actieve katalysator en werd geen deactivatie van de katalysator waargenomen. Deze bevindingen laten zien dat katalytische activiteit sterk wordt bepaald door de robuustheid van de katalysator tegen hydrolytische degradatie.

In ***hoofdstuk 5*** onderzoeken we de koppelingsreactie van arylhalide en carbonzuren. Deze reactie is een voorbeeld van een lastig te vormen C-heteratoombinding,die mogelijk is geworden door nikkel-katalyse. Gelijk aan andere nikkel-gekatalyseerde protocollen voor de synthese van C-heteratoom bindingen, wordt ook deze reactie bemoeilijkt door reactiepaden buiten de katalytische cyclus. Om deze ongewenste zijreacties te onderdrukken zijn niet-equimolaire ratios van reactanten vaak vereist. Om inzicht te verkrijgen in de katalytische cyclus en zijreacties, hebben wij de nikkel-gekatalyseerde carboxylaat *O*-arylatie reactie uitgevoerd met en zonder de toevoeging van een exogeen 2,2'-bipyridine-ligand. We laten zien dat voor de reactie in de afwezigheid van een exogeen ligand er gemakkelijke liganduitwisseling en reductieve eliminatie stappen bestaan (Figuur 3). Bovendien worden protodehalogenering en comproportionering als ongewenste zijreacties onderdrukt. Dit in tegenstelling tot de (dtbbpy)$NiBr_2$-gekatalyseerde reactie waar een overmaat van het carbonzuur-substraat is vereist om de reactiesnelheid van ligand uitwisseling te verhogen en de onproductieve comproportioneringsstap van Ni^{I} met Ni^{III} te voorkomen. Ons daaropvolgende spectroscopische onderzoek van het nieuwe ligandvrije (geen exogeen dtbbpy ligand) katalytische systeem laat zien dat tijdens katalyse het grootste gedeelte van Ni^{II} aanwezig is in [Ni$(Br)_x(OBz)_y$] als rusttoestand. Voor katalyse bleek echter de alkylamine-base

essentieel. Daarom wordt het katalytisch actieve complex waarschijnlijk gevormd door een kleine hoeveelheid van een nikkel complex waar de base als ligand functioneert. Voor de reductie van de Ni^{II} rusttoestand, in de afwezigheid van arylhalogenide, hebben wij een Ni^{I}-Ni^{II} dimeer als reactieproduct geïdentificeerd, welke ook arylbromides kon activeren.

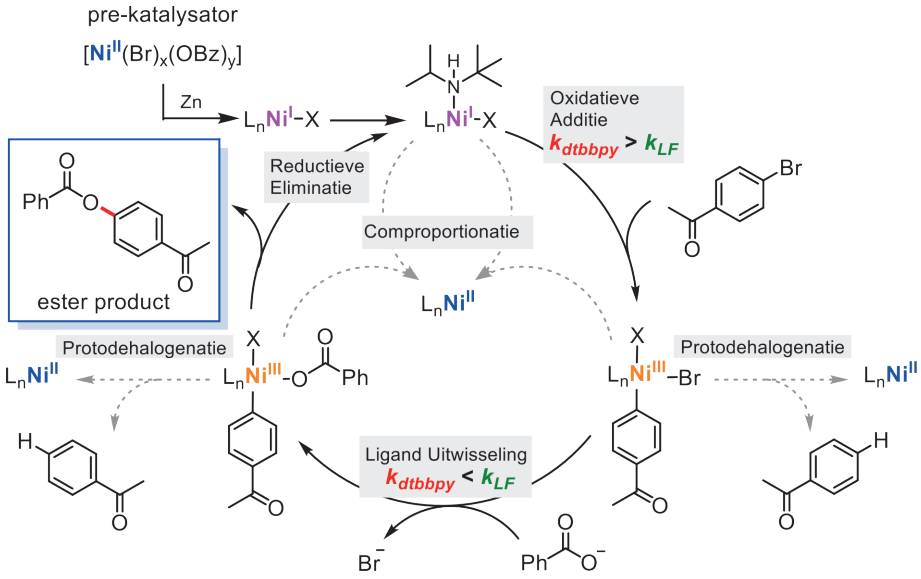

Figuur S3. Mechanistische hypothese voor nikkel-gekatalyseerde carboxylaat *O*-arylatie.

In de ***hoofdstukken 2***, ***3*** en ***4*** hebben we spectroscopische, computationele en kinetische studies uitgevoerd om de relatie tussen de katalytische activiteit en de structuur van de *in situ* gevormde katalysator in directe (poly)esterificatiereacties te onthullen. Ons onderzoek laat zien dat katalytische activiteit niet enkel wordt bepaald door de Lewiszuurgraad van het metaalcentrum. Liganden spelen een belangrijke rol tijdens katalyse omdat zij kunnen functioneren als interne base of waterstofbruggen kunnen vormen met de substraten. Zelfs liganden die traditioneel worden gezien als toeschouwers kunnen toch een effect hebben op de *in situ* vorming van de actieve katalysator. Zoals we laten zien voor de *n*-butyltin(IV) complexen waar de alkylstaart een gunstige zevengecoördineerde omgeving om het tinatoom forceert. Voor de op titanium gebaseerde katalysatoren geeft de toepassing van een multidentaat ligand een katalysator licht verhoogde stabiliteit tegen hydrolytische degradatie. Echter, voor dit type complex is de katalytische activiteit over het algemeen lager omdat het ligand het

actieve metaal centrum afschermt. Ondanks dat het een uitdaging blijft om heldere ontwerpregels voor de ontwikkeling van nieuwe Lewiszure katalysatoren gebaseerd op veelvoorkomende en niet-giftige metalen te geven, hebben we de volgende factoren geïdentificeerd als vereiste: 1) Een Lewiszuur metaalcentrum; 2) Gemakkelijke ligand-uitwisselingsreacties, een sterisch ongehinderd metaalcentrum; 3) Robuustheid van de katalysator, specifiek het vermogen om hydrolytische degradatie te weerstaan.

Gelijk aan de voorgaande hoofdstukken geeft ***hoofdstuk 5*** fundamentele inzichten in de katalytische cyclus van een esterificatiereactie. Onze studie laat zien dat er competitie bestaat tussen productieve katalyse en ongewenste zijreacties voor alle fundamentele elementaire stappen. Deze bevindingen geven een beter inzicht in de vaak voorgesteld zelfvoorzienende Ni^{I}/Ni^{III} katalytische cyclus en zijn daarmee relevant voor veel nikkel-gekatalyseerde C-heteroatoom binding-vormende reacties.

Dankwoord / Acknowledgements

Na iets meer dan vier jaar is het dan zo ver, het afronden van mijn proefschrift. Het uitvoeren van het onderzoek dat in dit proefschrift wordt besproken was niet mogelijk geweest zonder hulp. Daarom wil ik graag de mensen bedanken die mij hebben geholpen dit werk te voltooien.

Allereerst wil ik mijn promotoren **Moniek** en **Joost** bedanken. Beste **Moniek**, nu alweer 6 jaar geleden informeerde ik voor een masterstage bij jouw nieuwe groep in Amsterdam. Jij reageerde meteen enthousiast en voor ik het wist was ik onderdeel van de Sustainable Materials Characterization groep. Binnen de groep liet ons kennis maken met de bijzondere wereld van de X-ray technieken en stuurde ons langs de verschillende synchotrons van Europa. Het was een fantastische tijd! Dus toen jij informeerde of ik interesse had in promotieonderzoek hoefde ik daar ook niet lang over na te denken. Grote plannen waren er met verschillende onderzoeksvoorstellen maar helaas liet de financiering even op zich wachten. Gelukkig was er uiteindelijk dan toch een project dat van start kon gaan; onderzoek vanuit het ARC CBBC in samenwerking met AkzoNobel. Het onderzoek naar homogene katalysatoren voor de synthese van polyesters bleek een uitdagend project waar de X-ray technieken niet zo makkelijk op toe te passen waren. Totdat in de laatste maanden van mijn promotieonderzoek de synchotron toch opeens de beste optie om de rol van nikkel tijdens katalyse op te helderen. Via jouw contacten lukte het om midden in coronatijd af te reizen naar Engeland om metingen uit te voeren. Ik ben blij dat we zo toch onze eigen draai aan het onderzoek hebben kunnen geven en de “active site” in de spotlight hebben weten te zetten. Ik wens je veel succes met je onderzoekgroep in Groningen en wil je bedanken voor de begeleiding de afgelopen jaren.

Beste **Joost** in het begin van mijn promotieonderzoek wist ik me niet altijd goed raad met de vrijheid die jij gaf. Later kon ik deze aanpak meer waarderen en heeft het mij juist geholpen om mijn eigen ideeën te ontwikkelen. Hierdoor had ik het vertrouwen om zelf richting te geven aan het onderzoek en verder dan het originele project voorstel te kijken. Daarnaast hielpen jouw kritische vragen mij vaak weer in de juiste richting. Ook wil ik je bedanken voor de mogelijkheid om in mijn laatste jaar nog te verhuizen naar de HomKat groep. Waar ik me altijd zeer welkom en thuis heb gevoeld.

Beste **Ties** wat heb ik ongelofelijk veel van je geleerd! Ik weet nog goed dat ik in de eerste week van mijn masterstage toegaf dat ik al meer dan vier jaar niet meer op een lab had gestaan. Waarna jij tijdens de daarop volgende destillatie van PCl_3 mij er rustig doorheen

loodste. De hierop volgende jaren is er eigenlijk niet veel verandert, altijd was je bereid om suggesties te geven of een manuscript door te lezen. Jouw kennis van homogene katalyse, organometaalchemie en DFT waren onmisbaar voor het tot stand komen van dit proefschrift. Daarnaast heeft onze samenwerking geleid tot een aantal mooie publicaties. Ik heb genoten van het samen sleutelen aan de GC, de glovebox verbeteren met auto-onderdelen of de technische opdracht bij de stills. Naast de scheikunde delen we ook een passie voor het wielrennen met als jaarlijkse hoogte punt de Tour de France. Jouw tourpoule met de bijbehorende felbegeerde wissel labjassen was altijd weer een feest in het E-gebouw. Ties je hebt de rol van co-promoter met verve vervult! Bedankt hiervoor.

Beste **Keimpe** bedankt voor de begeleiding vanuit AkzoNobel. Jouw interesse en betrokkenheid bij het onderzoek, ook al was de toepassing soms ver weg, heb ik zeer gewaardeerd. Als start van het project had jij een week geregeld waarin ik het bedrijf mocht komen bezoeken. En in de afgelopen jaren was er altijd de mogelijkheid om samen met **Rogier** experimenten te doen in het polymeerlab in Sassenheim. Bovendien was AkzoNobel door jouw, **Jitte** en **Andre van der Linden** altijd goed vertegenwoordigd bij de CBBC meetings. Door deze aanpak heb ik een goed beeld gekregen van Akzonobel en besloten om hier ook te gaan werken.

Next, I would like to thank the members of my committee. **Roland Fischer**, thank you for being part of my comitte and taking the time to read my thesis. **Gertjan Gruter**, bedankt voor het deelnemen aan mijn promotiecommissie. **Jan van Maarseveen**, zoals velen heb ik genoten van de colleges organische chemie. Jouw bevlogenheid en enthousiasme waren zeer aanstekelijk. **Adri Minnaard**, bedankt voor het advies tijdens onze maandelijkse project meetings de afgelopen jaren. Het was altijd goed om een frisse blik te hebben op het onderzoek. **Chris Slootweg**, jouw onderzoek naar circulaire chemie heb ik altijd zeer inspirerend gevonden. **Bas de Bruin**, bedankt voor de kritische vragen, jouw inbreng in het laatste hoofdstuk van dit proefschrift en natuurlijk het mee brengen van de smeerolie.

Graag wil ik ook mijn collega's van de Sustainable Materials Characterization groep of te wel de "Trompetten" bedanken. **Bas** en **JP**, waar moet ik beginnen. Mannen wat hebben we een hoop mee gemaakt. Vele beamtime avonturen hebben we samen beleefd, die verplicht moesten beginnen met een biertje in de morgen op Schiphol. Opstap met het beruchte aluminium koffertje dat altijd weer door de douane moest worden geloosd. Nachten bij de synchotron met hamburgers uit de magnetron. Samen naar de X-ray conferentie in Krawkow of skiën bij Les Deux Alpes. Ik wil jullie graag bedanken voor de

fantastische tijd en ben dan ook blij dat jullie mijn paranimfen willen zijn. **Andreas** naast NMR specialist was jij toch vooral onze vaste gids tijdens de mannenavonden en ons mee opstap nam in Amsterdam en Berlijn. Ook heb Ik heb jouw ongezouten mening en kritische blik als wetenschapper kunnen waarderen. **Michelle** bedankt voor de gezelligheid op werk en tijdens de meettijden. Ik heb genoten van de tour tochtjes op de racefiets. **David** our X-ray expert who taught us everything about synchrotrons. I will never forget our ride to Switzerland with a car packed with chemicals and a fire extinguisher under my seat. **Dorette**, bedankt voor alle goede zorgen en het onderhoud aan ons lab.

Daarnaast wil ik ook graag de andere leden van Lab E0.09 bedanken. **Joen**, hoe jij de wetenschap bedrijft en dingen grondig uitzoekt heb ik altijd inspirerend gevonden. Jouw kennis van infraroodspectroscopie en metaalcarboxylaten kwam goed van pas binnen mijn onderzoek. Ik wil je dan ook bedanken voor de plezierige samenwerking. Daarnaast was het leuk om af en toe samen een rondje te wielrennen, waarbij ik toch vooral jouw achterwiel mocht zien. **Lambert**, het was altijd gezellig om samen met jouw op het lab te staan of koffie te drinken bij de apenrots. Na de vrije school en promotieonderzoek aan de UvA lopen onze levens nu weer synchroon bij AkzoNobel. Leuk dat we ook daar elkaar weer tegen komen. **Ed**, door jouw ben ik in gaan zien wat voor een mooie techniek massaspectrometrie is en dan natuurlijk vooral FD. Hierdoor wilde ik graag zelf kunnen meten, en onder jouw begeleiding lukte het om van vele metaal complexen prachtige MS-spectra te verkrijgen. Daarnaast heb ik genoten van het squash en padel spelen.

Ook wil ik graag mijn collega's van de HomKat groep bedanken, die mij zo liefdevol hebben geadopteerd. **Pim**, altijd voorzien van de laatste roddels bij de koffieautomaat. Natuurlijk zal ik nooit vergeten hoe jij mij het OLVG insloeg met een squashracket. **Felix** de closer, hosselaar, paperspinner, EPR-koning, bbq-meister, culinair kenner en aanvoerder van het HomKat zaalvoetbalteam. Je bent een man met vele talenten. Jouw geloof en opportunisme hebben zeker geholpen bij het afronden van het laatste hoofdstuk. Bedankt hiervoor. **Eva**, de epoxide koningin bedankt voor de DFT lessen. Helaas bleek al snel dat ik een digibeet was. **Nicole**, mede bewoner van Amsterdam-west. Het was altijd gezellig om samen de stad te door kruisen. **Pieter**, de man met de mooie verhalen over Hoogkarspel. Daarnaast weet je altijd weer het lab om te toveren tot een bruine kroeg met jouw voorliefde voor Hazes. Laten we snel maar weer een keer naar de Ruk en Pluk gaan. **Eline**, de onbetwiste labchief van E1.18 en bewaker van de vrijdagmiddag scooter megamix, succes met de laatste lootjes. **Bin**, my other neighbour at E1.18, your column skills were incredible. **Daniel**, I really like your organometallic chemistry but don't forget to use the

redox non-innocent ligands. Also, our favorite tour guide for good Chinese food preferable at Fulu. **Jianghua**, keep up the good work and don't be afraid for the organolithium reagents. **Valentinos** the porphyrin master, I always enjoyed our conversations during the borrels. **Demmy**, wat leuk dat we nog heel even samen op het lab hebben kunnen staan. Succes met de electrochemie. **Eddy**, cagemaster and mass magician, all the best with your incredible cage adventures. **Lotte**, het was altijd erg gezellig tijdens de CBBC meetings(borrels) en de term molecular mold zal ik nooit vergeten. **Rens**, de man die de meeste bellen heeft geteld, vergeet de triplo's niet! **Tom**, cage-chemie op een ander niveau. Zo groot dat ze niet meer gemeten kunnen worden maar wel heel mooi. **Wojciech**, Polish Power, thank you for the electrochemistry training and the good conversations. **Marie**, wat ben jij een harde werker. Vaak kwam ik je op de zaterdag tegen op Science Park. Succes met je onderzoek. **Tessel**, super cool dat de electron shuttle bus echt is gaan rijden. Heel veel plezier in Cambridge. **Tijmen**, heel veel succes met het opzetten van je start-up met de dye-synthesized solar cells. Daarnaast was het leuk om samen de CAIA cursus te mogen volgen. **Didjay**, hele mooie zonnencellen heb je in elkaar gezet, vooral de oranje gel natuurlijk. **David**, always nice talking to you about cool NMR techniques. **Xander**, altijd behulpzaam. **Roel**, jouw inzet en doorzettingsvermogen zijn bewonderenswaardig, eigenlijk moet er nog een groot cobalt-TPP feest komen. **Johan**, mooi om te zien hoe jij het andere CBBC project met AkzoNobel hebt ingevuld. Ook heb ik genoten van je optreden als Sinterklaas. **Jasslie**, heel veel succes met de kooien en de fotochemie. **Minghui**, you are such a kind person. Thank you for involving me in your amazing cobalt-TPP ring chemistry. **Cat**, your drawings are beautiful and I always enjoyed your cat pictures during your HomKat presentations. **Klaas**, wat hebben we gelachen tijdens de CAIA cursus. **Lukas**, leuk dat we nu collega's zijn bij AkzoNobel. **Joeri**, als een kanonskogel de berg af bij Les Deux Alpes. **Marianne**, bedankt voor alle goed gesprekken. **Simon**, thanks for all the support and fun times. **Fatna**, dankjewel voor alle ondersteuning op de achtergrond. **Sander**, altijd mooie verhalen over het Roeterseiland, die goede ouwe tijd. **Zohar**, keeping the music in tune at E1.05. **Xavier**, always available for a nice conversation. **Jarl Ivar**, bedankt voor jouw kritische blik op mijn onderzoek. **Tiddo**, ik heb genoten van de discussies bij de koffieautomaat. **Sonja**, great that you joined the HomKat group. All the best with your research.

Graag wil ik mijn familie en vrienden bedanken. Ook al was het onderwerp van katalyse en esters maken behoorlijk abstract toch hebben jullie de afgelopen jaren altijd interesse getoond in mijn (studie) onderzoek. Met een vraag over AkzoNobel, verf, duurzaamheid,

het groeien van kristallen of het publiceren van artikelen lieten jullie je betrokkenheid zien. Bedankt hiervoor.

Tot slot wil ik diegene bedanken die de afgelopen jaren altijd aan mijn zijde stond. Lieve **Gera** natuurlijk zijn we een heel goed team, maar er is meer dan dat. Jij geeft mij het vertrouwen en de motivatie om door te gaan en vooral meer uit mezelf te halen. Dit geldt natuurlijk niet alleen voor het promotieonderzoek. **Gera** Ik hou ontzettend veel van je en hoop dan ook op een mooie toekomst samen.

List of publications

Publications related to this thesis

1. **Titanium-catalyzed esterification reactions: beyond Lewis acidity.**
L.A. Wolzak[1,2,3,7,8], J.I. van der Vlugt[6,7,8], K.J. van den Berg[1,7,8,9], J.N.H. Reek[1,7,8,9], M. Tromp[1,7,8,9], T.J. Korstanje[1,3,7,8,9], *ChemCatChem*, **2020**, 12, 5229-5235.

2. **Mechanistic elucidation of monoalkyltin(IV)-catalyzed esterification.**
L.A. Wolzak[1,2,3,7,8], J.J. Hermans[1,7], F. de Vries[6], K.J. van den Berg[1,7,8,9], J.N.H. Reek[1,7,8,9], M. Tromp[1,7,8,9], T.J. Korstanje[1,3,7,8,9], *Catal. Sci. Technol.*, **2021**, 11, 3326-3332.

3. **Kinetic Studies on Lewis Acidic Metal Polyesterification Catalysts – Hydrolytic degradation is a Key Factor for Catalytic Performance.**
L.A. Wolzak[1,2,7,8], R. van Gemert[2], K.J. van den Berg[1,7,8,9], J.N.H. Reek[1,7,8,9], M. Tromp[1,7,8,9], T.J. Korstanje[1,7,8,9], *Catal. Sci. Technol.,* **2022**, 12, 2056-2060.

4. **Ligand-free nickel-catalyzed carboxylate *O*-arylation: Mechanistic insight into Ni^{I}/Ni^{III} cycles.**
L.A. Wolzak[1,2,5,7,8], J.H. Oudsen[7], F.J. de Zwart[4,7,8], S.A. Bartlett[5,7], B. de Bruin[4,7,8], J.N.H. Reek[1,7,8,9], M. Tromp[1,7,8,9], T.J. Korstanje[1,7,8,9], *Manuscript in preparation*.

1. Conceptual ideas
2. Laboratory work
3. DFT calculations
4. EPR measurements
5. XAS measurements
6. Single crystal XRD measurments
7. Data interpretation
8. Manuscript preparation
9. Project supervision

Publications outside this thesis

1.**Spectroscopic investigation of the activation of a chromium-pyrrolyl ethene trimerization catalyst.** B. Venderbosch, J.H. Oudsen, L.A. Wolzak, D.J. Martin, T.J. Korstanje, M. Tromp, *ACS Catal*. **2019**, 9, 1197-1210.

2. **Role of the ligand and activator in selective Cr-PNP ethene tri- and tetramerization catalysts: a spectroscopic study.** B. Venderbosch, L.A. Wolzak, J.H. Oudsen, T.J. Korstanje, M. Tromp, *Catal. Sci. Technol.,* **2020**, 10, 6212-6222.

3. **Catalytic Synthesis of 1*H*-2-Benzoxocins: Cobalt(III)-Carbene Radical Approach to 8-Membered Heterocyclic Enol Ethers.** M. Zhou, L.A. Wolzak, Z. Li, F.J. de Zwart, S. Mathew, B. de Bruin, *JACS*, **2021**, 143, 48.

4. **Phosphorus: Reserves, production, and applications**. M.A. de Boer, L.A. Wolzak, J.C. Slootweg, In: Phosphorus Recovery and Recycling. Springer Singapore, **2018**.